Stability of rigid and deformable roll coating flows

Martin John Gostling

Submitted in accordance with the requirements for the degree of

Doctor of Philosophy

The University of Leeds

Department of Physics and Astronomy

September 2001

The candidate confirms that the work submitted is his own and that appropriate credit has been given where reference has been made to the work of others.

ACKNOWLEDGEMENTS

Firstly, I would like to express my sincere thanks to my supervisor, Prof. Savage for his constant support and encouragement. I would also like to thank Prof. Gaskell for his role as Principal Investigator on the grant.

I would like to thank my friends and colleagues in the department of Physics and Astronomy and in particular to Chris and Dom for making my stay here so enjoyable.

Special thanks are due to my wife Alex for all her love and support and for putting up with me these last few months! Special thanks are also due to my parents, Richard and Barbara, and my family for all that they have done for me over many years.

Finally, I would like to thank the University of Leeds for awarding me a scholorship.

ABSTRACT

This thesis is concerned with developing suitable models for the investigation of instabilities in rigid and deformable roll coating flows. Consideration is restricted to Newtonian, incompressible fluids in the absence of inertia. In each coating flow analysed the steady two dimensional base state solutions of the system are explored before the stability of the system is considered.

The particular rigid roll coating flow that is studied in this thesis is the flow formed between an intermediate pair of contra-rotating rolls within a multiple roll coater. The base state is modelled using lubrication theory and the flow domain is terminated with simple boundary conditions. It is found that the form of the meniscus location solutions differ from those found in similar flows by previous workers and this motivates a detailed re-examination of the boundary conditions. A matched asymptotic analysis applicable for small capillary numbers Ca and small inter-roll gaps gives the leading order correction to the boundary conditions and it is found that the inclusion of the correction terms alter the results significantly. It is found that a critical roll speed ratio, S_c, exists beyond which no steady two dimensional solutions exist. A simple stability hypothesis predicts the upstream meniscus to be neutrally stable at S_c and this point is associated with bead break. Under certain operating conditions the stability hypothesis predicts multiple steady states.

The linear stability of this multiple roll coating flow is investigated. Special attention is given to the relationship between the wavelength of the disturbance and the form of the boundary conditions. The main predictions of the stability hypothesis are confirmed and an additional ribbing instability on the downstream meniscus is predicted.

The base flow of a deformable roll coater is investigated using lubrication theory for the fluid and a linear elastic plain strain model for the compliant layer. The boundary conditions developed for the multiple roll problem are extended to higher values of Ca. A finite element method is developed to numerically solve the governing equations. The effects of Youngs modulus E and layer thickness L on the steady state operation of the coater are investigated. Previous workers have used spring models to describe the compliant layer with the implicit assumption that E and L^{-1} have the same affect. Here it is shown that E and L^{-1} have a different effect upon the meniscus location in

the negative gap regime and hence the underlying assumption of all spring models is shown to be incorrect. The plain strain model is extended to include viscoelastic terms and it is shown that these terms can account for the discrepancy between experimental results and previous steady state elastic theories.

The linear stability of the deformable roll coater is investigated with the plain strain model being extended to account for lateral disturbances. The effect of E and L^{-1} on the stability of the system is investigated and it is found that in keeping with the steady state results, they have a different effect on the stability of the system in the negative gap regime. It is demonstrated that perturbations to the compliant layer play a negligible role in the stability analysis and it is shown how the viscoelastic extension to the base state can be incorporated.

PUBLICATIONS

GOSTLING, M. J., SAVAGE, M. D., & WILSON, M.C.T. 2001 Flow in a double-film-fed fluid bead between contra-rotating rolls Part2: bead break and flooding. *Euro. Jnl of Applied Mathematics* **12** 413–431.

SAVAGE, M. D., GOSTLING, M. J., GASKELL, P. H. & YOUNG, A. E. 2001 A model for deformable roll coating with negative gaps and incompressible compliant layers. *Accepted for publication J. Fluid Mech.*

GOSTLING, M. J. & SAVAGE, M. D. 2001 Linear stability analysis of deformable roll coating flows. *In preperation J. Fluid Mech.*

Contents

List of Figures

List of Tables

Chapter 1

Introduction

There are many situations in industry where a substrate is to be covered, or 'coated', with a continuous fluid layer as part of a manufacturing process; examples include the production of photographic film, lithographic plates, computer disks and television screens. The industrialist seeks to apply the fluid film quickly and evenly yet these two objectives are often incompatible since the faster the process is run, the less uniform the film becomes. It is the aim of this thesis to further our understanding of fluid flow in two particular coating processes - deformable roll and multiple roll coating.

1.1 Coating Processes

Coating processes are many and varied, figure 1.1 shows just a few examples. The spin coater (figure 1.1c) is suitable for the coating of discrete objects, e.g. computer disks, whereas the other examples are used when there is a continuous supply of the substrate through the coater. An example of this type of process is the production of photographic film; the film is coated before being cut for use in individual cartridges. In all such flows there are two features that are of overriding importance to the operator:

- the relationship between the operating conditions and the final layer thickness;
- flow stability and hence the uniformity of the coated layers.

The importance of having some control of both these features is clear since error in either could lead to the production of faulty goods. Since the coating process is often

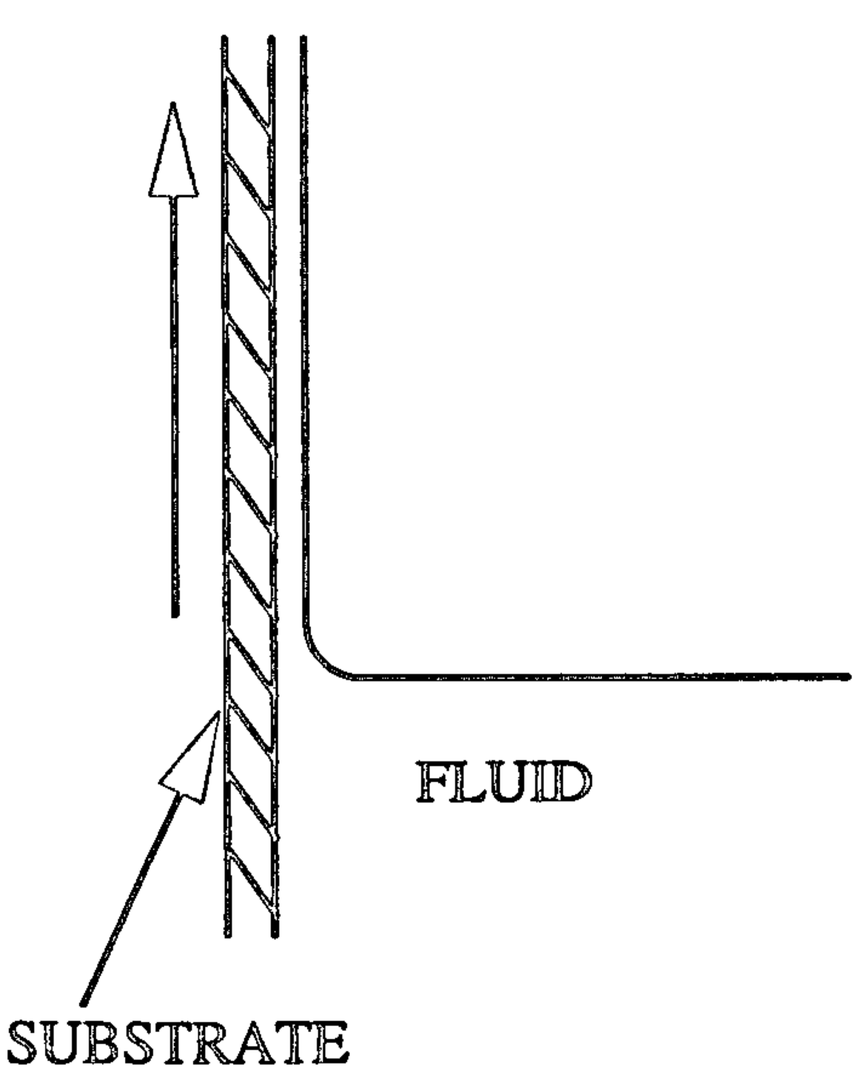

(a) Dip coater.

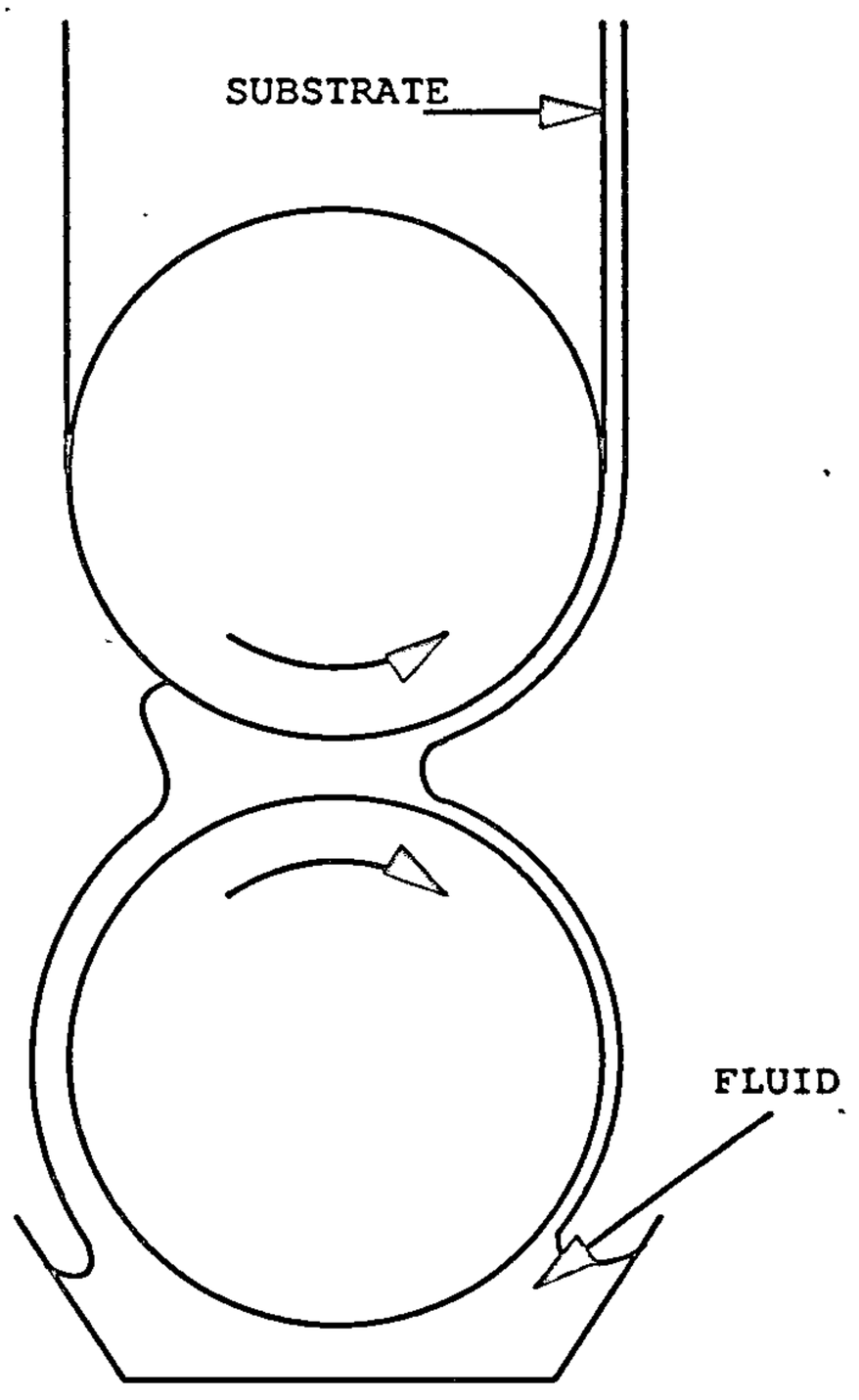

(b) Roll coater

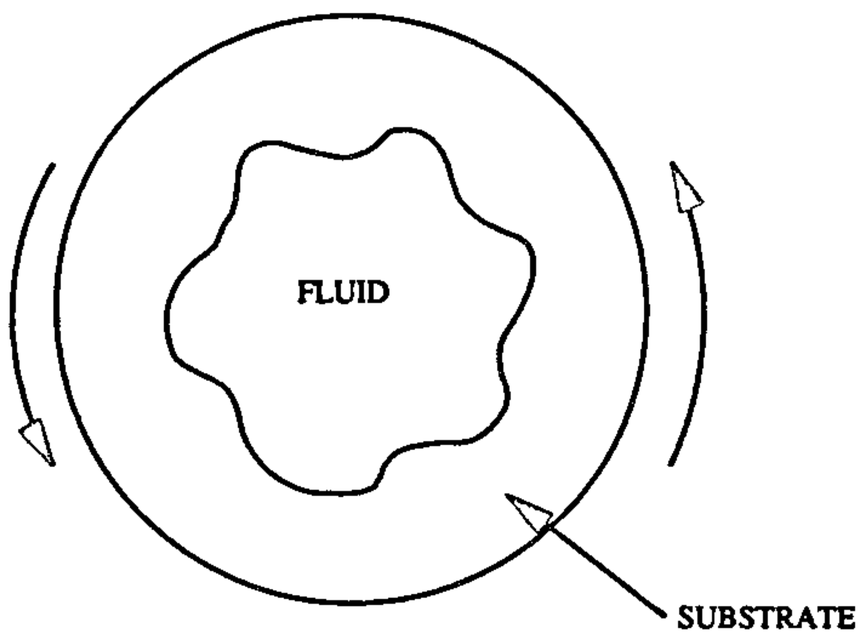

(c) Spin coater

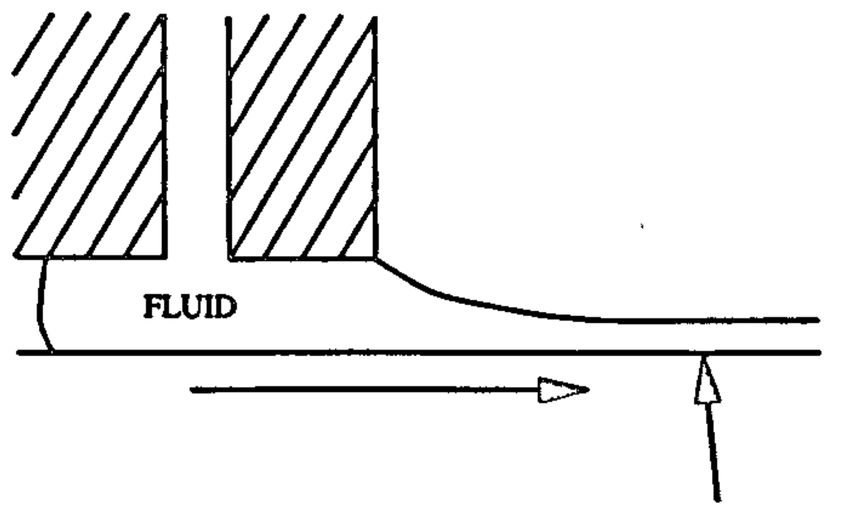

(d) Slot coater

Figure 1.1: Schematics of several industrial coating processes.

the slowest part of the production line, a detailed understanding of the coating flow will allow the coater to be run at its optimum rate, increasing overall productivity.

As well as being industrially important, many of the coating flows contain features that are of inherent interest from a purely academic standpoint and examples include linear and nonlinear instabilities, contact line dynamics and chaotic mixing. Due to the combination of academic interest and industrial importance there exists a substantial literature which is aimed at understanding the above features and the approaches taken range from detailed analytical models, through computer intensive simulations to experimental investigations.

As this thesis deals with two types of roll coater the roll coating process is now looked at in more detail.

1.2 Roll Coating

Roll coaters come in many different configurations and the simplest configuration consists of a pair of counter-rotating rigid rolls (a 'forward roll pair') as shown in figure 1.2. In this case the lower roller (pickup roller) withdraws fluid from the supply bath and transfers it to the substrate or web that rotates with the upper roller. Even this simple case of roll coating has two very distinct modes of operation; a starved mode and a fully flooded mode as shown in figure 1.2.

In the starved mode (figure 1.2a), often refered to as meniscus roll coating, a fluid bead is formed in the nip (the point of closest approach of the rollers) region. The alternative mode of operation is refered to as 'fully flooded' (figure 1.2b) since a build up of fluid upstream of the nip forms a significant reservoir of fluid. The intermediate state is refered to as 'moderately starved'. This straightforward setup can be radically changed by simply changing the direction of rotation of one roller to form a 'reverse roll pair' for which the above modes of operation also exist. The roll coaters analysed in this thesis operate in the forward mode.

In practice, there are often several intermediate rollers situated between the first and last rollers thus forming a multiple roll coater. The multiple roll coater shown in figure 1.3 is operating in the starved regime and it is this situation that provides the first of the problems considered in this thesis. The flow that is of interest here is the

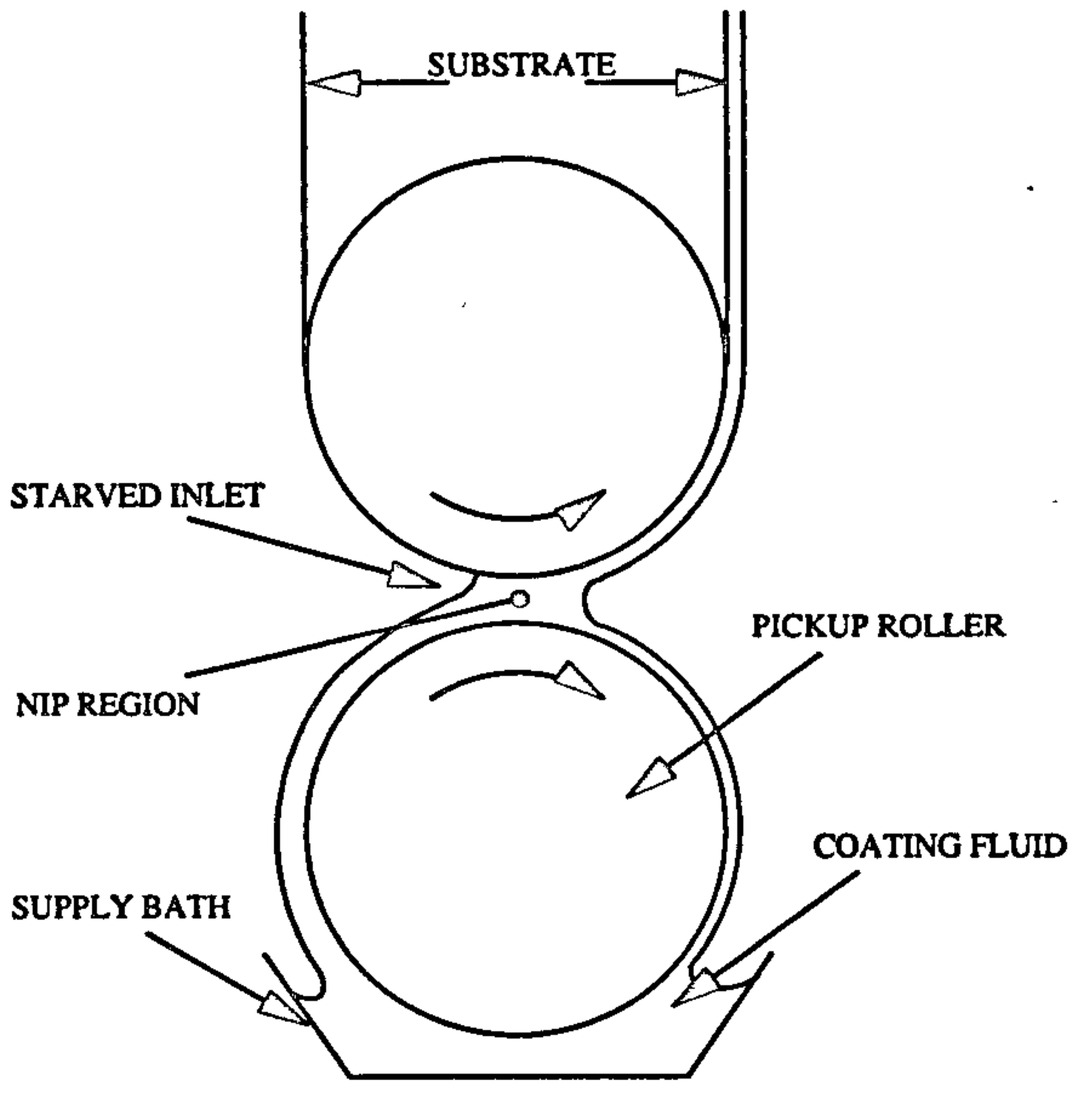

(a) Starved

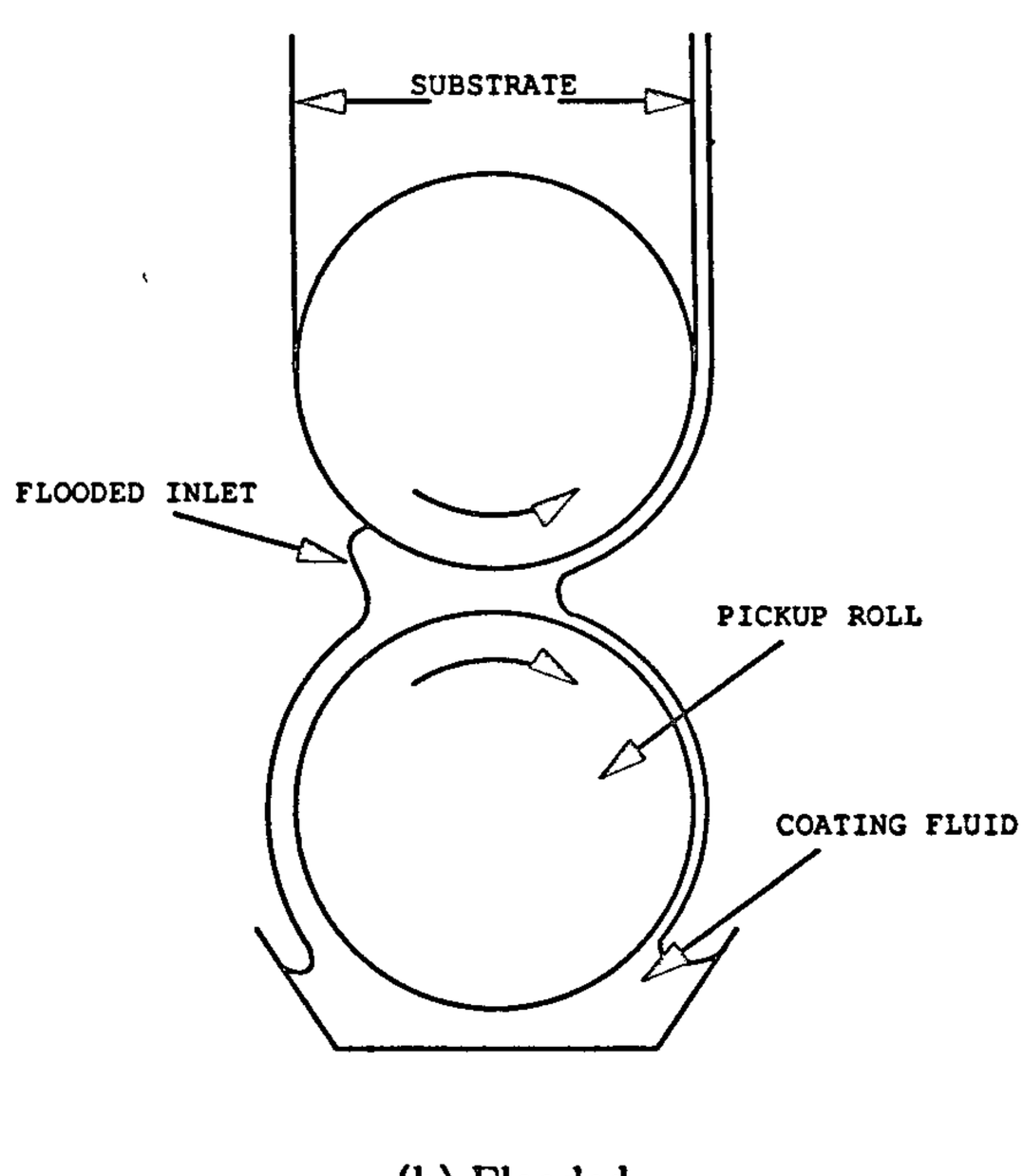

(b) Flooded

Figure 1.2: A forward roll coater operating in the (a) starved and (b)flooded regimes.

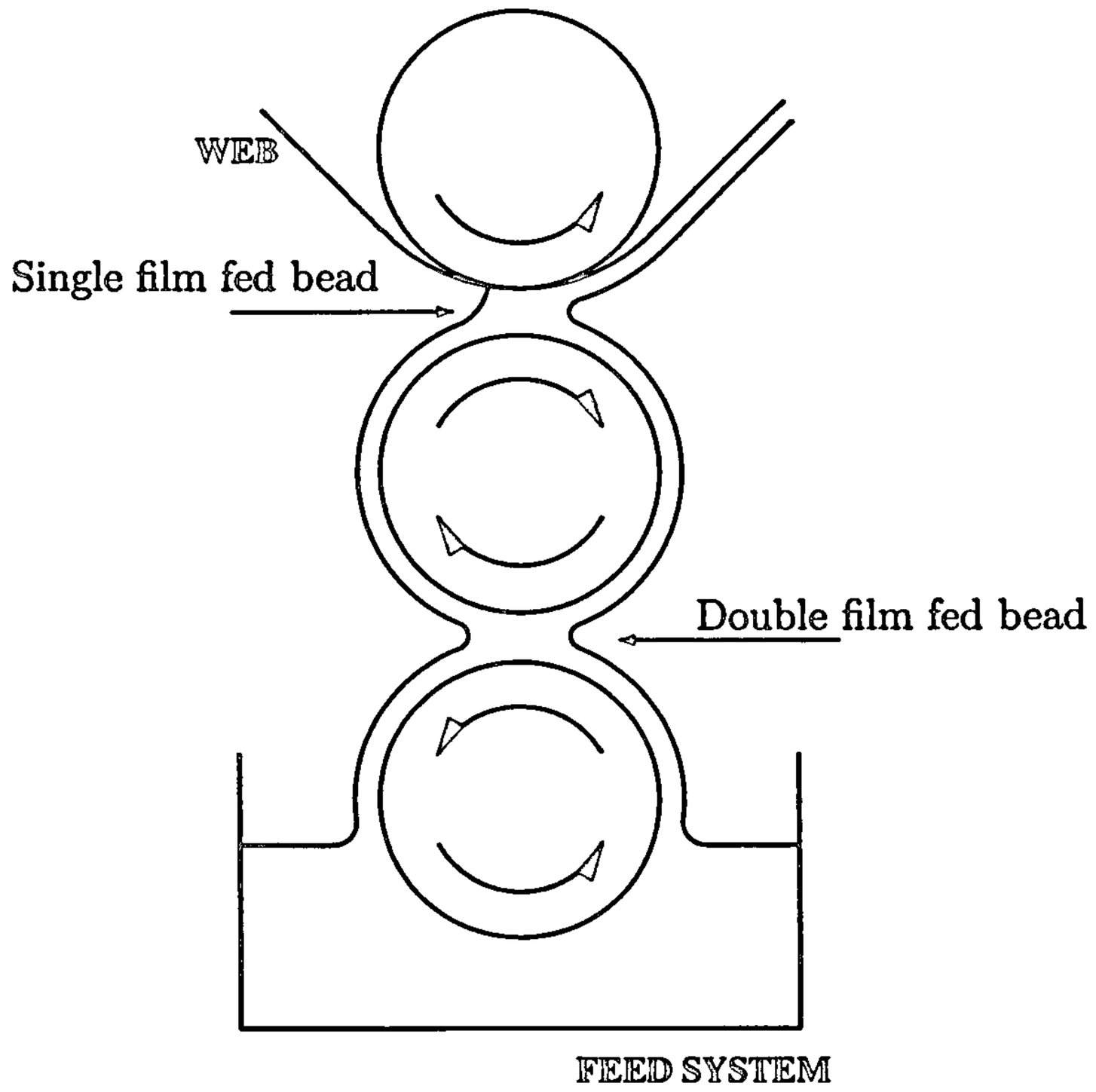

Figure 1.3: A mulitple roll coater operating in the starved regime.

flow generated between any pair of rollers (except the final roll pair) in such a multiple roll coater. This flow differs from that in a simple meniscus roll coater shown in figure 1.2 as a bead formed between any two adjacent rollers (except for the final roll pair) in a multiple roll coater will have an incoming fluid layer on each roller. This is in contrast to the meniscus coater or final roll pair in a multiple roll coater where there is one roller with a solid/fluid contact line. These two arrangements are refered to as double film fed (DFF) and single film fed (SFF), respectively. The fact that the contact line in the SFF bead is replaced with another incoming film in the DFF bead alters the structure of the flow and therefore the standard meniscus roll coating results, concerned with a two roll system (or the final roll pair in a multiroll coater), are invalid.

A further variation on the roll coating theme is to cover one or more of the rollers in a coating system with a compliant layer, an example of which is shown in figure 1.4. The compliant or deformable layer is often made from an elastomer which allows the rollers to be pressed together with the aim of producing a thinner final coated film thickness than can normally be achieved by rigid roll coating. In a deformable

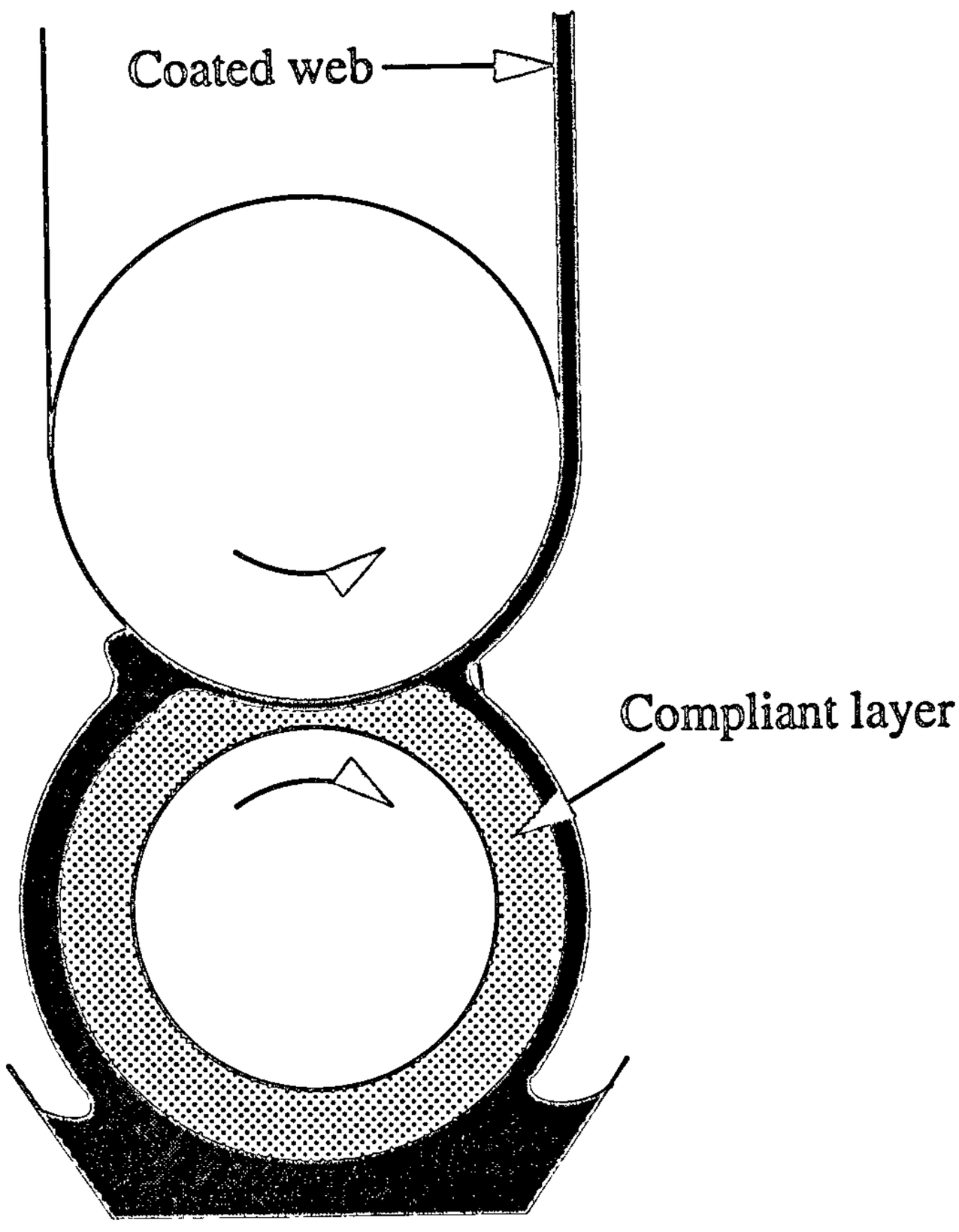

Figure 1.4: A deformable roll coater operating in the forward mode.

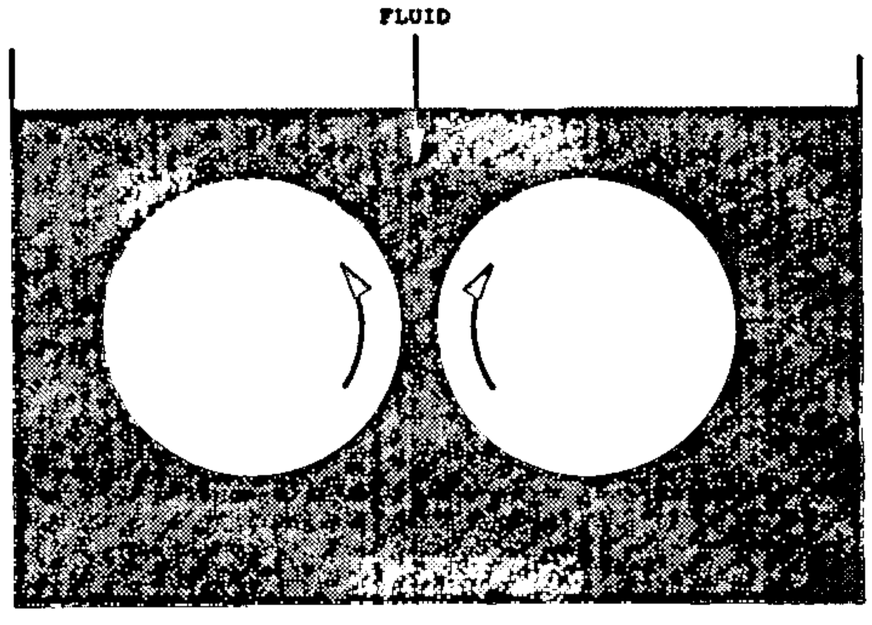

Figure 1.5: A fully flooded counter-rotating roll pair.

roll coater, the fluid and solid domains are coupled; the fluid pressure deforms the solid, which changes the profile of the gap thickness and this, in turn, affects the fluid pressure. It is this coupling of two distinct domains that provides the challenge when modelling deformable roll systems.

The following section contains a review of the rigid roll coating literature and in particular explains how lubrication theory has been used to model rigid roll systems. Section 1.4 contains a review of multiple roll coaters and section 1.5 includes a review of the deformable roll coating literature. The instabilities that affect roll coating flows are explained in section 1.6.

1.3 Rigid Roll Coating

As an introduction to rigid roll coating the case of a pair of equal speed counter-rotating rolls, each of radius R and fully immersed in fluid as shown in figure 1.5, will be considered. If the rolls are in close proximity, the flow in the nip region is almost rectilinear and therefore the lubrication theory of Reynolds (1886) is valid in this region. Assuming that there is no component of fluid velocity parallel to the axis of the rolls, lubrication theory leads to Reynolds equation for the fluid pressure, $P(X)$, in the nip region between the two rolls:

$$\frac{\mathrm{d}}{\mathrm{d}X}\left[B^3(X)\frac{\mathrm{d}P}{\mathrm{d}X}\right] = 12\mu U_R\frac{\mathrm{d}B}{\mathrm{d}X}. \tag{1.1}$$

X is the coordinate along the line of symmetry that runs through the gap between the two rolls, $B(X)$ is the gap width, U_R is the peripheral speed of the rollers and μ is the fluid viscosity. Reynolds equation has been used by many workers including Coyle et al.

(1986) and Gaskell et al. (1995) to model flows in roll coating geometries. Reynolds equation can also be written as

$$\frac{\mathrm{d}P}{\mathrm{d}X} = \frac{12\mu}{B^3}\left(U_R B - Q\right), \tag{1.2}$$

where Q is the flux past any X station. With increasing distance from the nip the fluid pressure decays to ambient (Rushack (1982)) which is taken in this thesis to be zero without loss of generality and so the following boundary conditions are imposed:

$$P(\pm\infty) = 0. \tag{1.3}$$

One further simplification is made and that is to use a parabolic approximation for the gap width:

$$B(X) = 2B_0 + \frac{X^2}{R}, \tag{1.4}$$

where $2B_0$ is the distance of closest approach between the rolls and R is the roll radius. For this parabolic approximation to be accurate it is required that $B_0/R \ll 1$ which is the case for roll coating flows. Under these conditions Reynolds equation can be solved analytically and a typical solution curve is shown in figure 1.6. The positive pressure upstream of the nip is caused by the convergent geometry whereas downstream, the diverging gap results in the pressure being sub-ambient.

The next step in modelling a roll coating flow is to replace the fully flooded flow downstream of the nip with a meniscus to give a flow of the form shown in figure 1.7. As the condition $P(+\infty) = 0$ is no longer valid two new conditions have to be found; a pressure balance at the meniscus and also a condition to locate the position of the meniscus. Several boundary conditions have been proposed and these are now reviewed.

1.3.1 Boundary Conditions

Working on the assumption that the fluid cannot support negative pressures due to the occurence of gaseous cavitation, Swift (1931) and Stieber (1933) independently suggested the following conditions:

$$P(X_D) = \left.\frac{\mathrm{d}P}{\mathrm{d}X}\right|_{X_D} = 0, \tag{1.5}$$

where X_D is the location of the meniscus. These conditions are refered to as the Swift-Stieber (SS) conditions or the Reynolds conditions and solving Reynolds equation subject to them gives a pressure field that is everywhere positive.

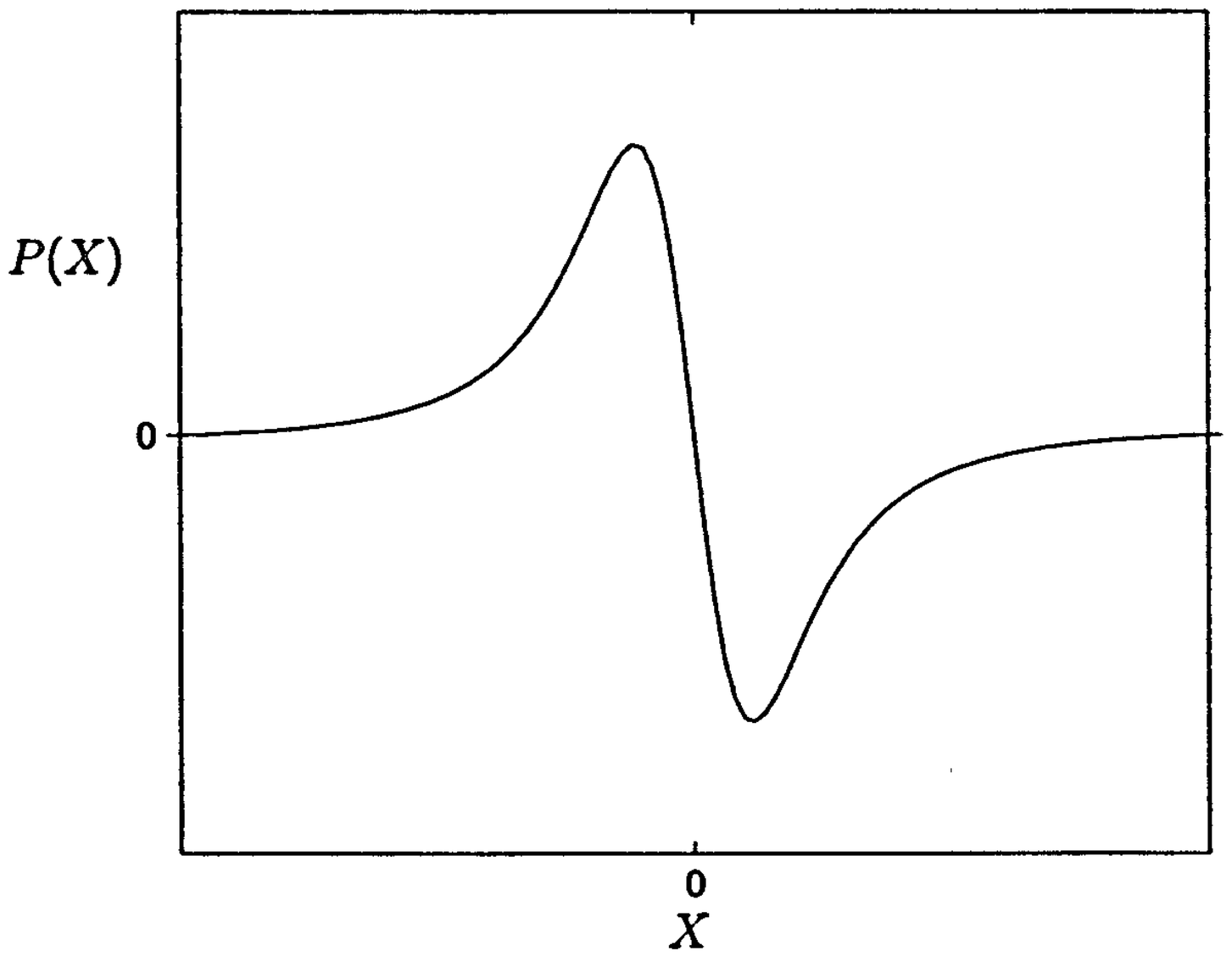

Figure 1.6: The pressure field formed between two counter rotating fully immersed rolls.

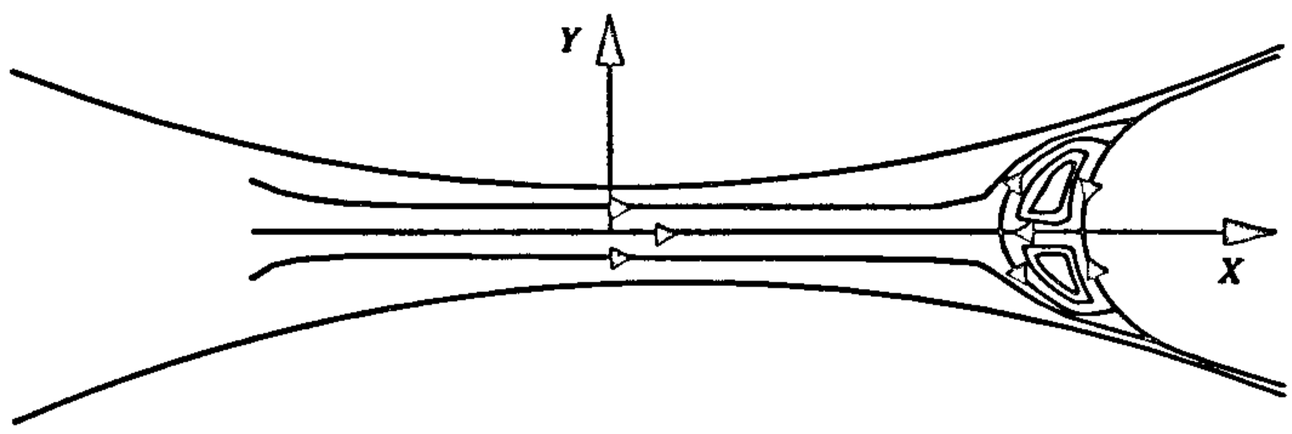

Figure 1.7: Typical streamlines found in a forward roll coater. Note the region of rectilinear flow in the nip region and the recirculations in the vicinity of the meniscus.

In constrast to the premise of the SS conditions, Schneider (1962) observed a region of flow recirculation immediately upstream of the meniscus and postulated that the pressure is sub-ambient in this region. Taylor (1963) reasoned that the flow splits into two regions as shown in figure 1.7; a two dimensional region in the vicinity of the meniscus and rectilinear flow elsewhere. Both Schneider and Taylor identified the capillary number, Ca, defined as

$$Ca = \frac{\mu U_R}{\gamma}, \tag{1.6}$$

where γ is the surface tension of the fluid, as having a significant effect on the structure of the flow in the meniscus region. The reason for this is that the capillary number represents the ratio of viscous and surface tension stresses. Therefore if $Ca \ll 1$ the flow in the meniscus region will be surface tension dominated leading to a capillary statics region whereas if $Ca \gg 1$ the flow will be viscous dominated with the surface tension playing an insignificant role. As the SS conditions do not allow the pressure to become sub-ambient it is clear that an alternative has to be formulated.

Birkhoff and Hays (1963) proposed the conditions

$$U = \frac{\partial U}{\partial Y} = 0 \qquad \text{at} \qquad (X, Y) = (X_S, 0), \tag{1.7}$$

where X_S is the point of flow separation and marks the start of the region of recirculation. If the assumption is made that $X_S = X_D$ then (1.7) can be used to locate the meniscus and these conditions are refered to as Prandtl-Hopkins (PH) conditions in the literature. In fact the second of these conditions is automatically satisfied in the case of equal roll speeds and the first can be recast as the following condition on the pressure gradient

$$\frac{\mathrm{d}P(X_S)}{\mathrm{d}X} = \frac{8\mu U_R}{B^2(X_S)}. \tag{1.8}$$

As the flow separation conditions represent only one independent condition an additional condition is required and this was provided by Greener and Middleman (1979) who modelled the pressure jump across the meniscus due to surface tension using the following:

$$P(X_D) = -\frac{T}{\mathcal{R}}, \qquad \mathcal{R} = \frac{1}{2}\left[B(X_D) - 2H^{\infty}\right], \tag{1.9}$$

where $\mathcal{R}$ is the radius of curvature of the meniscus and H^{∞} is the thickness of the coated film on each roll. The PH conditions have one large drawback and that is that

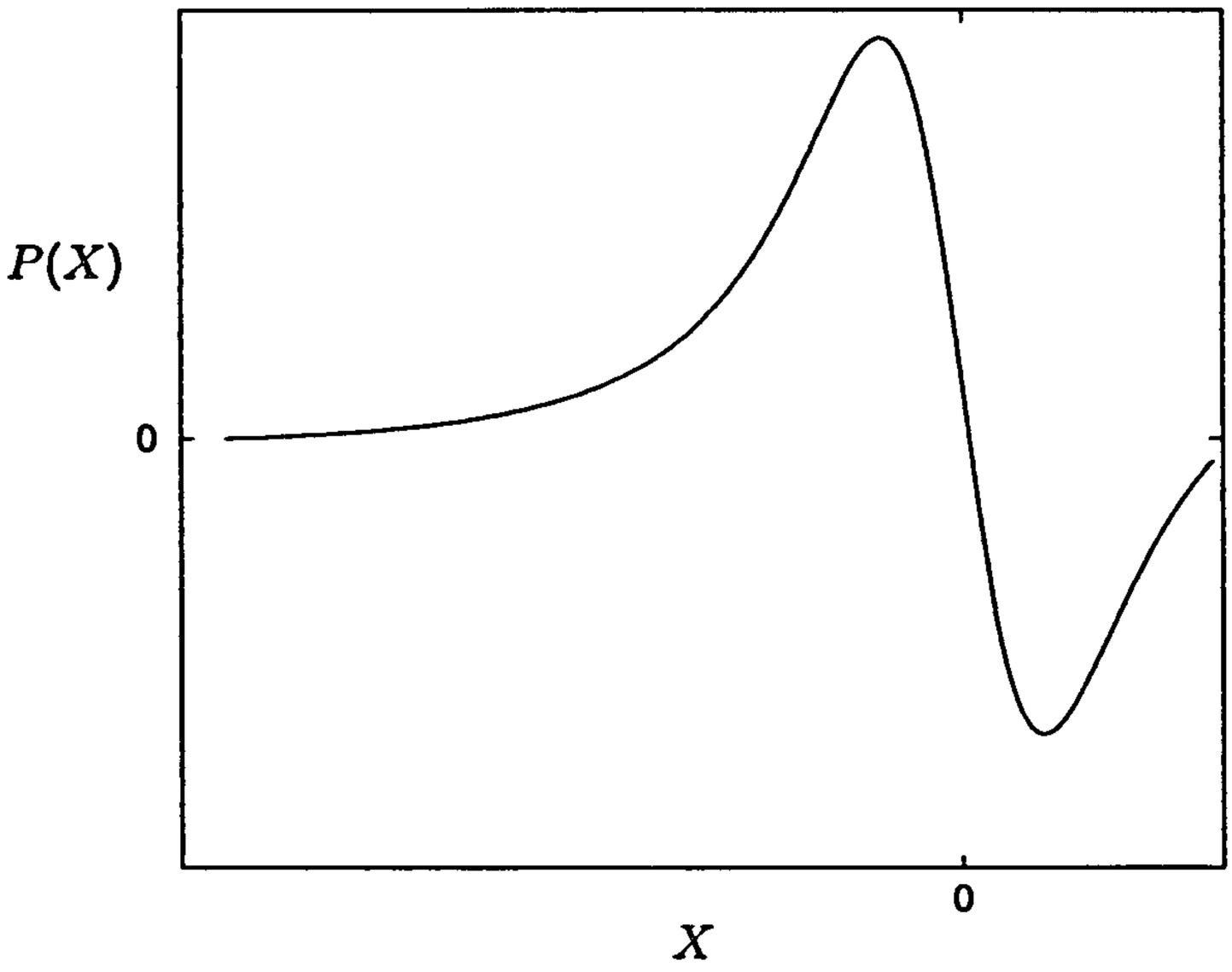

Figure 1.8: The pressure profile in forward roll coater with the PH conditions

they locate the point of flow separation and not the meniscus location. However, for $Ca > 1$ it has been shown that the recirculations dissappear with the flow separation point lying on the meniscus and thus for $Ca > 1$ the PH conditions are appropriate. A refinement of the PH conditions for unequal roll speed was provided by Gaskell *et al.* (1998).

A typical pressure profile for the PH conditions is shown in figure 1.8 and it can be seen that there exists a sub-ambient pressure loop as predicted by Taylor and which has been seen experimentally by Floberg (1965), Smith (1975) and Malone (1992).

Attempts have been made to model the flow using lubrication theory for the case of $Ca < 1$. Pitts and Greiller (1961) and Coyne and Elrod (1970) split the flow as suggested by Taylor (1963). However, they used severe approximations for the meniscus region; Pitts and Greiller assumed the profile of the free surface at the outset and Coyne and Elrod assumed a quadratic form for the component of velocity tangential to the free surface.

Later workers including Gaskell *et al.* (1995), Daniels (1998) and Wilson (1997)

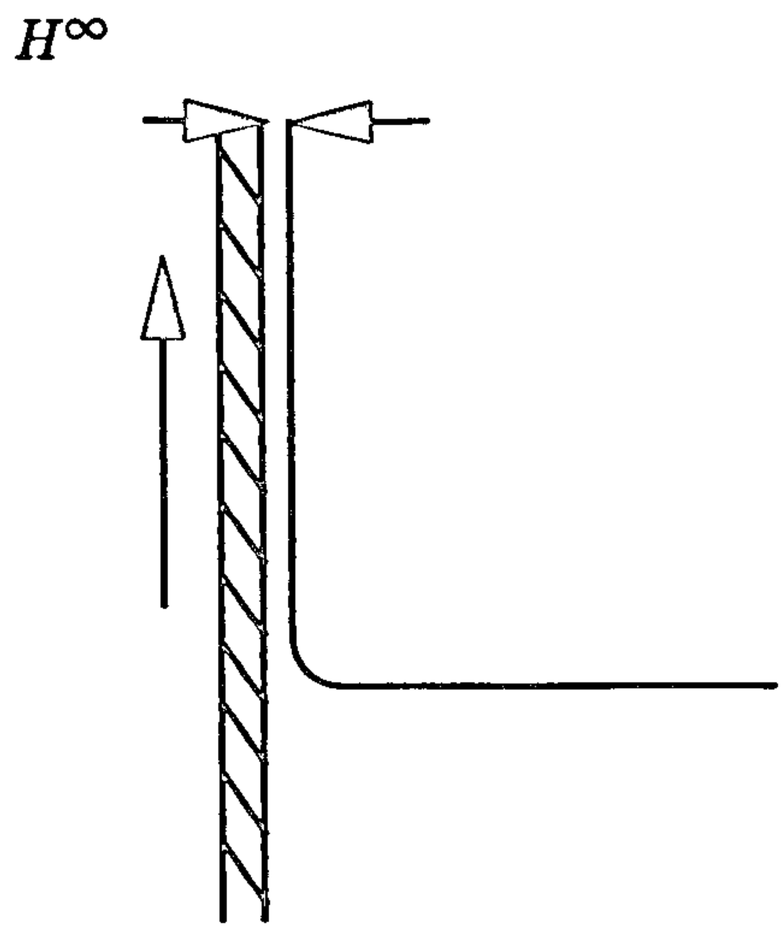

Figure 1.9: A thin film coats a plate that is extracted from a bath of fluid. This problem was studied by Landau and Levich.

have used the following condition for the final coated film thickness H^∞ due to Landau and Levich (1942):

$$H^\infty = 1.34\frac{B(X_D)}{2}Ca^{2/3}, \tag{1.10}$$

in conjuction with (1.9). (1.10) can be considered a direct replacement of (1.8) since (1.2) allows the pressure gradient to be written in terms of the flux and hence H^∞. The combination of (1.9) and (1.10) are known as the Landau Levich (LL) conditions. These boundary conditions were initially developed for the problem of dragging a coated plate from a bath of fluid (figure 1.9) by Landau and Levich and have since been shown to be asymptotically correct as $Ca \to 0$ in the closely related cases of the flow of a bubble in a fluid filled capillary tube (Bretherton (1961)) and two phase flow in a Hele-Shaw cell (Park and Homsy (1984)). The conditions were extended to the non-constant gap case by Reinelt (1995) and the formal confirmation of the applicability of this condition in a roll coating geometry is given in chapter 2 along with the leading order correction terms. Gaskell *et al.* (1995) demonstrated that the results of Reynolds equation solved subject to the LL condition were in good agreement with a finite element (F.E.) solution to the Navier-Stokes equations for a forward meniscus roll coater for the range $Ca < 0.01$

The above studies have all contained lubrication theory coupled with analytic boundary conditions that attempt to capture the physics of the meniscus region. An al-

ternative approach was taken by Rushack (1982) who solved the full 2-D Navier-Stokes equations in the region of the meniscus and matched these to a lubrication solution in the nip region. The results were found to be well represented by the formula

$$H^{\infty} = 0.54B(X_D)Ca^{1/2}, \tag{1.11}$$

in the range $0.01 < Ca < 0.1$. Note as with both the PH and LL conditions, (1.11) can be combined with (1.9) to form a pair of boundary conditions for Reynolds equation leading to an analytic solution. Thus, under certain conditions accurate results can be obtained by solving Reynolds equation analytically subject to suitable boundary conditions.

Coyle et al. (1986) also carried out a F.E. simulation and showed that the recirculations dissappear when $Ca \approx 0.7$ confirming the validity of the use of the PH conditions for equal roll speeds and high capillary numbers.

The fluid modelling in this thesis is based around the lubrication models described above. As has been demonstrated, lubrication models can give accurate results but this is dependent upon the application of suitable boundary conditions that are often only valid over a limited range of Ca. The problem of finding suitable boundary conditions is a major theme of this thesis; in chapter 2 the LL conditions used for $Ca \ll 1$ are put on a rigorous footing in terms of their application to roll coating geometries; chapter 3 contains the development of a 3-D extension to the LL conditions and chapter 4 includes a method of extending the asymptotic result so as to cover the range $0 < Ca < 10$.

1.4 Multiple Roll Coating

The case of multiple roll coaters was studied by Benjamin et al. (1995a,b) who examined how fluid is transfered through a system by constructing a flux balance for each roll pair. However Benjamin did not investigate the flow structure that exists in the nip region of each roll pair and this was carried out by Wilson (1997). Wilson used both a F.E. simulation and a lubrication model coupled with LL conditions to study the flow between an individual roll pair.

Wilson found that there was a maximum value of roll speed ratio beyond which no steady 2-D solutions existed. Excellent agreement was found between the lubrication theory and F.E. simulation for the pressure profile and coated film thicknesses for

$Ca = 0.01$. However, there was a discrepancy in the predictions of the upstream meniscus location.

1.5 Deformable Roll Coating

To put the research into deformable roll coating into context it is necessary to look at the preceeding work on dry contact mechanics and elastohydrodynamic lubrication (EHL). The dry contact literature provides a range of models that can be used to describe the compliant layer and the EHL work demonstrates how such models can be coupled with the governing fluid equations to provide a description of the fluid/solid interaction.

1.5.1 Dry Contact Mechanics

The classical problem of a sphere loaded against a linearly elastic half space was solved by Hertz (1882) and such a contact is known as Hertzian. In general, the surface deformation, $D(X)$, of the surface of a linearly elastic half space is related to the normal surface traction, $P(X)$, via

$$D(X) = \frac{2(1-\nu^2)}{\pi E} \int_{\Omega} \log(X-\xi) P(\xi) \mathrm{d}\xi, \tag{1.12}$$

where ν is Poisson's ratio, E is Youngs modulus and Ω is the region of contact. ν specifies how compressible the material is; if $\nu = 0$ the material is entirely compressible but if $\nu = 0.5$ the material is incompressible and the volume of the material is preserved. In deformable roll coaters the compliant layer is usually made from material for which $0.45 \leq \nu \leq 0.5$.

If the shape of the indentor is prescribed, as in the Hertzian contact, and the normal surface traction is to be found, (1.12) constitutes an inverse problem. Furthermore, (1.12) represents a non-local relationship between the surface traction and deformation; the deformation at a point depends upon the surface traction over the entire contact region. (1.12) could be used to study the compliant layer in a deformable roll coater but has generally been disregarded as the layer has a finite depth, which is not well approximated by an infinite half space.

For layers of finite depth two simple local models have been suggested. The first of these was the spring model of Winkler (1867) who assumed that the deformation at a

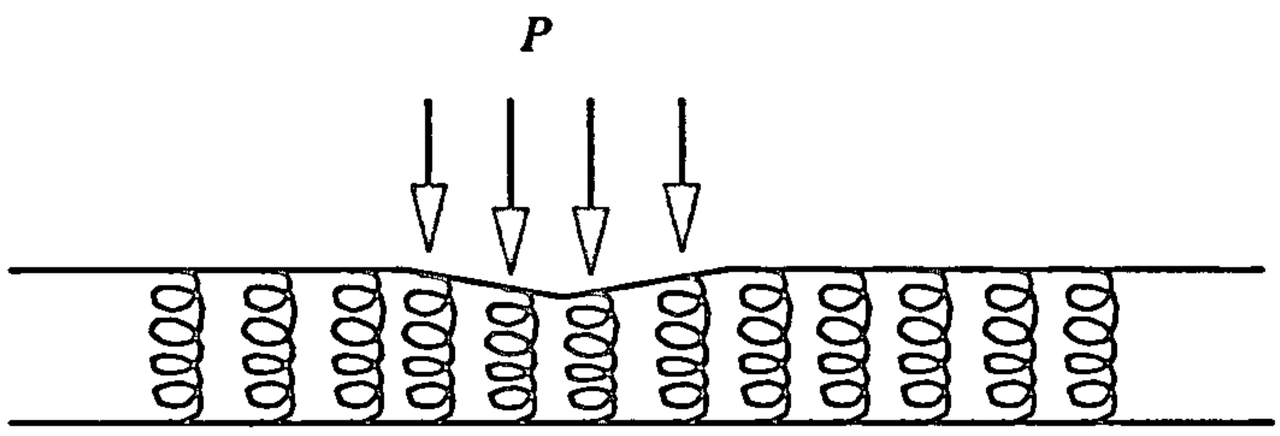

Figure 1.10: The CCM can be interpreted as an array of independent springs where the spring deformation is proportional to the applied pressure, P.

point is proportional to the normal surface traction at that point:

$$P(X) = K_{sp} D(X), \tag{1.13}$$

where K_{sp} is the constant of proportionality, refered to here as the spring constant. Models of this form will be refered to as Hookean spring models or as constrained column models (CCM's) and can be thought of as representing the solid as an array of independent springs as shown in figure 1.10. The spring constant is related to the layer properties via

$$K_{sp} = \frac{1-\nu}{(1+\nu)(1-2\nu)} \frac{E}{L}, \qquad \nu < 0.5, \tag{1.14}$$

where L is the layer thickness. Note, that this expression is invalid for $\nu = 0.5$ as an infinite force would be required to produce a finite deformation. An alternative local model, known as the incompressible column model (ICM), was proposed by Bentall and Johnson for the case of $\nu = 0.5$:

$$D(X) = -\frac{L^3}{E} \frac{\mathrm{d}^2 P}{\mathrm{d}X^2}. \tag{1.15}$$

Whereas (1.13) and (1.15) are local approximations an exact solution to the linearly elastic plane strain equations for a finite layer was provided by Bentall and Johnson (1968) who demonstrated that surface deformation and traction were related via

$$D(X) = \frac{2(1-\nu^2)}{\pi E} \int_\Omega K(X - X') P(X') \mathrm{d}X', \tag{1.16}$$

where the kernel function K is defined as

$$K(X) = \int_0^\infty \frac{(3-4\nu)\sinh 2\omega - 2\omega}{\omega\left((3-4\nu)\cosh 2\omega + 2\omega^2 + 5 - 12\nu + 8\nu^2\right)} \cos\left(\frac{\omega X}{L}\right) \mathrm{d}\omega. \tag{1.17}$$

This model is refered to as the full strip model (FSM). A plot of K is shown in figure 1.11 and it is clear that as $X/L \to 0$, $K \to \infty$ indicating that the largest contribution

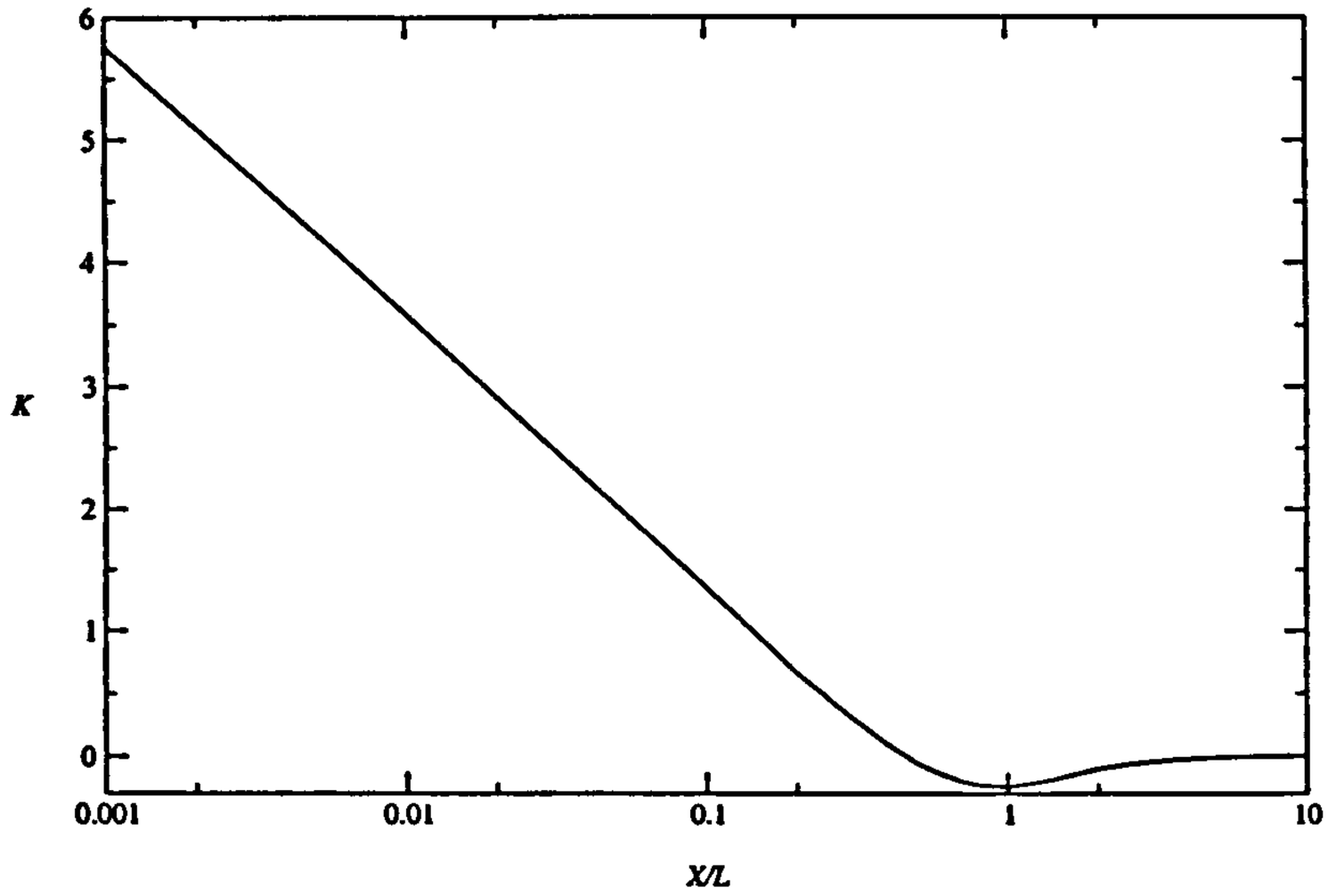

Figure 1.11: The kernel $K(X)$ of the FSM.

to the deformation at any point comes from the local traction. The curve in figure 1.11 is a straight line for small X/L as K has a logarithmic singularity at the origin. Bearing this in mind, it is conceivable that the local models (1.13) and (1.15) would be good approximations to (1.16) under certain conditions. This was examined by Johnson (1985) who found that the approximations were good only when the contact area greatly exceeded the layer thickness (i.e. they can be considered as thin layer approximations) in both cases and with the additional constraints and that $\nu < 0.4$ for the CCM and $\nu = 0.5$ for the ICM.

Young (1997) conducted a thorough comparison of the CCM, ICM and FSM models for a cylinder (of radius $\bar{R}$) and strip contact the results of which are shown in figures 1.12 and 1.13 and found that neither the CCM or ICM could adequately describe the contact over the full range of parameters. The parameter A quoted in the figure is the width of the contact area. It is worth noting that the comparison included several ad-hoc values of the CCM spring constant postulated by Carvalho and Scriven (see below).

All of these models are for static problems whereas roll coating is a dynamic problem. At first sight it would appear that this renders the above models irrelevant and what should really be considered are models for *rolling* dry contact based on equations that include terms relating to the inertia of the solid. In fact the terms relating to the

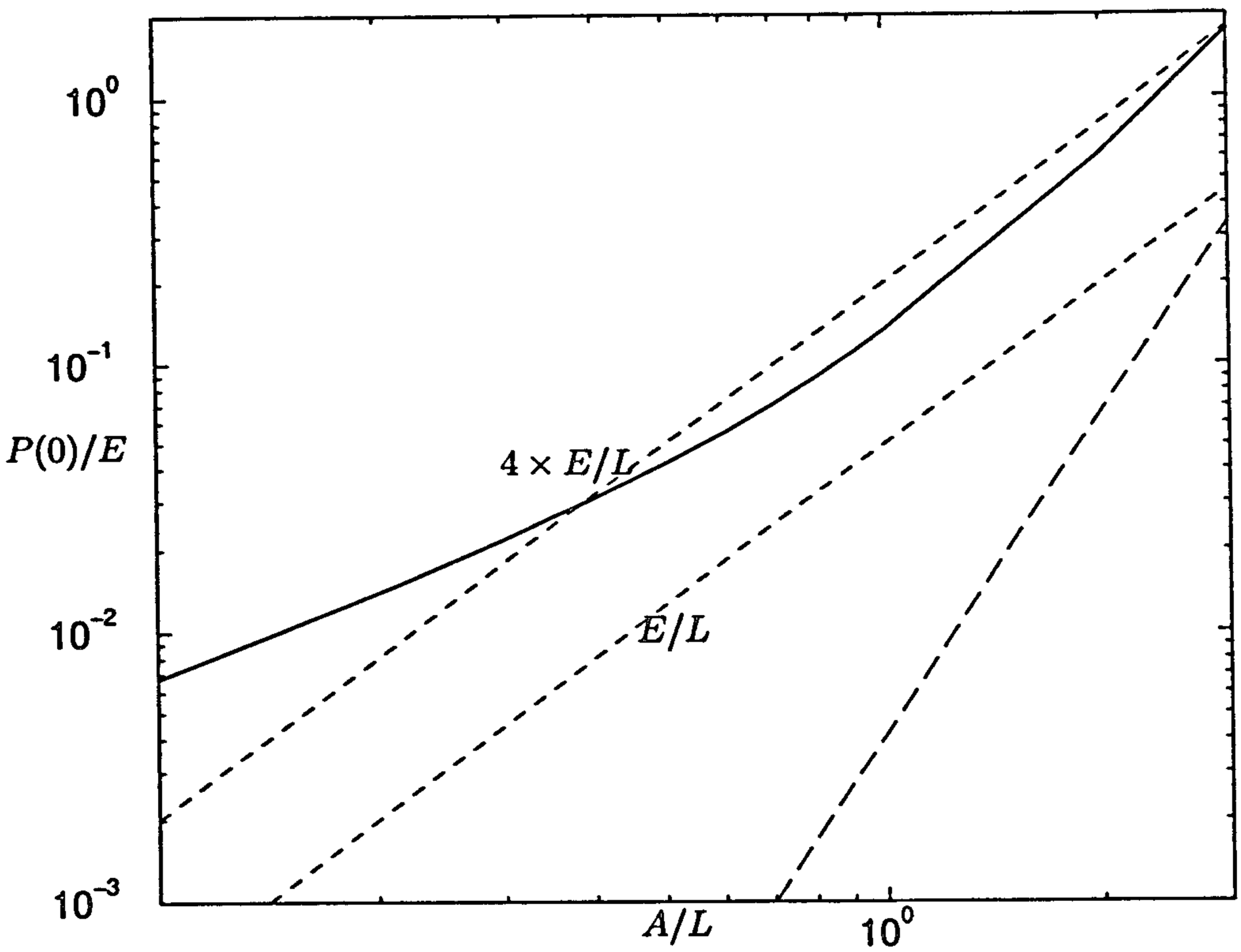

Figure 1.12: The variation of centreline pressure, $P(0)$, with A/L for each of the FSM (—), ICM (– –), and CCM (- - -) deformation models. Results are shown for the CCM with both $K_{sp} = E/L$ and $K_{sp} = 4 \times E/L$. $L/\bar{R} = 0.1$, $\nu = 0.5$. Young (1997).

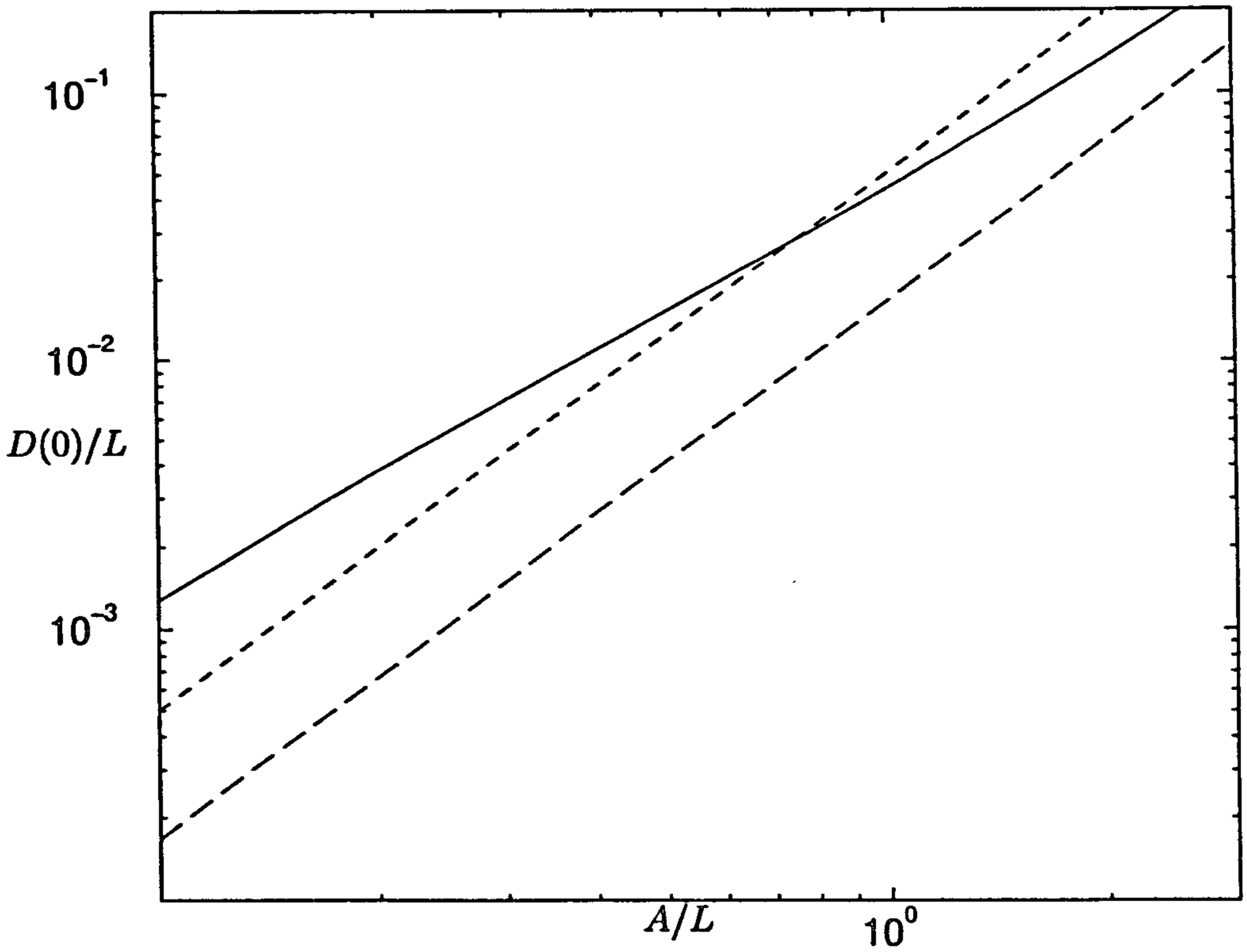

Figure 1.13: The variation of centreline deformation, $D(0)$, with A/L for each of the FSM (—), ICM (– –), and CCM (– – –) with $K_{sp} = E/L$ deformation models. $L/\bar{R} = 0.1$, $\nu = 0.5$. Young (1997).

inertia are only important when the roll speed approaches that of the speed of sound in the material (Johnson (1985)), a scenario not encountered in coating processes. As such, many rolling dry contact models are based on static equations. The reason that rolling dry contact does not have to be considered is that such models contain regions of both slip and stick whereas deformable roll coaters are fully lubricated by the coating fluid so there are no regions of stick. Hence, all that is required of the model is the deformation of the solid due to an applied load (the fluid pressure) and this is provided by the static models.

The models mentioned above are based around the theory of linear elasticity. In many cases the materials that are used to make the compliant layers in deformable roll coating devices display both nonlinear and viscoelastic properties (Cohu and Magnin (1997)) and these properties are discussed below.

Linear elasticity is based on the principal that the strains involved are infinitesimal yet when the strain becomes significant the stress - strain relationship ceases to be linear and elastomeric materials can show a deviation from linear behaviour at strains of about 10%. An important piece of work, as far as this thesis is concerned, was done by Batra (1980) who modelled the contact of a cylinder with a nonlinear elastic half space and found little difference with the equivalent linear elasticity result. In this thesis nonlinear effects are neglected. For further justification of the neglect of nonlinear effects see the work of Coyle discussed below.

Goryacheva (1998) presents governing equations for a linear viscoelastic solid, the so called Maxwell-Thomson model. The equations contain two viscoelastic parameters, the retardation time, T_ϵ and the relaxation time, T_σ. These time scales can be thought of as typical times that the strain and stress take to respond to an applied displacement or load, respectively. Gorycheva used this model to study the rolling contact of a rigid cylinder on a strip and this model is incorporated as an extension to the FSM in chapter 4. Bapat and Batra (1984) also studied the dry rolling contact of a cylinder on a finite-strain viscoelastic layer and found the expected asymmetries in the stress and deformation profiles due to the stress - strain histories.

1.5.2 Tribology

There is a large body of work in the field of tribology that is concerned with the lubricated rolling contact of cylinders and planes.

Tribologists have found that the pressures developed in the lubricating film are high enough to deform the solids and so any model must take this into account. Dowson and Higginson (1966) modelled the lubricating film via Reynolds equation and used linear elasticity to describe the solid behaviour. The similarities with this work and much of the roll coating literature are obvious but there are important differences. The differences arise from two key facts:

- the pressures encountered in EHL are far higher than in deformable roll coating with the magnitude of the pressure in the nip being far greater than that of the sub-ambient loop;
- the tribologist is concerned with the gap thickness within the contact region whereas the coating engineer is interested in the thickness of the fluid film extracted from the contact region via the meniscus.

Therefore, in EHL the SS conditions are often applied and useful results are achieved. However, these conditions fail to predict the sub-ambient pressure loop near to the meniscus as well as failing to accurately predict the location of the meniscus and consequently the coated film height. As the tribologist is concerned with the physics of the nip region this is permissible but from a coating perspective, accurate modelling of the meniscus is vital.

An important study was carried out by Hooke (1986) who was the first to couple together the FSM and lubrication theory using cavitation (SS) boundary conditions. Significant problems were encountered with the convergence of the numerical scheme. The boundary conditions were satisfied in an external iterative loop and an attempt to incorporate them into the main loop failed as it led to ill conditioning. However in this thesis, all variables are determined simultaneously in a single iterative loop.

1.5.3 Deformable Roll Coating

In contrast to rigid roll systems, the study of deformable roll systems is in its infancy with the majority of work being carried out in the past decade. The reason for this

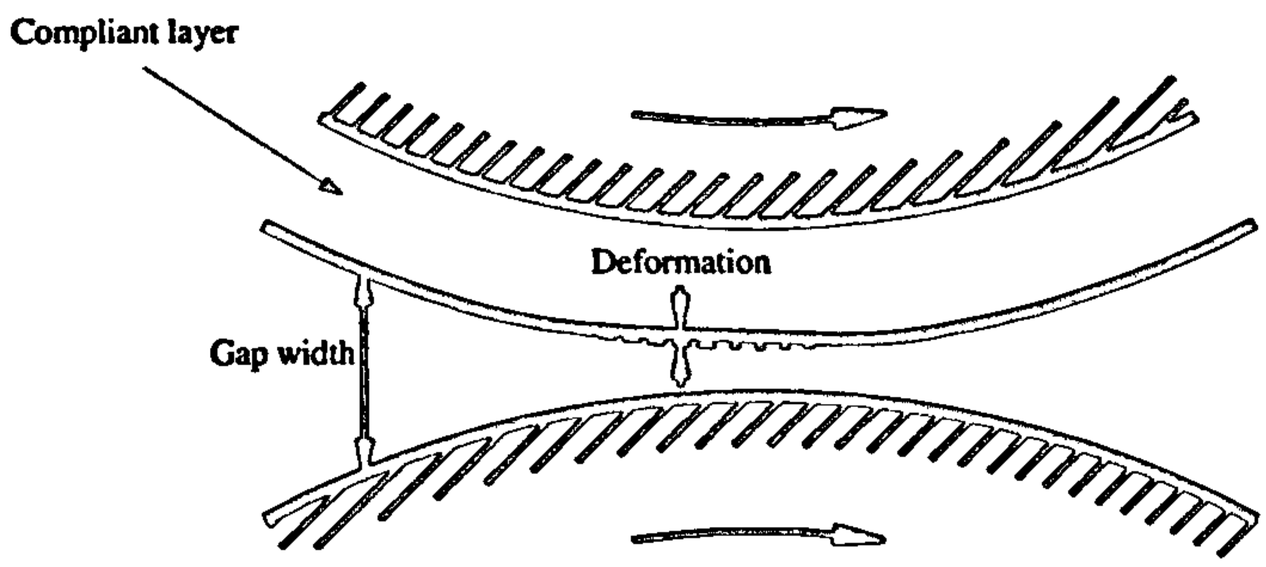

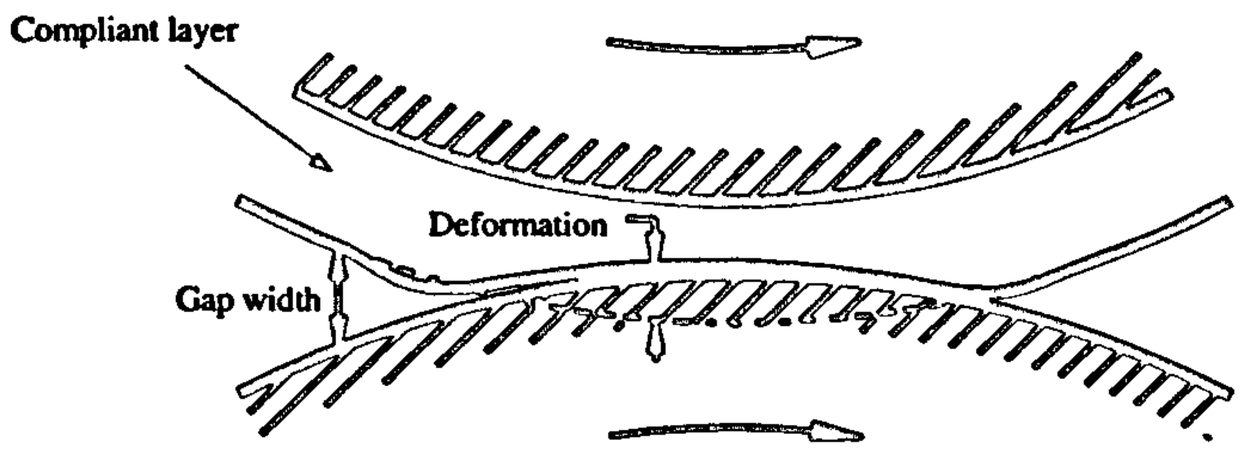

Figure 1.14: The positive and negative gap regimes of a deformable roll coater.

is simple - the compliant solid layer covering one of the rolls and its interaction with the coating fluid makes the modelling of a deformable roll system considerably more challenging than the rigid roll counterpart. Below is a brief summary of the modes of operation of a deformable roll coater followed by a review of the literature.

The compliant layer allows deformable roll coaters to operate in two distinct modes:

- Positive gap - when the centre to centre distance exceeds the sum of the roll radii;
- Negative gap - when the centre to centre distance is less than the sum of the roll radii.

These two regimes are shown in figure 1.14. The positive and negative gap regimes are also refered to as the lightly and highly loaded regimes due to the force required to hold the rolls in position. The parameter B_0 is equal to the clearance betweent the rolls in the positive gap regime and the amount of interference in the negative gap regime. In the positive gap regime the fluid pressure is not high enough to substantially deform the compliant layer and the system behaves much like a rigid roll coater - see figure 1.15

($H(X)$ is the gap width between the rolls). However, in the negative gap regime the compliant layer is substantially deformed and there is a strong interaction between the fluid and solid - see figure 1.16. In the negative gap regime the deformation is dominated by the shape of the indenting roll and the gap profile is almost constant through the nip region with a small nib, or constriction, near the downstream meniscus. Also the pressure assumes the profile of the normal traction in the equivalent dry contact. The results presented in figures 1.15 and 1.16 are taken from Young (1997).

Research into deformable roll coating began with the pioneering work of Coyle (1988a) who presented a simple analysis based on lubrication theory and SS conditions for the fluid coupled with a one-dimensional constrained column model (CCM) for the deformation of the compliant layer (which it should be noted is invalid in the context of incompressible materials). In doing so he was the first to attempt to predict the variation in resultant film thickness for both positive and negative-gap regimes. In a complementary experimental study of flow between deformable rolls, Coyle (1988b) produced film thickness measurements as a function of roll separating force; Adachi (1988) similarly presented results for a cylinder plate geometry. There is reasonable agreement between the two sets of data for positive-gaps but significant differences for negative-gap settings. Experimental results (Cohu & Magnin 1995, 1997) highlight the effect of the depth of the compliant layer on the resultant film thickness, indicating agreement with Coyle's theory for thick layers only. Indeed, they show that decreasing the thickness of the compliant layer tends to decrease the coating thickness significantly.

Recognising the shortcomings of the CCM, Coyle (1990c) employed a finite element formulation of the plane strain nonlinear elasticity equations, leaving the fluid model as before. However, the Reynolds conditions fail to predict a sub-ambient pressure loop in the region of the meniscus, the value of the layer thickness L used in the analysis was not recorded and the effect of the parameters on the meniscus position, X_D, was not investigated. Included in the work was a comparison between linear and nonlinear elasticity models for the compliant layer. The error in the linear model increased with the strain but for strains of 20% the error was <4%. As strains in deformable roll coaters rarely exceed 20% this provides further justification for the neglect of nonlinear terms in the present work.

Carvalho and Scriven (1994) attempted to validate the CCM used by Coyle by

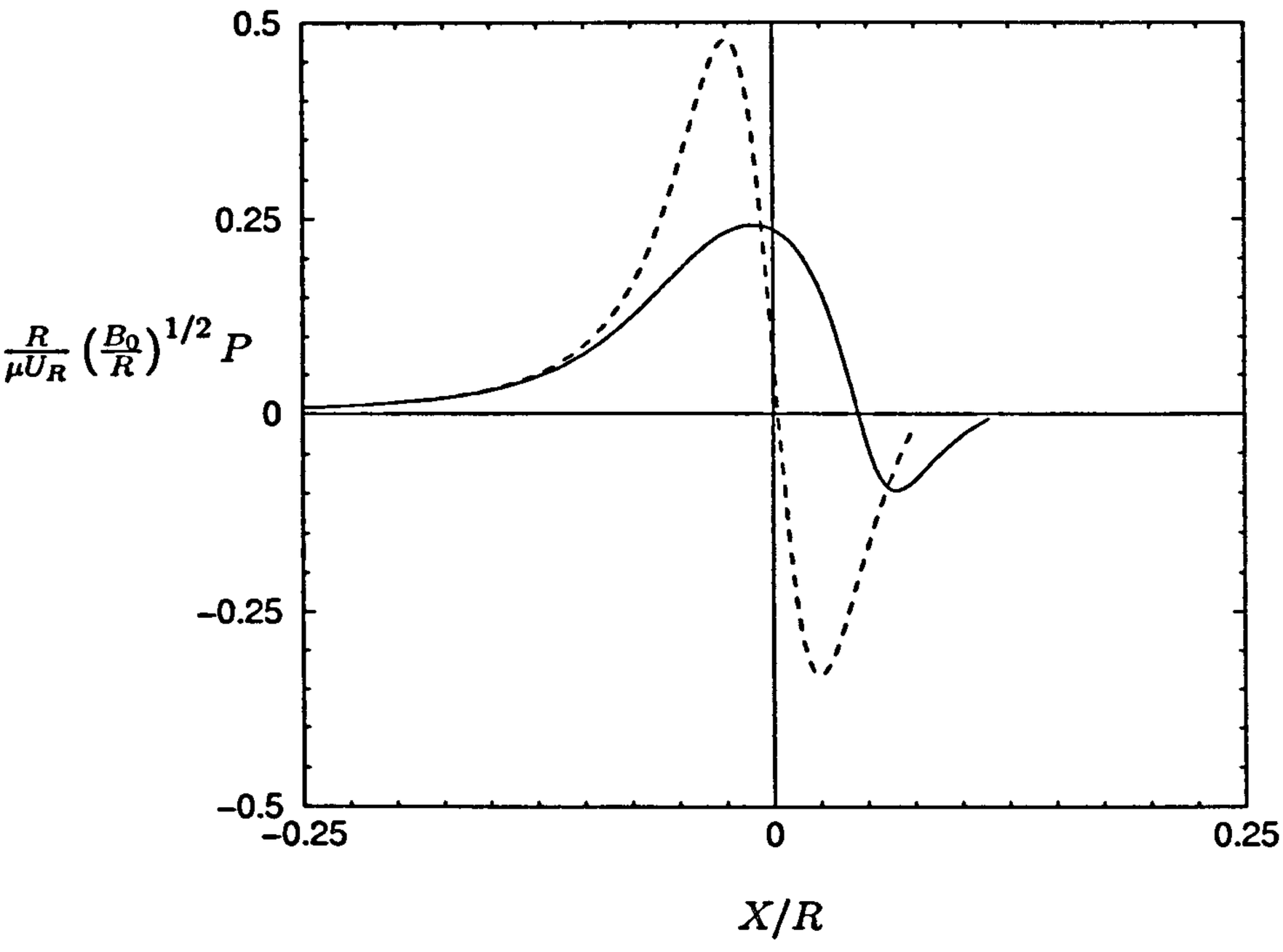

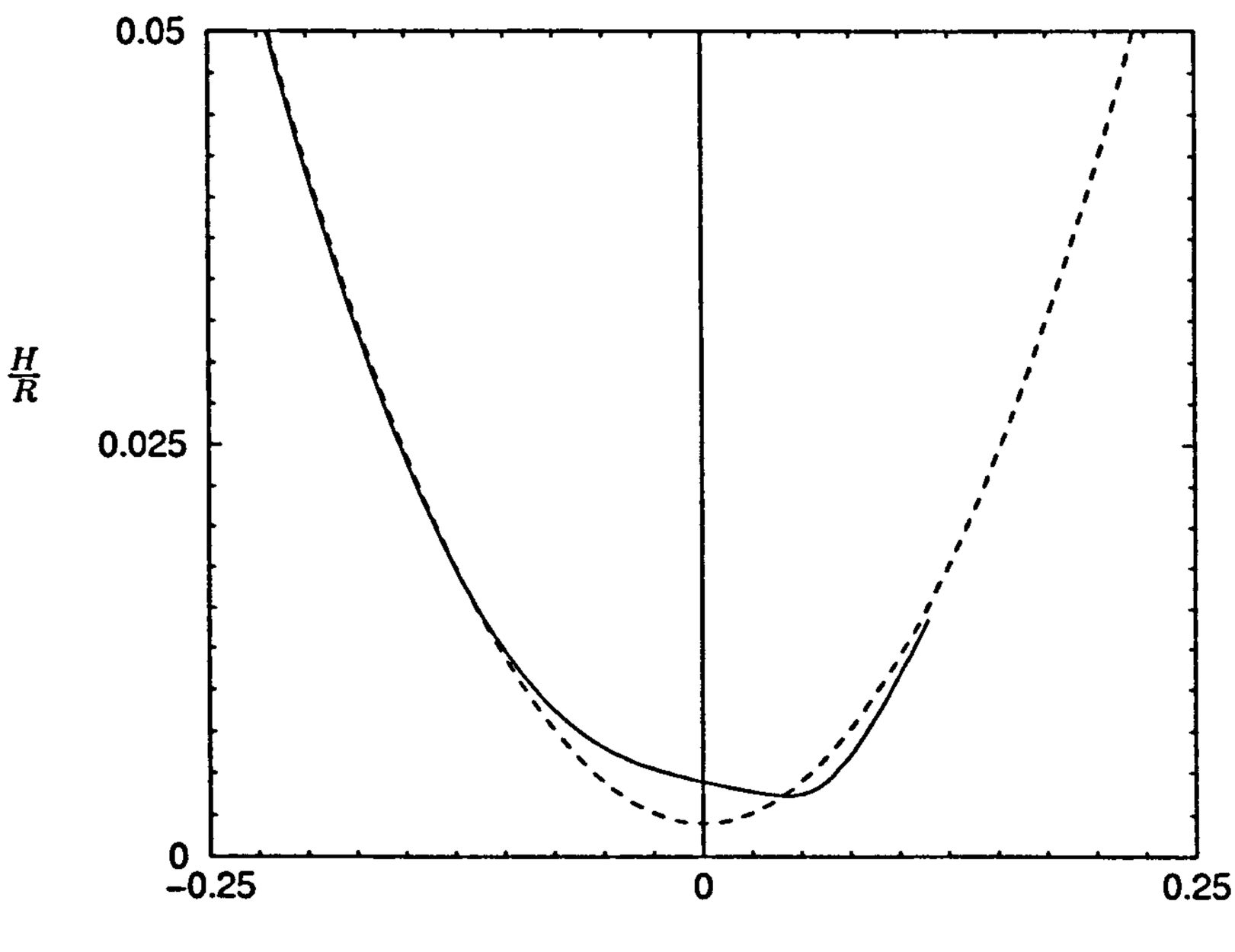

Figure 1.15: The pressure and gap profiles in a deformable roll coater operating in the positive gap regime. The equivalent rigid roll profiles (– –) are shown for comparison. $B_0/\bar{R} = 10^{-3}$, $\mu U_R/E\bar{R} = 10^{-5}$, $Ca = 1$, $L/\bar{R} = 0.1$

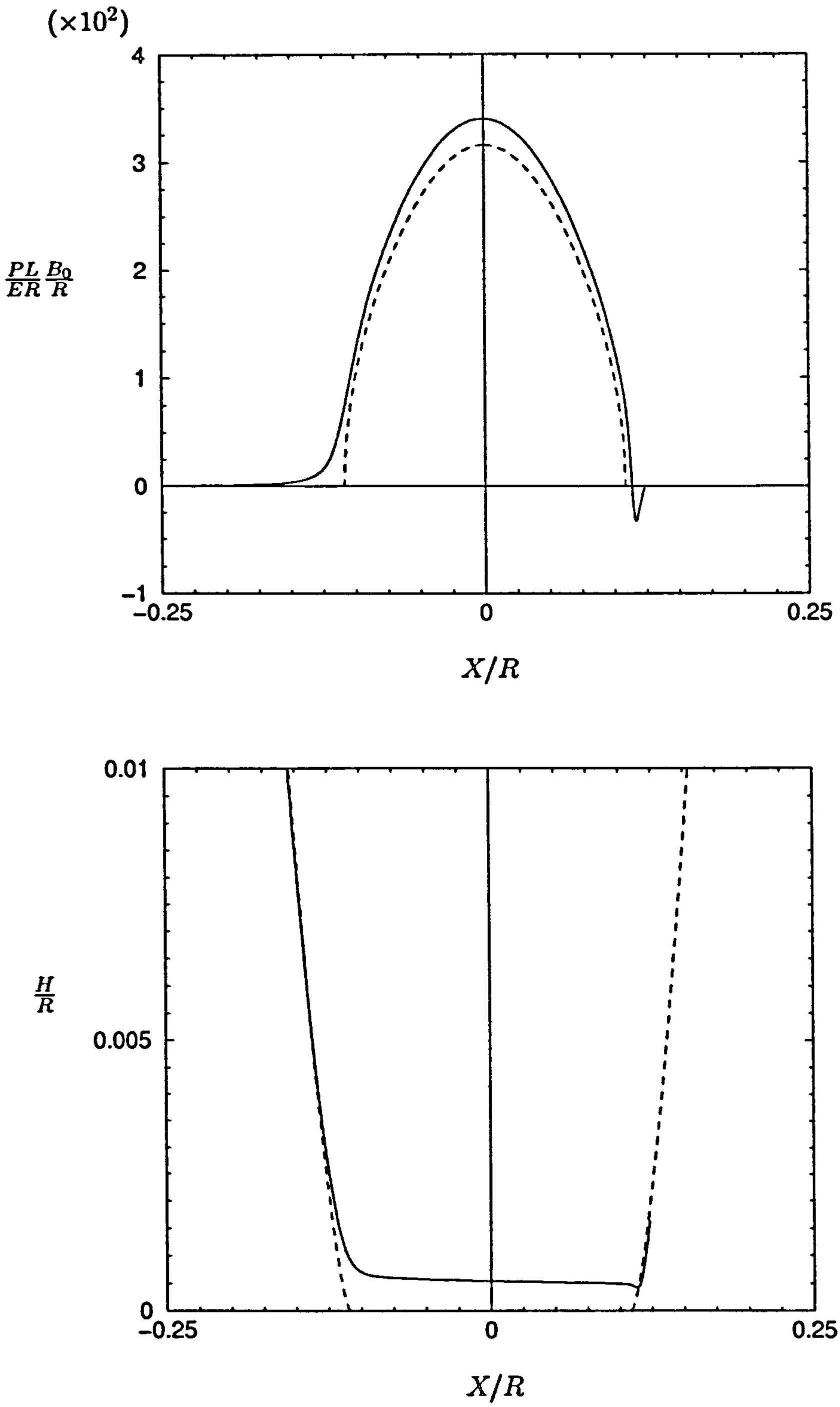

Figure 1.16: The pressure and gap profiles in a deformable roll coater operating in the negative gap regime. The equivalent dry contact profiles (– –) are shown for comparison. $B_0/\bar{R} = -5 \times 10^{-3}$, $\mu U_R/E\bar{R} = 10^{-6}$, $Ca = 1$, $L/\bar{R} = 0.1$

proposing and comparing several distinct models for the deformation of a compliant layer coupled with a fluid model for fully submerged rolls, i.e. no free surfaces present. They considered : (i) a one-dimensional Hookean spring model; (ii) a one-dimensional neo-Hookean model; (iii) a two-dimensional linear elasticity model (HSM) for which the deformable layer is regarded as an infinite half space – the other physical extreme to the CCM. Their results revealed that flow rate predictions obtained with each model differed by less than 10%. However, these results should be treated with a degree of caution as the effect of layer thickness was not explored and the HSM is only valid for deep layers.

Young (1997) compared the performance of the Hookean spring model (CCM) with $K_{sp} = E/L$ and $4E/L$ and the FSM coupled with the lubrication equations and found that the spring model is inadequate as it cannot accurately predict all system variables, particularly in the industrially relevant regime of $\nu \rightarrow 0.5$. However, subsequent to the work of Young, Carvalho and Scriven (1997b) recalibrated the spring model using a nonlinear plane strain model proposing a spring constant of

$$K_{sp} = 2\frac{E}{L}. \tag{1.18}$$

Carvalho and Scriven present results which show excellent agreement between the sophisticated nonlinear plane strain model and the simple recalibrated spring model for predictions of flow rate. However, as the computations were carried out in a domain fully flooded at both upstream and downstream, predictions of meniscus position were absent. Therefore the fundamental question of whether a suitably calibrated spring model could ever hope to adequately represent the physics of a deformable roll coater remains open. The approach taken in this thesis makes use of the observation that dimensional analysis demands that all spring models have a spring constant proportional to E/L and thus the use of a spring model contains an implicit assumption that E and L^{-1} have the same effect. Young compared and contrasted results from the FSM with two particular spring models for several values of E and concluded that these particular spring models were inadequate. An aim here is to examine the behaviour of the system as both E *and* L^{-1} are varied and hence to see if *any* spring model could produce accurate results.

A second fundamental problem that has arisen during the study of deformable roll coating is that there is a significant difference between experiment and even the

most elaborate elastic models. Whilst experimental error can be significant (Cohu and Magnin (1997) report up to 30%) this is still not enough to explain the discrepancies that have been observed. A possible reason for this is that the compliant layers are usually made of elastomeric material that are well known to be viscoelastic in nature. Carvalho and Scriven have produced two viscoelastic models, one using a spring model, the other a nonlinear plane strain model and they note that viscoelastic terms can make a significant difference to the predicted flow rate. A viscoelastic extension of the FSM is developed in chapter 4.

1.6 Roll Coating Instabilities

The fact that all the coating flows discussed can suffer from instabilities is a major problem for the coating industry as they lead to coating defects. Roll coaters suffer from a classic fluid instabilty, namely the 'ribbing instability'. The meniscus profile becomes non uniform in the direction of the axes of the rollers (the lateral direction) and this translates into an uneven coated film which is undesirable. The ribbing pattern is shown in figures 1.17 and 1.18. The meniscus profile varys in a periodic manner in the direction of the roller axes and is steady. Roll coaters that operate in the meniscus regime ($Ca \ll 1$) can suffer from an additional instability, namely 'bead break' which is when the fluid bead supported between the rollers collapses or blows out leading to the substrate being completely uncoated.

An early attempt to predict the operating conditions under which the flow in a forward rigid roll coater with a flooded inlet would become unstable was carried out by Pitts and Greiller (1961). The approach taken was to assume that the meniscus location was perturbed, giving rise to a wavy profile in the lateral direction and they demonstrated that the flow would be stable if and only if

$$\frac{\mathrm{d}}{\mathrm{d}X}\left(P+\frac{\gamma}{\mathcal{R}}\right)\Big|_{X_D} < 0, \tag{1.19}$$

where γ is the surface tension of the fluid and $\mathcal{R}$ is the radius of curvature of the meniscus. This condition will be refered to as the stability hypothesis (S.H.). It should be noted that this analysis was not a time dependent analysis and as such does not fully represent the time dependent transition to an unsteady state. However, it does provide a useful insight into how stability or otherwise can be achieved.

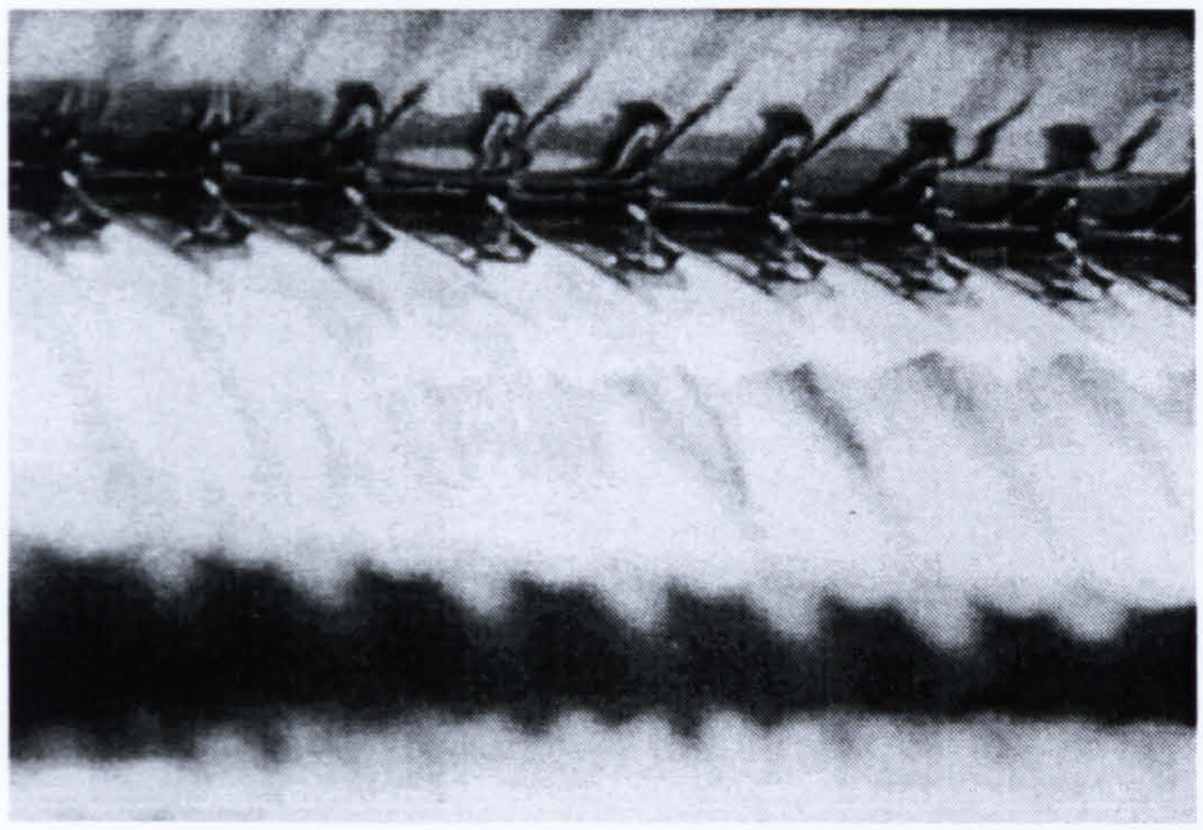

Figure 1.17: A photograph of the ribbing instability. The photograph shows the film split region at the downstream meniscus.

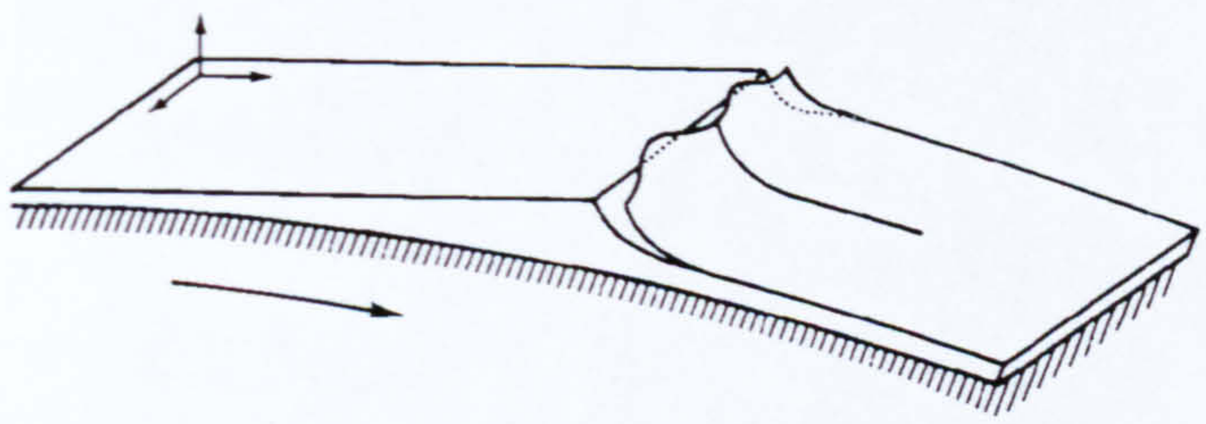

Figure 1.18: A schematic of the ribbing instability. The schematic represents a cross section of the downstream flow domain.

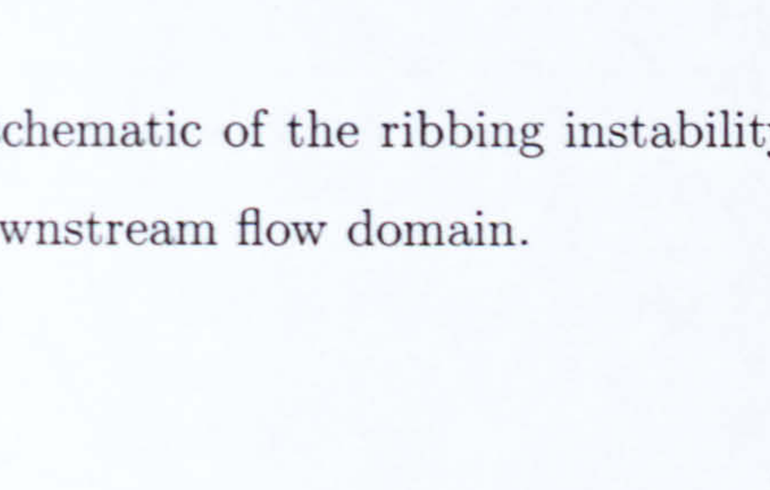

Figure 1.19: The meniscus perturbation considered by Savage.

The S.H. was derived independently at by Savage (1977) from a different standpoint. Savage considered the force on a perturbed 2-D meniscus as shown in figure 1.19 and showed it to be proportional to the left hand side of (1.19), if the force was restoring in nature the flow was deemed to be stable, otherwise the flow was said to be unstable.

The S.H. outlines a physical mechanism by which the meniscus can become unstable. If $\mathcal{R}$ is approximated by $B(X_D)/2$ then the S.H. implies the flow is stable iff

$$\left(\frac{\mathrm{d}P}{\mathrm{d}X} - \frac{\gamma}{B(X_D)^2}\frac{\mathrm{d}B}{\mathrm{d}X}\right)\bigg|_{X_D} < 0. \tag{1.20}$$

Therefore a positive pressure gradient at the meniscus has a destabilising effect and the diverging gap has a stabilising effect.

The ribbing instability is a spatially periodic, 3-D disturbance to the meniscus as shown in figures 1.17 and 1.18. Hence, to accurately predict the onset of this instability it is necessary to subject a 2-D base flow to a 3-D linear time dependent disturbance and determine whether the disturbance grows or decays.

Pearson (1960) was the first to theoretically study the ribbing instability using a 3-D linear stability analysis but the model lacked an appropriate boundary condition at the downstream meniscus. A steady state linear stability analysis was undertaken by Savage (1977) for the cylinder - plate geometry and by Fall (1978) for the wide angle spreader. The stability of the equal speed forward roll coater was analysed by Savage (1984) and the unequal speed case by Carter and Savage (1987). The time dependent response of flow in a cylinder and plate geometry was considered by Fall (1982), who obtained the growth rate of the disturbance as a function of the wavenumber. These studies demonstrated that there is a maximum value of Ca beyond which no steady solutions exist.

The above approaches all rely on being able to find boundary conditions for the lubrication equations that capture the physics of the 3-D flow at the meniscus. The question of what form these conditions should take is considered in more depth in chapter 3.

As in the steady state analysis, the problem of finding suitable boundary conditions can be sidestepped numerically by solving the Navier-Stokes equations in the vicinity of the meniscus. Bixler (1982) showed how the ideas of linear stability theory could be

extended to the finite element method in order to determine the stability of free surface coating flows. This approach was adopted by Coyle et al. (1990d) who studied the equal speed, fully flooded, forward roll coater.

The ribbing instability occurs on the downstream meniscus of a forward roll coater but in a SFF meniscus coater the upstream meniscus can become unstable leading to bead break. This phenomena has been reported by Malone (1992), Gaskell, Savage and Kapur (1998) and Kapur (1998) who showed that as either Ca or S (the roll speed ratio) are increased the upstream meniscus moved downstream, passing through the nip and eventually accelerating and colliding with the downstream meniscus. Three-dimensional perturbations to the two-dimensional SFF bead flow were considered by Daniels (1998) over a wide range of capillary numbers. In the meniscus coating regime, characterised by starved inlets and small capillary numbers ($Ca \ll 1$), his results showed there to be no three-dimensional instabilities; graphs of growth rate against wavenumber confirm that the most unstable waves are long waves - of zero wavenumber - on the upstream meniscus.

Rabaud et al. (1990) and Rabaud and Hakim (1991) observed DFF bead flow in the narrow gap between two non-concentric rotating cylinders when the total volume of fluid remains constant. The stability of both the upstream and downstream interfaces were investigated experimentally by Michalland (1992) and Michalland et al. (1996). They showed the presence of the ribbing instability on the downstream meniscus - when the total volume of fluid is large - and a three-dimensional instability on the upstream when the volume of fluid is small. Reinelt (1995) modelled the flow in this 'journal bearing' configuration and analysed its stability to small amplitude, three-dimensional perturbations. Of particular interest is the determination of the outgoing film thicknesses and the pressure jumps across each meniscus, which follows the work of Landau and Levich (1942), Bretherton (1961) and Park and Homsy (1984), and includes corrections due to the varying gap width, unequal roll speed and the presence of thin films attached to the rolls. This analysis is put on a more rigorous basis in chapter 2.

Another critical phenomena that can occur in meniscus roll coating is flooding of the upstream meniscus. This happens when the flow through the coater is increased which leads to a build up of fluid at the upstream meniscus and the system passes

through a moderately starved state until eventually it is flooded.

1.7 Outline of This Thesis

This thesis deals with the stability of two flows found in roll coating systems:

- The flow within a bead formed between an intermediate roll pair in a multiple roll system.
- The flow in a deformable roll coater.

There are many similarities in the method used to solve the two problems. The basic approach taken in each case is to perform a thorough investigation of the steady state 'base' flow followed by an analysis of a time dependent perturbation to the base flow in order to determine the stability or otherwise of the system. Throughout the thesis the emphasis is put on developing valid models as well as the subsequent results.

Chapter 2 contains the development of the steady state flow of a DFF bead formed between a pair of rigid counter-rotating rolls. The flow is described via the lubrication equations linked with the LL boundary conditions. It is found that this simple model does not satisfactorily explain the steady state flow in all cases and leads to a re-examination of the boundary conditions. A formal matched asymptotic framework is set up to confirm the correct form of the boundary conditions at the menisci. The S.H. is used to predict under what circumstances the flow may become unstable.

Chapter 3 builds on the work of chapter 2 by extending the examination of the boundary conditions to allow for the perturbed 3-D flow at the menisci. A 3-D linear stability analysis is then performed upon the steady state results of chapter 2.

Chapter 4 develops a model for the base flow in a forward deformable roll coater. The FSM is used to describe the compliant layer and the lubrication equations describe the fluid flow. As deformable roll coaters typically operate at higher values of Ca than rigid multiple roll coaters, an extension of the LL conditions is developed. The use of the linear FSM is justified by the work of Batra (1980) and Coyle (1990c) who showed there to be little difference between linear and non-linear results for the strains encountered in deformable roll coating. However, care should be taken when applying the results to deformable roll coaters if the particular compliant layer being

used is known to be highly non-linear at relatively low strains (<10%). The boundary conditions developed in the chapter 2 are recast and are valid over a wide range of Ca.

Chapter 5 contains a linear stability analysis for fluid flow in a deformable roll coater. The base flow of chapter 4 is perturbed and the stability techniques developed in chapter 3 are used again here.

Chapter 6 summarises the main results of the thesis and makes suggestions for future work.

Chapter 2

Multiple Roll Coater - Steady State Analysis

The aim of this chapter is to develop a model for the steady state operation of a roll pair from within a multiple roll coater so that the stability of the flow can then be analysed. Predictions of the bead break instability are made in this chapter using the stability hypothesis (S.H.) (1.19) which only requires base flow results whereas the 3-D linear stability analysis is left until the next chapter. As well as bead break predictions, the steady state results are also used to determine when flooding of the upstream region will occur.

A lubrication model is used with the Landau Levich (LL) ((1.9) and (1.10)) boundary conditions outlined in chapter 1. Preliminary results show that in certain limits the justification for the lubrication approximation disappears and this leads to a re-examination of the boundary conditions at the menisci. The two phase flow in a Hele-Shaw cell shown in figure 2.1 is related to the flow in a roll coater the difference being the fact that the flow domain in a Hele-Shaw cell is bounded by two parallel plates unlike the flow in roll coater that is bounded by the circular rolls. Park and Homsy (1984) performed a rigorous asymptotic analysis of the flow in the vicinity of the meniscus in the Hele-Shaw cell problem and showed that the LL boundary conditions should be corrected to take account of the finite thickness of the outgoing fluid films. The Park and Homsy corrected boundary conditions for the pressure, P, and

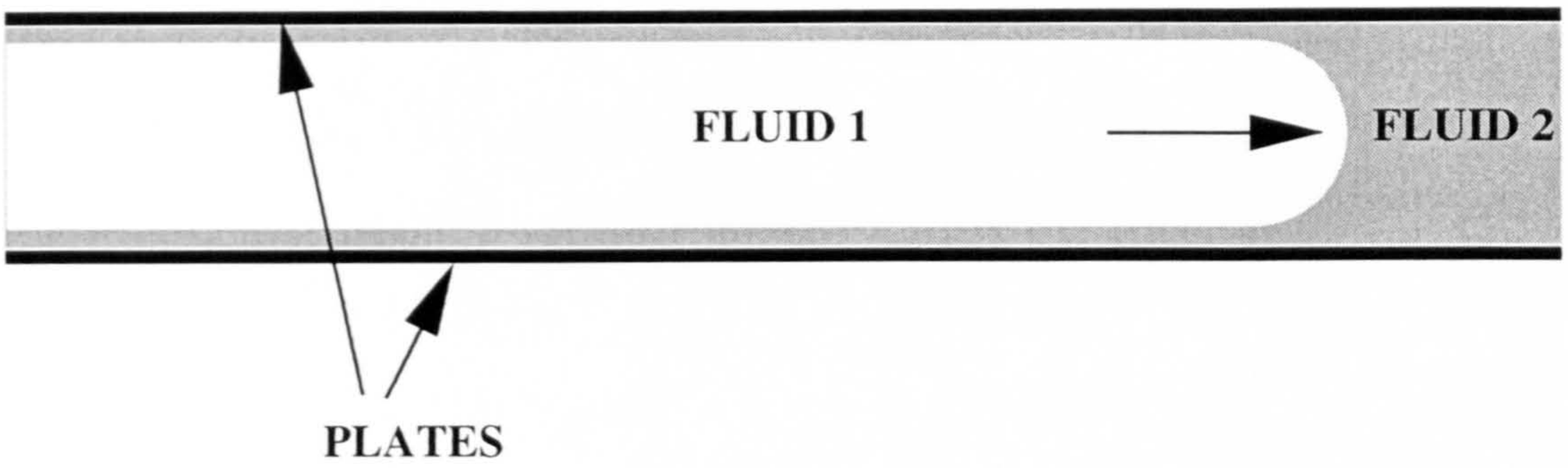

Figure 2.1: Two phase flow in a Hele Shaw cell. Fluid 1 is driven into fluid 2 and the flow is bounded by two parallel plates.

the coated film thickness, H^∞, are:

$$P(X_D) = -\frac{\gamma}{B(X_D)}\left(1 + 3.88Ca^{2/3}\right), \tag{2.1}$$

$$H^\infty = 1.34B(X_D)Ca^{2/3}, \tag{2.2}$$

where $B(X_D)$ is the semi-gap width between the rollers at the downstream meniscus, X_D. These conditions were first proposed by Bretherton (1961) in the study of a bubble flowing in a fluid filled capillary tube though the approach lacked the rigour of the matched asymptotic analysis of Park and Homsy.

Reinelt (1995) considered the journal bearing problem shown in figure 2.2. The journal bearing flow consists of a bead formed between two rotating eccentric cylinders. Thin films are pulled from the bead and coat the cylinder surface before re-entering the bead. Reinelt proposed a further correction to take account of the non-constant gap width and unequal roll speeds:

$$P(X_D) = -\frac{\gamma}{B(X_D)}\left(1 + 1.94(1 + S^{2/3})Ca^{2/3} + \left.\frac{\mathrm{d}B}{\mathrm{d}X}\right|_{X_D}\right), \tag{2.3}$$

where S is the ratio of the speeds of the two rolls. As will be seen in the following sections the journal bearing problem is similar to the DFF bead formed in a multiple roll coater though differs for two reasons; firstly the returning film can be set as a fraction of the outgoing film and secondly the journal bearing problem has two returning films and the volume of fluid is fixed whereas the DFF bead in the multiple roll coater has one returning film and the other incoming film is of fixed height. Following the example of Park and Homsy, the proposed conditions of Reinelt are confirmed in this

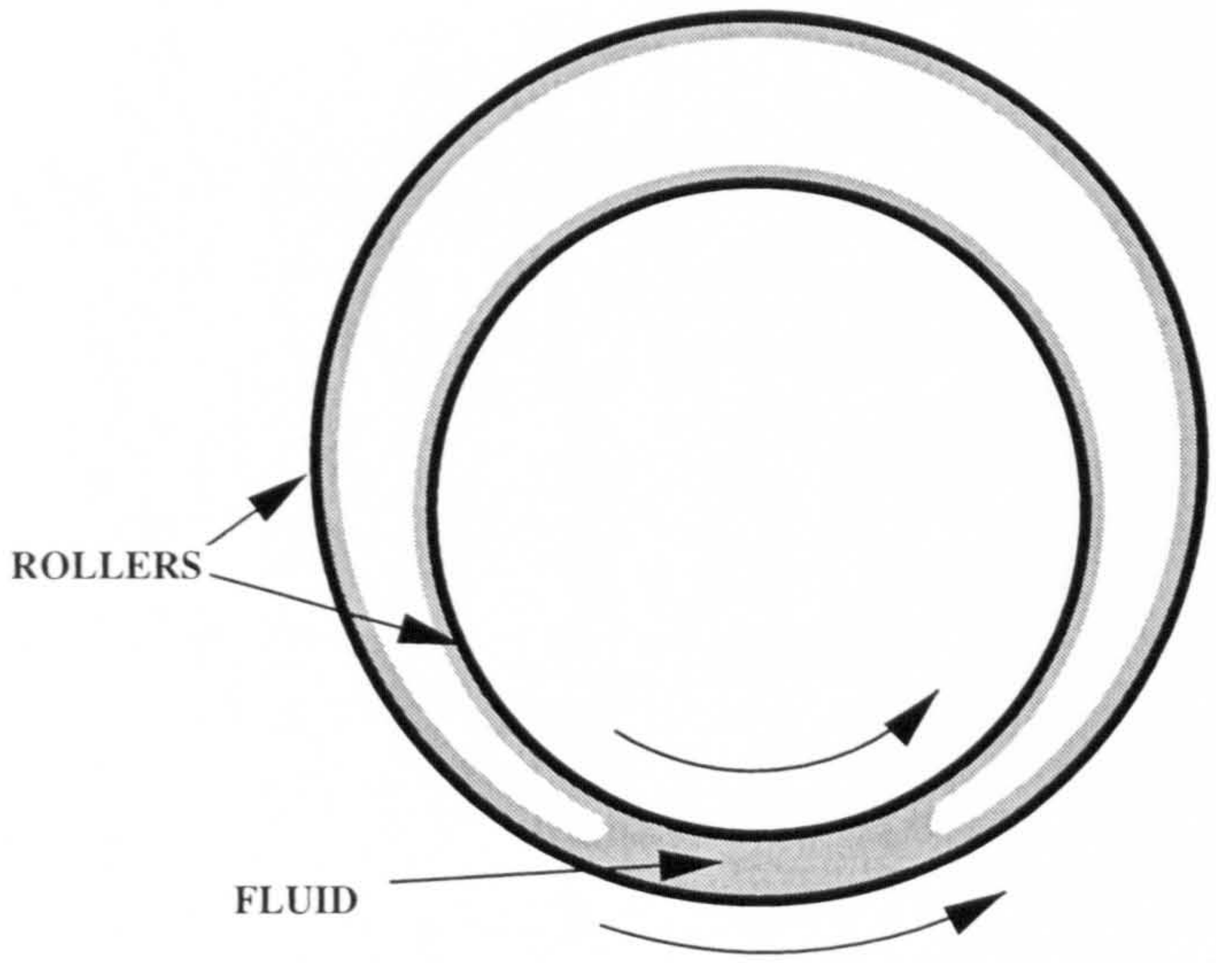

Figure 2.2: The journal bearing problem. A fluid bead forms in the gap between two rotating eccentric cylinders.

chapter by way of a matched asymptotic analysis. An additional reason for setting up the asymptotic framework is demonstrated in chapter 3 where it is used to formally develop the boundary conditions for the perturbed meniscus.

2.1 Mathematical model

In this chapter a double film fed (DFF) bead of fluid situated between an intermediate pair of rollers in a multiple roll system as depicted in figure 2.3 is considered. The incoming and outgoing film thicknesses on roll 1 (lower roll) are H_1 and H_3 and on roll 2 (upper roll) are H_2 and H_4, respectively. The other rolls in the system are accounted for by setting $H_2 = \zeta H_4$, with $0 \leq \zeta \leq 1$ and treating H_1 and ζ as parameters of the model. In a multiple roll system ζ is a function of the number, size and speed of the subsequent rolls in the system. Thus $\zeta = 1$ indicates no net fluid transfer between the rolls whilst $\zeta = 0$ corresponds to the case where H_2 is absent. Rolls 1 and 2, each of radius R, have peripheral speeds U_1 and U_2 respectively. The minimum gap between the rolls is $2B_0$.

The fluid is taken to be Newtonian and incompressible and as such the flow is

governed by the well known Navier-Stokes (Batchelor (1967)) equations

$$\rho\left(\frac{\partial}{\partial t}+\mathbf{U}.\nabla\right)\mathbf{U}=-\nabla P+\rho\mathbf{G}+\mu\nabla^2\mathbf{U}, \tag{2.4}$$

and the incompressiblity condition:

$$\nabla.\mathbf{U}=0. \tag{2.5}$$

$\mathbf{U}=(U,V)$, P, ρ and μ are the fluid velocity, pressure, density and viscosity respectively and $\mathbf{G}$ is the acceleration due to gravity. The system is described by several nondimensional parameters described below.

The roll speed ratio:

$$S=U_2/U_1; \tag{2.6}$$

the capillary number that represents that ratio of viscous to surface tension stresses:

$$Ca=\frac{\mu U_1}{\gamma}; \tag{2.7}$$

the Reynolds number that represents the ratio of inertial and viscous forces:

$$Re=\frac{\rho U_1 B_0}{\mu}; \tag{2.8}$$

the geometry ratio that represents the ratio of the Y and X length scales:

$$\delta=\sqrt{\frac{B_0}{2R}}; \tag{2.9}$$

the returning film fraction

$$\zeta=\frac{H_2}{H_4}; \tag{2.10}$$

the Stokes number that represents the ratio of gravitional and viscous forces:

$$St=\frac{\rho g B_0^2}{\mu U_1}; \tag{2.11}$$

and the input flux

$$\lambda=\frac{Q_i}{2B_0U_1}, \tag{2.12}$$

where Q_i is the incoming flux on roll 1 and is equal to U_1H_1. It is assumed that Ca, Re, St and δ are all much less than unity and that the flow is steady and independent of the axial coordinate. In the bulk of the bead, away from the interfaces, the variables are nondimensionalised with the following scales:

$$X\sim\sqrt{2B_0R},\quad Y\sim B_0,\quad U\sim U_1,\quad V\sim\sqrt{\frac{B_0}{2R}}U_1,\quad B(X)\sim B_0,\quad P\sim\frac{\mu U_1}{B_0}\sqrt{\frac{2R}{B_0}}, \tag{2.13}$$

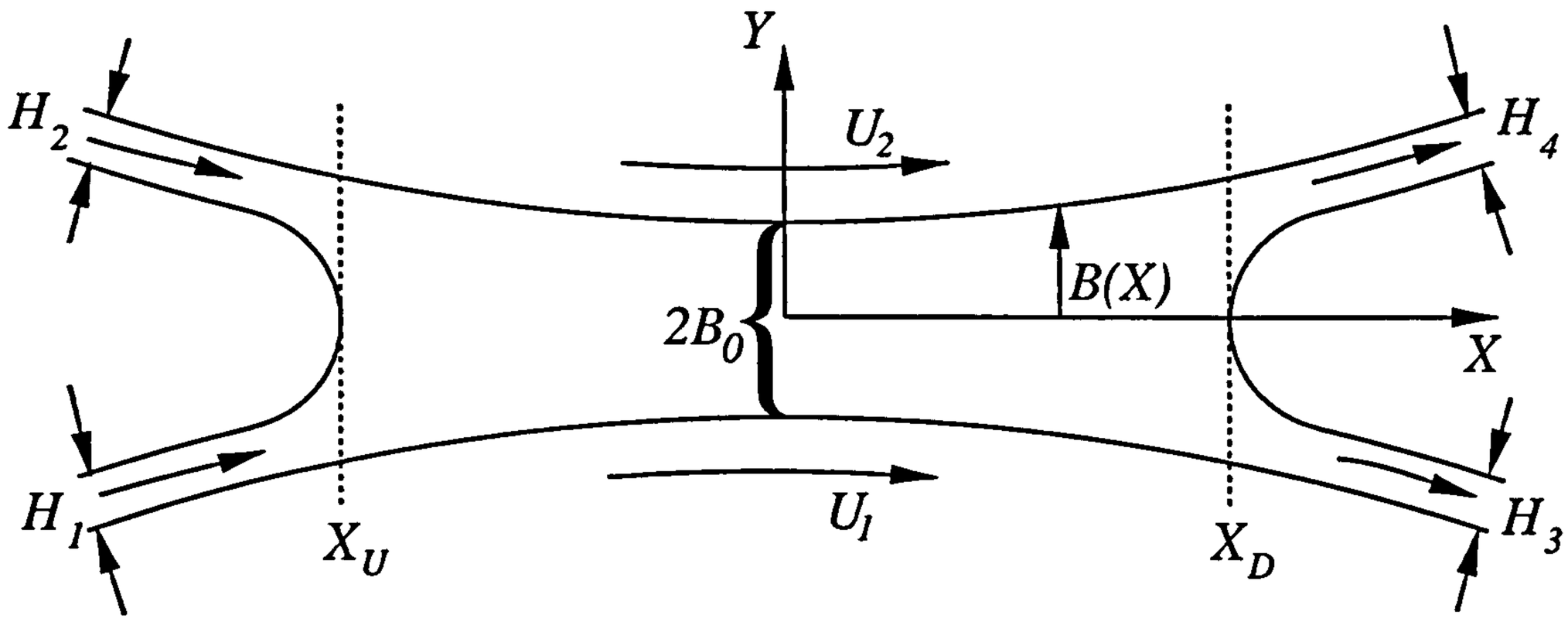

Figure 2.3: Double film fed bead between two adjacent rolls of a multiroll coater.

where

$$Y = B(X) = B_0 + R - \sqrt{R^2 - X^2}, \tag{2.14}$$

represents the semi-gap width and $B_0 = B(0)$. Note that the surface of roll 1 is given by $Y = -B(X)$ and that of roll 2 by $Y = B(X)$. These scales have been used many times before in the roll coating literature, (e.g. Coyle et al. (1986), Wilson (1997)). In the following upper/lower case letters represent dimensional/nondimensional variables, respectively.

The aim is to solve for the steady state locations of the upstream and downstream menisci, denoted by x_u and x_d respectively, for given values of the above input parameters.

2.1.1 Determination of x_d

The position of the downstream meniscus can be determined by a simple balance of the incoming and outgoing fluxes:

$$h_1 + Sh_2 = h_3 + Sh_4. \tag{2.15}$$

As $Ca \ll 1$ the Landau Levich relationships (1.10) for the outgoing heights h_3 and h_4 can be utilised:

$$h_3 = 1.337 b_d Ca^{2/3}, \tag{2.16}$$

$$h_2 = \zeta h_4 = 1.337 b_d \zeta (SCa)^{2/3}, \tag{2.17}$$

where $b_d = b(x_d) = 1 + x_d^2$. (2.16) and (2.17) allow h_3 and h_4 to differ due to unequal roll speed; it is proved in section 2.1.3 that this is the correct form of these expressions for $S \neq 1$. (2.15) - (2.17) and the fact that $h_1 = 2\lambda$, lead to the following expression for x_d

$$x_d^2 = \frac{2\lambda}{1.337(1 + (1-\zeta)S^{5/3})Ca^{2/3}} - 1, \tag{2.18}$$

from which the nondimensional flux q, scaled with $2U_1B_0$, follows directly

$$q = \frac{(1 + S^{5/3})\lambda}{1 + (1-\zeta)S^{5/3}}. \tag{2.19}$$

2.1.2 Determination of x_u

To find x_u it is necessary to solve for the flow field. The effect of assuming small Ca, Re, St and S on the governing fluid flow equations can be investigated by nondimensionalising the variables with the above scales. Using these scales, the Navier-Stokes equations become

$$Re\delta\left(u\frac{\partial u}{\partial x} + v\frac{\partial u}{\partial y}\right) = -\frac{\partial p}{\partial x} + \delta^2\frac{\partial^2 u}{\partial x^2} + \frac{\partial^2 u}{\partial y^2}, \tag{2.20}$$

$$Re\delta^3\left(u\frac{\partial v}{\partial x} + v\frac{\partial v}{\partial y}\right) = -\frac{\partial p}{\partial y} + \delta St g + \delta^4\frac{\partial^2 v}{\partial x^2} + \delta^2\frac{\partial^2 v}{\partial y^2}, \tag{2.21}$$

where it has been assumed that the y axis is vertical. The continuity equation is

$$\frac{\partial u}{\partial x} + \frac{\partial v}{\partial y} = 0. \tag{2.22}$$

Neglecting terms of $O(\delta^2, Re\delta, St\delta)$ these equations reduce to the well known lubrication equations:

$$\frac{\partial p}{\partial x} = \frac{\partial^2 u}{\partial y^2}, \tag{2.23}$$

$$\frac{\partial p}{\partial y} = 0. \tag{2.24}$$

Therefore, in the nip region, the cross stream pressure gradient ($\partial p/\partial y$) is negligible and thus p is independent of y at leading order. Also, the pressure gradient in the stream wise direction ($\partial p/\partial x$) is balanced by the viscous shear stress ($\partial^2 u/\partial y^2$). Now the governing the equations have been developed, the bounday conditions are formulated. On the roll surfaces the no slip boundary conditions are applied:

$$\mathbf{u}.\hat{\mathbf{t}}_2|_{y=b} = S, \qquad \mathbf{u}.\hat{\mathbf{t}}_1|_{y=-b} = 1, \tag{2.25}$$

where $\hat{\mathbf{t}}_1(x)$ and $\hat{\mathbf{t}}_2(x)$ are the unit vectors tangential to rolls 1 and 2, respectively, and are given by

$$\hat{\mathbf{t}}_1 = \begin{pmatrix} 1 \\ -2x\delta \end{pmatrix} + O(\delta^2), \qquad \hat{\mathbf{t}}_2 = \begin{pmatrix} 1 \\ 2x\delta \end{pmatrix} + O(\delta^2). \tag{2.26}$$

Thus, the boundary conditions reduce to

$$u(y=b) = S + O(\delta^2), \qquad u(y=-b) = 1 + O(\delta^2). \tag{2.27}$$

(2.23) can be integrated directly and the application of (2.27) leads to the following form of the horizontal velocity field

$$u = \frac{1}{2}\frac{\mathrm{d}p}{\mathrm{d}x}\left(y^2 - b^2\right) + \frac{S-1}{2b}y + \frac{S+1}{2}. \tag{2.28}$$

The nondimensional flux, q, past any x station can be calculated by simply integrating the velocity field between the two rollers:

$$2q = \int_{-b}^{b} u\mathrm{d}y = -\frac{2}{3}\frac{\mathrm{d}p}{\mathrm{d}x}b^3 + (1+S)b. \tag{2.29}$$

(2.19) gives q in terms of the systems parameters and thus (2.29) can be rearranged to give the integrated form of Reynolds equation for the pressure gradient

$$\frac{\mathrm{d}p}{\mathrm{d}x} = \frac{3}{2b^3}\left[(1+S)\,b - 2q\right]. \tag{2.30}$$

This is a first order differential equation with *two* associated boundary conditions:

$$p(x_u) = -\Delta P_u(x_u) = -\frac{\delta}{Ca}\frac{1}{b(x_u)}, \tag{2.31}$$

$$p(x_d) = -\Delta P_d(x_d) = -\frac{\delta}{Ca}\frac{1}{b(x_d)}, \tag{2.32}$$

where $\Delta P_i = p_a - p(x_i)$, $i = u, d$, represent the pressure drops across the interfaces, the radius of curvature at each meniscus is approximated by the associated semi-gap width and p_a is the ambient pressure, taken here to be zero. The problem is not over-prescribed as (2.31 a) enables us to find x_u by forming the function $f(x)$:

$$f(x) = p(x) + \Delta P_u(x) \tag{2.33}$$

where x_u simply satisfies $f(x_u) = 0$. f is given explicitly by

$$\begin{aligned} f = \frac{3}{4}(1+S)\left[\theta - \theta_d + \frac{1}{2}\sin 2\theta - \frac{1}{2}\sin 2\theta_d\right] - \frac{3}{4}q\left[\frac{3}{2}\theta - \frac{3}{2}\theta_d + \right. \\ \left. \sin 2\theta - \sin 2\theta_d + \frac{1}{8}\sin 4\theta - \frac{1}{8}\sin 4\theta_d\right] + \Delta P_u(x) - \Delta P_d(x_d) \end{aligned} \tag{2.34}$$

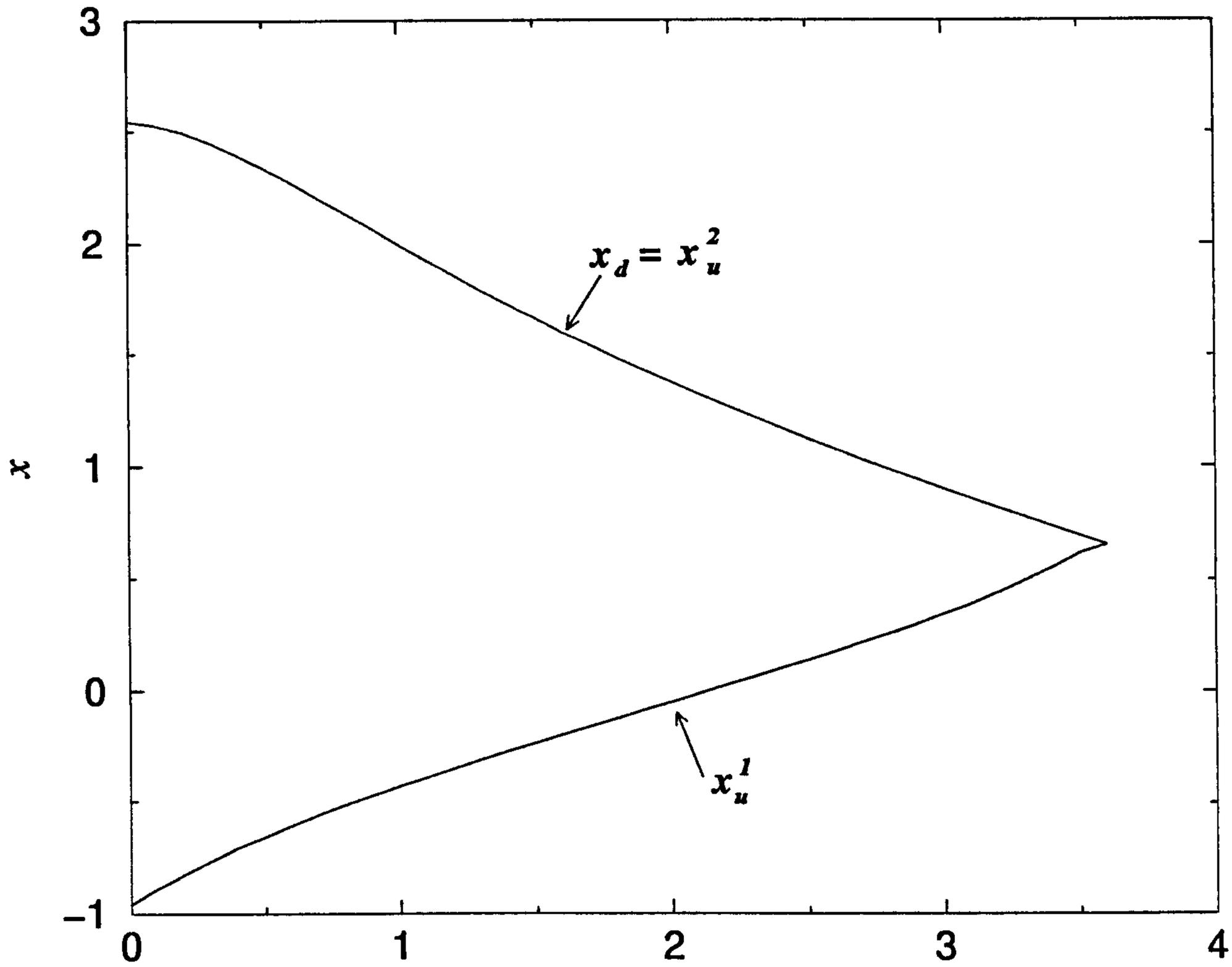

Figure 2.4: Mensicus positions against S. $Ca = 10^{-3}, \delta = 5 \times 10^{-3}, \lambda = 0.05, \zeta = 0.5$. The red line represents the downstream meniscus location solutions (in this case also equal to the second branch of upstream meniscus solutions)and the black line represents the first branch of the upstream meniscus location solutions.

where $x = \tan\theta$. The reader will note that x_d is also a root of f as defined in (2.33).

A typical plot of upstream and downstream menisci position against S is shown in figure 2.4 and it is interesting to compare this with the situation in the SFF case in figure 2.5, analysed by Kapur et al. (2000) where h_3 is replaced by a contact line. The differences are clear:

- for a given value of S, the SFF model has two values of the upstream meniscus location - both *distinct* from x_d - with one being stable (i.e. seen in practice) and the other unstable. In the DFF model there are two roots x_u^1 and x_u^2, one of

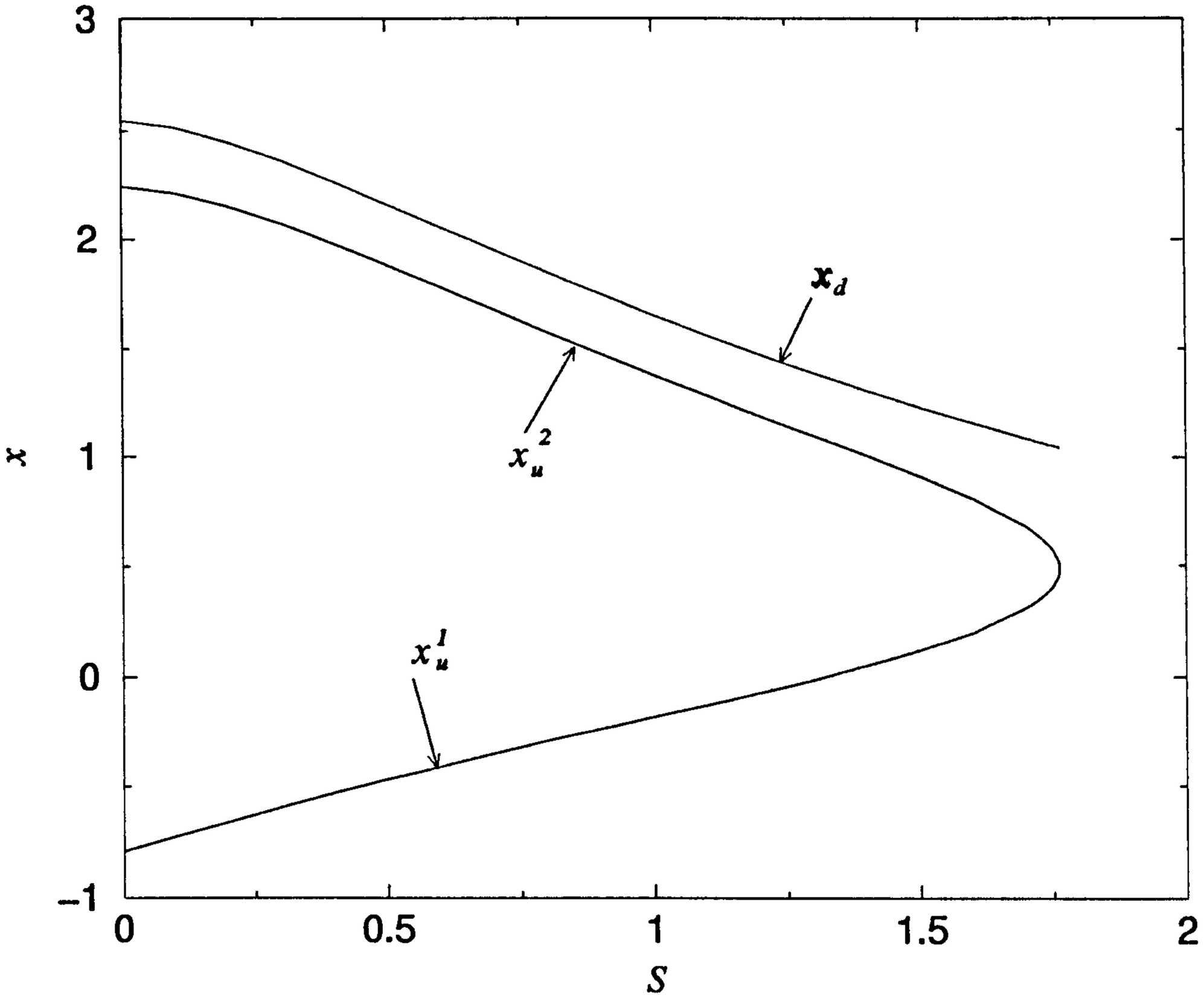

Figure 2.5: Meniscus positions against S for SFF model. — represents the downstream meniscus location curve. $Ca = 10^{-3}, \delta = 5 \times 10^{-3}, \lambda = 0.05, \zeta = 0.5$.

which is *coincident* with x_d (and hence non-physical).

- In the SFF case the variation of x_u with S exhibits a smooth turning point yet in the DFF case the x_u and x_d solution curves appear to meet in a corner. This apparent meeting of the menisci is a non-physical phenomenon and furthermore, lubrication theory is no longer strictly valid in this regime as the X and Y length-scales associated with the bead become comparable.

These differences could not easily be explained and led to a re-examination of the expressions employed for both the pressure drops and the outgoing film thicknesses.

2.1.3 Model refinements

This section uses the framework provided by Park and Homsy (1984) to systematically develop the boundary conditions first proposed by Reinelt (1995). There are several reasons for carrying out this formal development:

- Rigorous proof of the conditions suggested by Reinelt.
- Provide a framework that can be used to find the perturbed pressure boundary conditions needed for a linear stability analysis (see chapter 3).
- The form of the meniscus profile is found for the asymmetric case of $S \neq 1$ and could be compared with computations and experiment (Decre et al. (1995)) This was beyond the scope of the present work.

In order to find the pressure drops across the interfaces and the outgoing film thicknesses, the flow in the vicinity of the menisci needs to be considered. This is achieved at each interface in turn by analysing a capillary statics region (CSR), where capillary forces are dominant, and a transition region (TR), where capillary forces balance the viscous forces which dominate in the thin films far from the bead, and then matching the solutions of the two regions. These regions at the downstream meniscus are illustrated in figure 2.6. The downstream meniscus is analysed first and is followed by the upstream meniscus.

2.1.3.1 Downstream analysis

Governing equations of the CSR

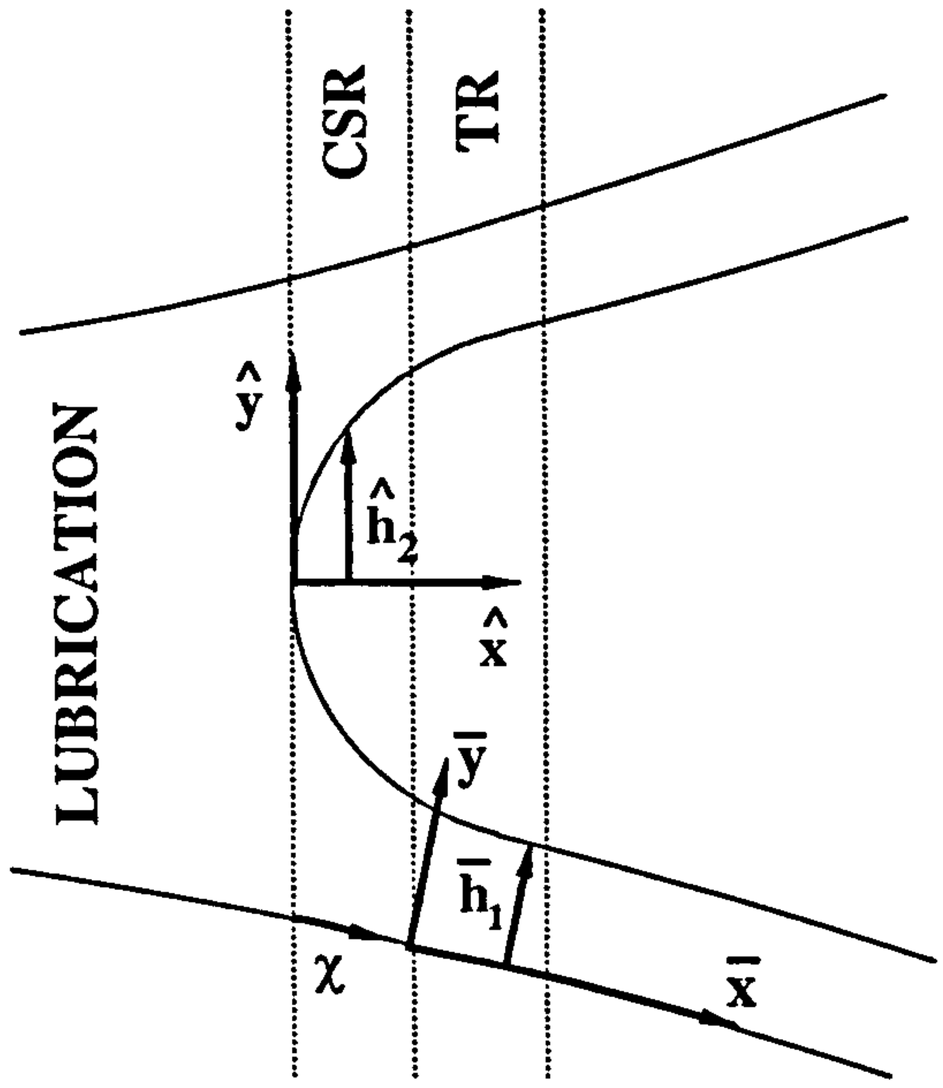

Figure 2.6: Regions and axes at downstream meniscus

Suitable scalings in the region of the downstream meniscus are:

$$X \sim B_D, \quad Y \sim B_D, \quad \mathrm{u} \sim U_2, \quad B(X) \sim B_D, \quad P \sim \sigma/B_D,$$

where $B_D = B(X_D) = R + B_0 - \sqrt{R^2 - X_D^2}$ and hence the solution in this region is dependent upon X_D.

After shifting the origin to the tip of the downstream meniscus and rescaling the variables the continuity equation and equation of motion in the vicinity of this interface are

$$\hat{\nabla}.\hat{\boldsymbol{u}} = 0, \qquad \hat{\nabla}\hat{p} = Ca\hat{\nabla}^2\hat{\boldsymbol{u}}, \tag{2.35}$$

and the normal stress balance is

$$\hat{p}_a - \hat{p} = \hat{\nabla}.\hat{\boldsymbol{n}} + O(Ca) \quad \text{on} \quad \hat{y} = \hat{h}. \tag{2.36}$$

$\hat{p}_a$ is the atmospheric pressure, $\hat{h}(\hat{x})$ represents the free surface profile and $\hat{\boldsymbol{n}}$ is the unit normal to the surface. Variables in this region, that have been non-dimensionalised as above, will be denoted by a 'hat'. (2.35) states that viscous forces are negligible in this region and thus only the pressure and free surface profile are solved for, leaving the flow field unknown. As $\hat{h}(\hat{x})$ is double valued it is split, as shown in figure 2.7, into 'lower' and 'upper' branches, $\hat{h}_1(\hat{x})$ and $\hat{h}_2(\hat{x})$ associated with the lower (roll 1) and

upper (roll 2) rolls, respectively. The normal stress balance then becomes

$$\hat{p}_a - \hat{p} = \Delta\hat{P} = \frac{(-1)^{i+1}\hat{h}_{i_{\hat{x}\hat{x}}}}{\left(1+\hat{h}_{i_{\hat{x}}}^2\right)^{3/2}} + O(Ca), \tag{2.37}$$

where i differentiates between the two branches of $\hat{h}$. (2.35) and (2.37) confirm that this is indeed a capillary statics region as the flow field does not enter the problem at leading order. Equation (2.37) is a differential equation for $\hat{h}_i$ containing an unknown constant, $\Delta\hat{P}$. Furthermore, (2.37) indicates that the surface profile can be found without solving for the flow field as the pressure drop across the meniscus is dominated by the surface tension of the fluid.

The formulation of the problem in this region is completed by imposing the following boundary conditions:

$$\hat{h}_1(\hat{x}=0) = \quad \hat{h}_2(\hat{x}=0) \quad = \hat{r}, \tag{2.38}$$

$$\hat{h}_{1_{\hat{x}}}(\hat{x}=0) = -\hat{h}_{2_{\hat{x}}}(\hat{x}=0) \quad = -\infty, \tag{2.39}$$

where (2.38) allows the solution to be asymmetric via the unknown constant $\hat{r}$ and (2.39) implicitly defines the origin of the CSR as the 'turning point' of the meniscus.

Governing equations in the TR

In the TR the fluid is drawn from the meniscus into thin films on each roll surface and thus here it is natural to adopt a curvilinear coordinate system $(\bar{x},\bar{y})$ as shown in figure 2.6 for the lower roll. A similar coordinate system associated with the upper roll exists, the analysis below holds for both rolls. Following previous workers (Bretherton (1961), Park and Homsy (1984)) the scales in this region, derived by balancing capillary and viscous stresses, are

$$P \sim \sigma/B_D, \quad U \sim U_1, \quad V \sim Ca^{1/3}U_1, \quad Y,H \sim Ca^{2/3}B_D, \quad X \sim Ca^{1/3}B_D,$$

and variables that have been non-dimensionalised with these scales are denoted by a 'bar'. In the following, $(\bar{x},\bar{y})$ refer to the TR coordinates on either roll. Neglecting terms of $O(Ca^{2/3})$ the governing equations reduce to the lubrication approximation:

$$\frac{\partial\bar{p}}{\partial\bar{x}} = \frac{\partial^2\bar{u}}{\partial\bar{y}^2}, \tag{2.40}$$

$$\frac{\partial\bar{p}}{\partial\bar{y}} = 0. \tag{2.41}$$

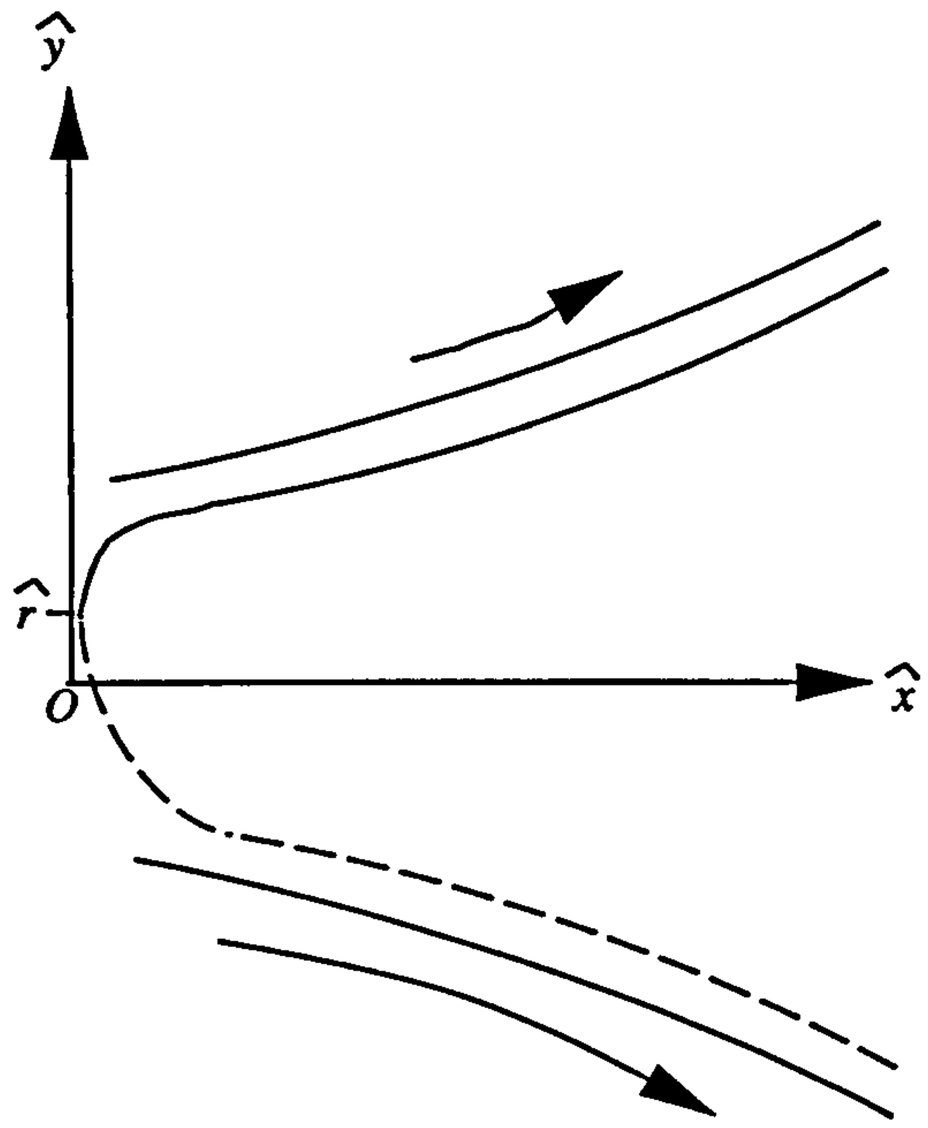

Figure 2.7: The meniscus is unsymmetric when $S \neq 1$ and to model this asymmetry the profile is split into two branches, $\hat{h}_1(\hat{x})$ (– –) and $\hat{h}_2(\hat{x})$ (—).

The tangential stress condition on the free surface is

$$\left.\frac{\partial \bar{u}}{\partial \bar{y}}\right|_{\bar{y}=\bar{h}_i} = 0. \tag{2.42}$$

The no slip condition on the roll surface is

$$\bar{u}|_{\bar{y}=0} = \kappa_i, \tag{2.43}$$

where $i = 1$ and $i = 2$ differentiate between the analysis of roll 1 and roll 2 respectively, therefore $\kappa_1 = 1$ and $\kappa_2 = S$. As $\bar{x} \to \infty$ the free surface height must approach that of the final coated film:

$$\bar{h}_i \to \bar{h}_i^{\infty} \quad \text{as} \quad \bar{x} \to \infty. \tag{2.44}$$

The normal stress balance is

$$\bar{p}|_{\bar{y}=\bar{h}_i} = \bar{h}_{i\bar{x}\bar{x}} \tag{2.45}$$

Matching condition

The two regions are linked by matching the film thickness between the roll surface and the interface. In the TR this quantity is simply given by $\bar{h}_i$ whereas in the CSR,

where it is denoted by $\hat{h}_{\perp_i}$, it is given by

$$\hat{h}_{\perp_i}(\hat{x}) = (\hat{b}(\hat{x}) - (-1)^i \hat{h}_i(\hat{x}))(1 + x_d^2 \delta^2 (\tfrac{1}{2} - 2\hat{x})) + O(\delta^3). \tag{2.46}$$

The semi-gap width relative to the CSR coordinates is $\hat{b}(\hat{x}) = 1 + 2\hat{x}x_d\delta + \hat{x}^2 b_d^2 \delta^2$. In order to facilitate the matching process it is useful to write $\hat{h}_{\perp_i}$ in terms of an arclength coordinate χ, shown in figure 2.6, and given by

$$\hat{\chi} = \hat{x}(1 - 2x_d^2 \delta^2 \hat{x}) + O(\delta^3). \tag{2.47}$$

This allows Van Dyke's matching rule (Hinch (1995)) to be used, resulting in

$$\lim_{\hat{\chi} \to \hat{l}_i} \hat{h}_{\perp_i} = Ca^{2/3} \lim_{\bar{x} \to -\infty} \bar{h}_i, \tag{2.48}$$

where $\hat{\chi} = \hat{l}_i$ is the origin of the TR on roll i. As this section is only concerned with the leading order correction due to the non-constant gap width, which will enter the solution at $O(\delta)$, terms of $O(\delta^2)$ can be neglected and the matching condition can be simplified to

$$1 + 2\hat{l}x_d\delta - \lim_{\hat{x} \to \hat{l}_i} \hat{h}_i = Ca^{2/3} \lim_{\bar{x} \to -\infty} \bar{h}_i. \tag{2.49}$$

This matching condition is utilised by firstly expanding h_i about $\hat{x} = l_i$, secondly rewriting the expansion in terms of $\bar{x}$ and finally by expanding the resultant expression about $\hat{l}_i^{00}$:

$$1 + 2\hat{l}x_d\delta - \left(\sum_{m \geq 0} \frac{Ca^{m/3} \bar{x}^m}{m!} \frac{\partial^m}{\partial \hat{x}^m} \right) \left(\sum_{n \geq 0} \left(\sum_{i,j \geq 0} Ca^{i/3} \delta^j l^{ij} \right)^n \frac{1}{n!} \frac{\partial^n}{\partial \hat{x}^n} \right) \hat{h}(\hat{x})|_{\hat{x}=l^{00}} = Ca^{2/3} \lim_{\bar{x} \to -\infty} \bar{h}_i. \tag{2.50}$$

The governing equations and associated boundary conditions of each region have been formulated and a matching condition linking the two regions has been stated. Now a solution in the form of a double expansion in the small parameters $Ca^{1/3}$ and δ is sought:

$$p = p^{00} + Ca^{1/3} p^{10} + \delta p^{01} + Ca^{1/3} \delta p^{11} + Ca^{2/3} p^{20} + \ldots, \tag{2.51}$$

$$h = h^{00} + Ca^{1/3} h^{10} + \delta h^{01} + Ca^{1/3} \delta h^{11} + Ca^{2/3} h^{20} + \ldots. \tag{2.52}$$

It is convenient to think of the Ca terms as corrections due to the finite thickness of the outgoing films and the δ terms as corrections due to the non-constant gap.

In the capillary statics region the flow field is not solved for, therefore asymmetries due to $S \neq 1$ which occur because of the no slip velocity conditions, only enter the problem via the transition region. However, the transition region enters the matching process at $O(Ca^{2/3})$ so until then the capillary statics solution must be symmetric and in particular $\hat{r}^{00} = 0$. Furthermore, the effect of the non-constant gap width enters at $O(\delta)$ so at $O(1)$ and $O(Ca^{1/3})$ the capillary statics region problem is exactly analogous to the Hele-Shaw cell problem discussed by Park and Homsy (1984) who found that $\Delta\hat{P}^{00} = 1$, $\hat{l}_i^{00} = 1$ and the surface profile at leading order to be

$$\hat{h}_i^{00} = (-1)^i(1-(1-\hat{x})^2)^{\frac{1}{2}}. \tag{2.53}$$

Thus at leading order the free surface is a circular arc. They also found that $\Delta\hat{P}^{10} = 0$, implying that $\hat{h}_i^{10} \equiv 0$.

The asymmetries due to unequal roll speed enter the matching condition at $O(Ca^{2/3})$ and this correction is now found.

The $O(Ca^{2/3})$ correction

The normal stress balance at $O(Ca^{2/3})$ is

$$\Delta\hat{P}^{20} = (-1)^{i+1}\left[\frac{\hat{h}_{i_{\hat{x}}}^{20}}{(1+\hat{h}_{i_{\hat{x}}}^{00^2})^{3/2}}\right]_{\hat{x}}, \tag{2.54}$$

with solution

$$\hat{h}_i^{20} = (-1)^{i+1}\frac{\hat{x}\Delta\hat{P}^{20}}{(1-(1-\hat{x})^2)^{\frac{1}{2}}} + \hat{r}^{20}, \tag{2.55}$$

and $\Delta\hat{P}^{20}$ and $\hat{r}^{20}$ are found from matching with the leading order solution from the TR which is now derived.

(2.40) can be solved, subject to (2.42) and (2.43), to produce

$$\bar{u} = \bar{p}_{\bar{x}}\left(\frac{\bar{y}^2}{2} - \bar{h}_i\bar{y}\right) + \kappa_i, \tag{2.56}$$

from which the flux, nondimensionalised with respect to $U_1 B_D Ca^{2/3}$, can be calculated:

$$\bar{q} = \int_0^{\bar{h}_i} \bar{u}\mathrm{d}\bar{y}, \tag{2.57}$$

$$= -\frac{1}{3}\bar{p}_{\bar{x}}\bar{h}_i^3 + \kappa_i\bar{h}_i. \tag{2.58}$$

Now the flux, $\bar{q}$, is independent of $\bar{x}$ and so is equal to the value at infinity, i.e. $\kappa_i\bar{h}_i^{\infty}$, where $\bar{h}_i^{\infty}$ is the final film thickness. Thus (2.58) can be rearranged to give the familiar

Landau Levich equation

$$\bar{h}^{00}_{i\bar{x}\bar{x}\bar{x}} = 3\kappa_i \frac{\bar{h}_i^{\infty^{00}} - \bar{h}_i^{00}}{\bar{h}_i^{00^3}}, \tag{2.59}$$

derived by Landau and Levich (1942) in relation to the problem of a plate being dragged from a bath of fluid. Making the transformation

$$\bar{X} = -(3\kappa_i)^{1/3} \frac{\bar{x} + \bar{s}_i}{\bar{h}_i^{\infty^{00}}}, \qquad \bar{H}_i = \frac{\bar{h}_i^{00}}{\bar{h}_i^{\infty^{00}}}, \tag{2.60}$$

leads to

$$\bar{H}^{00}_{i\bar{x}\bar{x}\bar{x}} = \frac{\bar{H}_i^{00} - 1}{\bar{H}_i^{00^3}}, \tag{2.61}$$

which has no dependency on S, thus $\bar{H}_1 \equiv \bar{H}_2$ and the subscripts are dropped hereafter. Imposing $\bar{H}^{00} \to \infty$ as $\bar{X} \to \infty$ and $\bar{H}^{00} \to 1$ as $\bar{X} \to -\infty$, leads to the following asymptotic expressions

$$\begin{aligned} \bar{H}^{00} &\sim \tfrac{1}{2}C_0\bar{X}^2 + C_1\bar{X} + C_2 \qquad \text{as } \bar{X} \to \infty, \\ \bar{H}^{00} &\sim 1 + Ae^{\bar{X}} \qquad\qquad\qquad\quad \text{as } \bar{X} \to -\infty. \end{aligned} \tag{2.62}$$

$\bar{s}_i$ is chosen such that C_1 is zero whilst A, C_0 and C_2 are determined by numerical integration of (2.61) and their values are 0.862, 0.643 and 2.895, respectively.

The matching condition at $O(Ca^{2/3})$ is:

$$\begin{aligned} -(-1)^i\Big(\frac{\bar{x}^2}{2}\hat{h}^{00}_{i\hat{x}\hat{x}}(\hat{l}_i^{00}) + \bar{x}\hat{l}_i^{10}\hat{h}^{00}_{i\hat{x}\hat{x}} + \frac{1}{2}\hat{l}_i^{10^2}\hat{h}^{00}_{i\hat{x}\hat{x}}(\hat{l}_i^{00}) + \hat{h}_i^{20}(\hat{l}_i^{00})\Big) \\ = (3\kappa_i)^{2/3}\frac{C_0}{2\bar{h}_i^{\infty^{00}}}\bar{x}^2 + (3\kappa_i)^{2/3}\frac{C_0}{\bar{h}_i^{\infty^{00}}}\bar{x}\bar{s}_i + C_2\bar{h}_i^{\infty^{00}} + (3\kappa_i)^{2/3}\frac{C_0}{2\bar{h}_i^{\infty^{00}}}\bar{s}_i^2. \end{aligned} \tag{2.63}$$

Note the fact that $\hat{h}_{i_{\hat{x}}}(\hat{l}_i^{00}) = 0$ has been used. The $\bar{x}^2$ terms give

$$\bar{h}_i^{\infty^{00}} = (3\kappa_i)^{2/3}C_0, \tag{2.64}$$

and thus the leading order expressions for the film heights (2.16) and (2.17) are confirmed. The $\bar{x}$ terms lead to

$$\hat{l}_i^{10} = \bar{s}_i. \tag{2.65}$$

Since $\hat{l}^{10}$ represents a correction to the origin of the TR, this states that the solution is independent of $\bar{s}_i$. The results of the remaining constant terms are

$$\Delta\hat{P}^{02} = C_0C_2\frac{3^{2/3}}{2}(1 + S^{2/3}), \tag{2.66}$$

$$\hat{r}^{20} = C_0C_2\frac{3^{2/3}}{2}(1 - S^{2/3}). \tag{2.67}$$

Substituting (2.66) and (2.67) into (2.55) gives the leading order asymmetrical contribution to the CSR free surface profile as

$$\hat{h}_i^{20} = (-1)^{i+1} \frac{1.94\left(1+S^{2/3}\right)\hat{x}}{\left(1-(1-\hat{x}^2)\right)^{\frac{1}{2}}} + 1.94\left(1-S^{2/3}\right) \tag{2.68}$$

This is the first time that either the expressions for the outgoing film heights for $S \neq 1$ have been confirmed or the asymmetrical contribution to the CSR free surface profile has been found.

The non-constant gap width corrections which enter the problem at $O(\delta)$ are now calculated.

The $O(\delta)$ correction

The $O(\delta)$ solution is similar in form to (2.55), the $O(Ca^{2/3})$ solution. Now the $O(\delta)$ matching condition is

$$2x_d \hat{l}_i^{00} - (-1)^i \hat{h}_i^{01}(\hat{l}_i^{00}) = 0, \tag{2.69}$$

the first term coming from the $\hat{b}$ contribution to $\hat{h}_{\perp_i}$. This condition gives

$$\Delta\hat{P}^{01} = -2x_d, \quad \text{and} \quad \hat{r}^{01} = 0. \tag{2.70}$$

Thus the correction due to the non-constant gap is simply proportional to the gradient of the gap where the meniscus forms and the solution is symmetric at this order.

The $O(\delta)$ correction to the surface profile in the TR, after a transformation similar to (2.60), is

$$\bar{H}^{01}_{\bar{X}\bar{X}\bar{X}} = \frac{3\bar{H}^{01} - 2\bar{H}^{00}\bar{H}^{01} - \bar{H}^{00}R}{\bar{H}^{00^4}} \tag{2.71}$$

where $R = \bar{h}_i^{\infty^{01}}/\bar{h}_i^{\infty^{00}}$. The asymptotic behaviour of $\bar{H}^{01}$ is

$$\begin{aligned} \bar{H}_i^{01} &\sim \tfrac{1}{2}D_0\bar{X}^2 + D_1\bar{X} + D_2 \qquad \text{as } \bar{X} \to \infty, \\ \bar{H}_i^{01} &\sim R + (B - RA\bar{X})e^{\bar{X}} \qquad \text{as } \bar{X} \to -\infty. \end{aligned}$$

As the $O(1)$ solution is independent of $\bar{s}_i$, it can be chosen so that $D_1 = 0$. Thus there are four unknown constants D_0, D_2, B and R and numerical integration of the third order equation (2.71) gives

$$R = -1.556D_0, \quad B = -0.853D_0, \quad D_2 = -2.04D_0. \tag{2.72}$$

The $\bar{x}^2$ terms from the $O(Ca^{2/3}\delta)$ matching condition are

$$(-1)^i \frac{1}{2}\left(\hat{l}_i^{01}\hat{h}^{01}_{i_{\bar{x}\bar{x}\bar{x}}} + \hat{h}^{01}_{i_{\bar{x}\bar{x}}}\right) = (3\kappa_i)^{2/3}\frac{D_0}{2h_i^{\infty^{00}}}, \tag{2.73}$$

and these give

$$D_0 = -2x_d \bar{h}_i^{\infty^{00}} / (3\kappa_i)^{2/3} \tag{2.74}$$

which in turn leads to

$$\bar{h}_i^{\infty^{01}} = 2x_d C_0 (3\kappa_i)^{2/3}. \tag{2.75}$$

Thus the correction to the outgoing film thickness has been confirmed as being proportional to the gap gradient.

Therefore the downstream pressure jump and outgoing film thicknesses, including the leading order corrections due to the non-constant gap width and finite thickness of the outgoing films are of the following form:

$$\Delta \hat{P}_d = 1 - 2x_d\delta + 1.94(1 + S^{2/3})Ca^{2/3} + O(Ca, \delta^2, Ca^{2/3}\delta), \tag{2.76}$$

$$\bar{h}_i^{\infty} = 1.337\kappa_i^{2/3}(1 + 2x_d\delta) + O(Ca^{2/3}, \delta^2, Ca^{1/3}\delta). \tag{2.77}$$

2.1.3.2 Upstream analysis

The analysis for the upstream menisci is largely similar to that of the downstream with two main differences. The first difference is that x_d needs to be replaced by $-x_u$ in the $O(\delta)$ terms as this is the distance from the nip to the upstream interface. The second difference enters via the no slip boundary conditions on the roll surfaces used in the TR analysis since at the downstream interface the thin films are being pulled from the bead whereas at the upstream interface they are being pushed into the bead. Therefore the $O(Ca^{2/3})$ correction needs to be recalculated as the leading order solution in the TR will have a different form.

In the TR the free surface profile is governed by an equation equivalent to (2.59):

$$\bar{h}_{i\bar{x}\bar{x}\bar{x}}^{00} = -3\kappa_i \frac{\bar{h}_i^{\infty^{00}} - \bar{h}_i^{00}}{\bar{h}_i^{00^3}}. \tag{2.78}$$

Making the transformation

$$\bar{X} = (3\kappa_i)^{1/3} \frac{\bar{x} + \bar{s}_i}{\bar{h}_i^{\infty}}, \qquad \bar{H}_i = \frac{\bar{h}_i}{\bar{h}_i^{\infty}}, \tag{2.79}$$

where $\bar{h}_i^{\infty}$ now represents the thickness of the incoming films, results in (2.61). However, this time the solution is required to decay as $\bar{X} \to \infty$ rather than as $\bar{X} \to -\infty$, as was the case at the downstream meniscus. This means that the asymptotic behaviour of

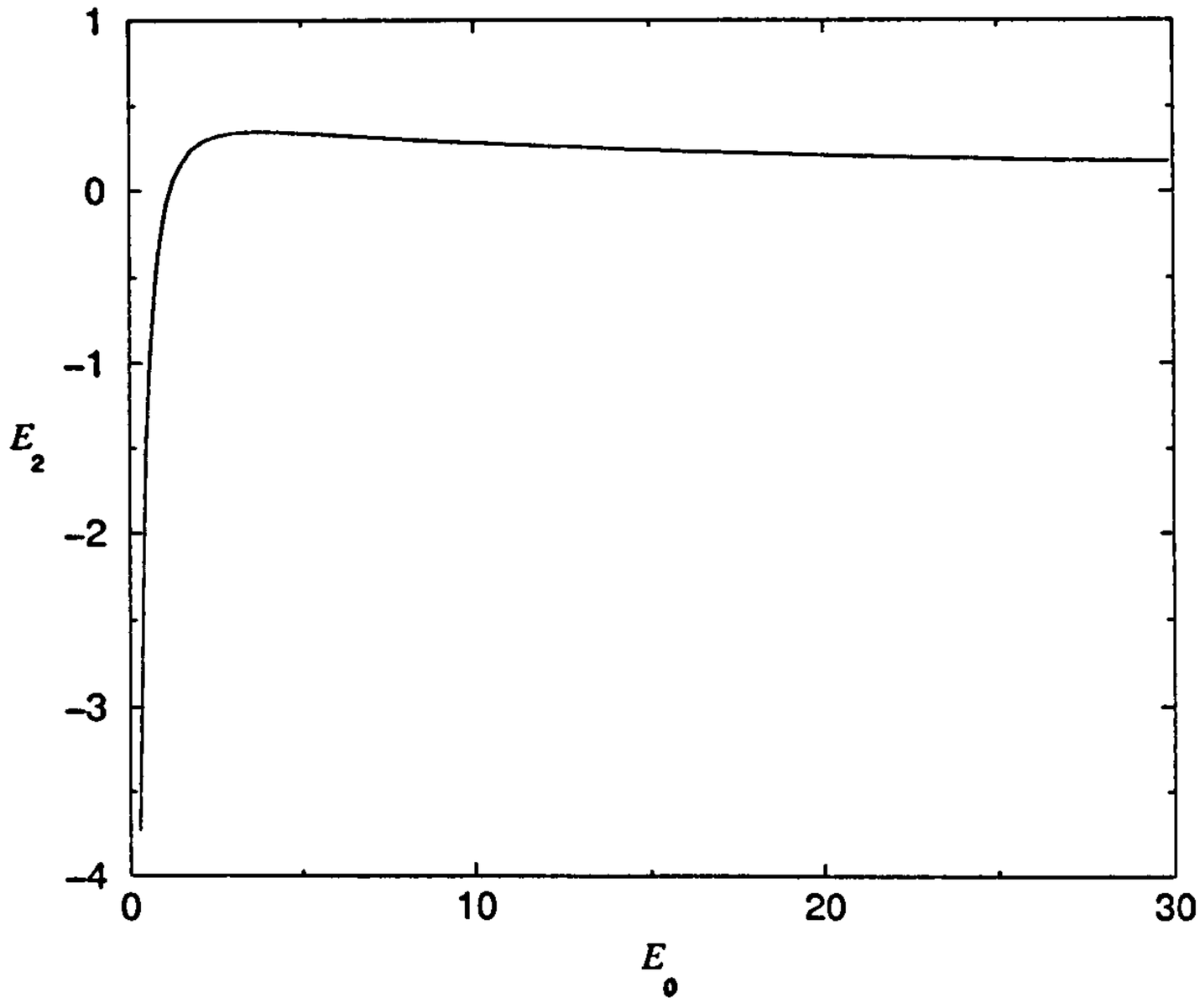

Figure 2.8: E_2 against E_0

$\bar{H}_i^{00}$ is

$$\begin{aligned} \bar{H}_i^{00} &\sim \tfrac{1}{2}E_{0_i}\bar{X}^2 + E_{2_i} && \text{as } \bar{X} \to -\infty, \\ \bar{H}_i^{00} &\sim 1 + e^{-\bar{X}/2}(I_i \cos\tfrac{\sqrt{3}}{2}\bar{X} + J_i \sin\tfrac{\sqrt{3}}{2}\bar{X}) && \text{as } \bar{X} \to \infty. \end{aligned}$$

Note that this is a third order equation with boundary conditions containing four unknowns, thus three of the unknowns can be found as functions of the fourth via numerical integration of (2.61). In this case, (2.59) was integrated numerically for a range of E_{0_i} giving the corresponding values of E_{2_i}, I_i and J_i. Figure 2.8 shows E_2 as a function of E_0. The matching condition at $O(Ca^{2/3})$, at the upstream interface, is similar to (2.63) with the $\bar{x}^2$ terms producing:

$$E_{0_1} = \frac{2\lambda}{(3Ca)^{2/3}b_u}, \qquad E_{0_2} = \frac{b_d}{b_u}\zeta C_0. \tag{2.80}$$

The constant terms give:

$$\Delta\hat{P}_u^{02} = \frac{\lambda}{Ca^{2/3}b_u}E_{2_1} + \frac{b_d\zeta(3S)^{2/3}C_0}{2b_u}E_{2_2}, \tag{2.81}$$

$$\hat{r}^{20} = \frac{\lambda}{Ca^{2/3}b_u}E_{2_1} - \frac{b_d\zeta(3S)^{2/3}C_0}{2b_u}E_{2_2}. \tag{2.82}$$

Therefore the pressure jump at the upstream interface is

$$\Delta\hat{P}_u = 1 + 2x_u\delta + \frac{\lambda}{b_u}E_{2_1} + \frac{b_d\zeta(3S)^{2/3}C_0}{2b_u}E_{2_2}Ca^{2/3}. \tag{2.83}$$

Again, this is the first time the shape of the upstream meniscus has been found for $S \neq 1$ and the form of the boundary conditions has been confirmed.

2.1.3.3 Summary of model refinements

A matched asymptotic analysis has been performed to find the correct form of the boundary conditions as $Ca \to 0$. The corrected form of the outgoing film thicknesses h_3 and h_4 has been shown to be:

$$h_3 = 1.337 h_d (1 + 2x_d\delta) Ca^{2/3}, \tag{2.84}$$

$$h_4 = 1.337 h_d (1 + 2x_d\delta) S^{2/3} Ca^{2/3}, \tag{2.85}$$

and the pressure drops across each interface are:

$$p(x_d) = -\Delta P_u = -\frac{\delta}{Ca h_d}\left(1 - 2x_d\delta + 1.94(1 + S^{2/3}) Ca^{2/3}\right), \tag{2.86}$$

$$p(x_u) = -\Delta P_d = -\frac{\delta}{Ca h_u}\left(1 + 2x_u\delta + \frac{\lambda}{h_u} E_{2_1}\right. \tag{2.87}$$

$$\left. + \frac{1.337\zeta h_d S^{2/3}}{2h_u} E_{2_2} Ca^{2/3}\right). \tag{2.88}$$

E_{2_i} is related to E_{0_i} numerically via (2.61) where

$$E_{0_1} = \frac{2\lambda}{(3Ca)^{2/3} b_u}, \quad E_{0_2} = \frac{0.643 h_d \zeta}{b_u}.$$

The higher order terms can simply be thought of as corrections to the radii of curvature of the interfaces, the $O(\delta)$ terms due to the non-constant gap width and the $O(Ca^{2/3})$ terms taking into account the presence of the thin films. x_d and x_u are solved for as before with f remaining as defined in (2.33) and (2.34), the only difference being the ΔP's are now defined via (2.86) and (2.87).

As terms of $O(Ca)$ are neglected yet terms of $O(\delta)$ are retained, for consistency it is required that $Ca << \delta << 1$.

2.1.4 Stability analysis

Daniels (1997) demonstrated that for small capillary numbers in the case of the SFF bead, the upstream interface could become two dimensionally unstable. These results were supported by the experiments of Kapur et al. (2000) who demonstrated that when the speed ratio S is increased from zero, a critical value is reached at which the

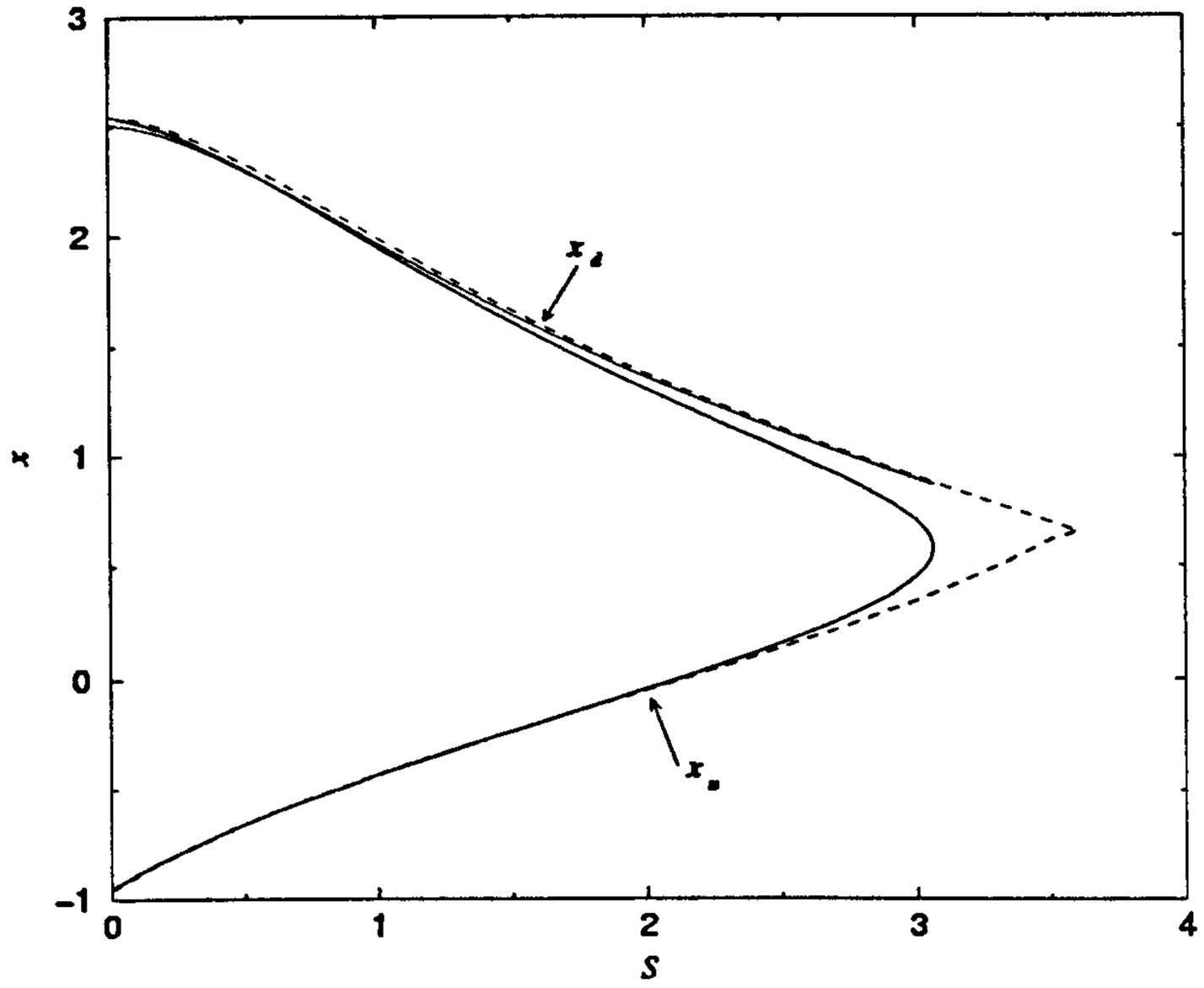

Figure 2.9: Menicus positions against S. — HOM; - - - LOM. $Ca = 10^{-3}, \delta = 5 \times 10^{-3}, \lambda = 0.05, \zeta = 0.5$. Red curves represent downstream meniscus locations, black curves represent upstream meniscus locations.

bead collapses. The instability leading to the collapse is thought to be two dimensional as no three dimensional disturbances (in the axial direction) were observed. The S.H. (1.19) can be used to indicate whether a 2-D perturbation to a meniscus results in a stabilising/destabilising force and furthermore it only requires steady state results. As such the S.H. is used in this chapter with it being noted that (1.19) is equivalent to the statement that the bead is deemed to be stable if and only if

$$\frac{\mathrm{d}f}{\mathrm{d}x} > 0. \tag{2.89}$$

2.2 Results

2.2.1 Effect on meniscus locations and S_c

Figure 2.9 shows a typical plot of menisci positions against speed ratio S and it allows the effect of the small terms to be seen. The dashed line represents the leading order model (LOM) where the correction terms are neglected and the solid line represents the refined higher order model (HOM). As S is increased both models predict that the

menisci move towards each other and in each case there is a maximum value of S, S_c say, beyond which no two dimensional steady state solutions exist. S_c represents the point at which the two roots of f become one, hence the gradient of f is zero here. Therefore according to (2.89) the bead is neutrally stable here and thus S_c is associated with the critical speed ratio at which the bead collapses. The reader will note that this result indicates that the LOM predicts a bead of infinitesimal width to be stable which is clearly unphyscial, and so provides further motivation for deriving the HOM. It is clear that at relatively low values of S the correction terms play a minor role as the differences between the predictions of the two models is minimal. This explains why Wilson (1997) obtained good agreement between lubrication theory and F.E. simulation over a significant range of S even though the correction terms were not included in the lubrication analysis. However, as S_c is approached the predictions begin to differ more substantially culminating in a 20% difference in the predicted value of S_c. Furthermore, for each S the HOM produces two values of x_u, each distinct from x_d, and the corner is replaced by a smooth turning point. Thus the addition of the small terms produces results similar in form to the SFF model and significantly alters the prediction of S_c and hence the critical operating conditions.

It is possible to estimate the discrepancy in the predicted values of S_c by approximating f^H (where the H superscript refers to the HOM) by a parabola in the region of $x_c = x_u(S_c)$:

$$f^H = \frac{f^H_{xx}}{2}(x - x_c)^2 + O((x - x_c)^4). \tag{2.90}$$

Assuming the difference between f^H and f^L (where the L superscript refers to the LOM) to be small then for some function $\Delta(x)$:

$$f^L = \frac{f^H_{xx}}{2}(x - x_c)^2 + \Delta(x) + O((x - x_c)^4), \quad \text{where} \quad |\Delta| \ll 1. \tag{2.91}$$

f^L is zero when $f^H_{xx}(x - x_c)^2/2 \sim \Delta$, i.e. when $x - x_c \sim \Delta^{1/2}$, assuming $|f^H_{xx}| \sim 1$. Assuming the roots of f^L to be symmetric about x_c and the rate of contraction of the bead to be constant suggests that the discrepency in S_c scales with $2(2\Delta/f^H_{xx}(x_c))^{1/2}$. Therefore the difference in the prediction of S_c is always larger than the size of the correction terms.

Figure 2.10 shows the number of two dimensionally stable solutions in ζ, S space as calculated by the HOM. Values of (ζ, S) that lie within the grey area have one stable

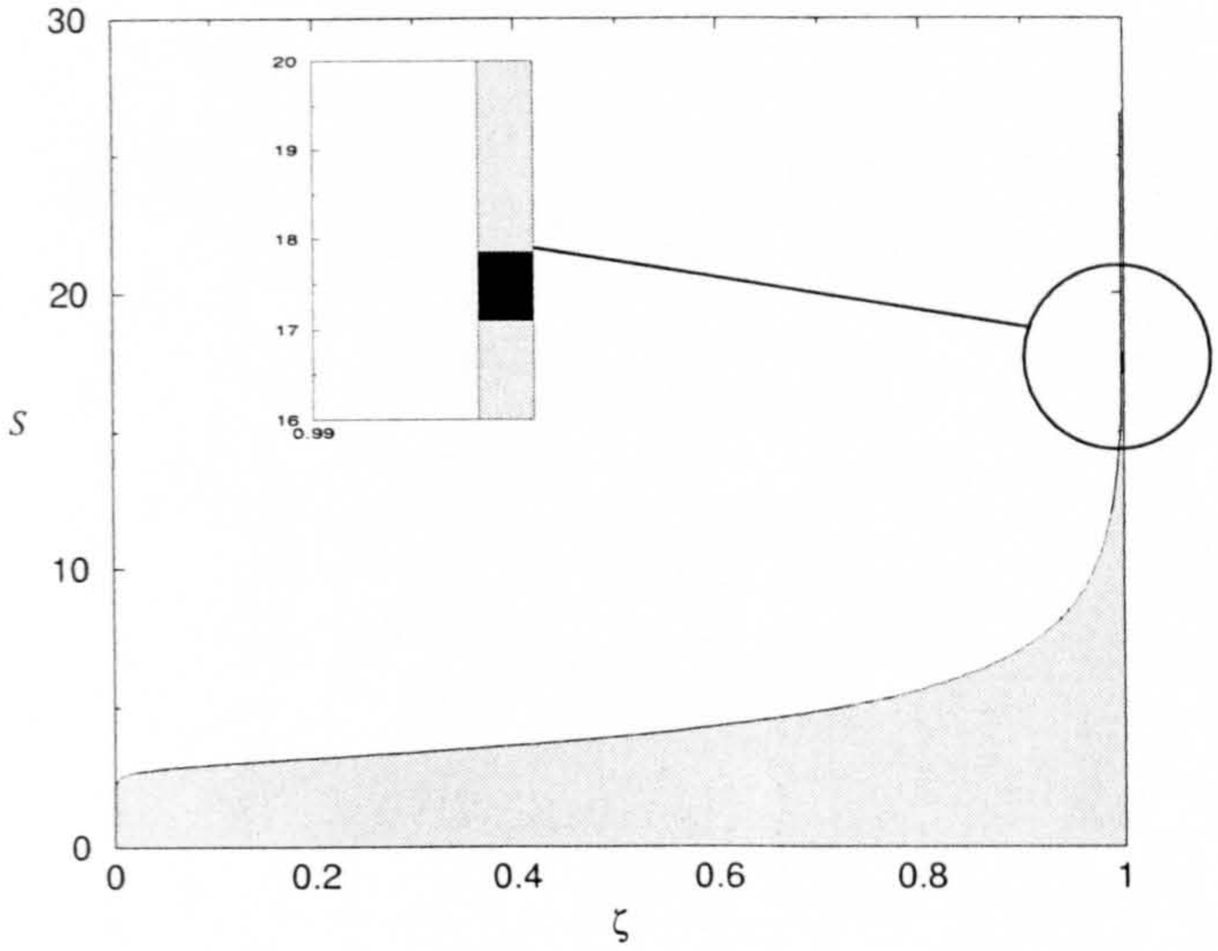

Figure 2.10: Number of two dimensionally stable solutions when $Ca = 10^{-3}$, $\delta = 5 \times 10^{-3}$, $\lambda = 0.08$. White regions have no 2-D stable solutions, grey regions have one and black regions have two.

solution, in the black region there are two and elsewhere there are none. Thus as $\zeta \to 1$ the range of S for which stable solutions exist increases drastically and for certain values of S there are multiple stable solutions. As $\zeta \to 0$ the returning film thins and the comparison of these results with previous theoretical and experimental investigations for a SFF bead is of interest. These two limits are explored in detail below.

2.2.2 The limit $\zeta \to 1$

Figures 2.11(a) to (f) show menisci position plots for values of ζ ranging from 0.99 to 1.0. Figures 2.11(a) and (b), where $\zeta = 0.99$ and 0.997 respectively, are similar to figure 2.9 and the turning point of x_u is identified with the onset of bead break. The LOM has again been plotted for comparison and here the difference in predictions of S_c is in the region of 25%. In figure 2.11(c) the HOM predicts the x_u curve to have three, rather one, turning points. According to (2.89) the sections of the curve below point 1 and between points 2 and 3 will be two dimensionally stable and thus for a small range of S there is no longer a unique two dimensionally stable steady state. In addition at point 1 the bead is neutrally stable and if S is increased further then the bead could either collapse or jump to the section of the solution curve between points 2 and 3.

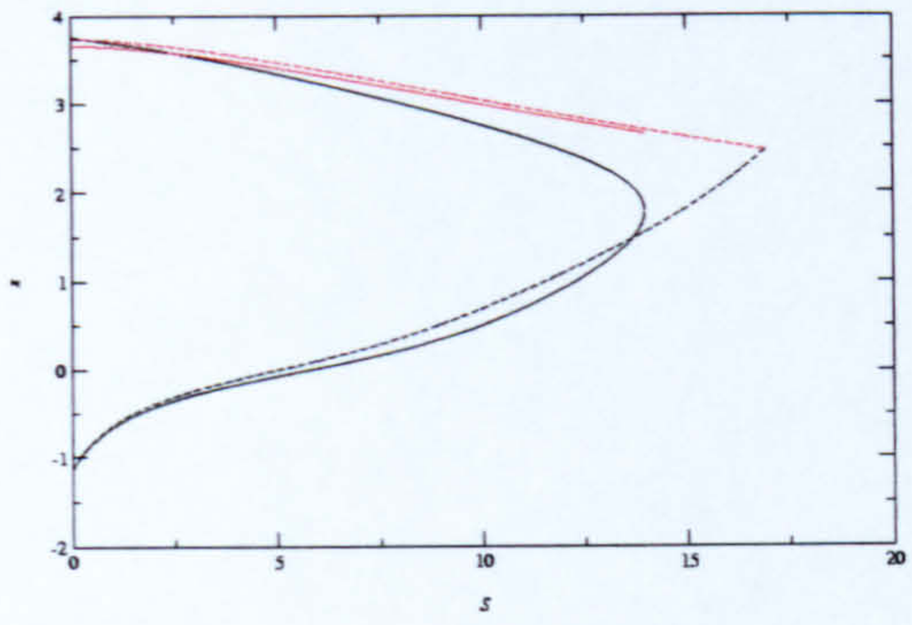

(a) $\zeta = 0.99$

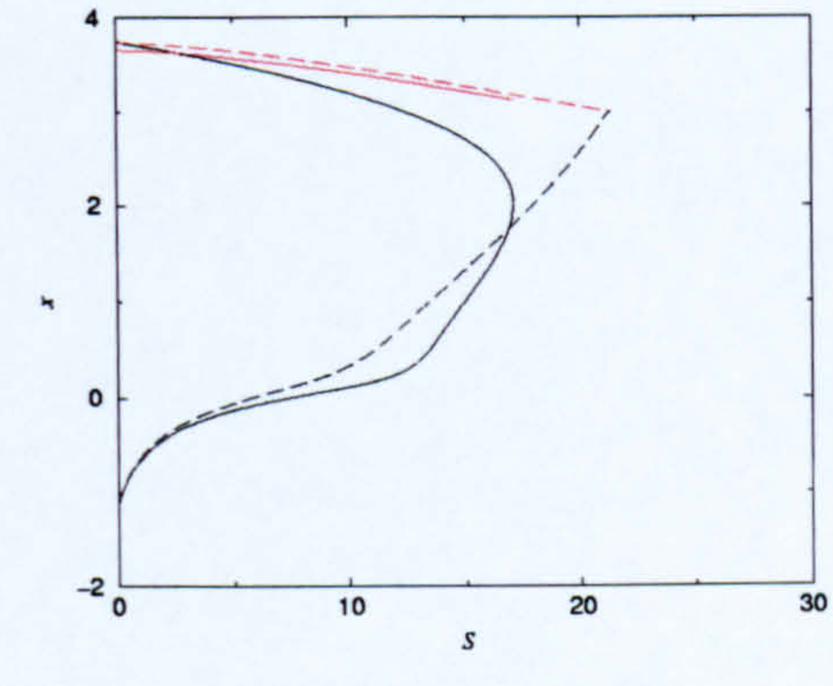

(b) $\zeta = 0.997$

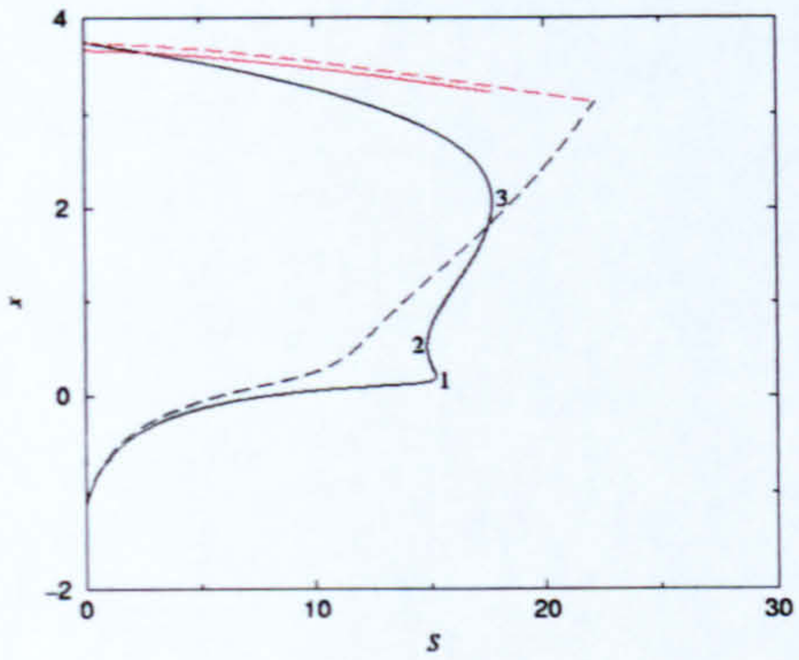

(c) $\zeta = 0.99775$

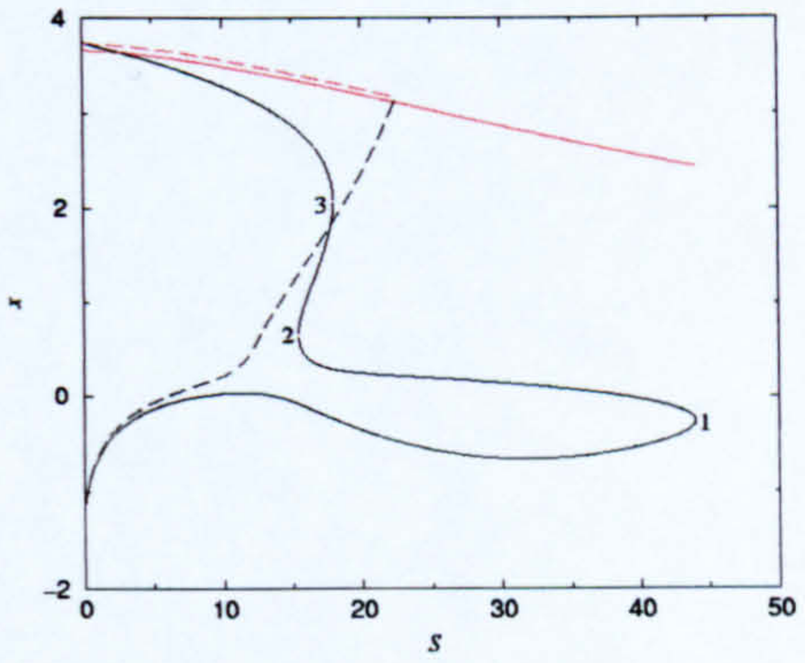

(d) $\zeta = 0.998$

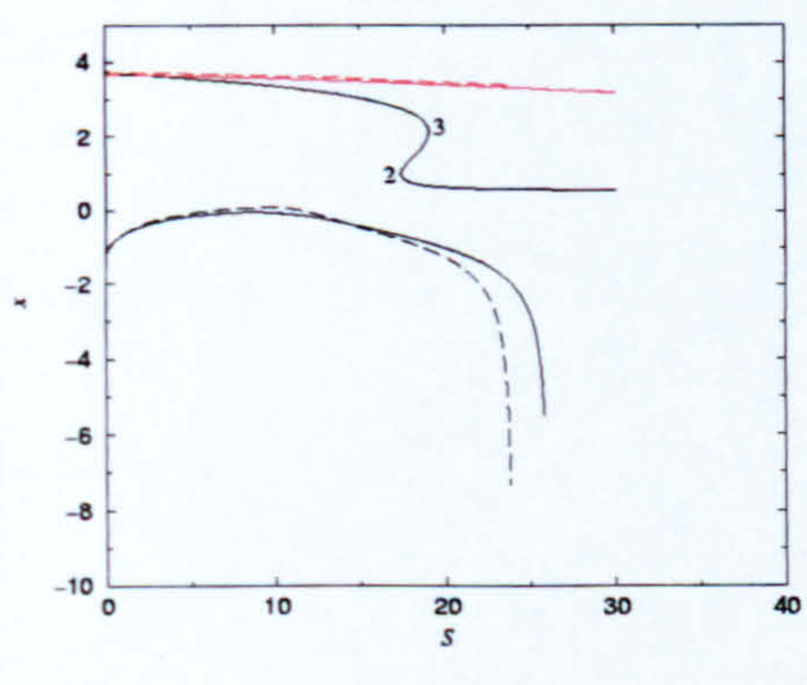

(e) $\zeta = 0.999$

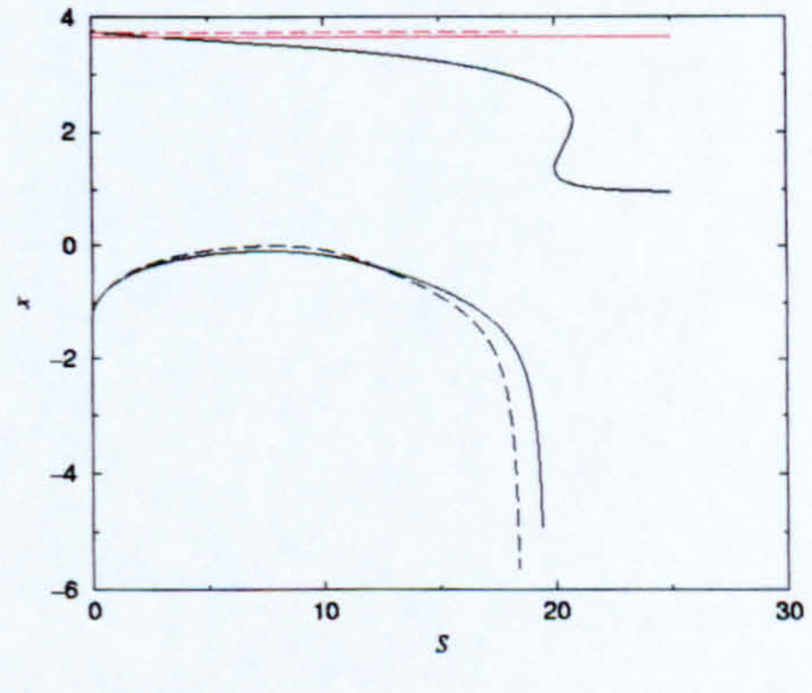

(f) $\zeta = 1.0$

Figure 2.11: Menisci positions against S for different values of ζ. —- HOM; - - - LOM. Red curves represent downstream meniscus locations, black curves represent upstream meniscus locations. $Ca = 10^{-3}$, $\delta = 5 \times 10^{-3}$, $\lambda = 0.1$.

Increasing ζ further leads to a dramatic increase in the 'lobe' between points 1 and 2 as figure 2.11(d) shows and then incrementing S still further gives rise to a change in the form of the x_u solution curve, i.e. it is no longer continuous, see figure 2.11(e). It appears that there is a value of ζ at which the lobe 'snaps' and in figure 2.11(e) the turning points analogous to those in figure 2.11(c) have been labelled. Tracing the x_u solution curve from $S = 0$ in figures 2.11(e) and (f) only temporarily results in bead contraction before it begins to expand again and then at some value of S, S_f say, the upstream meniscus moves rapidly outwards - a feature which is identified as 'upstream flooding'. Despite the fact that three dimensional instabilities cannot be ruled out in figures 2.11(e) and (f) the plots do mimic the experimental results of Benkreira et al. (1981) and Benjamin (1994) who investigated the flux through a DFF bead. Benjamen reported that for a DFF bead with $Ca = 0.83$ and $S = 1$, when the flux q equalled 1.315 the upstream interface flooded and the flow became three dimensional. Benkreria measured the flux through a moderately starved DFF bead (steady and 2-D) over a wide range of capillary numbers ($10^{-2} - 10$) and found it to be constant and equal to $0.651(1 + S)$. These experimental results are similar to the theoretical value of $\frac{2}{3}(1 + S)$ for the flux through a fully flooded pair of rolls and suggest that when the flux through a DFF bead approaches this value then the inlet floods. Table 2.1 shows, for various values of λ and ζ, the value of $q/(1 + S)$ for $S = S_f(\lambda, \zeta)$. The values are similar to those obtained experimentally and provide the rationale for associating S_f, where the steady state solutions predict the upstream interface to move rapidly outwards, with the point of transition from a starved to moderately starved inlet. In each of figures 2.11(e) and (f) there is a second branch of x_u solutions and in both cases this branch contains a section of two dimensionally stable states, though it is only in the former that the two dimensional stable sections of each branch coexist over a range of S. The two distinct phenomena of bead break (figure 2.11(a)) and flooding (figure 2.11(f)) are predicted by both the LOM and HOM and are supported by experiment. However, the states represented by figures 2.11(b)-(e) differ so little in their values of ζ it is doubtful whether this intermediate behaviour could be demonstrated by experiment. In addition, the route taken between bead break and flooding differs qualitatively between the models and it is unclear whether the effect of further terms would overide the significant changes shown here in the

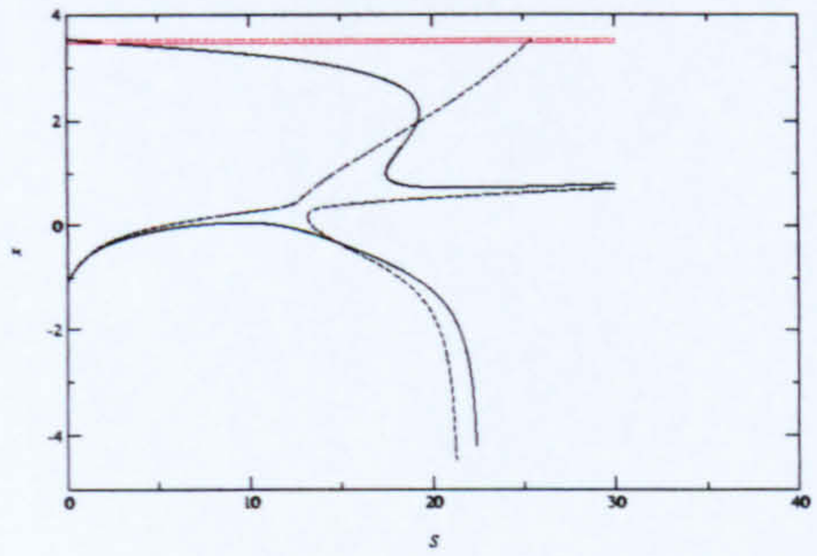

(a) $\lambda = 0.09$

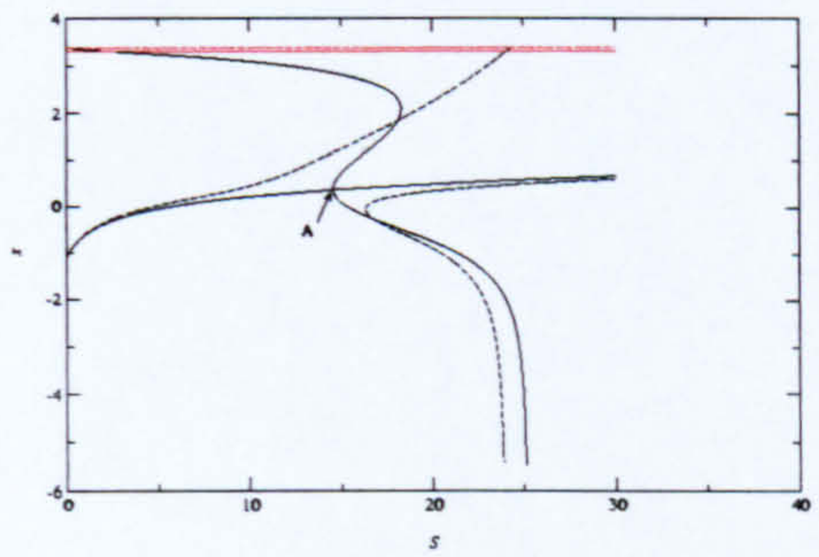

(b) $\lambda = 0.08323$

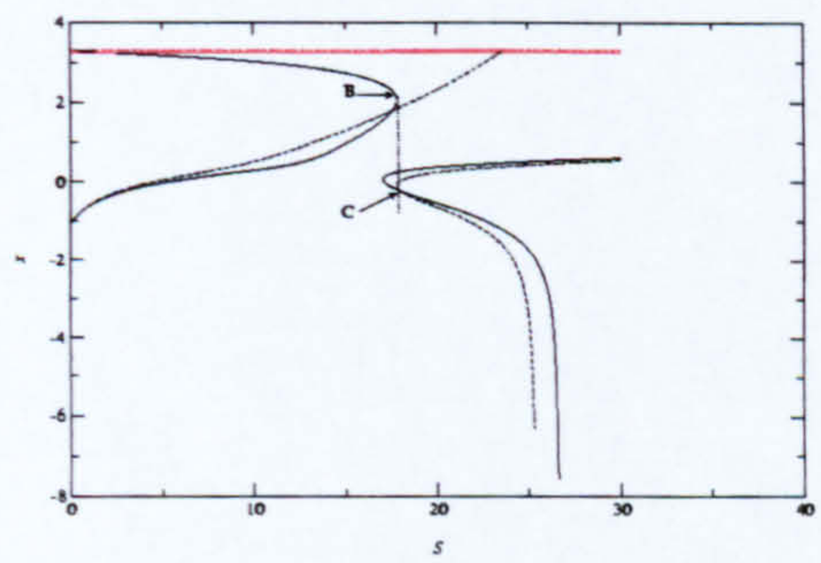

(c) $\lambda = 0.08$

Figure 2.12: Menisci locations against S for different values of λ. —- HOM; - - - LOM. Red curves represent downstream meniscus locations, black curves represent upstream meniscus locations. $Ca = 10^{-3}$, $\delta = 5 \times 10^{-3}$, $\zeta = 1.0$.

λ	ζ	$\frac{q}{1+S}\|_{S_f}$
0.1	1.0	0.695
0.09	1.0	0.693
0.08	1.0	0.691
0.1	0.999	0.691

Table 2.1: The value of the flux at S_f for several values of λ and ζ.

HOM predictions due to slight changes in ζ. Despite this figures 2.11(b)-(e) do serve to illustrate how the physical transition from bead break to flooding is predicted according to the LOM and HOM, which represent successive refinements to an asymptotic theory, and highlight the possibility of multiple stable states during this transition. It should be noted that the next refinement to the model (i.e. the $O(Ca)$ correction to the boundary conditions) would require a numerical solution to the flow field and is beyond the scope of this thesis.

Figures 2.12(a)-(c) are meniscus location plots for $\zeta = 1$, each at a different value of λ. Figure 2.12(a) is similar to figures 2.11(e) and (f), there are two branches for x_u, with the lower one exhibiting upstream flooding behaviour. When λ is decreased the two branches join as in figure 2.12(b). Here as S is increased from zero the bead gradually contracts until point A is reached, beyond which there are three local choices for x_u, the upper and lower choices initially being two dimensionally stable and eventually leading to bead break and flooding, respectively. As λ is decreased further there are again two branches, see figure 2.12(c). In this case increasing S from zero leads to the upstream interface moving downstream, passing through the nip and reaching the critical point B where the bead becomes two dimensionally neutrally stable and could either collapse or jump to the point C whereby further increases in S would lead to flooding.

2.2.3 The limit $\zeta \rightarrow 0$

Figure 2.13 shows a typical plot for a small value of ζ. All the menisci location plots generated at low values of ζ have this form and the differences in the predicted value of S_c between the HOM and the LOM are in the region of 35%. The interest here lies in the comparisons with both the modelling and experiments for the SFF system.

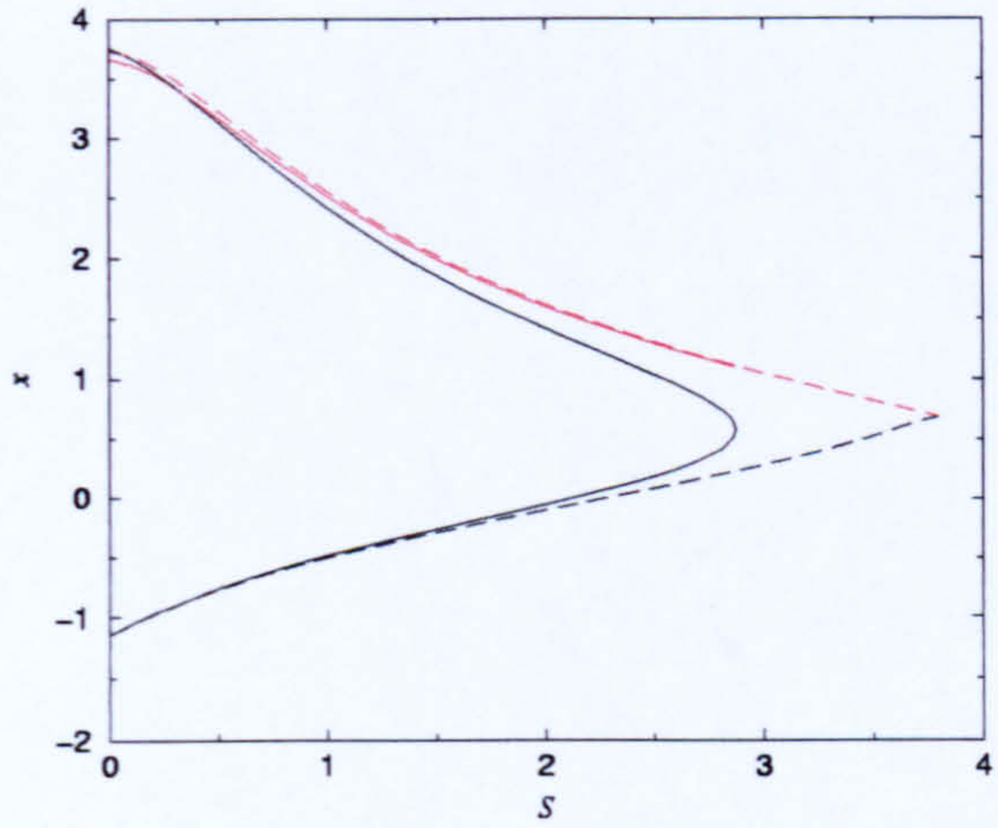

Figure 2.13: Menisci locations against S. —- HOM; - - - LOM. Red curves represent downstream meniscus locations, black curves represent upstream meniscus locations. $Ca = 10^{-3}$, $\delta = 5 \times 10^{-3}$, $\lambda = 0.1$, $\zeta = 0.01$

The downstream meniscus location, x_d, is determined from balancing incoming and outgoing fluxes so that when $\zeta \ll 1$ the returning film plays a negligible role and the result would be very close to that of the SFF model. The upstream location, x_u, is determined by balancing capillary and hydrodynamic pressures yet in the SFF model the capillary pressure is a function of the imposed contact angle, therefore it is possible to vary this contact angle until the HOM and the SFF model give the same pressure drop across the upstream interface and hence the same value of x_u. Table 2.2 shows this 'effective contact angle' for various small values of ζ.

When $\zeta = 0.025$ the effective contact angle is small, as would be expected with the presence of a returning film. However, as ζ is decreased the effective contact angle grows siginificantly and when $\zeta = 10^{-4}$ it is 57.37^o. During the experiments of Kapur (1998) the upper roll was scraped in an attempt to replicate a dry incoming surface, however the scraping leaves behind a thin residual film whose thickness is less than 1% of the outgoing film. In these experiments 'apparent contact angles' in the region of 50^o were found, in agreement with the effective contact angles desrcibed above. Thus the HOM, with small ζ, produces results in accord with the SFF model with realistic imposed contact angles and could therefore form the basis of a precursor film model for such systems, removing the inherent difficulties associated with modelling the contact

ζ	Effective contact angle
0.025	2.98^o
0.01	12.22^o
0.001	30.57^o
0.0001	57.37^o

Table 2.2: Comparison with contact angle results

line.

The reason that the HOM, a model for the DFF bead is capable of producing pressure drops at the upstream meniscus similar to the SFF model is due to the form of the constant E_{2_2} in (2.87). E_{2_2} becomes large and negative as $\zeta \rightarrow 0$ so the 'small' correction terms to ΔP_u become more significant in this limit and eventually the ordering of the series breaks down and results are no longer obtainable.

2.3 Summary

In this chapter the steady state solutions of DFF bead formed between an intermediate pair of contra-rotating rolls in a multiple roll coater have been investigated.

Lubrication theory was used to model the fluid flow and the flow domain was initially terminated with simple boundary conditions. The menisci positions were solved for as the roll speed ratio was varied. It was found that there was a critical value of S, S_c, beyond which no 2-D steady solutions exist. However, the form of the solution curves in the vicinity of S_c did not agree with results presented by other workers for similar flows. Furthermore, a simple stability hypothesis appeared to indicate that beads of infinitesimal size are stable. The form of the solution curves in the vicinity of S_c also suggest that lubrication theory is not valid here.

The above points led to a re-examination of the boundary conditions. A matched asymptotic analysis confirmed corrections to the boundary conditions suggested by Reinelt (1995). The inclusion of these small correction terms dramatically altered the form of the solution curves in the vicinity of S_c. Infinitesimal beads were no longer predicted to be stable and the value of S_c was changed by up to 35%.

The stability hypothesis predicts that the turning points of the solution curves

represent states with a 2-D neutrally stable upstream meniscus and it was postulated that this state represents the occurence of bead break. As bead break would lead to failure of the coating process, it is clear that the inclusion of the small correction terms is vital to accurately predict the range of operation of a multiple roll system.

As $\zeta \rightarrow 1$ it is possible for the upstream interface position to move rapidly outwards as S is increased and this is associated with flooding. The precise values of ζ and λ dictate whether the bead will collapse or flood as S is increased, and under certain conditions a pair of solution branches exist, one exhibiting bead break behaviour and the other flooding behaviour. Three-dimensional instabilities cannot be ruled out in this region of parameter space, however the predictions of flooding agree qualitatively with experimental results.

In the limit $\zeta \rightarrow 0$, the small terms play an important role in modelling the pressure jump at the upstream interface. The calculated effective contact angles are in agreement with observed apparent contact angles.

Chapter 3

Double film fed roll coater - stability analysis

3.1 Introduction

Chapter 2 was a steady state analysis of the returning film problem. It was found that a detailed analysis of the boundary conditions was vital as the inclusion of small terms could have significant effects. A simple stability hypothesis indicated that the flow became unstable at the turning points of the steady state solution curves. It is an aim of this chapter to test this hypothesis via a rigorous 3-D linear stability analysis. It was also shown in the previous chapter that in some regions of parameter space the S.H. predicts that multiple stable steady states exist and in this chapter an attempt is made to determine which of these states are seen in practice.

As has been previously mentioned, the returning film problem is similar to the journal bearing problem considered by Reinelt (1995). Reinelt carried out a 3-D linear stability analysis and did indeed find that the turning points of the solution curves marked the onset of instability. However, the double film fed roll coater is a different physical set up to the journal bearing; firstly the returning film can be set as a fraction of the outgoing film and secondly the journal bearing problem has two returning films and the volume of fluid is fixed whereas the DFF bead in the multiple roll coater has one returning film and the other incoming film is of fixed height. There are two further points that distinguish this work from that of Reinelt. Firstly, when considering the journal bearing problem, Reinelt did not find any solution curves for which there

was potentially more than one stable state as was the case in chapter 2. Secondly, Reinelt did not formally calculate the correction to the pressure drop and outgoing film thicknesses. The latter of these two points is investigated using the formal framework set up in the previous chapter where it was used to confirm the boundary conditions developed by Reinelt in the steady case. However, in this chapter the formalism comes into its own as it reveals the true relationship between the pressure jump and the wavenumber of the perturbation.

3.2 Mathematical model

The stability of the system is studied by applying a small disturbance to the menisci locations and analysing the response. Any disturbance can be split into its Fourier components and so it is sufficient to consider the effect of a disturbance of the form

$$X_D = X_D^0 + \xi X_D' \sin KZ e^{\Sigma T}, \tag{3.1}$$

$$X_U = X_U^0 + \xi X_U' \epsilon \sin KZ e^{\Sigma T}, \tag{3.2}$$

where $|\xi X_D'/X_D^0| \ll 1$ and $|\xi X_U' \epsilon/X_U^0| \ll 1$, X_D^0 and X_U^0 are the steady state menisci locations found in chapter 2, T is time and Σ and K are the growth rate and wavenumber of the perturbation, respectively. ϵ is a measure of the relative size of the disturbances of the two menisci and is an unknown to be determined. The choice of X_D' and X_U' are arbitrary and are taken to be B_D and B_U respectively to simplify the algebra of section 3.2.2.1.

Under certain conditions $\Re(\Sigma) < 0 \; \forall \; K$ and the system is said to be linearly stable as any disturbance will decay exponentially in time. For other operating conditions $\Re(\Sigma) > 0$ over a range of K and any perturbation with a Fourier component that falls within this range will grow exponentially and hence the system is linearly unstable. Between these two sets of conditions lies the unique state where $\Re(\Sigma) < 0 \; \forall \; K$ except for one value, K^* say, where $\Re(\Sigma)|_{K=K^*} = 0$ and $\frac{\partial \Re(\Sigma)}{\partial K}|_{K=K^*} = 0$. Under these conditions the system is said to be neutrally stable. The model described below aims to find Σ for any set of operating conditions and hence predict the stability of the system under those conditions. For an unstable set of operating conditions it is possible to find on which interface the disturbance manifests itself by analysing the size of the respective disturbances; if $|X_D'| \gg |X_U' \epsilon|$ then the downstream interface is said to be unstable

with the upstream meniscus remaining stable, $|X'_D| \ll |X'_U\epsilon|$ implies the reverse and $|X'_D| \sim |X'_U\epsilon|$ indicates that both menisci are unstable.

The model will be based on the framework established in chapter 2 and as such the flow domain can be split into a nip, capillary statics and transition region.

3.2.1 The Nip Region

The scales for the nip region are given by (2.13) along with

$$W \sim \xi U_1, \qquad Z \sim K^{-1} \sim \sqrt{2B_0R}, \qquad T \sim \Sigma^{-1} \sim \frac{\sqrt{2B_0R}}{U_1}, \tag{3.3}$$

where W is the velocity in the lateral (Z) direction and ξ is the amplitude of the disturbance. The scaling in the lateral direction is deemed to be a typical wavelength of the disturbance. The nondimensional perturbations to the menisci are

$$x_d = x_d^0 + \xi x'_d \sin kze^{\sigma t}, \tag{3.4}$$

$$x_u = x_u^0 + \xi x'_u \epsilon \sin kze^{\sigma t}. \tag{3.5}$$

It is assumed that the response to the perturbation is sinusoidal with the same wavelength and growth rate as the perturbation. The perturbed pressure and velocity fields are given as

$$p = p^0 + \xi p' \sin kze^{\sigma t} = p^0 + \xi(g_d + \epsilon g_u)\sin kze^{\sigma t}, \tag{3.6}$$

$$\mathbf{u} = \mathbf{u^0} + \mathbf{u}' \sin kze^{\sigma t}, \tag{3.7}$$

where U^0 and P^0 are the steady state results of chapter 2. The pressure perturbation has been written as a linear combination of the two functions g_u and g_d to make the dependency upon ϵ explicit. Applying the above scales to the Navier-Stokes equations leads to the following lubrication equations at $O(\xi)$:

$$\frac{\partial p'}{\partial x} = \frac{\partial^2 u'}{\partial y^2}, \tag{3.8}$$

$$\frac{\partial p'}{\partial y} = 0, \tag{3.9}$$

$$\frac{\partial p'}{\partial z} = \frac{\partial^2 w'}{\partial y^2}. \tag{3.10}$$

The associated no slip boundary conditions are

$$u' = w' = 0 \qquad \text{on} \qquad y = \pm b(x). \tag{3.11}$$

u' can be found by integrating (3.8) and applying (3.11):

$$u' = \frac{p'_x}{2}\left(y^2 - b^2\right), \tag{3.12}$$

and similarly:

$$w' = \frac{p'_z}{2}\left(y^2 - b^2\right). \tag{3.13}$$

The fluxes in the x and z directions at $O(\xi)$ are

$$q^x = \int_{-b}^{b} u' \mathrm{d}y \qquad \text{and} \qquad q^z = \int_{-b}^{b} w' \mathrm{d}y, \tag{3.14}$$

respectively. The $O(\xi)$ flux balance is simply

$$\frac{\partial}{\partial x} q^x + \frac{\partial}{\partial z} q^z = 0, \tag{3.15}$$

which results in the 2D Reynolds equation:

$$\frac{\mathrm{d}^2 p'}{\mathrm{d}x^2} + \frac{3}{b}\frac{\mathrm{d}b}{\mathrm{d}x}\frac{\mathrm{d}p'}{\mathrm{d}x} - k^2 p' = 0. \tag{3.16}$$

This is the governing differential equation of the perturbed system.

3.2.2 Boundary Conditions

In order to solve this 2^{nd} order differential equation and find both the growth rate σ and the ratio of the perturbation magnitudes ϵ, four boundary conditions are needed consisting of a pressure jump and a kinematic condition at each meniscus.

The pressure jump condition at the downstream meniscus can be found by replacing x_d with $x_d + \xi \sin kz$ in (2.86), expanding for small ξ and then neglecting terms of $O(\xi^2)$. This results in

$$\begin{aligned} p'(x_d^0) = g'_d(x_d^0) \quad &= \quad -b_d \delta p_x^0(x_d) - \frac{\delta}{Cab_d}\Big[- 2x_d\delta\xi\Big(1 - 2x_d\delta \\ &\qquad +1.94(1+S^{2/3})Ca^{2/3}\Big) - 2\delta^2\xi b_d + \Delta P_d^{lat}\Big], \qquad (3.17) \\ g'_u(x_d^0) \quad &= \quad 0. \qquad (3.18) \end{aligned}$$

The ΔP_d^{lat} term is the leading order contribution from the additional curvature due to the 3-D nature of the perturbation and its precise form is discussed later.

The pressure contribution at the upstream interface is found in a similar way and can be written in a concise form by making use of the function f defined in chapter 2

(2.33):

$$p'(x_u^0) = \epsilon g_u(x_u^0) = \epsilon \left[-b_u \delta \left. \frac{\mathrm{d}f}{\mathrm{d}x} \right|_{x_u^0} - \frac{\delta}{Ca} \frac{1}{b_u} \Delta P_u^{lat} \right], \tag{3.19}$$

$$g_d(x_u^0) = 0. \tag{3.20}$$

The correct form of ΔP_d^{lat} and ΔP_u^{lat} is now discussed.

In the past workers (e.g. Daniels (1998)) have used

$$\frac{\Delta P_d^{lat}}{\delta^2 b_d^2} = -\frac{\Delta P_u^{lat}}{\delta^2 b_u^2} = -k^2. \tag{3.21}$$

i.e. it has been assumed that the additional pressure term is inversely proportional to the lateral curvature. The form of the denominators in (3.21) comes from the choice of scales and the choice of X'_U and X'_D. The lateral curvature is taken to mean the curvature of the curve formed by the intersection of the meniscus and the plane $y = 0$ and for a long wave disturbance at leading order this curvature is $-k^2$. Intuitively this seems plausible but there is an assumption that the addition of the 3-D disturbance does not alter the form of the cross sectional profile of the free surface. Here 'cross sectional profile' is used to indicate the curve defined by the intersection of the meniscus and the plane $z = 0$, i.e. in the 2-D case the h^{ij}'s of chapter 2. Park and Homsy (1984) showed that in the long wave limit ($k \to 0$) this assumption was incorrect and the additional term is

$$\frac{\Delta P_d^{lat}}{\delta^2 b_d^2} = -\frac{\Delta P_u^{lat}}{\delta^2 b_u^2} = -\frac{\pi}{4} k^2. \tag{3.22}$$

The factor of $\pi/4$ arises because the presence of the lateral perturbation actually leads to a change in the form of the cross sectional profile. Put another way, there is a contribution to the cross sectional curvature as well as to the lateral curvature and the sum of the two results in (3.22).

However, the analysis of Park and Homsy, whilst true for *any amplitude* of wave, was limited to the *long wave* ($k \to 0$) case. Although this assumption has been made here by the choice of scale for Z (3.3), in a linear stability analysis it is the amplitude that is small, in fact infinitesimally so, and not necessarily the wavenumber (inversely proportional to the wavelength). In fact it is anticipated that the pressure jump will be a function of k and using an asymptotic analysis, based on the framework set up in chapter 2, it is possible to find the pressure drop when a sinusoidal disturbance, of *any*

wavelength but *small amplitude*, is applied to the meniscus position and to investigate the link between (3.21) and (3.22).

3.2.2.1 Formal development of pressure jump due to lateral curvature

The framework of chapter 2 is extended to include terms of $O(\xi)$ in the expansion. As this section is solely concerned with finding the pressure jump due to the additional lateral curvature which will enter the problem at $O(\xi)$ it is therefore unnessecary to solve the TR problem as this enters at $O(Ca^{2/3})$ and so no asymmetries due to $S \neq 1$ will be present. As no asymmetries are present at $O(\xi)$, it is only necessary to find the solution to one branch of $\hat{h}$ and here the lower branch, corresponding to $i = 1$ in the analysis of chapter 2, is chosen. For the rest of this section all subscripts referring to the two branches are dropped. The $O(\xi)$ pressure jump is found at the downstream meniscus and the result extends in a straightforward manner to the upstream meniscus.

The scales in the CSR are as before and in addition the lateral length and velocity scales are

$$Z \sim B_D, \qquad W \sim \xi U_1,$$

where, as before, a 'hat' denotes a variable in the CSR. The scale for Z has been chosen to be the same as that for X and Y in the CSR and this allows the relationship between the pressure drop and the wavenumber to be examined without presupposing a long wavelength disturbance. Using the above scales leads to the following normal stress balance:

$$\Delta\hat{P} + O(Ca) = \frac{-1}{(1+\hat{h}_{\hat{x}}^2+\hat{h}_{\hat{z}}^2)^{3/2}}\left(\hat{h}_{\hat{x}\hat{x}}\left(1+\hat{h}_{\hat{z}}^2\right)+\hat{h}_{\hat{z}\hat{z}}\left(1+\hat{h}_{\hat{x}}^2\right)-2\hat{h}_{\hat{x}}\hat{h}_{\hat{z}}\hat{h}_{\hat{x}\hat{z}}\right). \quad (3.23)$$

A solution of the form

$$\hat{h} = \hat{h}^{000}(\hat{x}-\xi\sin\hat{k}\hat{z}e^{\sigma t})+\xi\sin\hat{k}\hat{z}e^{\sigma t}\hat{h}^{001}(\hat{x}-\xi\sin\hat{k}\hat{z}e^{\sigma t})+O(\xi^2,\delta,Ca^{2/3}), \quad (3.24)$$

will be sought and to simplify the algebra the variable $\hat{m}$ is introduced:

$$\hat{m} = \hat{x}-\xi\sin\hat{k}\hat{z}e^{\sigma t}. \quad (3.25)$$

The wavenumber in this section has been scaled by B_D^{-1} and this gives $\hat{k} = \delta b_d k$. The boundary conditions are analogous to (2.38) and (2.39):

$$\hat{h}(\hat{m}=0) = 0, \quad (3.26)$$

$$\hat{h}_{\hat{x}}(\hat{m}=0) = -\infty, \quad (3.27)$$

A solution of the form (3.24) has been chosen as it allows the straightforward application of these boundary conditions and in particular (3.27) which dictates that the solution has an infinite gradient at $\hat{x} = \xi \sin \hat{k}\hat{z}e^{\sigma t}$.

If the origin of the transition region, $\hat{l}$, is defined as being when $\hat{m} = \hat{l}$, it is clear that the results of chapter 2 still hold if $\hat{x}$ is everywhere replaced by $\hat{m}$, i.e. the leading order result becomes

$$\hat{h}^{000} = -(1-(1-\hat{m})^2)^{1/2}, \tag{3.28}$$

$$= -(1-(1-(\hat{x}-\xi \sin \hat{k}\hat{z}e^{\sigma t}))^2)^{1/2}. \tag{3.29}$$

At first it appears that this leads to a problem in the ordering of the series as $\hat{h}^{000}$ contains an $O(\xi)$ contribution. The obvious alternative would be to expand (3.24) as a Taylor series in $\xi \sin \hat{k}\hat{z}$ giving, for example, the $O(\xi)$ term as

$$-\sin \hat{k}\hat{z}e^{\sigma t}\hat{h}^{000}_{\hat{x}}(\hat{x}) + \sin \hat{k}\hat{z}e^{\sigma t}\hat{h}^{001}(\hat{x}).$$

This approach was indeed attempted but was found to suffer from severe drawbacks associated with the behaviour at the tip of the meniscus. At this point the gradient of $\hat{h}$ is infinite and so the Taylor expansion breaks down. However, it is still possible to construct a framework in which $\hat{h}$ as defined in (3.24) remains finite by insisting on terms of the same order cancelling. For instance, continuing the above example, this would require

$$\hat{h}^{001} \to \hat{h}^{000}_{\hat{x}}(\hat{x}) \quad \text{as} \quad \hat{x} \to 0 \quad \Rightarrow \quad \hat{h}^{001} \to -\frac{1}{\hat{x}^{1/2}} \quad \text{as} \quad \hat{x} \to 0.$$

This highlights the fundamental difference between the two approaches for it shows that in this case $\hat{h}^{001}$ is required to become infinite at the origin whereas if the Taylor expansion had not been performed, it would remain finite and equal to 0. It is this behaviour at the origin that creates problems when the Taylor expansion is performed as $\hat{h}^{001}$ appears in the equations that determine higher order terms such as $\hat{h}^{011}$. It was found that if this approach was followed, these differential equations would have solutions which could not satisfy the boundary conditions at the meniscus tip. The idea of expanding $\hat{h}(\hat{x} - \xi \sin \hat{k}\hat{z})$ was thus abandoned and the approach detailed above, giving solutions in terms of $\hat{m}$, was adopted.

The $O(\xi)$ normal stress balance in the CSR is:

$$\frac{\hat{h}^{001}_{\hat{m}\hat{m}}}{1+\hat{h}^{000^2}_{\hat{m}}} - \frac{3\hat{h}^{000}_{\hat{m}\hat{m}}\hat{h}^{000}_{\hat{m}}}{(1+\hat{h}^{000^2}_{\hat{m}})^2}\hat{h}^{001}_{\hat{m}} - \hat{k}^2\hat{h}^{001} = \Delta\hat{P}^{001}(1+\hat{h}^{000^2}_{\hat{m}})^{1/2} - \hat{k}^2\hat{h}^{000}_{\hat{m}}. \tag{3.30}$$

Substituting for $\hat{h}^{000}$ leads to

$$(2\hat{m}-\hat{m}^2)\hat{h}^{001}_{\hat{m}\hat{m}}+3(1-\hat{m})\hat{h}^{001}_{\hat{m}}-\hat{k}^2\hat{h}^{001}=\frac{\Delta P^{001}}{(2\hat{m}-\hat{m}^2)^{1/2}}-\frac{(\hat{m}-1)\hat{k}^2}{(2\hat{m}-\hat{m}^2)^{1/2}}. \quad (3.31)$$

A solution is found by constructing a complementary function, followed by a particular integral. The complementary function is found by solving the equivalent homogeneous problem which, after making the simple transformation $\hat{m}=2\hat{m}'$, is

$$\hat{m}'(1-\hat{m}')\hat{h}^{001}_{\hat{m}'\hat{m}'}+\frac{3}{2}(1-2\hat{m}')\hat{h}^{001}_{\hat{m}'}-k^2\hat{h}^{001}=0. \quad (3.32)$$

This is a particular case of the well known hypergeometric equation:

$$\hat{m}'(1-\hat{m}')F_{\hat{m}'\hat{m}'}+\left[c-(a+b+1)\,\hat{m}'\right]F_{\hat{m}'}-abF=0 \quad (3.33)$$

with $a=1-\sqrt{1-\hat{k}^2}$, $b=1+\sqrt{1-\hat{k}^2}$ and $c=3/2$ and F being the hypergeometric function. In the region $|m'|<1$, the solution to the hypergeometric equation can be expressed as the following power series:

$$F(a,b,c;\hat{m}')=\sum_{n=0}^{\infty}c_n\hat{m}'^n, \quad (3.34)$$

where

$$c_n=\frac{\Gamma(c)}{\Gamma(a)\Gamma(b)}\frac{\Gamma(a+n)\Gamma(b+n)}{\Gamma(c+n)\Gamma(n+1)}. \quad (3.35)$$

and Γ is the gamma function. Furthermore, if $F(a,b,c;\hat{m}')$ is a solution of the hypergeometric equation, it can be shown that a second independent solution (Dennery and Krzywicki (1967)) is

$$\hat{m}'^{1-c}F(b-c+1,a-c+1,2-c;\hat{m}'). \quad (3.36)$$

The particular integral is

$$\frac{\hat{m}-1}{(2\hat{m}-\hat{m}^2)^{1/2}}+\frac{\Delta P^{001}}{(1-\hat{k}^2)(2\hat{m}-\hat{m}^2)^{1/2}}, \quad (3.37)$$

and so the general solution is

$$\begin{aligned}\hat{h}^{001}=\alpha F(a,b,c;\hat{m}/2)+\beta\hat{m}^{1-c}F(b-c+1,a-c+1,2-c;\hat{m}/2)\\ +\frac{\Delta P^{001}}{(1-\hat{k}^2)(2\hat{m}-\hat{m}^2)^{1/2}}+\frac{\hat{m}-1}{(2\hat{m}-\hat{m}^2)^{1/2}},\end{aligned} \quad (3.38)$$

where a, b and c are as given above and α and β are constants to be determined. The matching condition is simply

$$\hat{h}^{001}(\hat{m}=\hat{l}^{000}=1)=0. \quad (3.39)$$

Applying this, (3.26) and (3.27) gives

$$\alpha = 0, \tag{3.40}$$

$$\beta = \frac{1}{\sqrt{2} - F(b-c+1, a-c+1, 2-c, 1/2)}, \tag{3.41}$$

$$\begin{aligned} \Delta P^{001} &= \frac{(\hat{k}^2-1)F(b-c+1, a-c+1, 2-c, 1/2)}{\sqrt{2} - F(b-c+1, a-c+1, 2-c, 1/2)} \\ &= \frac{(\hat{k}^2-1)\cos\left(\frac{\pi}{2}\sqrt{1-\hat{k}^2}\right)}{1-\cos\left(\frac{\pi}{2}\sqrt{1-\hat{k}^2}\right)}. \end{aligned} \tag{3.42}$$

Therefore the dependency upon k of the pressure drop due to the 3-D nature of the disturbance has been found with $\Delta P_d^{lat} = -\Delta P_u^{lat} = \Delta P^{001}$. A plot of $-\Delta P^{001}/\hat{k}^2$ is shown in figure 3.1 and the long and short wave limits can be shown analytically to be

$$\Delta P^{001} \rightarrow -\frac{\pi}{4}\hat{k}^2 \quad \text{as} \quad \hat{k} \rightarrow 0, \tag{3.43}$$

$$\Delta P^{001} \rightarrow -\hat{k}^2 \quad \text{as} \quad \hat{k} \rightarrow \infty. \tag{3.44}$$

Therefore, the long wave length limit agrees with (3.22) and the short wave limit agress with (3.21). Thus, for the first time, the relationship between the wavenumber and the lateral curvature has been found. It is clear that either (3.21) or (3.22) could provide legitimate boundary conditions with the correct choice depending upon the regime of interest. Experimental evidence points towards bead break being a 2-D disturbance (Kapur (1999)) and the wavelength of the ribbing instability being much greater than the gap width (Hasegawat and Sorimachi (1993)) and so each would fall under the long wave category and (3.22) would be the correct choice. In fact the long wave nature of the perturbation has already been assumed twice in this chapter; once in the formulation of the 2-D Reynolds equation and once in the perturbed pressure boundary conditions. The terms in the perturbed pressure boundary condition formed by replacing x_d^0 with $x_d^0 + \xi x_d' \sin \hat{k}\hat{z}e^{\sigma t}$ actually represent the long wave length limit of the true form of these terms. The k dependency of these terms could be formed by solving for higher order terms such as $\hat{h}^{011}$ but this was beyond the scope of this thesis.

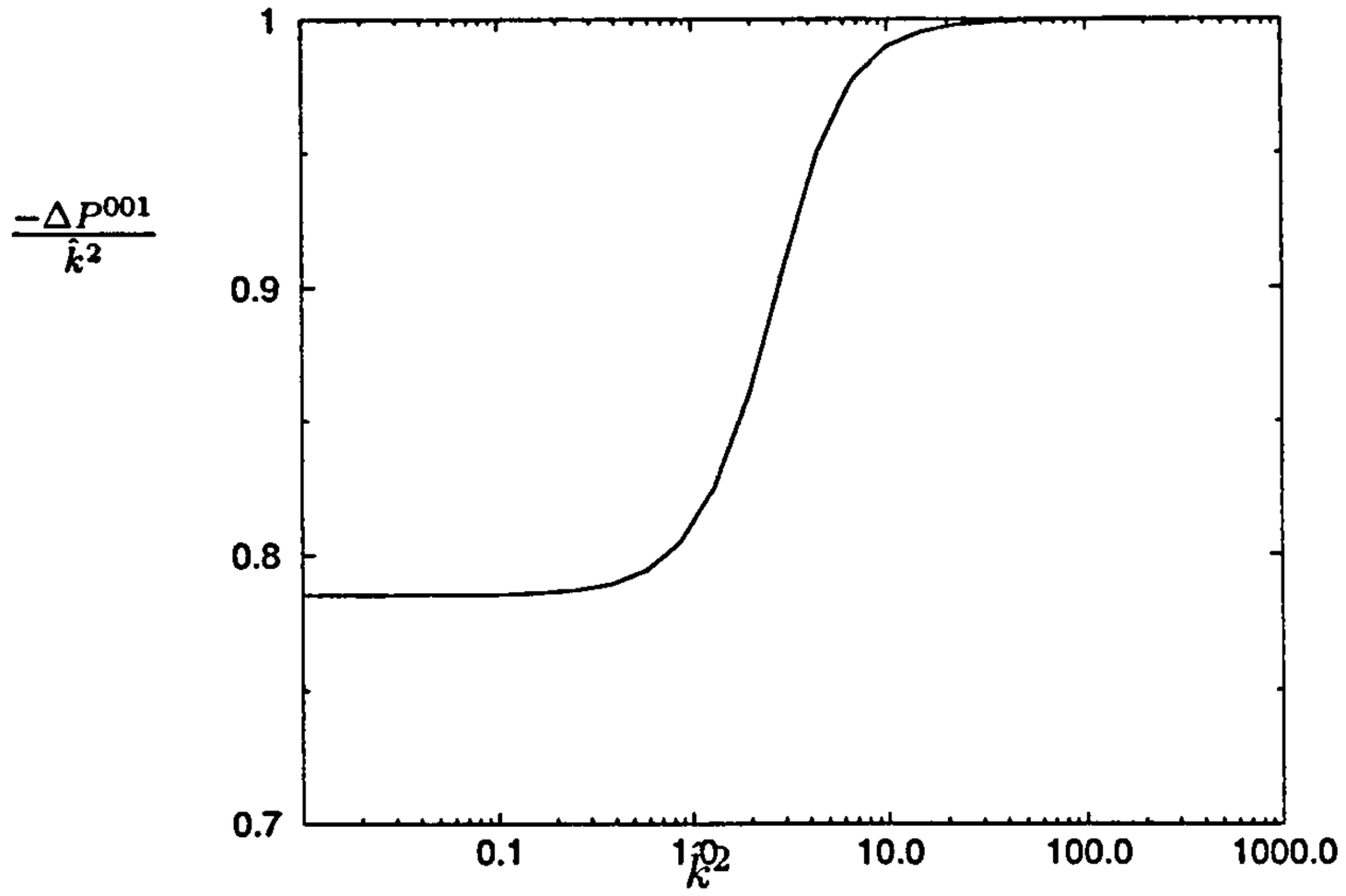

Figure 3.1: A plot of $-\Delta P^{001}/\hat{k}^2$ against $\hat{k}^2$.

3.2.2.2 Kinematic boundary conditions

At each meniscus a flux balance can be written that takes account of the time dependence of the free surface. The starting point is the free surface kinematic condition

$$\frac{\partial H}{\partial T} + (\mathbf{U}.\nabla)(H - Y) = 0 \quad \text{on} \quad Y = H. \tag{3.45}$$

$Y = 0$ represents the roll surface and H the height of the free surface from the roll as shown in figure 3.2. Although this brief analysis is concerned with the outgoing film on the lower roll the results are extended later. (3.45) can be nondimensionalised using the nip region scales and neglecting terms of $O(\xi^2)$ this becomes

$$\frac{\partial h}{\partial t} + u\frac{\partial h}{\partial x} - v = 0 \quad \text{on} \quad y = h. \tag{3.46}$$

Neglecting terms of $O(\delta\xi)$ the continuity equation is

$$\frac{\partial u}{\partial x} + \frac{\partial v}{\partial y} = 0, \tag{3.47}$$

and this enables u to be written in terms of v and therefore (3.46) to be rewritten as

$$\frac{\partial h}{\partial t} + \frac{\partial q}{\partial x} = 0, \tag{3.48}$$

where q is the nondimensional flux and equal to

$$q = \int_0^h u\mathrm{d}y. \tag{3.49}$$

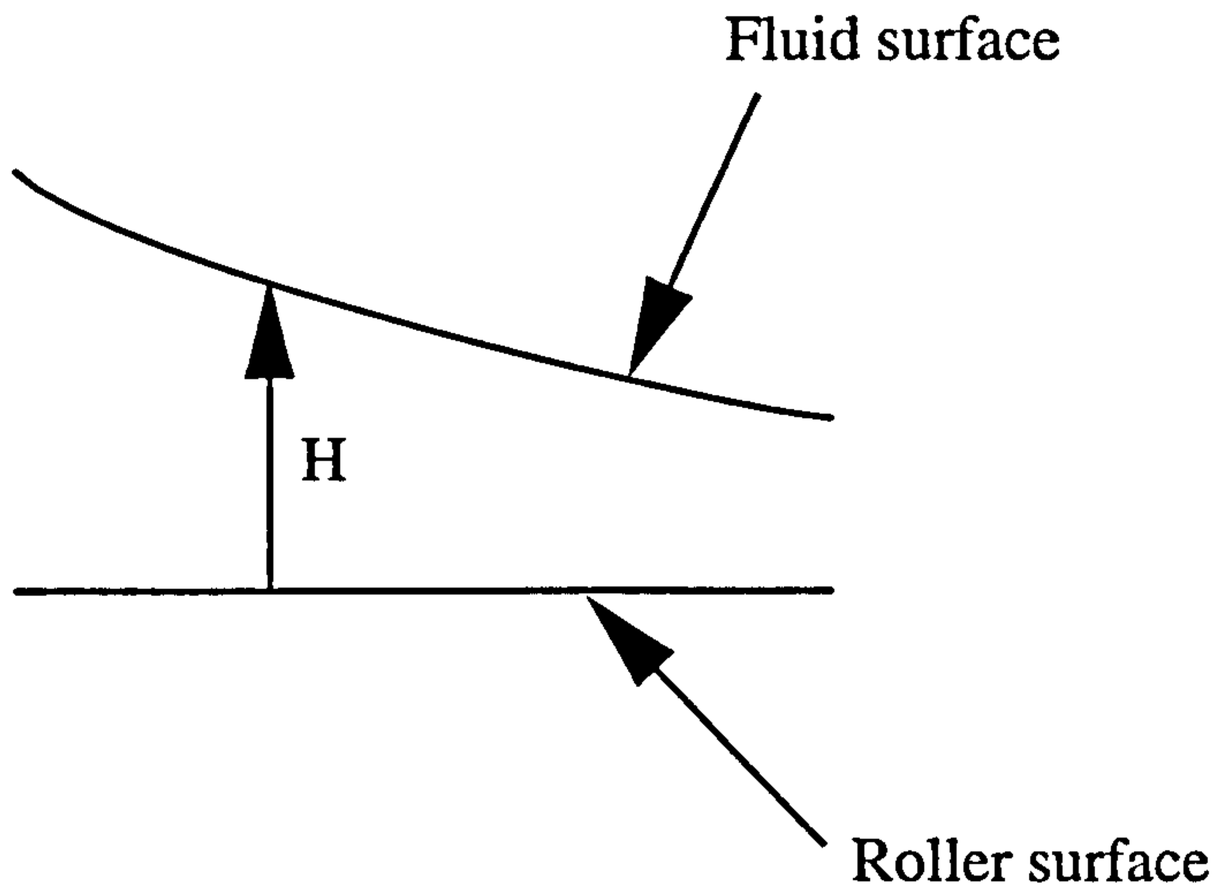

Figure 3.2: The definition of H.

In the long wavelength limit $\Delta P^{001} \sim O(\delta^2)$ and so the $O(\xi)$ contribution to h becomes negligible. Thus (3.24) implies that neglecting terms of $O(\delta^2\xi)$ and $O(\xi^2)$ leads to

$$h = h(x - \xi \sin kze^{\sigma t}), \tag{3.50}$$

and so

$$\frac{\partial h}{\partial t} = -\sigma\xi \sin kze^{\sigma t}\frac{\partial h}{\partial x}. \tag{3.51}$$

Thus the $O(\xi)$ contribution to (3.48) can be written as

$$\sigma\frac{\partial h}{\partial x} = \frac{\partial q'}{\partial x}, \tag{3.52}$$

where q' is the $O(\xi)$ contribution to the flux. (3.52) can be integrated to give

$$\begin{aligned}
\sigma(b_d - h^{\infty^0}) &= -\sigma\int_{\xi\sin kze^{\sigma t}}^{\infty}\frac{\partial h}{\partial x}\mathrm{d}x, \\
&= -\int_{\xi\sin kze^{\sigma t}}^{\infty}\frac{\partial q'}{\partial x}\mathrm{d}x, \\
&= q'|_{\xi\sin\hat{k}\hat{z}e^{\sigma t}} - q'|_{\infty}.
\end{aligned}$$

Thus the rate of change of the meniscus position is proportional to the difference between the fluxes entering and leaving the meniscus region. The expressions for the incoming and outgoing fluxes are

$$q'|_{\xi\sin kze^{\sigma t}} = \int_{-b_d}^{0} u'|_{x_d^0}\mathrm{d}y = -\frac{1}{3}p_x'|_{x_d^0}b_d^3, \tag{3.53}$$

$$q'|_{\infty} = h_3' = 2\times 1.337 b_d\delta\left(x_d + \delta b_d(1+\frac{\pi}{4}k^2)\right)Ca^{2/3}. \tag{3.54}$$

The k^2 term in the outgoing flux expression was given by Park and Homsy (1984). A similar situation holds on the upper roll and this can be combined with the above to give the kinematic boundary condition at the downstream meniscus:

$$\sigma b_d^2 \delta (2 - 1.337(1+S^{2/3})(1+2x_d)Ca^{2/3}) = -\frac{2}{3}\, p'_x|_{x_d}\, b_d^3 - 2 \times 1.337 b_d \delta (1+S^{5/3})(x_d + b_d(1+k^2))Ca^{2/3}. \tag{3.55}$$

A similar calculation at the upstream meniscus gives

$$\sigma \epsilon b_u^2 \delta \left(2 - \frac{2\lambda}{b_u} - 1.337\zeta (SCa)^{2/3}\frac{b_d}{b_u}\right) = -\frac{2}{3}\, p'_x|_{x_u}\, b_d^3. \tag{3.56}$$

Previous workers (Reinelt (1995), Daniels (1998)) have assumed this relationship without the above justification. ϵ can be eliminated from the above two flux balances to give the following quadratic for the growth rate:

$$AB\sigma^2 + \sigma\left(BC - Bg'_{d_x}(x_d) - Ag'_{u_x}(x_u)\right) + g'_{d_x}(x_d)g'_{u_x}(x_u) - g'_{d_x}(x_u)g'_{u_x}(x_d) - Cg'_{u_x}(x_u) = 0, \tag{3.57}$$

where A, B and C are given by

$$A = -\frac{3}{2}\delta b_d^{-1}\left(2 - 1.337(1+S^{2/3})(1+2x_d)Ca^{2/3}\right), \tag{3.58}$$

$$B = -\frac{3}{2}\delta b_u^{-1}\left(2 - \frac{2\lambda}{b_u} - 1.337\zeta (SCa)^{2/3}\frac{b_d}{b_u}\right), \tag{3.59}$$

$$C = -3 \times 1.337 b_d^{-2}\delta\left(1+S^{2/3}\right)\left(x_d + \delta b_d\left(1+\frac{\pi}{4}k^2\right)\right)Ca^{2/3}. \tag{3.60}$$

3.2.2.3 Perturbed incoming film

In the above analysis the question of how to treat the returning film has been sidestepped. The coated film on the upper roll is uneven as it leaves the meniscus and the question that has yet to be answered is how should this film be modelled as it enters the upstream meniscus - should it be treated as a uniform or an uneven film?

The coated film height as it leaves the downstream meniscus is

$$H_4^{\infty} = H_4^{\infty^0} + H_4^{\infty\prime}\sin KZe^{\Sigma T}. \tag{3.61}$$

The liquid film then completes one revolution of the upper roll before re-entering the bead at the upstream meniscus and thus the perturbed contribution to the incoming film height at time T is

$$H_2^{\infty\prime}\sin KZe^{\Sigma(T-2\pi R/U_2)}. \tag{3.62}$$

Using (3.3) the exponential factor can be written as

$$e^{\sigma t}e^{-\sigma x/S\delta}. \tag{3.63}$$

Therefore if the growth rate is positive and larger than $O(S\delta)$, $e^{-\sigma/S\delta} \ll 1$ and the perturbed contribution to the incoming film is negligible. If the perturbed contribution to the incoming film is neglected completely then the error from doing so will increase as σ decreases to zero and then becomes negative. However, this chapter is concerned with the onset of instability ($\sigma = 0$) and the form of any unstable states (for which $\sigma > 0$). Thus neglecting the perturbed incoming films can be expected to give rise to a slight error in the prediction of onset of instability and a smaller error in predicting the form of the instability (e.g. the wavelength).

Even when the errors discussed above are at their maximum, as the incoming film is only of $O(\zeta Ca^{2/3})$, it is expected that they would be small and thus the neglection of the perturbed returning film is justified.

3.2.2.4 Solution method

The 2-D Reynolds equation (3.16) was solved numerically subject to (3.17) - (3.20) for both g_u and g_d. The NAG routine D02HAF which uses a shooting and matching technique was used for the numerical integration. The results of the numerical solution were fed into (3.57) which was solved for both roots of σ and ϵ was subsequently calculated.

3.3 Results

Figure 2.9 shows how the 2-D steady state menisci positions vary as S is increased for a typical set of operating parameters, $Ca = 10^{-3}, \delta = 5 \times 10^{-3}, \lambda = 0.05, \zeta = 0.5$. In particular, for the HOM that is of interest here, the solution curve for x_u has a turning point at $S = S_c$ beyond which there no 2-D steady state solutions and at which point the S.H. predicts the upstream meniscus to be neutrally stable. As such the turning point was associated with the occurence of the bead break instability. The 3-D linear stability of the system under these operating conditions is now investigated.

For the operating conditions refered to above there are two values of x_u each distinct from x_d; the stability of the upstream value (refered to as the upstream branch)

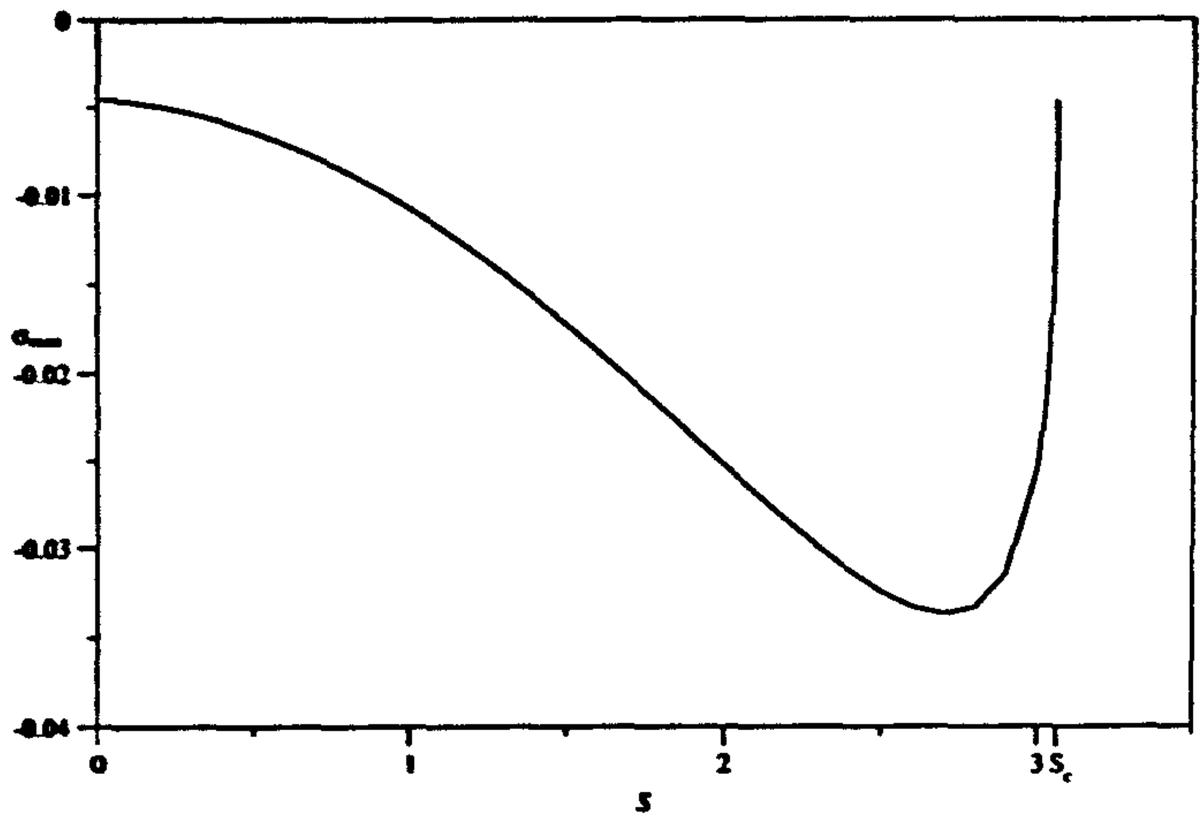

Figure 3.3: The variation in the maximum growth rate with S for the upstream branch. $Ca = 10^{-3}, \delta = 5 \times 10^{-3}, \lambda = 0.05, \zeta = 0.5$

is considered first followed by the downstream value (refered to as the downstream branch). For a given value of S the growth rate was calculated over a range of values of k and the maximum value, σ_{max} say, was recorded. The corresponding values of k and ϵ are refered to as k_{max} and ϵ_{max}, respectively. Figure 3.3 shows how σ_{max} varies with S. It is clear from the figure that $\sigma_{max} < 0 \; \forall \; S < S_c$ and furthermore that $\sigma_{max} \rightarrow 0$ as $S \rightarrow S_c$. Therefore, the upstream branch represents a stable set of solutions and the turning point is neutrally stable. The point where $\sigma_{max} = 0$ is never actually reached. The underlying reason for this is that the point S_c is never reached in the 2-D steady state solutions; it is possible to increase S by ever smaller amounts to get arbitrarily close but the limit is never reached. In the steady state results $\partial x_u / \partial S$ became infinite at S_c and figure 3.3 indicates that the same happens to the gradient of the $\sigma_{max}(S)$ curve. Therefore it has been infered that the growth rate curve will pass through $\sigma_{max} = 0$ at S_c.

Figure 3.4 plots the ratio of the amplitudes of the disturbance on each menisci against S. From the figure it is clear that as $S \rightarrow S_c$, the amplitude ratio $b_u \epsilon_{max} / b_d$ increases rapidly in magnitude, becoming much larger than unity. Thus at the turning point, where it has already been demonstrated that $\sigma_{max} = 0$, it can be said that it is the upstream meniscus that is neutrally stable. In the calculations for the upstream branch, σ_{max} corresponded to $k = 0$ at all values of S and therefore at the turning point the upstream meniscus is neutrally stable with $\sigma_{max} = 0$ and $k_{max} = 0$. Thus the

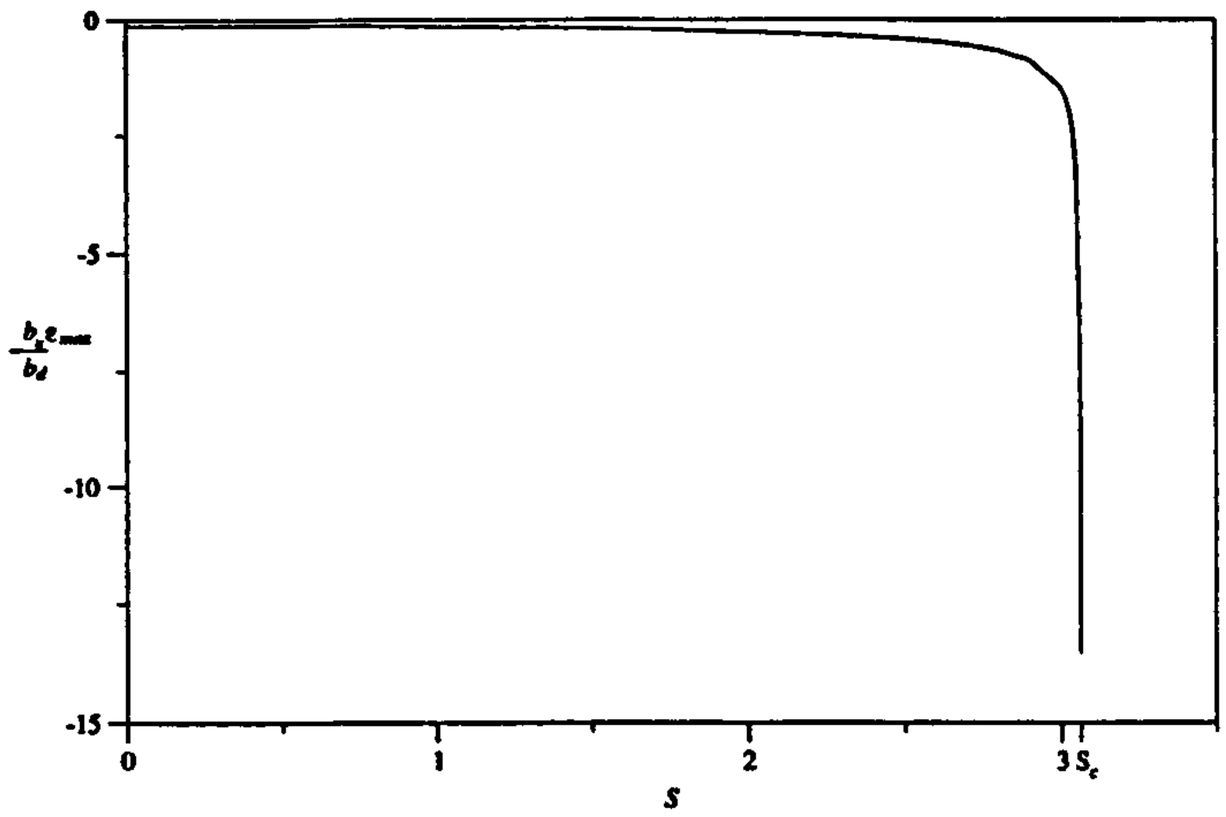

Figure 3.4: The variation in the ratio of the amplitudes of the disturbances with S for the upstream branch. $Ca = 10^{-3}, \delta = 5 \times 10^{-3}, \lambda = 0.05, \zeta = 0.5$

S.H. correctly predicted the stability of the upstream branch and the state of stability at the turning point.

The downstream branch is now considered. Figure 3.5a shows how the growth rate varies with S for the downstream branch. In this case σ_{max} is everywhere positive indicating that all solutions on this branch are linearly unstable. It can be seen that σ_{max} falls to zero as S_c is approached and this is consistent with the turning point representing a neutrally stable state. Figure 3.5b shows how the ratio of the amplitudes of the disturbances varies with S. Away from S_c the ratio is $O(1)$ and so both menisci are unstable and the disturbance grows on each interface. However, as S_c is approached, the ratio rises rapidly in favour of the upstream meniscus and so the disturbance on this interface would dominate. Figure 3.5c shows the variation of the wavenumber with S and shows that away from S_c, where both menisci are unstable, the instability is 3-D in nature as $k_{max} > 0$. As S_c is approached the wavenumber approaches zero and again this consistent with the above interpretation of the turning point being a state of neutral stability with $\sigma_{max} = 0$ and $k_{max} = 0$.

Therefore, the S.H. successfully predicted the upstream branch to be stable and the downstream branch to be unstable with the turning point representing a 2-D neutrally stable state and as before this point is associated with the phenomenon of bead break. In fact the S.H.'s accurate prediction of the state of the turning point is no coincidence. In chapter 2 it was stated that the turning point corresponded to $\mathrm{d}f/\mathrm{d}x = 0$ and (3.19)

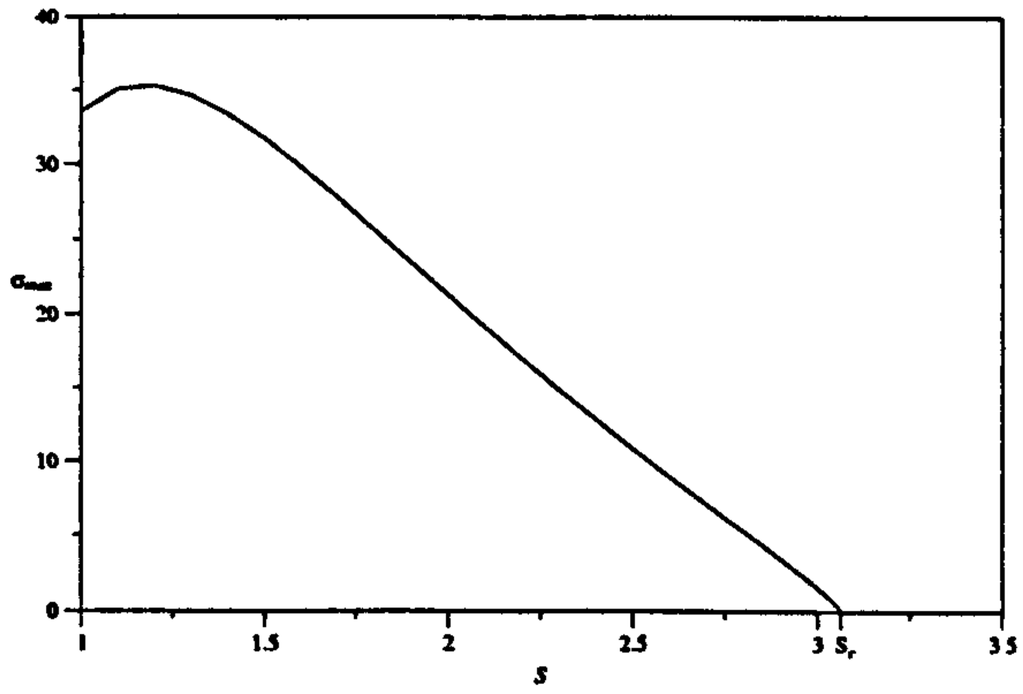

(a) The variation in the maximum growth rate with S.

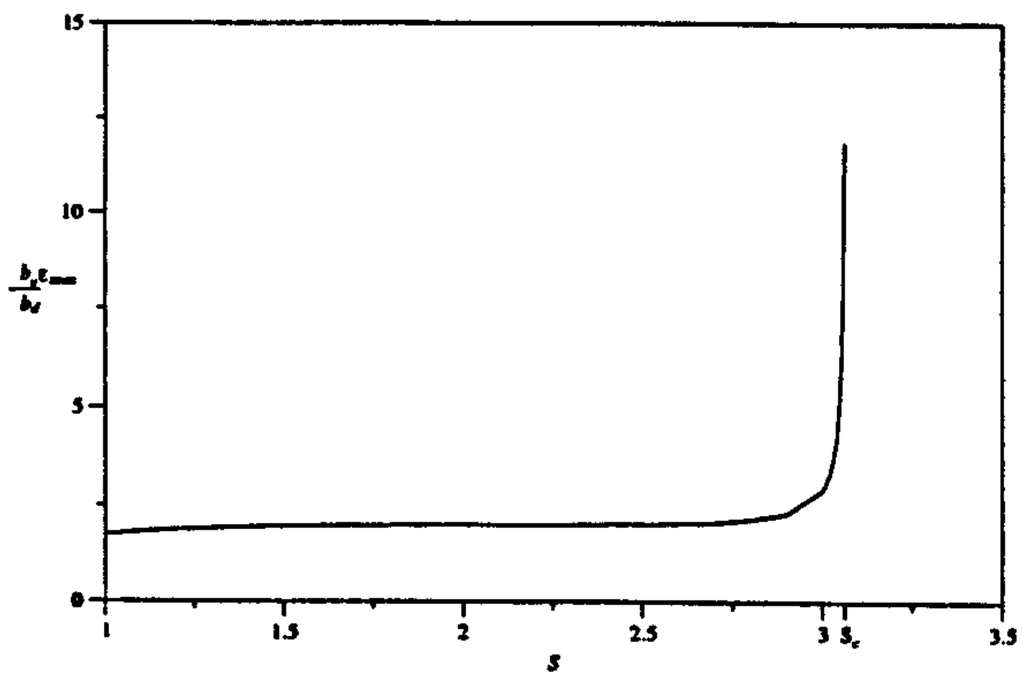

(b) The variation in the ratio of the amplitudes of the disturbances with S.

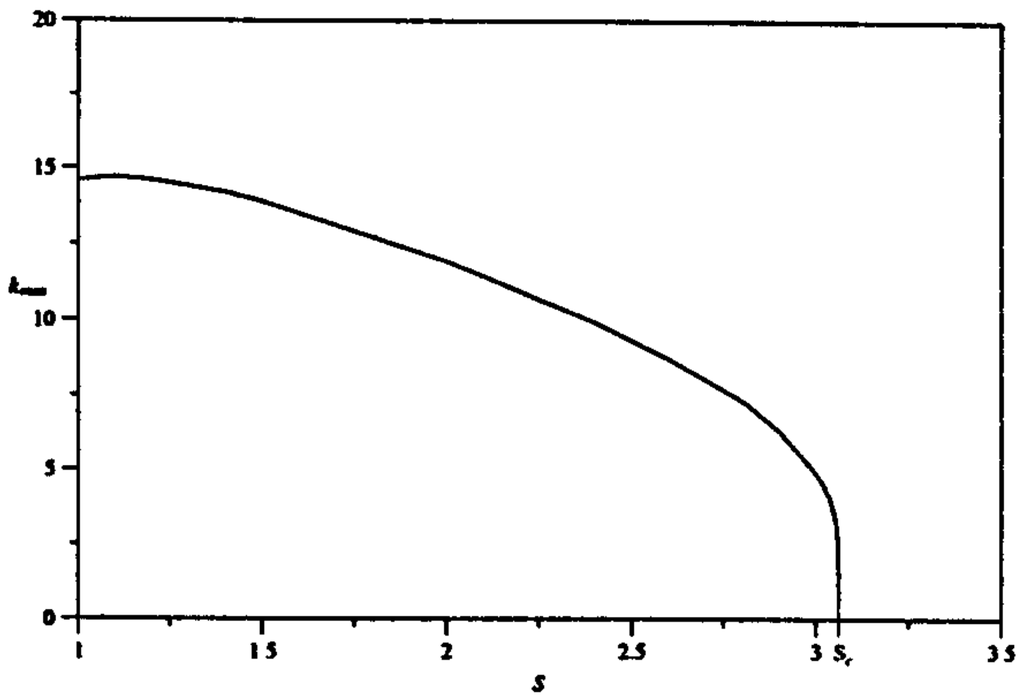

(c) The variation in the wavenumber with S.

Figure 3.5: Variation in linear stability variables with S for the downstream branch. $Ca = 10^{-3}, \delta = 5 \times 10^{-3}, \lambda = 0.05, \zeta = 0.5$

shows that if $k = 0$ (and hence $\Delta P_u^{lat} = 0$) then $g'_u(x_u) = 0$. In conjunction with (3.18) it can be shown that this implies $g'_u(x) \equiv 0$ which when substituted into the quadratic for σ (3.57) gives one of the roots to be zero. Thus at a turning point the system is always neutrally stable with respect to 2-D ($k = 0$) disturbances.

3.3.0.5 $\zeta \rightarrow 1$, λ fixed

Figure 2.11 shows a series of solution curves for slightly different values of ζ and in some cases there exist multiple states that were predicted to be stable by the S.H.. The linear stability of these solution curves is now examined.

$\zeta = 0.997$

Figure 2.11b shows how the menisci positions vary with S when $\zeta = 0.997$. The solutions curves are similar in form to the case considered in the previous section. A linear stability analysis revealed that the system behaved in exactly the same way as the above case; the upstream branch is stable, the turning point represents a state where the upstream branch is 2-D neutrally stable and the downstream branch is everywhere unstable with both menisci being unstable away from S_c.

$\zeta = 0.998$

The 2-D steady state curves for $\zeta = 0.998$ are shown in figure 2.11d and it is clear that the x_u solution curve differs from the above cases as it possesses two turning points. Furthermore, the S.H. predict that all states along the upstream branch are stable until the turning point marked '1' in figure 2.11d is reached at which point the upstream meniscus was predicted to be 2-D neutrally stable. The branch between points 2 and 3 in figure 2.11d was also predicted to be stable with the remaining parts of the solution curve unstable.

Figure 3.6 summarises the results of the linear stability analysis. The stability of the states is shown on the upstream menisucs solution curve, the downstream solution curve is plotted for reference. The analysis revealed that the upstream branch becomes unstable before point 1 is reached. The point of neutral stability occurs at $S = 31.9$, marked S_1 in figure 3.6. At S_1 the wavenumber corresponding to $\sigma = 0$ is larger than zero and the ratio of the amplitudes is much less than unity and so S_1 marks the onset of a 3-D disturbance on the downstream meniscus. Between S_1 and point 1 the maximum growth rate is everywhere positive, $k_{max} > 0$ and $b_u \epsilon_{max}/b_d \ll 1$ and thus

it is inferred that these states have a 3-D unstable downstream meniscus. In figure 3.6 these states have been marked as having ribbing on the downstream meniscus though strictly speaking it is unclear from the linear analysis whether uniform ribs will occur or whether a more complicated time dependent structure will develop as seen by Rabaud et al. (1990).

The situation is largely similar between points 1 and 2 with the downstream menis-cus being 3-D unstable. However, as point 2 is approached, $\sigma_{max} \rightarrow 0$ and $k_{max} \rightarrow 0$ and the amplitude ratio rises rapidly past unity indicating that point 2 represents a state with a 2-D neutrally stable upstream meniscus. When S is 0.7% greater than it is at point 2, the amplitude ratio has fallen to below 0.01 and so the transition from a 2-D neutrally stable upstream state at the turning point to states with 3-D unstable downstream menisci is indeed rapid. If the system was in the neutrally stable state corresponding to point 2 and S was decreased further it is unclear from the linear stability analysis what would happen.

The solution curve between turning points 2 and 3 is stable though as each turning point is approached $\sigma_{max} \rightarrow 0$, $k_{max} \rightarrow 0$ and the amplitude ratio becomes much larger than unity. Point 3 is associated with bead break but as stated above, it is unclear what happens at point 2.

The downstream portion of the solution curve behaves in the same way as previous cases with both menisci being unstable.

These results confirm that for values of S lying between those that correspond to points 1 and 2 there are two stable states. It remains unclear though as to whether with a larger disturbance than the infinitesimal one considered here, the system could jump from one linearly stable state to another and if so how large such a disturbance would need to be.

$\zeta = 0.999$

The solution curves for $\zeta = 0.999$ are shown in figure 2.11e. Again the S.H. predicts multiple stable states though the situation differs from the $\zeta = 0.998$ case as the curve has split into two distinct parts. The results of the linear stability analysis are shown in figure 3.7.

The linear stability analysis of the upstream branch between $S = 0$ and $S = S_f$ concurs with S.H. predictions; $\sigma_{max} < 0$ everywhere and as $S_{max} \rightarrow S_f$ then $\sigma_{max} \rightarrow 0$,

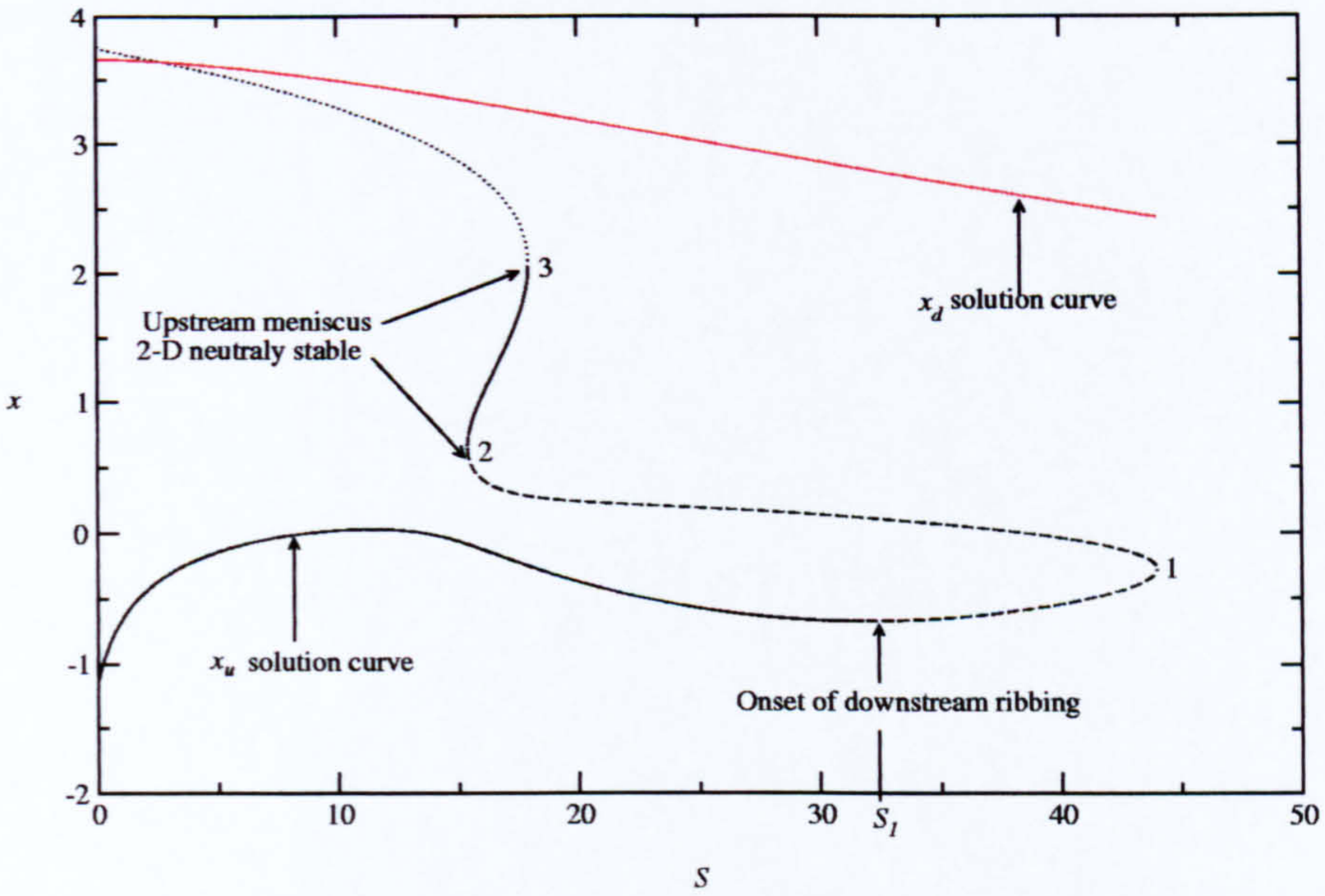

Figure 3.6: The stability states of the DFF bead when $\zeta = 0.998$, $Ca = 10^{-3}$, $\delta = 5 \times 10^{-3}$, $\lambda = 0.1$; the upstream meniscus solution curve is divided as follows: (—-) the bead is linearly stable, (– –) downstream meniscus is 3-D unstable and $(\cdots)$ both menisci are 3-D unstable. The downstream mensicus location curve is also shown (—).

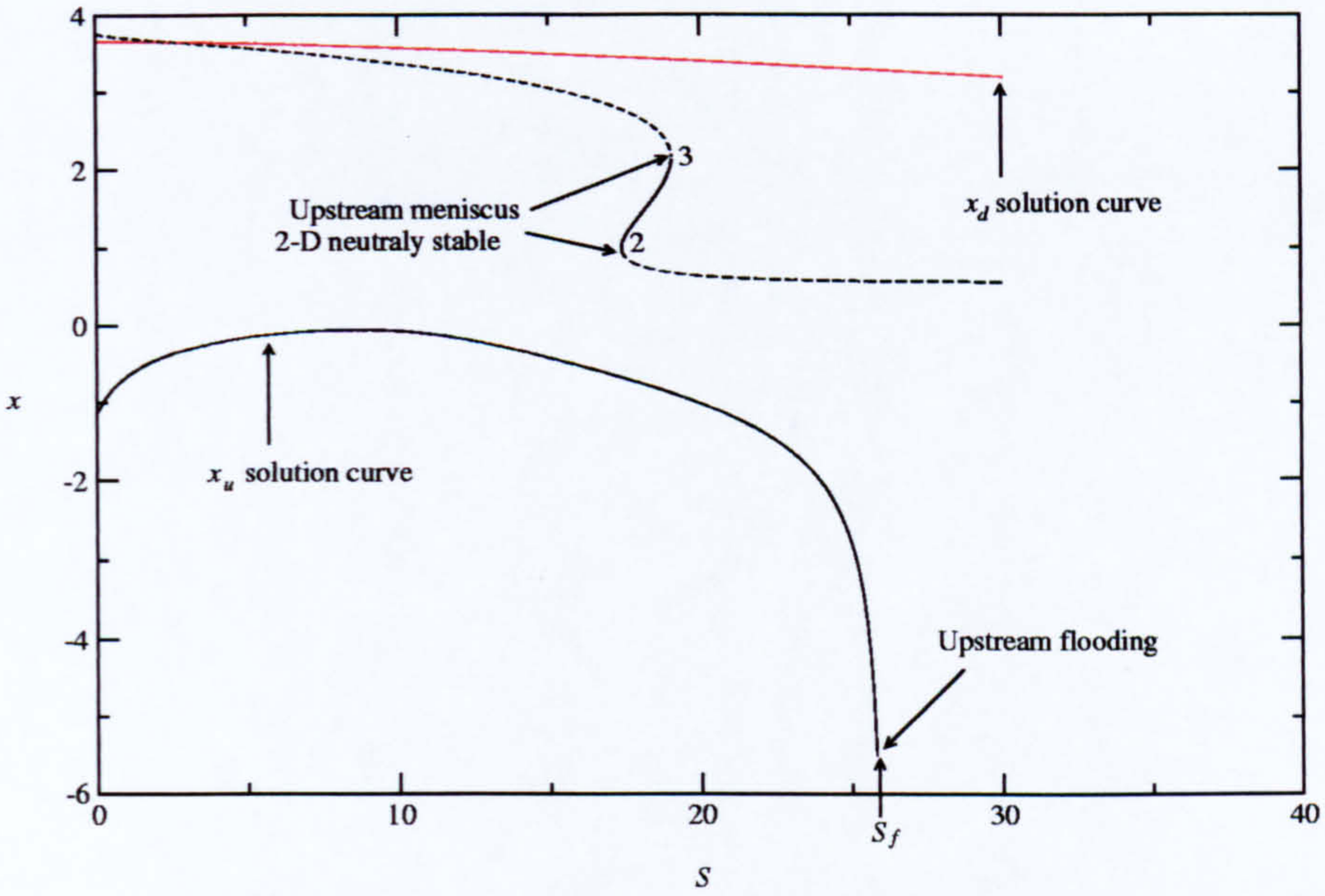

Figure 3.7: The stability states of the DFF bead when $\zeta = 0.999$, $Ca = 10^{-3}$, $\delta = 5 \times 10^{-3}$, $\lambda = 0.1$; the upstream meniscus solution curve is divided as follows: (—-) the bead is linearly stable, (– –) downstream meniscus is 3-D unstable and $(\cdots)$ both menisci are 3-D unstable. The downstream mensicus location curve is also shown (—).

$k_{max} \to 0$ and $b_u \epsilon_{max}/b_d \gg 1$ implying that the state on the upstream branch at $S = S_f$ has a 2-D neutrally stable upstream meniscus. For reasons set out in chapter 2 this state is associated with upstream flooding.

The part of the solution curve between points 2 and 3 is stable with both turning points representing states with 2-D neutrally stable upstream menisci. Moving along the upstream branch that originates from point 2, there is a rapid fall in the amplitude ratio (as in the $\zeta = 0.998$ case) and both σ_{max} and k_{max} are everywhere positive. Thus this branch is associated with the downstream menisci being 3-D unstable. Point 3 is again associated with bead break and the downstream branch has both menisci 3-D unstable.

These results confirm that as ζ approaches unity and $\lambda = 0.1$, the system changes from one that is susceptible to bead break to one that it susceptible to flooding and that under certain conditions multiple steady states exist.

3.3.0.6 $\zeta = 1$, λ variable

$\lambda = 0.09$

The solution curves for $\lambda = 0.09$ are shown in figure 2.12a. In this case the 2-D steady state behaviour of the system is similar to the $\zeta = 0.999$, $\lambda = 0.1$ case and the linear stability analysis showed that the stability of the system behaved in an exactly analogous way.

$\lambda = 0.08323$

The solution curves for $\lambda = 0.08323$ are shown in figure 2.12b. This case is of special interest because as S is increased from zero x_u is single valued until point A is reached beyond which there are three possibilities for x_u. The results of the linear stability are summarised in figure 3.8.

The states lying on the part of the x_u solution curve between $S = 0$ and point A are all stable. As point A is approached the maximum growth rate and corresponding wavenumber approach zero and the amplitude ratio is large. Therefore point A corresponds to a state with a 2-D neutrally stable upstream meniscus. If S is increased past A and either the upstream or downstream branches are followed, the growth rate is negative and the bead is stable. On the upstream branch $\sigma_{max}, k_{max} \rightarrow 0$ as $S \rightarrow S_f$ and this corresponds to upstream flooding. If the downstream branch is followed the linear stability analysis again agrees with the S.H. in predicting the downstream turning point to be the point at which bead break occurs. If the middle branch is followed then the amplitude ratio falls rapidly and both σ_{max} and k_{max} are positive. Thus the states lying on this branch have a 3-D unstable downstream meniscus.

Therefore at point A the system is delicately balanced - a further increase in S could eventually lead to *either* bead break, upstream flooding or a state with an instability (possibly ribbing) appearing on the downstream interface.

$\lambda = 0.08$

The 2-D steady state curves for the case of $\lambda = 0.08$ are shown in figure 2.12c and the linear stability of the system under these conditions is shown in figure 3.9.

As S increases from zero the bead passes through a succession of stable states until the upstream meniscus becomes 2-D neutrally stable at point B. It is thought that this point corresponds to bead break but the linear stability analysis cannot rule out the possibility that the bead could jump to the state corresponding to point C. The

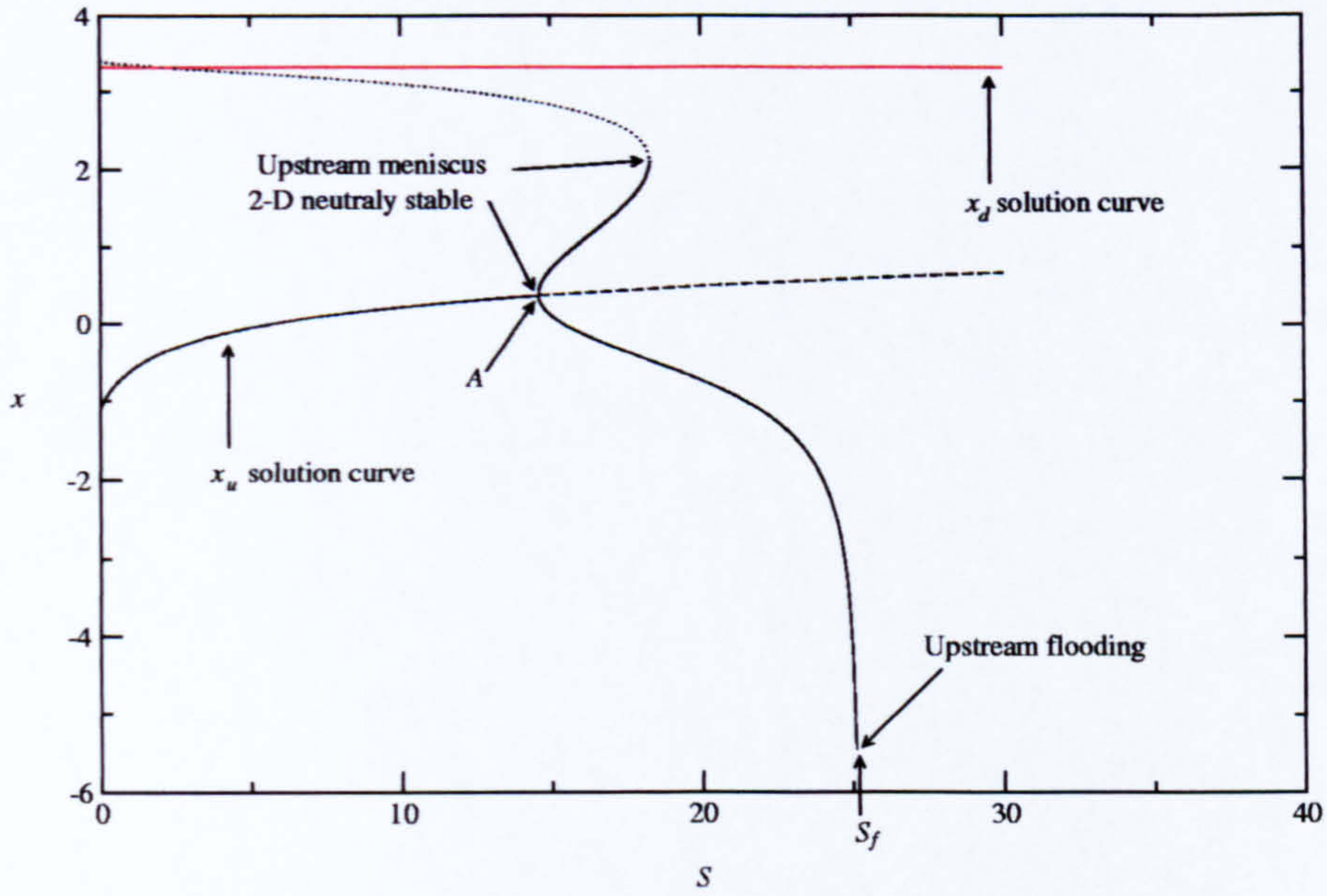

Figure 3.8: The stability states of the DFF bead when $\zeta = 1.0$, $Ca = 10^{-3}$, $\delta = 5 \times 10^{-3}$, $\lambda = 0.08323$; the upstream meniscus solution curve is divided as follows: (—-) the bead is linearly stable, (– –) downstream meniscus is 3-D unstable and $(\cdots)$ both menisci are 3-D unstable. The downstream mensicus location curve is also shown (—).

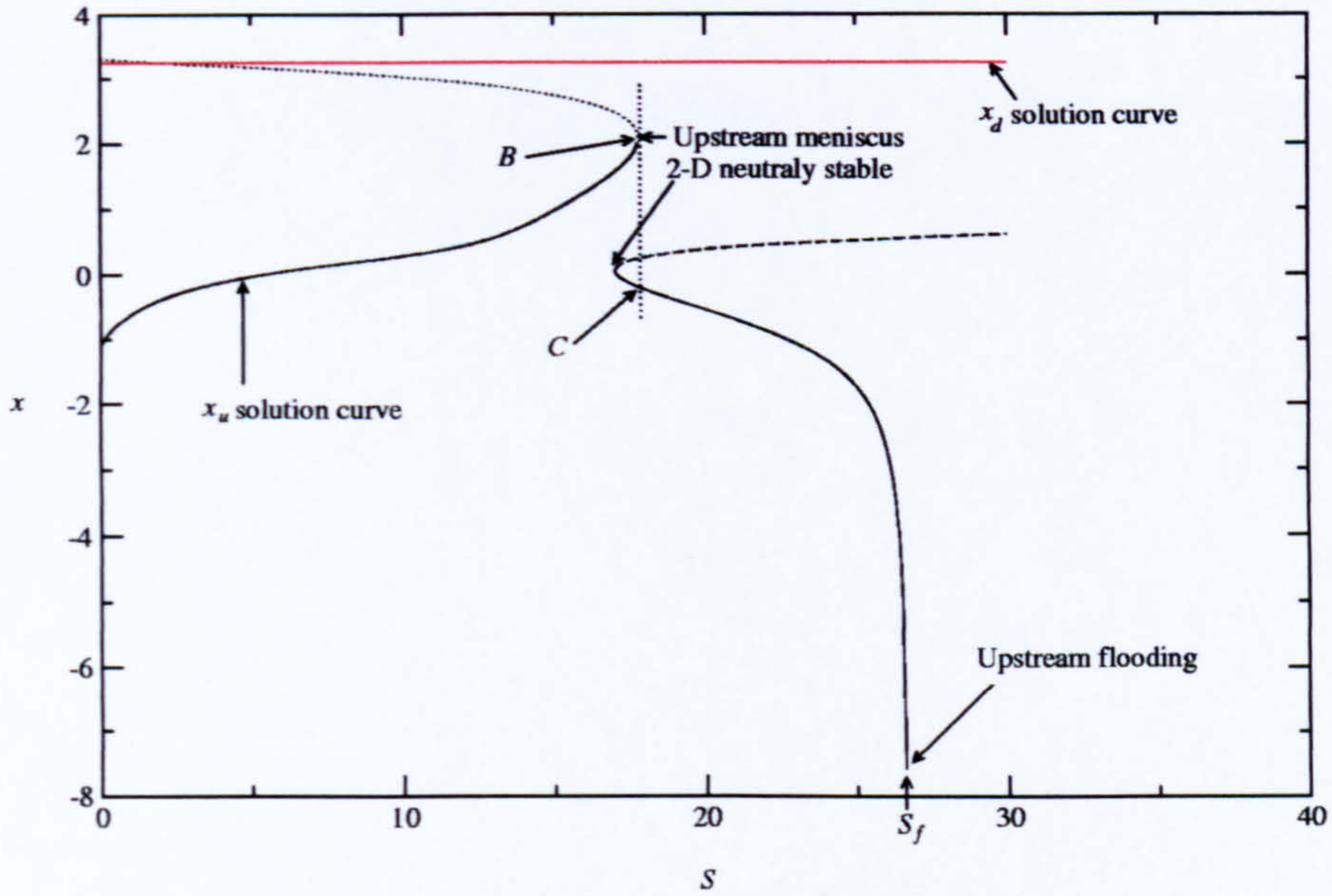

Figure 3.9: The stability states of the DFF bead when $\zeta = 1.0$, $Ca = 10^{-3}$, $\delta = 5\times10^{-3}$, $\lambda = 0.08$; the upstream meniscus solution curve is divided as follows: (—-) the bead is linearly stable, (– –) downstream meniscus is 3-D unstable and $(\cdots)$ both menisci are 3-D unstable. The downstream mensicus location curve is also shown (—).

upstream branch that point C lies on is stable until S_f is reached at which point the upstream meniscus is again 2-D neutrally stable. The remaining set of solutions that exist past point B all have 3-D unstable downstream menisci.

As the values of ζ and λ vary by small quantities in the above analysis it is unlikely all of these results are reproducable in the laboratory. However, whilst the results shown in figures 3.6 and 3.8 rely on very precise values of λ and ζ, the range of values over which two steady states exist is broader and should be reproducable. Also the analysis shows at which values of λ and ζ the transition from a system that would suffer from bead break to one that would suffer from flooding is likely to occur.

3.4 Summary

In this chapter the linear stability of a DFF bead has been investigated.

The 2-D Reynolds equation was used to model the pressure perturbation and suitable boundary conditions were developed. Close attention was paid to the form of the

boundary conditions and in particular the relationship between the pressure jump due to the 3-D nature of the disturbance and the wavenumber was investigated using the framework established in chapter 2. Both long and short wave limits of this relationship were established and were used to show how different forms of the boundary condition used by several authors are linked.

Kinematic conditions were established at both menisci. The conditions were similar in form to previous workers but the conditions were put on a more rigorous footing.

The model was used to investigate the linear stability of the DFF bead and in particular to look at whether the predictions made by the S.H. in the previous chapter were valid. The S.H. predicted that turning points corresponded to states with a 2-D neutrally stable upstream meniscus and this was confirmed by numerical solutions to the linear stability analysis. It was demonstrated that the linear stability analysis always predicts the bead to be neutrally stable with respect to 2-D disturbances ($k = 0$) at the turning points. The S.H. also predicted regions of parameter space where two steady, 2-D stable, states exist and this was confirmed by the analysis of this chapter. The linear stability analysis predicted several solution branches that had unstable downstream menisci and whilst the S.H. did not predict this form of instability, it did indicate that these states would be unstable.

The linear stability analysis also confirmed that there exist a set of values of λ and ζ for which the system is finely balanced between bead break and flooding. In these cases it would be preferable from the industrialist's point of view to follow the branch leading to flooding as this critical phenomenon occures at a higher value of S than bead break in all cases considered.

Therefore it has been shown that the performance of a multiple rigid roll coater can be limited by the bead formed between an intermediate roll pair suffering from either bead break, flooding or the downstream meniscus becoming 3-D unstable.

Chapter 4

Deformable roll coating - steady state

4.1 Introduction

The previous chapters have demonstrated the importance of having a sufficiently accurate steady state model before attempting a stability analysis and it is the aim of this chapter to formulate such a model for the forward deformable roll coater.

Lubrication theory is again used for the fluid model but as the capillary numbers encountered in deformable roll coating are up to $O(1)$, the boundary conditions of chapters 2 and 3 do not apply and instead a method of extending the asymptotic results to higher capillary numbers is developed. The compliant layer model is based upon the integral equation developed by Aleksandrov (1962) and Bentall and Johnson (1968) from the plane strain equations of linear elasticity theory and which was utilised by Young (1997). In the past there has been a discrepancy between theoretical predictions and experimental measurements and so the compliant layer model is extended to take account of linear viscoelastic effects in order to see whether this could explain the difference.

Recently Carvalho and Scriven (1999) carried out a stability analysis of a deformable roll coater using the Navier-Stokes equations for the fluid model and a Hookean spring model for the compliant layer. The spring model used is interesting as the spring constant was calibrated with an impressive nonlinear plane strain model giving the spring constant as $K_{sp} = 2E/L$. Although Young showed the spring model could

not give reliable results for two particular spring constants ($K_{sp} = E/L, 4E/L$) it was not demonstrated that a calibrated model such as the one proposed by Carvalho and Scriven could not provide accurate results. In this chapter a more general approach is taken with the aim of showing that any spring model, no matter what the spring constant, will give inaccurate results.

4.2 Formulation of a mathematical model

4.2.1 Modes of operation and governing parameters

A deformable roll-pair may be operated in one of two modes: fixed-gap or fixed-load. In the former roll separation, $2B_0$, is set by the adjustment of mechanical stops, while in the latter the same is achieved by varying an external force, W, applied across the roll-pair.

In fixed-gap operation W is the roll separating force, which is a dependent variable, whereas for fixed-load operation B_0 is a dependent variable. In addition, roll separation may be set either at a positive gap where the centre to centre distance is greater than the sum of the roll radii, or at a negative gap where the rolls would be in interference if undeformed — as illustrated in figure 4.1.

In the following section a model is formulated using a fixed gap regime and W is subsquently calculated. The roll pair geometry is approximated by a rigid roll and a compliant strip as shown in figure 4.2. The effective roll radius, $\bar{R}$, is set via

$$2/\bar{R} = 1/R_1 + 1/R_2, \tag{4.1}$$

where R_1 and R_2 are the radii of the original roll pair, thus preserving the gap width in the nip region at leading order. In reality the stress and strain fields would differ slightly from those calculated using this geometric approximation due to the initial curvature of the solid. In principle it would be possible to obtain a series solution to the circular strip problem using polar coordinates, though this was beyond the scope of the thesis. Note, in the previous chapters S had a different meaning as it was used to denote the roll speed ratio. In this chapter the rolls have equal speeds and the intended meaning of S will be clear from the context. The parabolic approximation for the roll

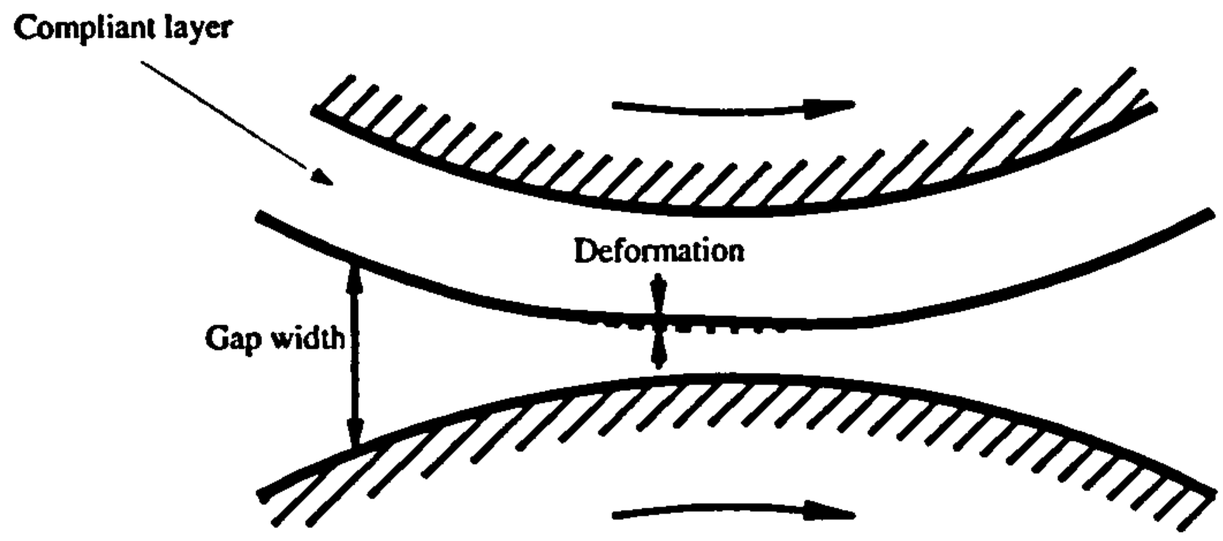

(a) positive gap regime

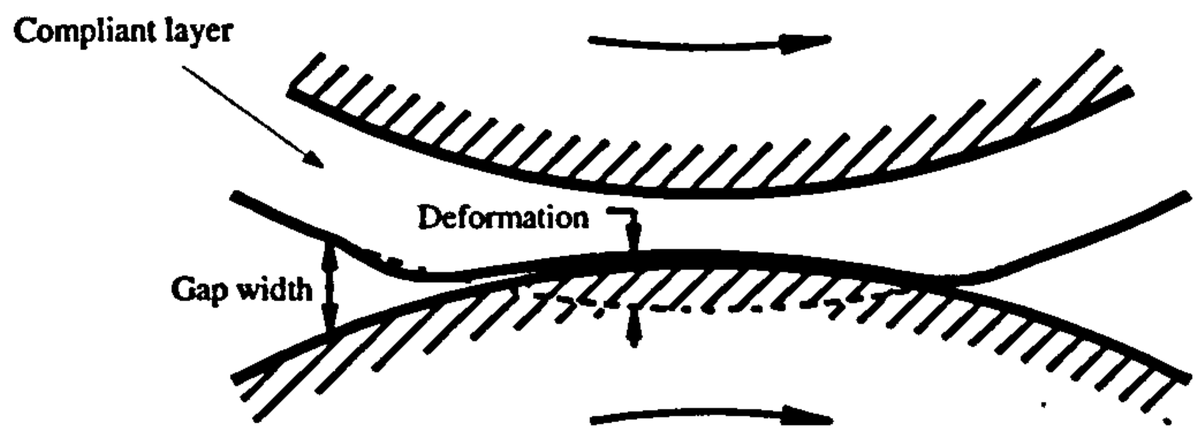

(b) negative gap regime

Figure 4.1: Schematics of the contact region in the positive and negative gap regimes of deformable roll coating. The undeformed roll profile is also shown (- -).

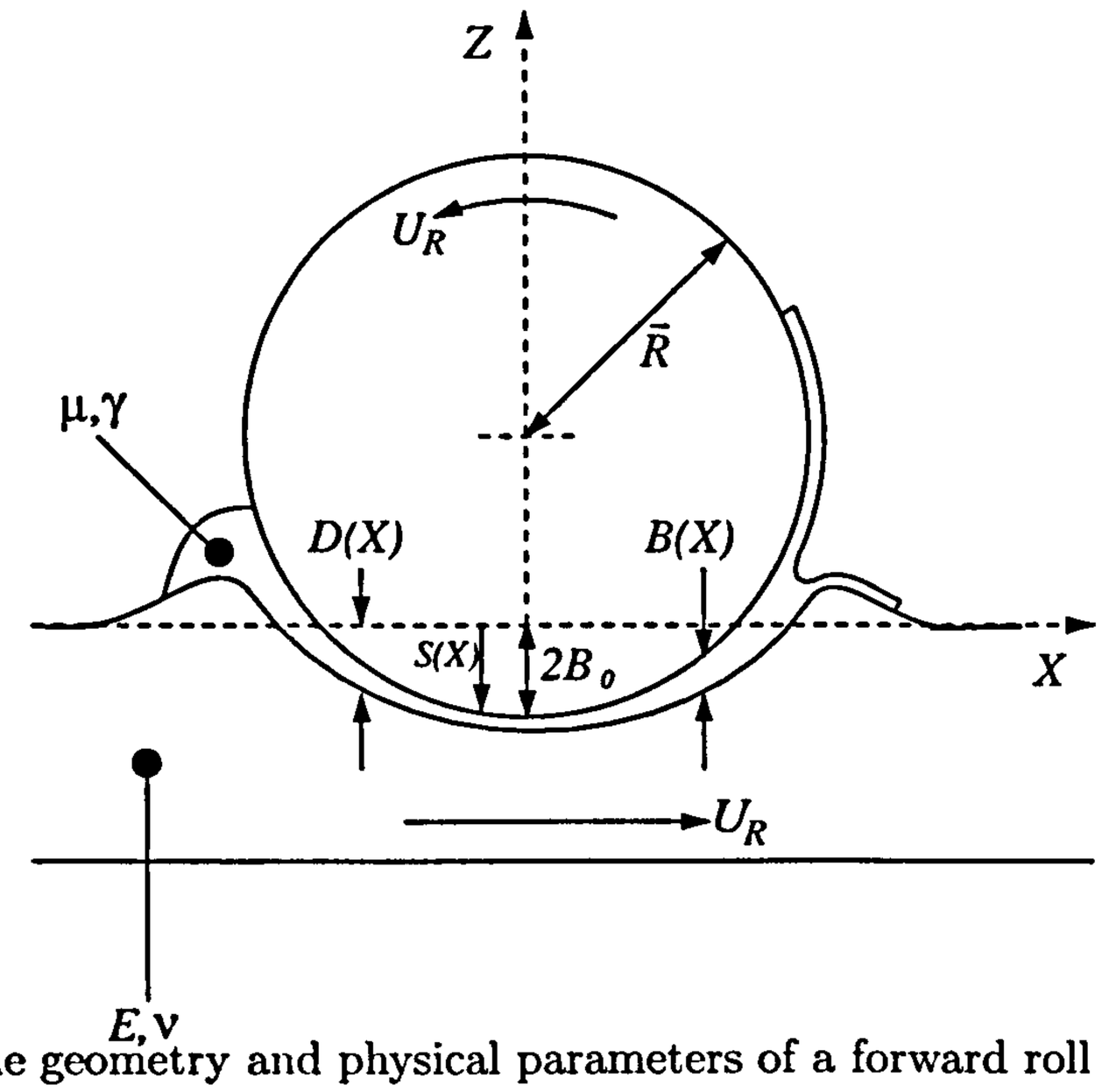

Figure 4.2: The geometry and physical parameters of a forward roll coating device.

surface, $S(X)$, is used again and is defined as

$$S(X) = 2B_0 + \frac{X^2}{2\bar{R}}. \tag{4.2}$$

B_0 is defined such that $B_0 > 0$ corresponds to a positive gap setting and $B_0 < 0$ corresponds to a negative gap setting. $D(X)$ is the surface deformation and therefore the total gap width, $B(X)$, is

$$B(X) = S(X) + D(X). \tag{4.3}$$

4.2.2 Fluid model

The governing fluid equations were developed formally in chapter 2 using a scaling analysis. However, in this chapter although all results are presented in a nondimensional form, the equations are required to be in dimensional form to aid the computation (see section 4.3) and therefore they are briefly set out below.

The coating fluid is assumed to be Newtonian and incompressible in nature and the flow to be steady and therefore the Navier Stokes and continuity equations hold:

$$\rho \boldsymbol{U}.\nabla \boldsymbol{U} = -\nabla P + \rho \boldsymbol{G} + \mu \nabla^2 \boldsymbol{U}, \tag{4.4}$$

$$\nabla.\boldsymbol{U} = 0, \tag{4.5}$$

where ρ, μ and $\boldsymbol{U}$ represent the fluid density, viscosity and velocity, respectively and $\boldsymbol{G}$ is the acceleration due to gravity. Several assumptions and approximations will be made to facilitate a solution to this set of four nonlinear partial differential equations and these are set out below.

Firstly, it is assumed that roll coaters operate in the regime $B_0 \ll \bar{R}$ and hence the use of the lubrication approximation is valid. The second assumption is that body forces are negligible and finally it is assumed that there is no variation in the flow field in the lateral direction. Under these assumptions the Navier Stokes equations are well approximated by the lubrication equations

$$\frac{\partial P}{\partial X} = \mu \frac{\partial^2 U}{\partial Y^2}, \tag{4.6}$$

$$\frac{\partial P}{\partial Y} = 0, \tag{4.7}$$

where the error is $O(B_0/\bar{R})$. (4.6) indicates that the pressure gradient in the X-direction is balanced by the viscous shear force whereas (4.7) states that the pressure is constant

across the gap. Each roll has peripheral speed U_R and the no slip boundary conditions

$$U(X,-D) = U_R, \qquad U(X,S) = U_R, \tag{4.8}$$

are deemed to hold on the roll surfaces. Integrating (4.6) and applying (4.8) leads to Reynolds equation

$$\frac{\mathrm{d}P}{\mathrm{d}X} = \frac{12\mu U_R}{B^3}\left(B - 2H^{\infty}\right), \tag{4.9}$$

where H^{∞} is the final coated film thickness on each roll. This can also be written as

$$\frac{\mathrm{d}}{\mathrm{d}X}\left[\frac{B^3(X)}{\mu U_R}\frac{\mathrm{d}P}{\mathrm{d}X}\right] = 12\frac{\mathrm{d}B}{\mathrm{d}X}. \tag{4.10}$$

Note, it is assumed that the film split is symmetric between the two rolls, i.e. the coated film thickness on each roll is the same.

4.2.2.1 Boundary Conditions

In order to complete the fluid model three boundary conditions are needed to find the coated film thickness H^{∞}, the meniscus position X_D and the constant arising from integration of Reynolds equation (4.9). The first of these conditions is straightforward: as the rolls are understood to be operating with a fully flooded inlet then the pressure will decay rapidly upstream of the nip and approach atmospheric pressure (taken to be zero here), i.e.

$$P(X) \to 0 \qquad \text{as} \qquad X \to -\infty. \tag{4.11}$$

Ruschak (1982) used a scaling analysis to confirm this form of the boundary condition. The remaining two conditions require closer inspection. The lubrication approximation, and hence Reynolds equation, is valid when the flow is essentially rectilinear which is certainly true away from the film split. However, in the region of the meniscus the flow field becomes fully two dimensional and the lubrication approximation breaks down. Therefore the challenge lies in finding conditions that capture the essential physics of the 2-D film split region yet can be applied to the 1-D Reynolds equation. Many authors have suggested strategies to overcome this problem and these range from ad-hoc empirical rules through formal matched asymptotic expansions to computational methods. All of these have their merits and the pertinent ideas are reviewed in chapter 1.

The computational approach (Ruschak (1982)) could be applied over an arbitrary capillary number range as well as being the most accurate yet despite these plus points the method was discarded. The reasons for this are two fold. Firstly, the algorithim developed by Rushack would have to be adapted to cope with an initially unknown solid boundary geometry and secondly (and more importantly) it would add to the already significant computational cost of solving the deformable problem.

All of the 'analytic' boundary conditions suffer from one major drawback - the fact that they are limited to a particular range of Ca. Thus to cover an extended range of Ca several of the expressions would have to be utilised, each covering a section of Ca space. This approach has been adopted by previous workers (Daniels (1998), Young (1997)) but suffers from the fact that the predictions of the model do not vary in a smooth manner as Ca is varied, instead a 'jump' in the predictions is seen at the cross over point from one set of conditions to another. Since Ca is a vital parameter in the determination of the system's stability, it would be advantageous to use a boundary condition valid over the full range of Ca encountered, enabling a search for the critical conditions to be carried out in a smooth manner. Therefore, an alternative form of the conditions was sought.

The attempt to find an alternative simple condition was guided by work on a related problem by Quere (1999) and two requirements:

- the conditions had to agree with the asymptotic results of chapter 2 as $Ca \rightarrow 0$,
- the expression for coated film thickness should not result in $H^{\infty} \rightarrow \infty$ as $Ca \rightarrow \infty$. This is a clear problem with the present alternatives.

In the closely related problem of the flow of a bubble in a tube, Quere quotes the following condition ('Taylor's law') for the thickness of the fluid layer between the bubble and the tube wall:

$$H^{\infty} = \frac{B_D}{2} \frac{1.34Ca^{2/3}}{1 + 3.35Ca^{2/3}} \tag{4.12}$$

It can be seen that in the limit $Ca \rightarrow 0$, this expression agrees with the asymptotic expression given by Bretherton. A fundamental problem with the Bretherton expression is that it grows unbounded as Ca increases, negating its validity as Ca becomes large. The effect of introducing the denominator means that Taylor's law does not suffer the same problem. The numerical factor of 3.35 was found by matching the expression to

experimental data. Quere found that this expression gave excellent agreement with the experimental results of Taylor over the range $Ca < 1$. As Quere was purely interested in the film thickness and not the pressure drop across the bubble/fluid interface, no equivalent expression for the stress jump across the interface was given. Taking Taylor's law as a motivation, simple boundary conditions are now developed for both the final film height and the pressure drop across the menicus and the results are then compared with the computational results of Coyle et al. (1986).

In chapter one it was shown that the pressure drop across the downstream meniscus was given by:

$$P(X_D) = -\frac{\gamma}{B_D}\left(1 - \left.\frac{\mathrm{d}B}{\mathrm{d}X}\right|_{X_D} + 2.91Ca^{2/3}\right). \tag{4.13}$$

An intuitive way to think of this expression is to consider it as an expansion of

$$P(X_D) = -\frac{\gamma}{R_D}, \tag{4.14}$$

where R_D is the radius of curvature of the meniscus tip and is given by

$$R_D = \frac{1}{2}\left(B_D + \underbrace{\frac{1}{2}B_D\left.\frac{\mathrm{d}B}{\mathrm{d}X}\right|_{X_D}}_{\text{non-constant gap width term}} - \underbrace{2.91B_DCa^{2/3}}_{\text{finite film height term}}\right). \tag{4.15}$$

The factors of $1/2$ arise due to the fact that B_D represents the total gap in this chapter whereas it represented the semi-gap width in chapter 2. (4.15) leads to a simple physical interpretation when the radius of curvature is approximately equal to $B_D/2$ with small corrections due to the non-constant gap width and the finite thickness of the outgoing films. The Landau Levich expression for film thickness is $H^\infty = 1.34B_DCa^{2/3}/2$ but this can be interpreted as a leading order approximation to $H^\infty = 1.34R_DCa^{2/3}$. Substituting for R_D from (4.15) then gives

$$H^\infty = 1.34\left(\frac{1}{2}B_D + \frac{1}{4}B_D\left.\frac{\mathrm{d}B}{\mathrm{d}X}\right|_{X_D} - 2.91H^\infty\right)Ca^{2/3}, \tag{4.16}$$

which rearranges to give

$$H^\infty = \frac{1}{2}\frac{1.34B_DCa^{2/3}}{1+3.88Ca^{2/3}}\left(1+\frac{1}{2}B_X\right) \tag{4.17}$$

Note, in the case of a capillary tube $B_X = 0$ and this expression is similar to Taylor's law.

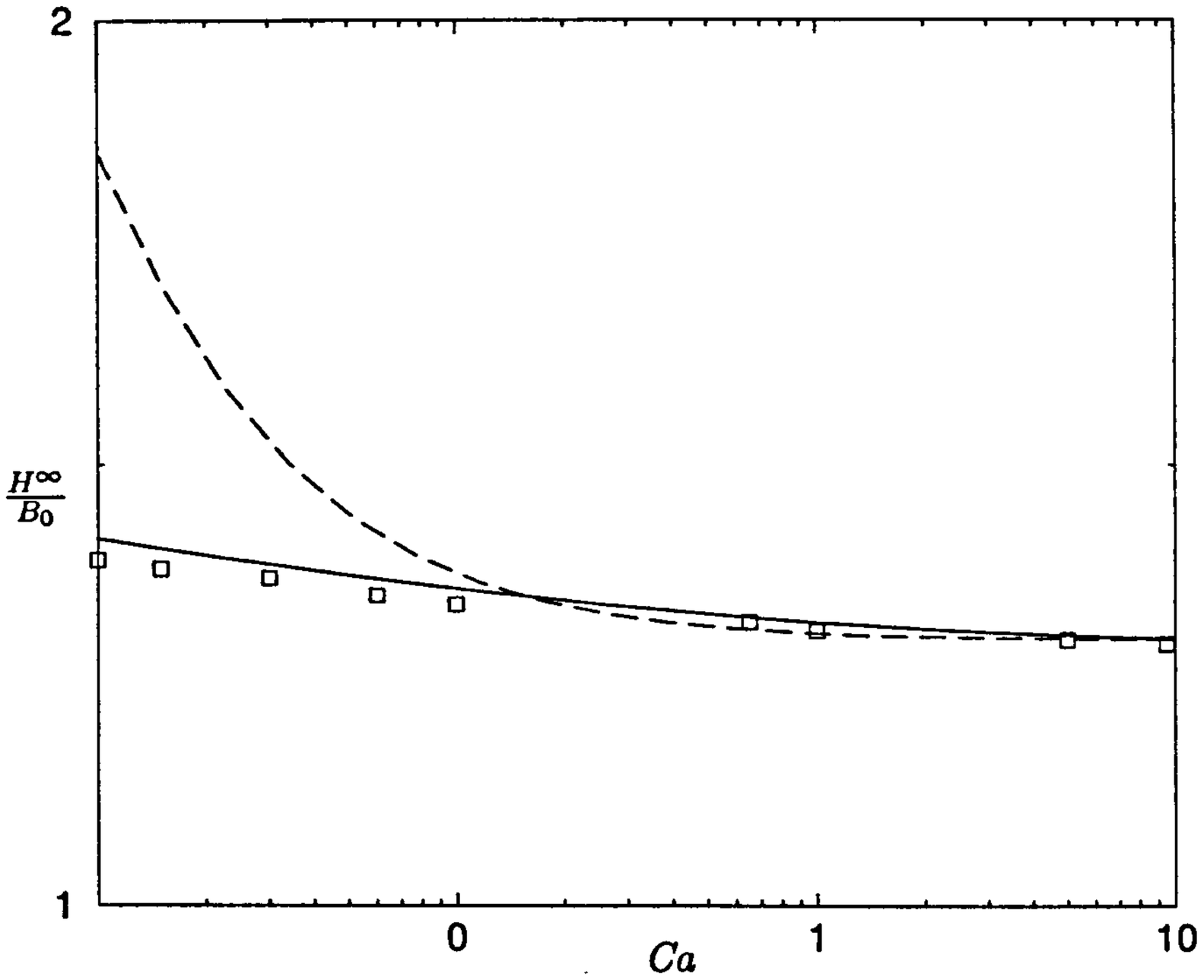

Figure 4.3: Coated film thickness predictions for the finite element model of Coyle (□) and lubrication theory with Prandtl Hopkins conditions (– –) and modified Landau Levich conditions (—). $B_0/\bar{R} = 10^{-3}$.

Reynolds equation was solved subject to (4.14), with R_D defined by (4.15), and (4.17) and the results were compared against the computations of Coyle et al. (1986) and results are shown for the film thickness in figure 4.3 and in figure 4.4 for the meniscus position. It can be seen that the predictions are in excellent agreement for a range of Ca covering 10^{-3}-10. This level of agreement for an analytic condition over such a range is unprecedented and represents a significant break through as in the past workers have had to switch from one condition to another as they move through Ca space.

Therefore a fluid model, valid over a wide range of Ca, has been developed and the governing equations for the compliant layer are now discussed.

4.2.3 Governing equations for the compliant layer

The compliant layer is described by the Maxwell-Thomson model (Goryacheva (1998)) which allows for the inclusion of linear viscoelastic effects. The constitutive equations

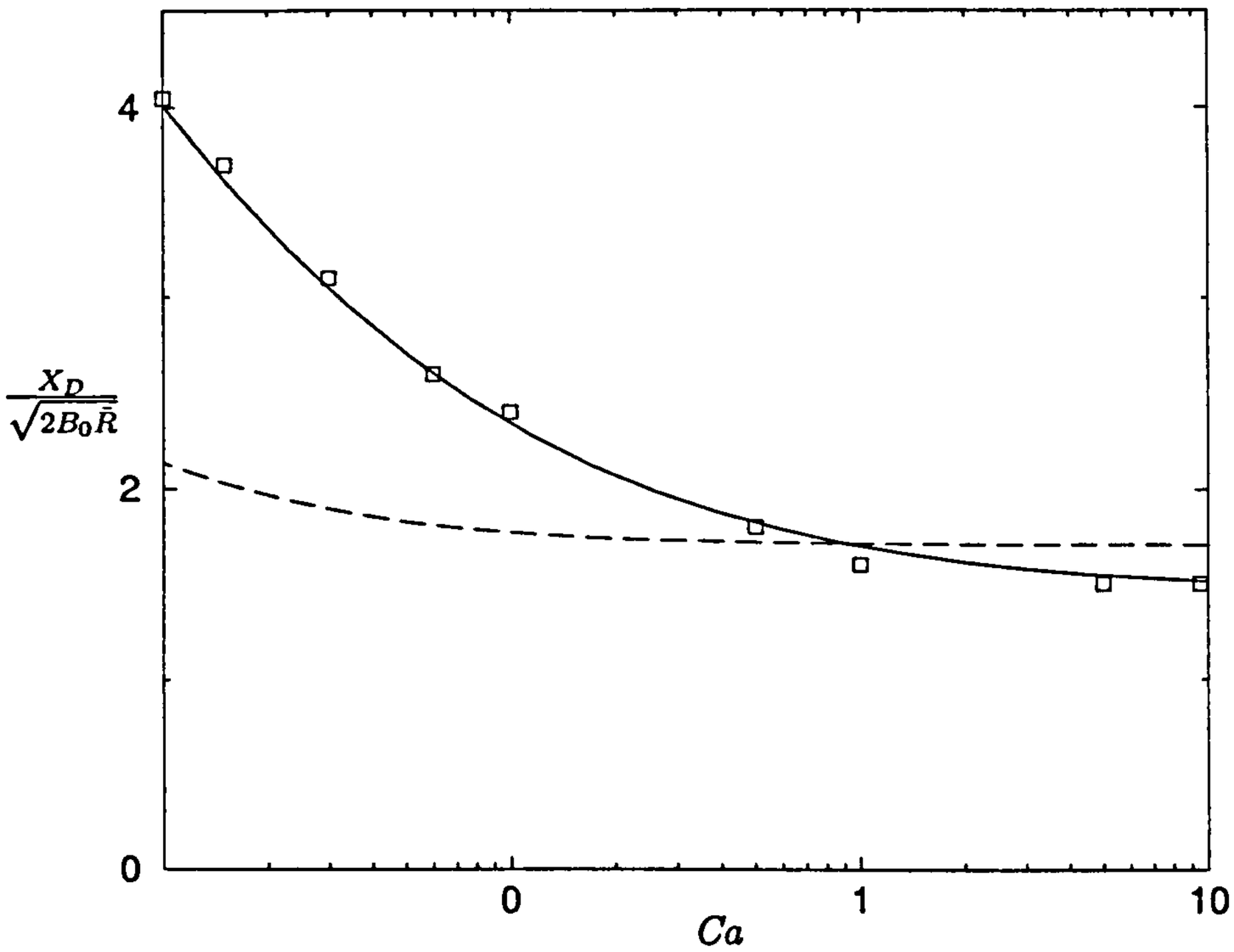

Figure 4.4: Meniscus location predictions for the finite element model of Coyle (□)and lubrication theory with Prandtl Hopkins conditions (– –) and modified Landau Levich conditions (—-). $B_0/\bar{R} = 10^{-3}$

linking the strain, ϵ^0_{ij}, and the stress, σ^0_{ij}, take the form:

$$\epsilon^0_{X^0X^0} + T_\epsilon \frac{\partial \epsilon^0_{X^0X^0}}{\partial T} = \frac{1-\nu^2}{E}\left(\sigma^0_{X^0X^0} + T_\sigma \frac{\partial \sigma^0_{X^0X^0}}{\partial T}\right) - \frac{\nu(1+\nu)}{E}\left(\sigma^0_{Y^0Y^0} + T_\sigma \frac{\partial \sigma^0_{Y^0Y^0}}{\partial T}\right) \tag{4.18}$$

$$\epsilon^0_{Y^0Y^0} + T_\epsilon \frac{\partial \epsilon^0_{Y^0Y^0}}{\partial T} = \frac{1-\nu^2}{E}\left(\sigma^0_{Y^0Y^0} + T_\sigma \frac{\partial \sigma^0_{Y^0Y^0}}{\partial T}\right) - \frac{\nu(1+\nu)}{E}\left(\sigma^0_{X^0X^0} + T_\sigma \frac{\partial \sigma^0_{X^0X^0}}{\partial T}\right) \tag{4.19}$$

$$\epsilon^0_{X^0Y^0} + T_\epsilon \frac{\partial \epsilon^0_{X^0Y^0}}{\partial T} = \frac{1+\nu}{E}\left(\sigma^0_{X^0Y^0} + T_\sigma \frac{\partial \sigma^0_{X^0Y^0}}{\partial T}\right), \tag{4.20}$$

where T_ϵ is a retardation time and T_σ is a relaxation time. The coordinates (X^0, Y^0) represent a material frame of reference which is fixed relative to the compliant layer and is related to the laboratory frame, in which the axis of the roll is fixed and the deformation and pressure profiles are steady, via:

$$X = X^0 + U_R T, \qquad Y = Y^0. \tag{4.21}$$

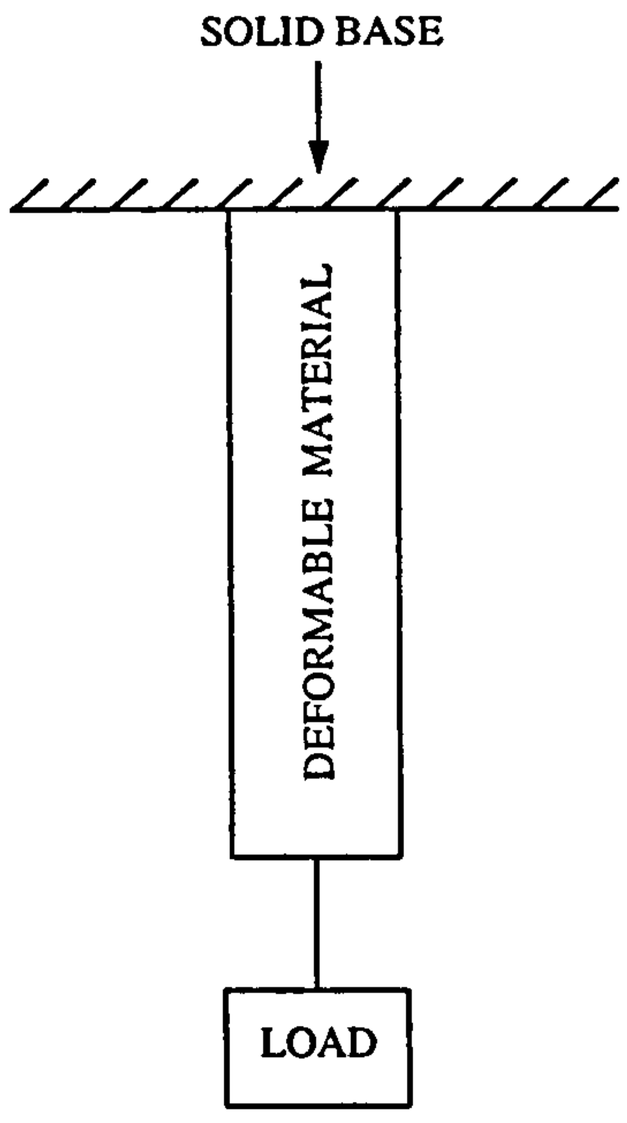

Figure 4.5: A length of deformable material attached to a solid base with a suspended load. Gravity acts vertically downwards.

Two nondimensional quantities describing the viscoelastic behaviour can be defined, the Deborah number

$$De = \frac{T_\epsilon U_R}{\sqrt{|B_0|}\bar{R}}, \tag{4.22}$$

which represents the ratio of the retardation time to a typical timescale of the flow and

$$T_r = \frac{T_\epsilon}{T_\sigma}, \tag{4.23}$$

the ratio of the two viscoelastic timescales. The inclusion of the strain rate and stress rate terms allows for the modelling of simple linear viscoelastic effects whereas setting T_ϵ and T_σ equal to zero recovers the plane strain linear elasticity equations.

The parameterisation of the system is completed by defining E_S, the ratio of viscous to elastic forces:

$$E_S = \frac{\mu U_R}{E\bar{R}}, \tag{4.24}$$

and a layer thickness parameter:

$$\frac{L}{\bar{R}}. \tag{4.25}$$

Typically $E_S \ll 1$ and $L/\bar{R} \sim 0.1$.

The effect of the time dependent terms can be demonstrated by considering a 1-D example and setting T_σ and T_ϵ to zero in turn. Consider a length of material, for which

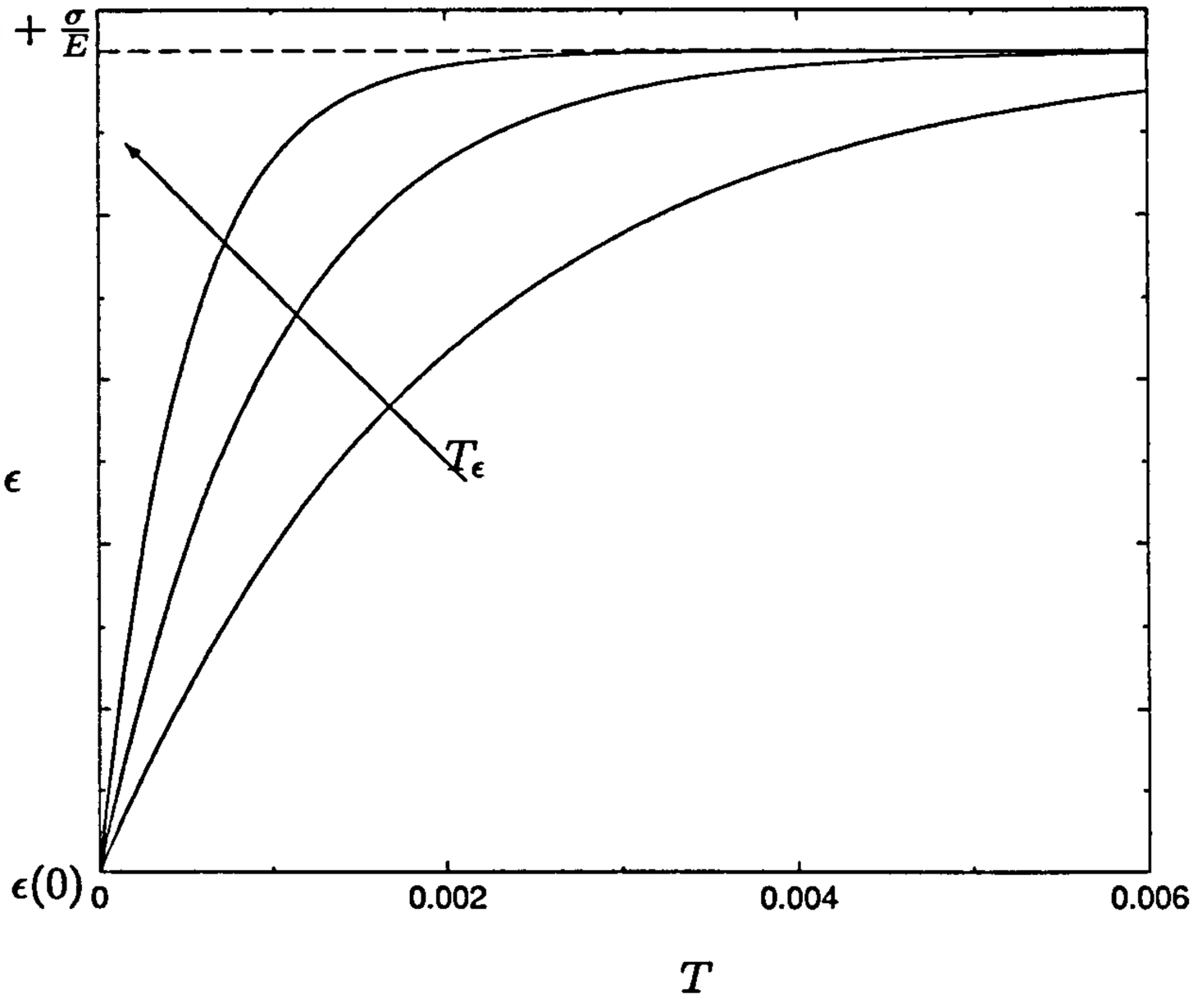

Figure 4.6: Evolution of strain for several values of T_ϵ and the elastic limit.

$T_\sigma = 0$, with a load suspended from it for $T > 0$ as shown in figure 4.5. In this case the applied stress σ, equal to the load divided by the cross sectional surface area, is constant. Therefore the strain is governed by

$$\epsilon + T_\epsilon \frac{\partial \epsilon}{\partial T} = \frac{\sigma}{E}, \tag{4.26}$$

which can be solved to give

$$\epsilon = \epsilon(0) + \frac{\sigma}{E}\left(1 - e^{-T/T_\epsilon}\right). \tag{4.27}$$

The strain is plotted in figure 4.6 for several values of T_ϵ. The strain approaches the elastic value exponentially and T_ϵ governs the rate of approach.

A similar situation holds for a length of material, with $T_\epsilon = 0$, that is stretched to a fixed (constant in time) length. The strain is then constant and the stress is given by

$$\sigma = \sigma(0) + E\epsilon\left(1 - e^{-T/T_\sigma}\right). \tag{4.28}$$

Therefore the inclusion of the rate of strain and of the rate of stress terms in (4.18) - (4.20) allows for simple viscoelastic effects to be modelled. The model is phenomenological and is intended to give an indication of how the viscoelastic properties of the compliant layer affect the performance of the coater.

For the equivalent elastic model the plane strain equations can be solved to give an integral equation giving the surface deformation in terms of the surface traction (1.16). Here the situation is complicated by the inclusion of the viscoelastic terms but making the transformation:

$$\epsilon^0_{ij} + T_\epsilon \frac{\partial \epsilon^0_{ij}}{\partial T} = \epsilon_{ij} + T_\epsilon U_R \frac{\epsilon_{ij}}{\partial X} = \epsilon^*_{ij}, \tag{4.29}$$

$$\sigma^0_{ij} + T_\sigma \frac{\partial \sigma^0_{ij}}{\partial T} = \sigma_{ij} + T_\sigma U_R \frac{\sigma_{ij}}{\partial X} = \sigma^*_{ij}, \tag{4.30}$$

$$U_S + T_\epsilon U_R \frac{\partial U_S}{\partial X} = U^*_S \quad , \qquad V_S + T_\epsilon U_R \frac{\partial V_S}{\partial X} = V^*_S, \tag{4.31}$$

where U_S and V_S are the displacements in the X^0 and Y^0 directions, produces the variables ϵ^*_{ij} and σ^*_{ij} that satisfy the equations of an isotropic linear elastic material. The subscript S is used to differentiate the solid displacement variables from the fluid velocity variables. Thus the integral equation from the elastic case (1.16) can be used for the transformed variables giving:

$$D^*(X) = \frac{(1-\nu^2)}{\pi E} \mathrm{Re} \int_{-\infty}^{\infty} \tilde{K}(\omega) \left(\tilde{P}(\omega) + T_\sigma U_R \widetilde{\frac{\mathrm{d}P}{\mathrm{d}X}}(\omega) \right) \mathrm{e}^{i\omega X/L} \mathrm{d}\omega, \tag{4.32}$$

where $\tilde{P}$ is the Fourier transform of P defined as

$$\tilde{P} = \int_{-\infty}^{\infty} P(X) e^{-i\omega X/L} \mathrm{d}X, \tag{4.33}$$

D^* is the value of the transformed vertical displacement V^*_S on the surface and

$$\tilde{K}(\omega) = \frac{(3-4\nu)\sinh 2\omega - 2\omega}{2\omega(\omega^2 + (1-2\nu)^2 + (3-4\nu)\cosh^2 \omega)}. \tag{4.34}$$

Noting that D^* is simply the value of V^* on the compliant layer surface, D can be found by solving the first order equation (4.31) to give

$$D(X) = \frac{1}{T_\epsilon U_R} \int_{-\infty}^{X} D^*(S) \mathrm{e}^{(S-X)/T_\epsilon U_R} \mathrm{d}S. \tag{4.35}$$

Contributions to the deformation from the tangential traction forces have been discarded as they are of the order $O((B_0/\bar{R})^{3/2})$ and $O((B_0/\bar{R})^{-3/2} E^{3/2}_S)$ in comparison to the normal forces in positive and negative gaps, respectively. This completes the description of the viscoelastic extension to the full-strip deformation model (FSM).

4.3 Numerical methods

The numerical scheme employed here has its basis in the finite element method for solving PDE's and, whilst it borrows from the ideas developed by Young (1997), there are several important differences. In this section the finite element method will be briefly introduced before it is applied to the test case of a rigid roll coater and finally a strategy for simultaneously solving the differential and integral equations is presented.

4.3.1 The finite element method

The finite element (F.E.) method is a well established method for numerically solving PDE's and is regularly used to solve problems in a wide range of areas including heat transfer, fluid mechanics, electromagnetism and even financial market modelling. As such there is a large body of literature concerned with the mathematical basis, development and application of the method, which includes Huebner (1975) and the reader is refered to this and similar texts for further information. The following is a brief and basic introduction to the F.E. method.

The fundamental idea of the F.E. method is to discretise the solution domain into contiguous subdomains (elements) and, within each subdomain, to approximate the solution to the differential equation by a suitable finite combination of basis functions. Within each element the combination of basis functions is chosen such that the error, weighted over each element, is minimised. The 1-D example below will illustrate the idea further.

Suppose $\mathcal{L}$ is a differential operator and the function $F(X)$ satisfies the equation

$$\mathcal{L}F = G(X) \qquad X \in \Omega, \tag{4.36}$$

where $\Omega = [a, b]$ is the solution domain. Ω is divided into say, N, elements as depicted in figure 4.7. Let the basis functions for element i be ψ_k^i, $k = 1, 2, ..m$. Then within element i, F can be approximated as

$$F(X) \approx F^i(X) = \sum_{k=0}^{m} \alpha_k^i \psi_k^i(X) \quad \text{if } X \in \Omega^i, \tag{4.37}$$

where the α_k's are unknowns that are found by minimising some average sense of the error. As (4.37) is an approximation, an error function, E^i, for the i^{th} element can be

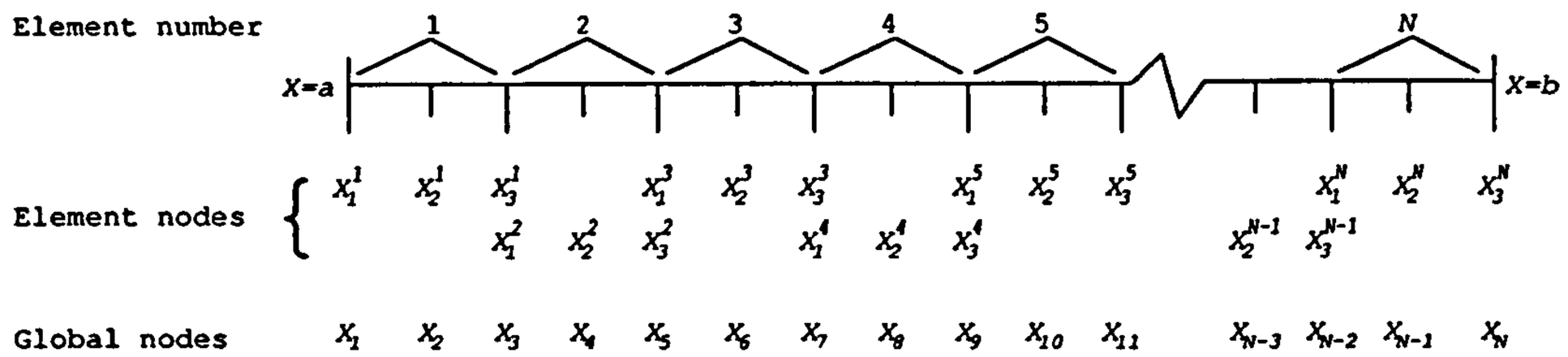

Figure 4.7: The division of the solution domain and the relationship between the global and element nodes.

written as

$$E^i(X) = \mathcal{L}(F^i) - G(X) \qquad X \in \Omega^i, \tag{4.38}$$

An average of this error, R_k^i, weighted with respect to some function $W_k^i(X)$, is defined as

$$R_k^i = \int_{\Omega^i} W_k^i(X) E^i(X) \mathrm{d}X. \tag{4.39}$$

The aim of the F.E. method is to choose the α_k^i's such that $R_k^i = 0 \; \forall \; k$. In this work the well known Galerkin F.E. method is used, for which $W_k^i = \psi_k^i$, $k = 1, 2, ...m$. Therefore, there are m equations:

$$R_k^i = \int_{\Omega^i} \psi_k^i E^i \mathrm{d}x = 0, \quad k = 1, 2, ...m, \tag{4.40}$$

for the m unknowns α_k^i, $k = 1, 2...m$ connected with element i. Thus the approximate solution is defined such that the weighted average error over each element in zero.

It should be noted that for F to be continuous, it is required that

$$F^i(X) = F^{i+1}(X) \qquad \forall \qquad X \in \Omega^i \cap \Omega^{i+1}, \qquad i = 1, 2, ..N-1. \tag{4.41}$$

This requirement and the idea of nodal unknowns is now discussed.

Suppose within element i, m points (labelled X_k^i, $k = 1, 2, ...m$) are chosen such that $X_j^i < X_{j+1}^i \; \forall \; j$ and $\Omega^i = [X_1^i, X_m^i]$ - see figure 4.7 (which displays the m=3 case). These points are refered to as nodes. Futhermore, suppose the basis functions are chosen such that

$$\psi_k^i(X_j^i) = \delta_{kj}, \tag{4.42}$$

where δ_{kj} is the Kronecker delta. Therefore,

$$F^i(X_j^i) = \sum_{k=1}^{m} \psi_k^i(X_j^i)\alpha_k^i = \alpha_j^i, \tag{4.43}$$

and thus the α_k^i's represent the value of the approximation at the nodes and are thus refered to as nodal unknowns. It is convenient to think of $R_k^i = 0$ as an equation for α_k^i. In simple terms, the F.E. method can be thought of as varying the nodal unknowns until the weighted average of the local error is minimised.

So far the discussion has revolved around finding equations for the nodal unknowns within an element. The final step is to incorporate these equations into a global set. Figure 4.7 shows how the element nodes X_j^i are linked to the global nodes X_l and this relation can be expressed via

$$X_{(m-1)(i-1)+j} = X_j^i, \qquad i = 1, 2, ...N, \quad j = 1, 2, ...m, \tag{4.44}$$

and similarly for the nodal unknowns:

$$\alpha_{(m-1)(i-1)+j} = \alpha_j^i, \qquad i = 1, 2, ...N, \quad j = 1, 2, ...m. \tag{4.45}$$

It is clear that $X_m^i = X_1^{i+1}$ and for continuity it is required that

$$\alpha_m^i = \alpha_{(m-1)(i-1)+m} = \alpha_{(m-1)i+1} = \alpha_1^{i+1}. \tag{4.46}$$

and therefore the total number of independent nodal unkowns is equal to the total number of nodes, NUMNODES, which is

$$\texttt{NUMNODES} = N(m-1) + 1. \tag{4.47}$$

However, Nm residual equations have been defined in total. The situation is rectified by defining the global equations recursively:

do $i = 1, N$

do $j = 1, m$

$$R_{(m-1)(i-1)+j} = R_{(m-1)(i-1)+j} + R_j^i \tag{4.48}$$

end do

end do

The syntax used here is from the FORTRAN computer language. Thus the total number of global equations is the same as the total number of independent nodal unknowns. The final set of equations is

$$R_l(\alpha_1, \alpha_2, ..., \alpha_n) = 0, \qquad l = 1, 2, ..., \texttt{NUMNODES}. \tag{4.49}$$

This theory is now applied to the case of a forward rigid roll coater where the numerical results can be tested against an analytic solution before the deformable case is considered.

4.3.2 Application of F.E. method to rigid roll coating

For this work, quadratic basis functions were chosen, giving $m = 3$. The coefficients of the constant, linear and quadratic terms can be calculated from (4.42). The reason for the choice is that the accuracy of the numerical solution can be improved by increasing either N or m which will also have the effect of increasing the computational expense of the algorithim. Quadratic polynomials were used as Young (1997) demonstrated that they are more efficient than linear polynomials as the value of N needed to achieve a given accuracy is less. Cubic polynomials would be more efficient still for a simple rigid roll coater but the expressions developed below for the integral equation would become more involved. Hence quadratic polynomials were thought to give a good balance between efficiency and ease of use.

The pressure and gap thickness are written in terms of the basis functions:

$$P(X) \approx \sum_{k=1}^{3} \psi_k^i(X) P_k^i \qquad X \in \Omega^i, \quad k = 1,2,3, \tag{4.50}$$

$$B(X) \approx \sum_{k=1}^{3} \psi_k^i(X) B_k^i \qquad X \in \Omega^i, \quad k = 1,2,3, \tag{4.51}$$

where the B_k^i's and the P_k^i's are the gap and pressure nodal unknowns. $B_k^i = S_k^i + D_k^i$ where S_k^i and D_k^i are the rigid and deformable contributions to the gap thickness, respectively. When both rolls are rigid $D_k^i = 0 \ \forall \ i$ and k and as S is a quadratic function of X (4.51) is an exact expression in this case. In order to show the quadratic nature of these approximations explicitly, it is possible to rewrite (4.50) and (4.51), for example

$$P \approx a_{i_0} + a_{i_1} X + a_{i_2} X^2 \qquad X \in \Omega^i, \tag{4.52}$$

where a_{i_0}, a_{i_1} and a_{i_2} are given by

$$a_{i_0} = \frac{\lambda_i^2 P_1^i + 3\lambda_i P_1^i X_1^i - 4\lambda_i P_2^i X_1^i + \lambda_i P_3^i X_1^i + 2P_1^i X_1^{i^2} - 4P_2^i X_1^{i^2} + 2P_3^i X_1^{i^2}}{\lambda_i^2} \quad (4.53)$$

$$a_{i_1} = \frac{-3\lambda_i P_1^i + 4\lambda_i P_2^i - \lambda_i P_3^i - 4P_1^i X_1^i + 8P_2^i X_1^i - 4P_3^i X_1^i}{\lambda_i^2}, \quad (4.54)$$

$$a_{i_2} = 2\frac{P_1^i - 2P_2^i + P_3^i}{\lambda_i^2}. \quad (4.55)$$

λ_i is the length of element i, i.e. $\lambda_i = X_3^i - X_1^i$. The residuals can now be formed by substituting (4.50) and (4.51) into Reynolds equation (4.10) and then performing the weighting and integration to give:

$$R_k^{lub^i} = \int_{X_1^i}^{X_3^i} \psi_k^i \left[\frac{\mathrm{d}}{\mathrm{d}x} \left(\frac{\psi_j^{i^3} B_j^{i^3}}{\mu U_R} \frac{\mathrm{d}\psi_l^i}{\mathrm{d}X} P_l^i \right) - 12 \frac{\mathrm{d}\psi_q^i}{\mathrm{d}X} B_q^i \right] \mathrm{d}x = 0, \quad k = 1,2,3; \quad i = 1,2,...N. \quad (4.56)$$

Note that the summation convention is being used over the subscripts. The superscript *lub* is used to denote the fact that these residuals arise from the lubrication equations. Integrating by parts leads to

$$\begin{aligned} R_k^{lub^i} = & \left[\psi_k^i \frac{\psi_j^{i^3} B_j^{i^3}}{\mu U_R} \frac{\mathrm{d}\psi_l^i}{\mathrm{d}X} P_l^i \right]_{X_1^i}^{X_3^i} - \int_{X_1^i}^{X_3^i} \frac{\mathrm{d}\psi_k^i}{\mathrm{d}X} \frac{\psi_j^{i^3} B_j^{i^3}}{\mu U_R} \frac{\mathrm{d}\psi_l^i}{\mathrm{d}X} P_l^i \mathrm{d}x \\ & - 12 \int_{X_1^i}^{X_3^i} \psi_k^i \frac{\mathrm{d}\psi_q^i}{\mathrm{d}X} B_q^i \mathrm{d}x = 0, \quad k = 1,2,3; \quad i = 1,2,...N. \end{aligned} \quad (4.57)$$

The term in square brackets is non-zero only when $k = 1$ or 3 and when the global equations are formed these terms cancel except in the case of the first and final global nodes which are dealt with later. Thus this term is now dropped and (4.57) can be written as

$$R_k^{lub^i} = A_{kl}^i P_l^i + C_k^i, \quad (4.58)$$

where A_{kl}^i and B_k^i are given by:

$$A_{kl}^i = -\int_{X_1^i}^{X_3^i} \frac{\mathrm{d}\psi_k^i}{\mathrm{d}X} \frac{\psi_j^{i^3} B_j^{i^3}}{\mu U_R} \frac{\mathrm{d}\psi_l^i}{\mathrm{d}X} \mathrm{d}x, \quad (4.59)$$

$$C_k^i = ,-12 \int_{X_1^i}^{X_3^i} \psi_k^i \frac{\mathrm{d}\psi_q^i}{\mathrm{d}X} B_q^i \mathrm{d}x. \quad (4.60)$$

These element residual equations are assimilated into a global set, denoted by $\mathbf{R}^{lub} = 0$, using the recursive technique outlined in the previous section. Thus the residual equations corresponding to Reynolds equation have been found.

4.3.2.1 Boundary Conditions

The boundary conditions now have to be included in the formulation. The condition $P(-\infty) = 0$ is imposed by simply setting $P_1 = 0$ in the global equations as well as removing the residual equation corresponding to the node X_1 as there is now one less nodal unknown to be found. As this condition is theoretically meant to be applied at $X = -\infty$, X_1 is chosen to be sufficiently large and negative so that any further increase in magnitude has a negligible effect on the numerical solution. The H^{∞} condition (4.17) is incorporated by using Reynolds equation to write the pressure gradient at the mensicus in terms of the outgoing film height:

$$\frac{B_D^3}{\mu U_R}\left.\frac{\mathrm{d}P}{\mathrm{d}X}\right|_{X_D} = B_D - 2H^{\infty} = B_D\left(1 - \frac{1.34Ca^{2/3}}{1+3.88Ca^{2/3}}\left(1+\frac{1}{2}B_X\right)\right) \tag{4.61}$$

which is equal to the term in square brackets in (4.57) for $R^{lub}_{\texttt{NUMNODES}}$ and so $R^{lub}_{\texttt{NUMNODES}}$ has an additional contribution of

$$B_{\texttt{NUMNODES}}\left(1 - \frac{1.34Ca^{2/3}}{1+3.88Ca^{2/3}}\left(1+\frac{1}{2}B_i^N\frac{\mathrm{d}\psi_i^N}{\mathrm{d}X}\right)\right). \tag{4.62}$$

The extra contribution to R_1^{lub} from the square bracket term in (4.57) is not included as it is assumed that X_1 is chosen to be sufficiently upstream so that the pressure gradient is negligible. Another equation has to be introduced so that X_D (=$X_{\texttt{NUMNODES}}$) can be solved for. This is simply the condition on the pressure jump at the meniscus (4.14) and is written as

$$R^{pd} = P_{\texttt{NUMNODES}} + \frac{2\gamma}{B_{\texttt{NUMNODES}}\left(1+\frac{1}{2}B_i^N\frac{\mathrm{d}\psi_i^N}{\mathrm{d}X} - 3.88Ca^{2/3}\right)} = 0, \tag{4.63}$$

where R^{pd} refers to the pressure drop residual. The fact that X_D is unknown implies that the solution domain itself is unknown at the outset. To overcome this problem all nodes are defined in terms of X_D as follows:

$$X_i = \frac{(i-1)(X_D - X_1)}{\texttt{NUMNODES}-1} + X_1, \qquad 1 \le i \le \texttt{NUMNODES}. \tag{4.64}$$

Thus X_D enters the definition of each residual through the limits of integration. Therefore, for the rigid roll problem, the final set of equations is

$$\mathbf{R}(\mathbf{u}) = \begin{pmatrix} \mathbf{R}^{lub}(\mathbf{u}) \\ R^{pd}(\mathbf{u}) \end{pmatrix} = \mathbf{0}, \tag{4.65}$$

where $\mathbf{u}$ denotes the vector of unknowns:

$$\mathbf{u} = (P_2, P_3, ..., P_{\texttt{NUMNODES}}, X_D). \tag{4.66}$$

4.3.2.2 Solution Method

The final set of equations was solved iteratively using Newton's method. Newton's method works by assuming that the present estimate of the solution, u^n say, is sufficently close to the correct solution, u^* say, such that the following first order Taylor expansion is valid:

$$0 = R(u^*) \approx R(u^n) + \left.\frac{\partial R}{\partial u}\right|_{u^n} \delta, \tag{4.67}$$

where $\delta = u^* - u^n$. Therefore, the next improvement on the present estimate is given by

$$u^{n+1} = u^n - \left[\left.\frac{\partial R}{\partial u}\right|_{u^n}\right]^{-1} R(u^n). \tag{4.68}$$

The scheme is said to be quadratic as this is the order of the first term that was neglected in the Taylor expansion and is the rate at which the error (δ) decreases.

4.3.2.3 Rigid Roll Results

A fully flooded upstream and downstream analytic solution was used to provide an initial guess for the Newton iteration and the numerical solution was then compared with the analytic solution of Reynolds equation with the pressure drop and outgoing film height conditions applied. Figure 4.8 shows both the analytic and computed solution for a particular set of parameters. The numerical results were produced with $N = 100$, giving NUMNODES $= 201$ and the maximum difference between the analytic and computed pressure profiles was found to be $< 0.05\%$. This degree of accuracy is easily sufficient for the needs of this work and the majority of the results in this chapter were produced using $N = 100$.

The results for rigid roll coating were reviewed in the introduction and so the form of the pressure curve in figure 4.8 is only briefly discussed now. As the nip ($X = 0$) is approached from $-\infty$, the gap width is narrowing and the pressure rises above ambient. After passing through the nip the pressure becomes sub-ambient as the gap widens and, due to the pressure drop across the meniscus, the flow field is terminated at a sub-ambient pressure where the pressure gradient is positive.

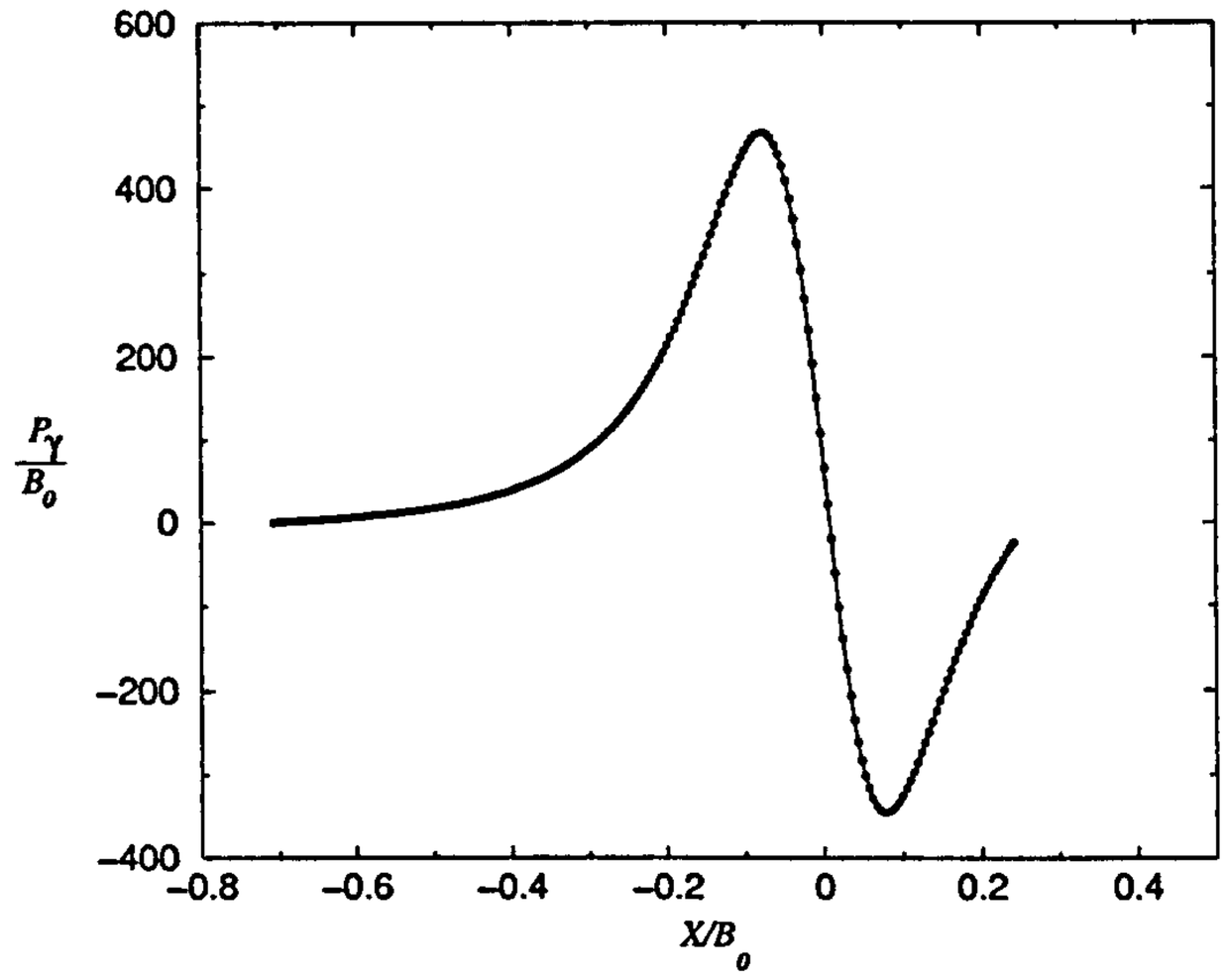

Figure 4.8: The pressure profile for a rigid roll coater calculated analytically (—) and computationally ($\cdots$). $Ca = 1$, $B_0/\bar{R} = 0.01$.

4.3.3 Application of F.E. method to deformable roll coating

When the lower roller is allowed to deform the gap thickness terms, B_k, are no longer equal to S_k but have a contribution from the unknown deformation, D_k. These extra unknowns can be solved for via the integral equation (4.32). The integrand of this equation can be written either in terms of the pressure (1.16) or in terms of the Fourier transform of the pressure (4.32) and the latter was chosen for this numerical scheme. Young (1997) used (1.16) but encountered numerical difficulties as the integrand is singular at $X' = X$ and it was hoped that this could be overcome by using the alternative formulation. For the rest of the thesis attention will be restricted to the industrially relevant case of $\nu = 0.5$.

The formulation will first be described for elastic layers ($T_\sigma = T_\epsilon = 0$) and then extended to viscoelastic layers.

Elastic layer formulation

The integral is evaluated by replacing $\tilde{P}$ in the integrand with the Fourier transform of the F.E. approximation. This then allows the deformation unknowns, D_k, to be written in terms of the pressure unknowns. Therefore, the first step is to calculate the

Fourier transform of the pressure approximation:

$$\tilde{P}(\omega) \approx \frac{L^2}{\omega^2} \sum_{e=1}^{N} \Bigg\{ 2a_{e_2} \left[X_3^e e^{-i\omega X_3^e/L} - X_1^e e^{-i\omega X_1^e/L} + \frac{L}{i\omega} e^{-i\omega X_3^e/L} - \frac{L}{i\omega} e^{-i\omega X_1^e/L} \right] + a_{e_1} \left[e^{-i\omega X_3^e/L} - e^{-i\omega X_1^e/L} \right] \Bigg\} - \frac{L}{i\omega} e^{-i\omega X_D/L} P(X_D), \tag{4.69}$$

where it has been assumed that $P(X) = 0$ for $X \leq X_1$. The final term in (4.69) arises from the fact that there is a discontinuity in P at X_D due to the pressure jump condition and for $X > X_D$, $P(X) = 0$. The transformed pressure approximation can be substituted into (4.32) to give

$$D(X) = \frac{2(1-\nu^2)}{\pi E} \{ L^2 \sum_{e=1}^{N} (2a_{e_2} [X_3^e C(\frac{X - X_3^e}{L}) - X_1^e C(\frac{X - X_1^e}{L}) + LS(\frac{X - X_3^e}{L}) - LS(\frac{X - X_1^e}{L})] a_{e_1} [C(\frac{X - X_3^e}{L}) - C(\frac{X - X_1^e}{L})]) - LP(X_D) N(\frac{X - X_D}{L}) \}, \tag{4.70}$$

where

$$C\left(\frac{X}{L}\right) = \int_0^\infty \frac{\sinh 2\omega - 2\omega}{2\omega^3(\omega^2 + \cosh^2 \omega)} \cos\left(\frac{\omega X}{L}\right) \mathrm{d}\omega, \tag{4.71}$$

$$S\left(\frac{X}{L}\right) = \int_0^\infty \frac{\sinh 2\omega - 2\omega}{2\omega^4(\omega^2 + \cosh^2 \omega)} \sin\left(\frac{\omega X}{L}\right) \mathrm{d}\omega, \tag{4.72}$$

$$N\left(\frac{X}{L}\right) = \int_0^\infty \frac{\sinh 2\omega - 2\omega}{2\omega^2(\omega^2 + \cosh^2 \omega)} \sin\left(\frac{\omega X}{L}\right) \mathrm{d}\omega. \tag{4.73}$$

In the above ν has been set to 0.5. Note that these integrands are finite at the origin and thus all problems due to singular integrands encountered by Young, who used the alternative form of integral equation (1.16), have been removed. Before the simulations were performed, S, C and N were evaluated over a wide of range of X/L. The results were stored in a file that could be read whenever required during the simulation. If the value of S, C or N was not stored at the value of X/L required the value was interpolated from nearby values that had been calculated. The advantage of this process is that the computationally expensive evaluations of the integrals that define S, C and N only had to be done once, before any simulations were done.

In (4.70) D depends on the pressure unknowns via the a_{e_i}'s which are given by (4.53) - (4.55), and this dependency can be made explicit by substituting for the a_{e_i}'s

to give

$$R_i^{def} = D_i - \sum_{e=1}^{N} \frac{1}{\lambda_e^2}\Big\{\big(2k_{e_2} - (3\lambda_e + 4X_1^e)k_{e_1}\big)P_1^e + \big(-4k_{e_2} + \big(4\lambda_e + 8X_1^e\big)k_{e_1}\big)P_2^2 + \big(2k_{e_2} - (\lambda_e + 4X_1^e)k_{e_1}\big)P_3^3\Big\} - \frac{3}{2\pi E}LP(X_D)N(\frac{X - X_D}{L}), \quad 1 \le i \le \texttt{NUMNODES} \tag{4.74}$$

where

$$\lambda_e = X_3^e - X_1^e, \tag{4.75}$$

$$k_{e_1} = \frac{3L^2}{2\pi E}\left(C(\frac{X_i - X_3^e}{L}) - C(\frac{X_i - X_1^e}{L})\right), \tag{4.76}$$

$$k_{e_2} = \frac{3L^2}{2\pi E}\Big(X_3^e C(\frac{X_i - X_3^e}{L}) - X_1^e C(\frac{X_i - X_1^e}{L}) + LS(\frac{X_i - X_3^e}{L}) - LS(\frac{X_i - X_1^e}{L})\Big), \tag{4.77}$$

and R_i^{def} are the residuals relating to the deformation integral equation. If the P_{e_i}'s are written in terms of global unknowns then (4.74) represents a linear relationship between the deformation and pressure nodal unknowns and can be written in the form

$$R_i^{def} = D_i - K_{ij}P_j \qquad 1 \le i, j \le \texttt{NUMNODES}. \tag{4.78}$$

The entries of the square matrix K_{ij} are found from (4.74). The full set of equations to be solved for the elastic layer problem is

$$\boldsymbol{R}(\boldsymbol{u}) = \begin{pmatrix} \boldsymbol{R}^{lub}(\boldsymbol{u}) \\ \boldsymbol{R}^{def}(\boldsymbol{u}) \\ R^{pd}(\boldsymbol{u}) \end{pmatrix} = \boldsymbol{0}, \tag{4.79}$$

where the unknowns to be solved for are

$$\boldsymbol{u} = (P_2, P_3, ..., P_N, D_1, D_2, ..., D_N, X_D). \tag{4.80}$$

The numerical method was verified by using Newton's method to solve (4.79) comparing results with those obtained by Young (1997). Young used the same model for the compliant layer and also used lubrication equations for the fluid model but terminated the flow domain with a variety of boundary conditions. For the sake of comparison $Ca = 1$ was chosen and for this value Young used the PH conditions (1.8) and these conditions were incorporated here by changing (4.61) appropriately. Young also neglected the correction to R_D used in (4.63) and so this was also changed temporarily

for the purposes of this comparison. Results were compared for $E_S = 10^{-5}$, $L/\bar{R} = 0.1$ and $Ca = 1$ for several values of $B_0/\bar{R}$ in the range $-0.01 \leq B_0/\bar{R} \leq 0.01$ and for $N = 100$ and the difference in predictions was <0.5%.

An analytic solution to the equivalent rigid roll problem was used as an initial guess for the iterative scheme in the positive gap regime. Results in the negative gap regime were achieved by parameter continuation in B_0. It is for this reason that the governing equations have been kept in dimensional form since if B_0 appeared in the non-dimensional scheme great difficulties would arise as B_0 passed through zero from positive to negative gap regimes.

The above method is now extended to include the viscoelastic terms.

Extension to viscoelastic layer

For the viscoelastic layer there is an additional contribution to the integrand of the deformation integral equation (4.32) proportional to

$$T_\sigma U_R \widetilde{\frac{\mathrm{d}P}{\mathrm{d}X}}. \tag{4.81}$$

The Fourier transform of the pressure gradient is

$$\int_{-\infty}^{\infty} \frac{\mathrm{d}P}{\mathrm{d}X} e^{-i\omega X/L} \mathrm{d}X = P(X_D) e^{-i\omega X_D/L} + \frac{i\omega}{L} \tilde{P}(\omega). \tag{4.82}$$

When $\tilde{P}$ was calculated for the elastic case there was a contribution due to the pressure jump of $-LP(X_D)e^{-i\omega X_D/L}/i\omega$. In the case of the pressure gradient, this term will cancel with the first term on the right hand side of (4.82) and so the transformed pressure gradient is proportional to $\tilde{P}$ minus this final term, the constant of proportionality being $i\omega/L$. This simple relationship in conjunction with the relationship between the integrands of S, C and N means that the viscoelastic effect can be incorporated by replacing C with $C + T_\sigma U_R N/L$, S with $S - T_\sigma U_R C/L$ and D_i with D_i^* in (4.74). This results in a relationship between the P_i and an intermediate set of nodal unknowns, D_i^*, that describe D^*. D^* is approximated by a quadratic within each element in a similar fashion to the D and P approximations. The relationship can be written in the form

$$\begin{aligned} D_i^* &= K_{ij}^* P_j \qquad i = -(2M+1), -(2M+1)+1, ..., -3, -2, 1, 2, ..., 2N+1, \\ &\qquad\qquad j = 1, 2, ...N. \end{aligned} \tag{4.83}$$

which is analogous to (4.78). The lower range for i in (4.83) is due to the solution domain being extended for $X < X_1$ to capture the stress/strain history of the compliant layer. An additional M elements were added to the solution domain. These additional nodes are labelled:

$$X_1^{-M} < X_2^{-M} < X_3^{-M} = X_1^{-(M-1)} < X_2^{-(M-1)} < X_3^{-(M-1)} < \ldots \\ \ldots < X_1^{-1} X_2^{-1} < X_3^{-1} = X_1^1., \tag{4.84}$$

and the global numbering system is

$$X_{-(2M+1)} < X_{-(2M+1)+1} < .... < X_{-3} < X_{-2} < X_1. \tag{4.85}$$

The numbering of the D_i^* follows the same convention and elements 1 to N are numbered as before. As D^* is approximated by a quadratic within each element, it is possible to write

$$D^*(X) \approx b_{e_0} + b_{e_1} X + b_{e_2} X^2, \qquad X \in [X_1^e, X_3^e], \tag{4.86}$$

where the b_{e_i}'s are analogous to the a_{e_i}'s defined by (4.53) - (4.55) the only difference being that the P_i's are replaced by D_i^*'s. Substituting (4.86) into (4.35) eventually leads to

$$D(X_i) = D_i = D_i^* + T_\epsilon U_R \sum_{e=-M}^{n} [\frac{e^{(X_1^e - X_i)/T_\epsilon U_R}}{\lambda_e^2} \{ [4m_e - (3\lambda_e + 4X_1^e) n_e] D_{e_1}^* + \\ [-8m_e + (4\lambda_e + 8X_1^e) n_e] D_{e_2}^* + [4m_e - (\lambda_e + 4X_1^e) n_e] D_{e_3}^* \}], \tag{4.87}$$

where

$$m_e = e^{\lambda_e / T_\epsilon U_R} (T_\epsilon U_R - X_2^e) - (T_\epsilon U_R - X_1^e), \tag{4.88}$$

$$n_e = 1 - e^{\lambda_e / T_\epsilon U_R}. \tag{4.89}$$

This expression is for when X_i corresponds to an endpoint of an element, say X_3^n. If X_i corresponds to a midpoint X_2^n say, then X_3^n in the final term of the sum in (4.87) should be replaced by X_2^n - including in the definition of λ_e. (4.87) represents a linear relationship between the D_i^*'s and the D_i's and can thus be written in the form

$$D_i = G_{ij} D_j^*, \qquad j = -(2M+1), -(2M+1)+1, ..., -3, -2, 1, 2, ..., 2N+1, \\ i = 1, 2, ...N, \tag{4.90}$$

where the G_{ij} can be found from (4.87). (4.83) then gives

$$D_i = G_{ij} K_{jk}^* P_k. \tag{4.91}$$

The residual equations relating to the deformation integral equation can be redefined to take into account the viscoelastic terms

$$R_i^{def} = D_i - G_{ij}K_{jk}P_k. \tag{4.92}$$

Using this definition of R^{def} the effect of viscoelastic terms can be implemented. As a check on this scheme the behaviour of the solutions as T_ϵ and $T_\sigma \to 0$ were studied and it was found that the elastic case was recovered in this limit as expected.

4.4 Equilibrium flow

4.4.1 Elastic compliant layer

The equilibrium flow analysis in the following section is based on the above model which incorporates (i) the lubrication approximation for a thin film, (ii) extended LL conditions valid over a wide range of Ca, (iii) the FSM deformation model for an incompressible layer ($\nu = 0.5$) and (iv) no viscoelastic effects, i.e. $T_\sigma = T_\epsilon = 0$. The viscoelastic effects are examined in section 4.5.

Results are presented from two different perspectives: that of *fixed-gap* operation and *fixed-load* operation, which are favoured by academic researchers and industrial operators, respectively. For fixed-gaps the distinction is made between positive and negative gap operation, whereas for fixed-loads, the distinction is made between lightly-loaded, and heavily loaded regimes of EHL and in each case the aim is to explore the effects due to layer thickness and elasticity.

It is possible to gain insight into the expected behaviour of the roller pair through a simple dimensional analysis. In the positive gap/lightly loaded regime the pressure is assumed to be dominated by viscous forces giving:

$$P \sim \frac{\mu U_R}{B_0}\left(\frac{\bar{R}}{B_0}\right)^{1/2}, \tag{4.93}$$

whereas in the negative gap/highly loaded regime the deformation scales with the extent of the interference:

$$D \sim B_0, \tag{4.94}$$

and in both the positive and negative gap regimes the strain in the compliant layer is balanced with the stress:

$$\frac{D}{L} \sim \frac{P}{E}. \tag{4.95}$$

Thus in each regime either the scale for D or P is given and the stress-strain balance provides the remaining scale. This last balance suggests that L and E^{-1} may have the same effect. A scale for the dimensional flux, Q, in the negative gap/highly loaded regime can be obtained by assuming that through the contact region the film thickness, H, is almost constant and therefore balancing the pressure gradient and the viscous stress gives:

$$Q \sim UB \sim UR\left(\frac{\mu U_R}{E\bar{R}}\right)^{1/2}\left(\frac{L}{\bar{R}}\right)^{1/2}\left(\frac{\bar{R}}{B_0}\right)^{1/4}. \tag{4.96}$$

Thus it appears that L and E^{-1}, or equivalently E_S where it is assumed that μU_R is constant, may have similar effects on the flux in this regime. The physical basis for the apparent similarity between E_S and L via (4.95) is straightforward; it is simply that to make a given indentation requires a higher load if the compliant layer is made harder (increasing E) or shallower (decreasing L). This argument suggests that the spring models could be correct and this is tested in the following investigation by determining the effect of L and E_S on the physical variables P, D, Q and X_D. Results are presented in a non-dimensional form making use of the following variables:

$$\lambda = \frac{H^{\infty}}{\bar{R}} = \frac{Q}{2U_R\bar{R}}, \qquad x_d = \frac{X_D}{\bar{R}}, \qquad f = \frac{W}{\mu U_R}. \tag{4.97}$$

Note that this nondimensional scheme is different to that employed in chapters 2 and 3.

4.4.2 Fixed gap operation

4.4.2.1 The positive gap regime

Varying the layer properties (layer thickness and elasticity) affects deformations to the compliant layer and consequently λ and x_d. Intuitively we would expect elastic deformations to increase by using either a softer layer of material or a thicker layer of the same. Figure 4.9 confirms that, for positive gaps, deformations do increase with increasing L and with increasing E_S (decreasing E). Figures 4.10 and 4.12 show that the behaviour of λ and x_d at large $B_0/\bar{R}$ is similar to that for rigid rolls, with both decreasing as $B_0/\bar{R}$ is reduced. Furthermore, for a constant gap $B_0/\bar{R}$, both λ and x_d are seen to increase with E_S and with L. Hence we may conclude that, throughout the positive gap regime, E_S and L have the same effect on layer deformation and on the system variables λ and x_d.

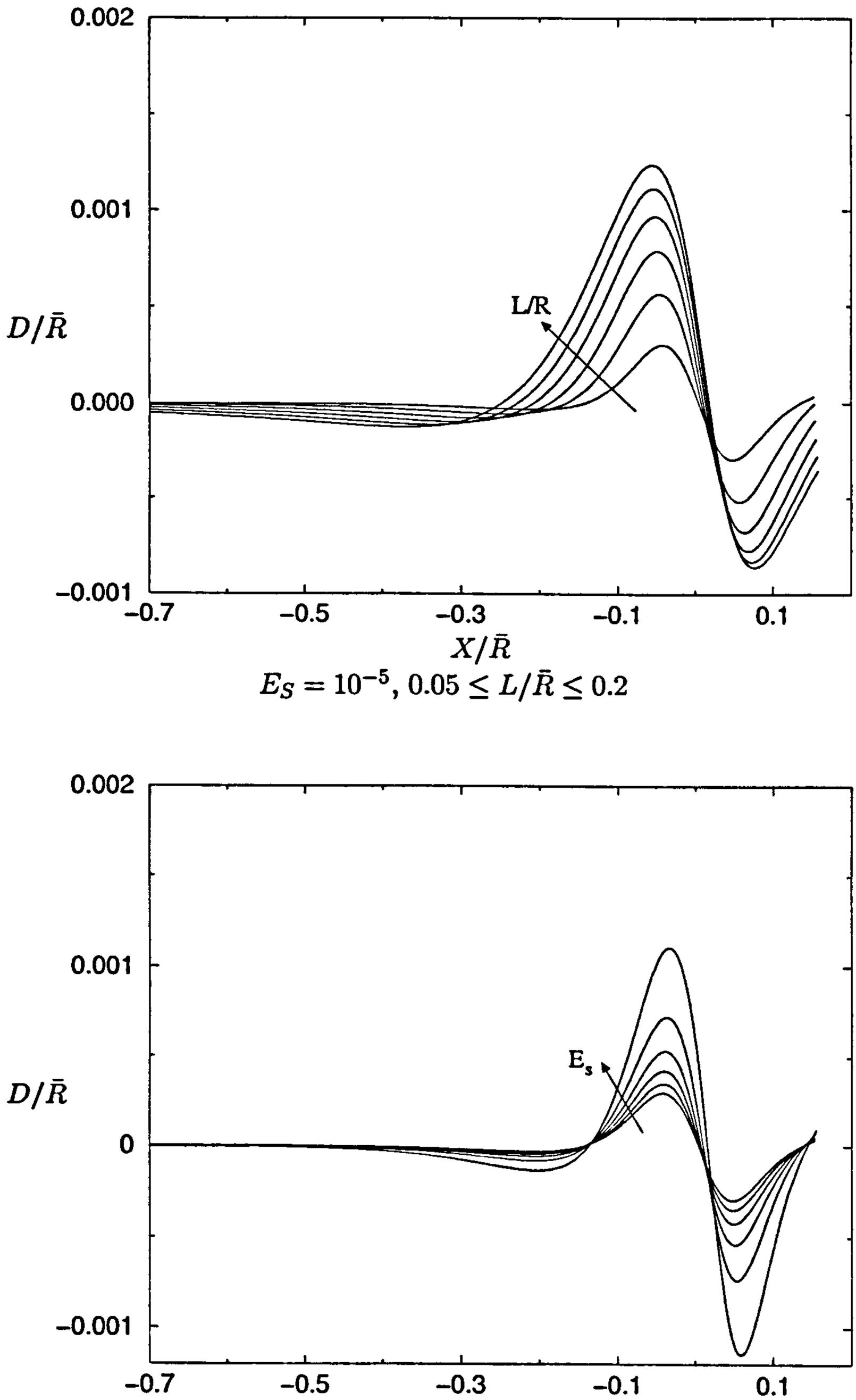

Figure 4.9: Deformation profiles. $B_0/\bar{R} = 4 \times 10^{-3}$, $Ca = 1$.

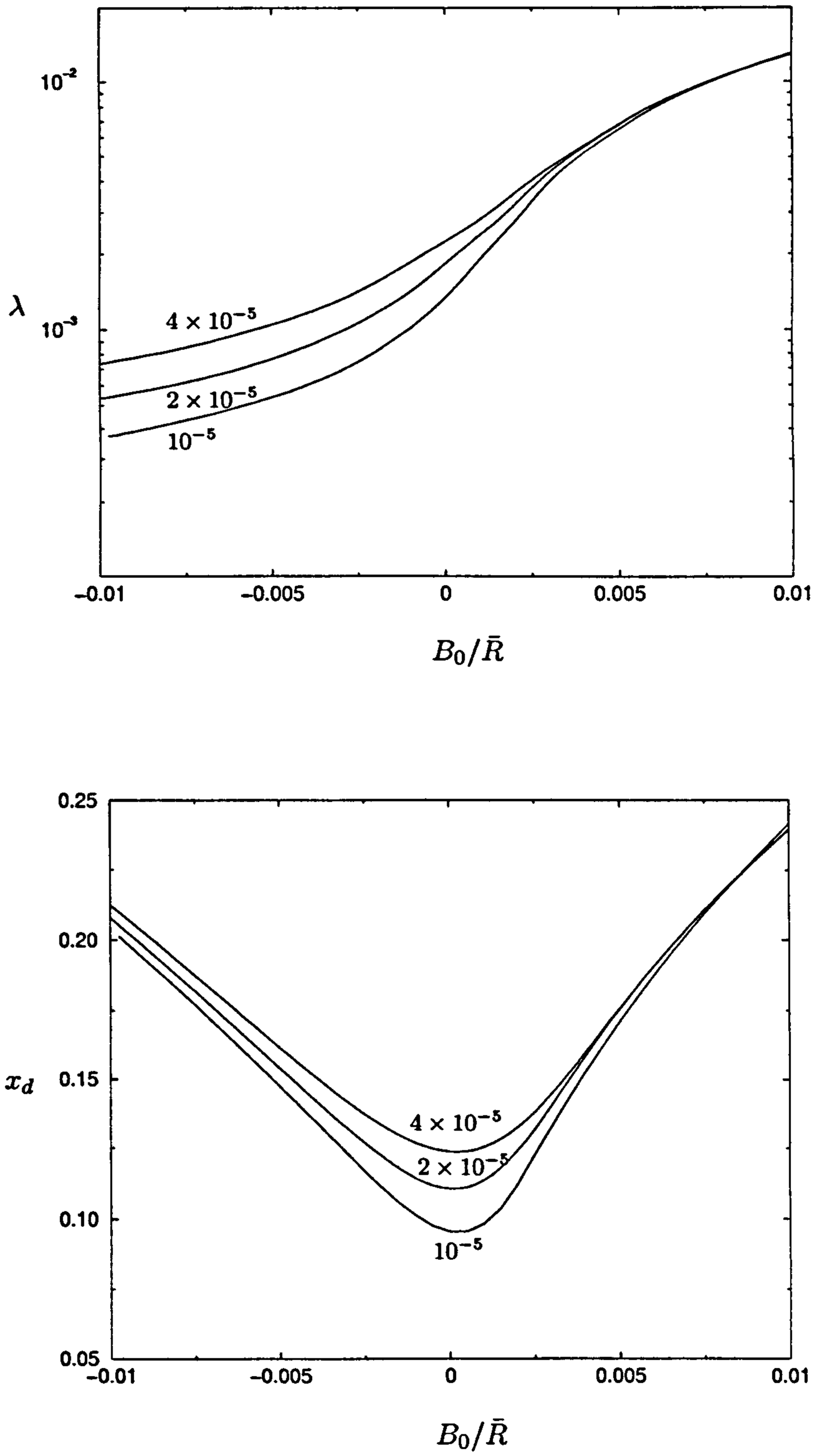

Figure 4.10: The variation of λ and x_d with $B_0/\bar{R}$ for the FSM deformation model with $L/\bar{R} = 0.05$ fixed and $E_S = 4 \times 10^{-5}, 2 \times 10^{-5}$, and 10^{-5}, $Ca = 1$.

4.4.2.2 The negative gap regime

In the contact region, the rigid roll acts as an indentor, the degree of indentation is of $O(B_0)$ and both layer thickness, L, and E_S have little effect on the elastic deformations within the contact region. They do, however, significantly affect the pressure where the profile remains similar and close to the dry contact case. Figure 4.11 confirms that the pressure maximum decreases with both L and E_S as suggested via relation (4.95).

In addition figures 4.10 and 4.12 show that E_S and L have the same effect on flow rate as is the case for positive gaps. Therefore, E_S and L have had a similar effect on the field variables in all cases investigated so far and the argument for the use of a spring model appears to be strong. It is worth noting at this point that when Carvalho and Scriven (1997b) compared results of a plane strain model and a spring model in the negative gap regime, they had a flooded downstream region and so only considered flow rate results and neglected to look at the effect on x_d which is now considered.

The overall effects of E_S and $L/\bar{R}$ on x_d are clearly different. Figure 4.10 shows that, for a given $L/\bar{R}$, x_d increases with E_S whereas figure 4.12 indicates that, for a given E_S, x_d increases with $L/\bar{R}$ for "small negative gaps" and decreases with $L/\bar{R}$ for "large negative gaps". Thus these results could not be reproduced by a model in which the solid is parameterised by a single constant, proportional to E/L. Therefore the conclusion to be drawn is that all sring models, no matter what the calibration, are invalid.

The differing effects of E_S and $L/\bar{R}$ on x_d cannot be explained on the basis of earlier scaling arguments, rather it is necessary to examine "layer swelling" at the edge of the contact region. The reader will note that it is essential to predict x_d accurately in order to subsequently analyse the stability of the liquid film and the meniscus.

4.4.2.3 Layer Swelling at the Edge of the Contact Region

For negative gaps figures 4.10 and 4.12 reveal the different effects of elasticity E_S and layer thickness $L/\bar{R}$ on x_d. In the former case x_d increases with E_S whereas in the latter x_d may move either towards or away from the nip as $L/\bar{R}$ increases depending on the magnitude of $B_0/\bar{R}$. This behaviour is more clearly illustrated by selecting particular values of $B_0/\bar{R}$ ($B_0/\bar{R} = -2.0 \times 10^{-3}$, -5×10^{-3} and -7.5×10^{-3}) and plotting the variation of X_D with E_S ($L/\bar{R}$ fixed) and with $L/\bar{R}$ (E_S fixed). Figure

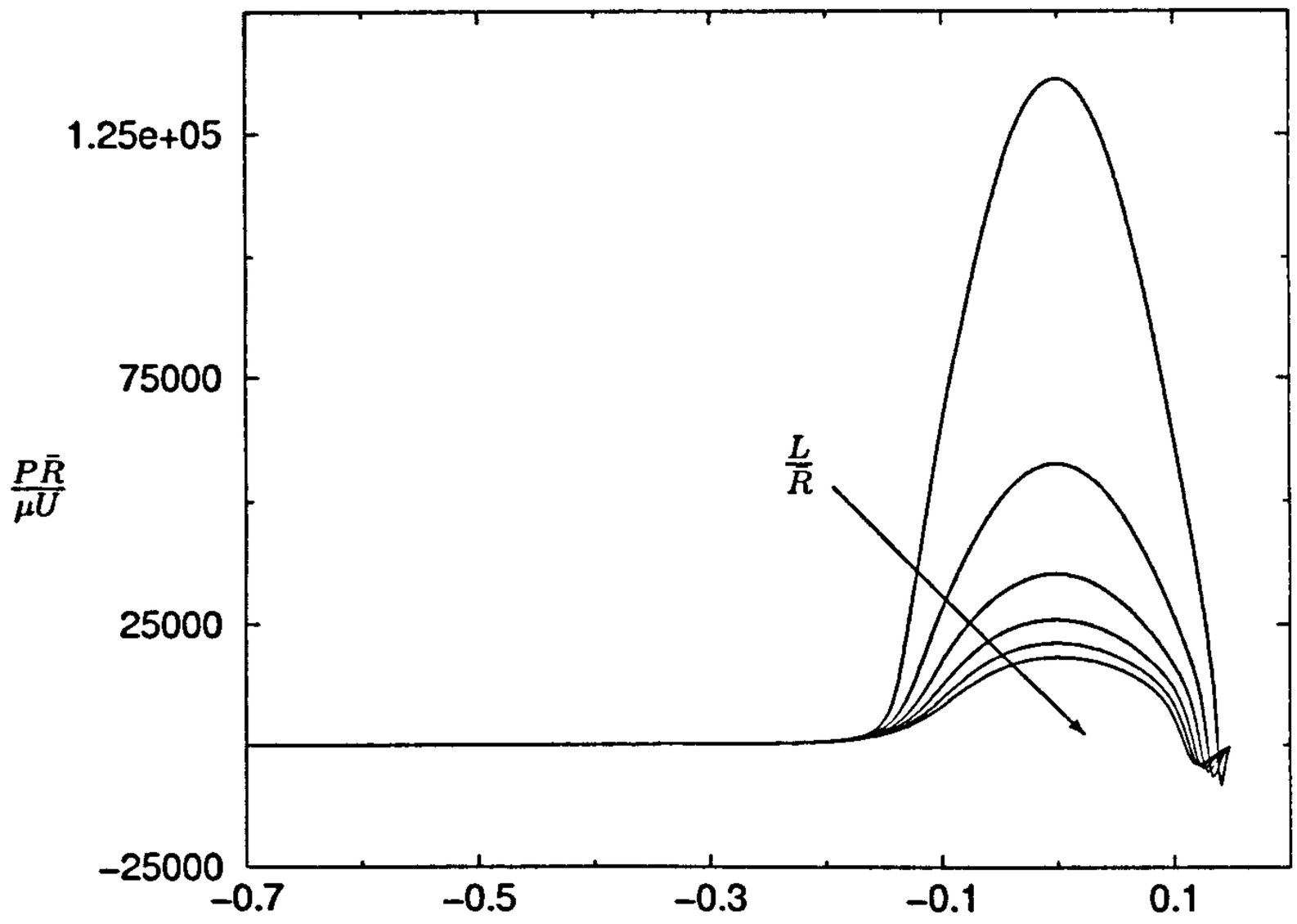

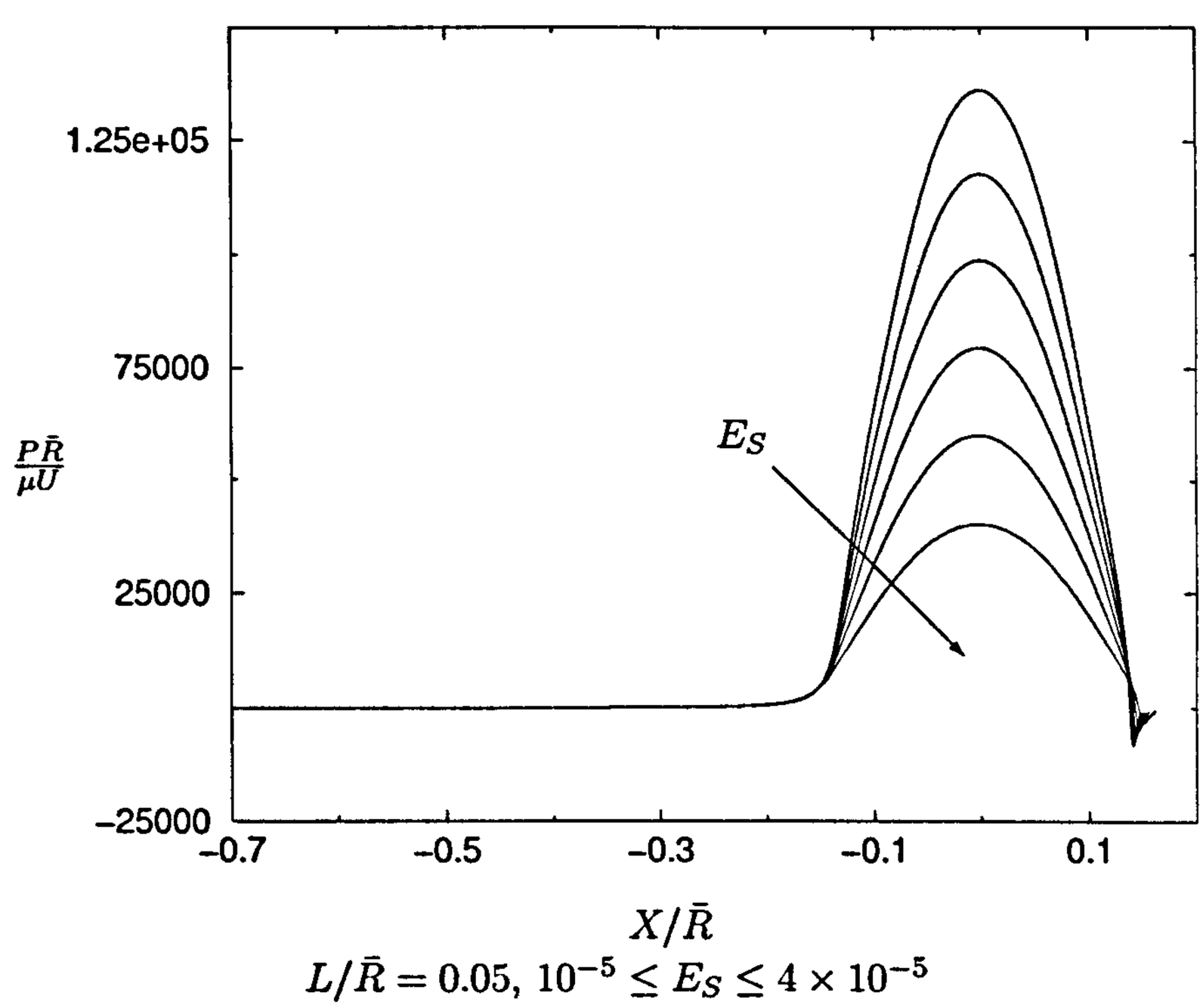

Figure 4.11: Pressure profiles. $B_0/\bar{R} = -7.5 \times 10^{-3}$, $Ca = 1$.

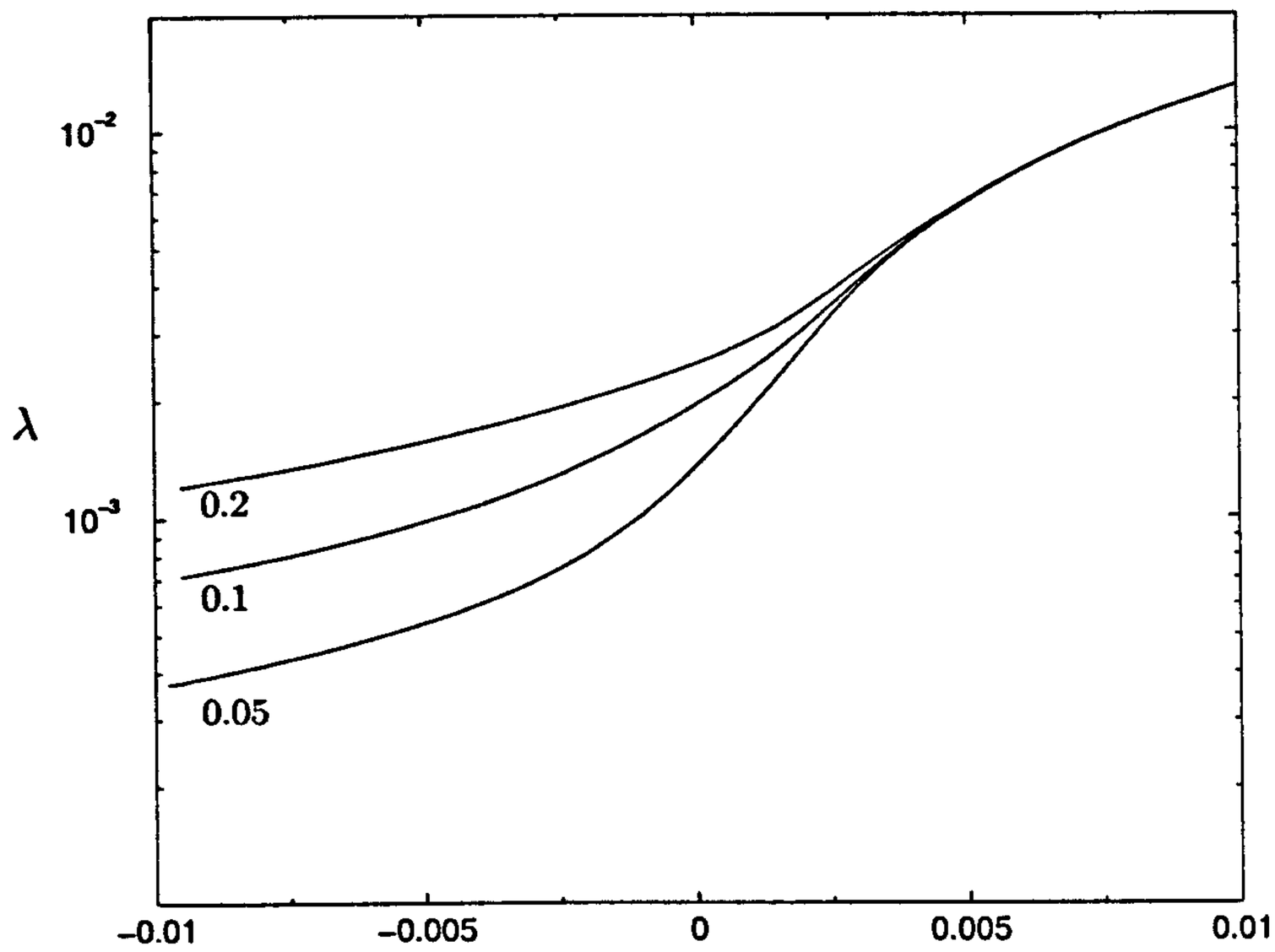

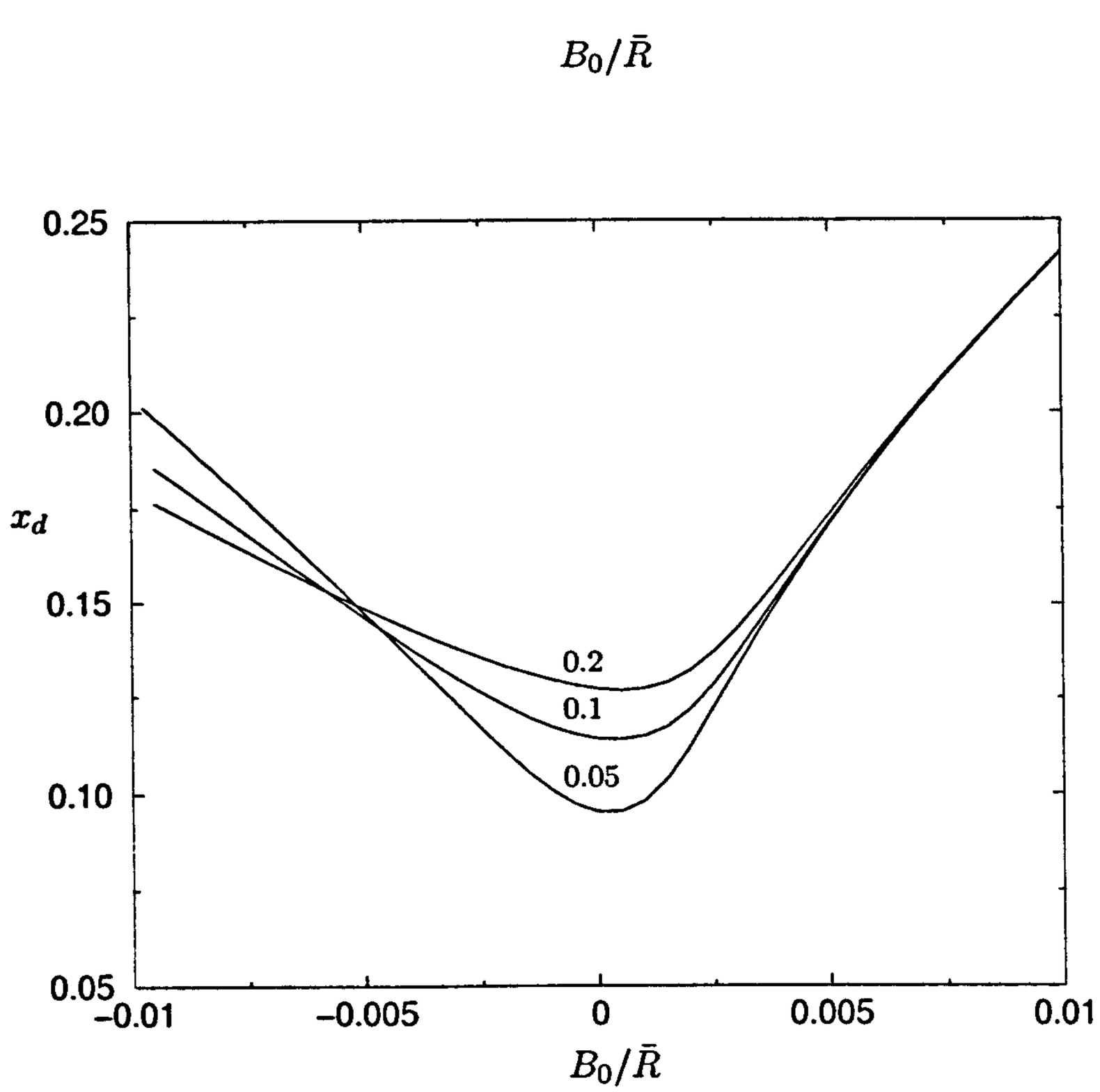

Figure 4.12: The variation of λ and x_d with $B_0/\bar{R}$ for the FSM deformation model with $E_S = 10^{-5}$ fixed and $L/\bar{R} = 0.05$, 0.1 and 0.2, $Ca = 1$.

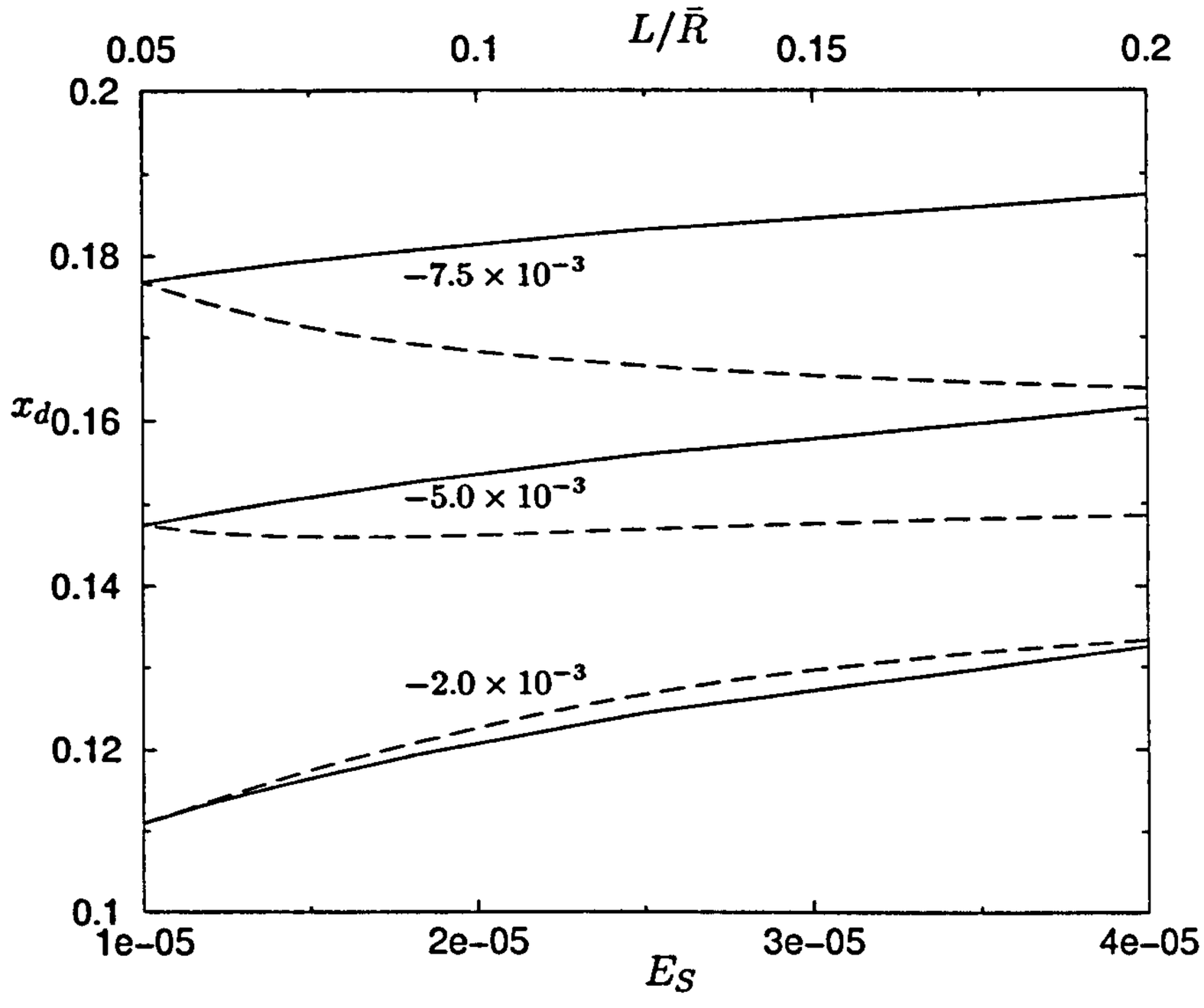

Figure 4.13: Variation of meniscus position with both E_S $(L/\bar{R} = 0.1)$(—) and with $L/\bar{R}$ $(E_S = 10^{-5})$(- - -) for three values of $B_0/\bar{R}$. $B_0/\bar{R} = -2.0 \times 10^{-3}$, -5.0×10^{-3} and -7.5×10^{-3}, $Ca = 1$.

4.13 shows x_d increasing with E_S in each case whereas it has x_d increasing with $L/\bar{R}$, for $B_0/\bar{R} = -2.0 \times 10^{-3}$, decreasing with $L/\bar{R}$, for $B_0/\bar{R} = -7.5 \times 10^{-3}$, and remaining almost constant for $B_0/\bar{R} = -5.0 \times 10^{-3}$.

The key to explaining the different effects of E_S and $L/\bar{R}$ on x_d is to first consider their effect on $D(X_D)/\bar{R}$, that is on layer swelling at the edge of the contact region. Figure 4.14 reveals that, for each of the three values of $B_0/\bar{R}$, $D(X_D)/\bar{R}$ has little variation with E_S. However, for the same three values of $B_0/\bar{R}$, $D(X_D)/\bar{R}$ increases with L/R. Hence L/R has significantly more effect on layer swelling than does E_S.

The behaviour of x_d in figure 4.13 can now be explained by referring to two expressions for the gap thickness at x_d,

$$B(X_D) = 2B_0 + D(X_D) + \frac{X_D^2}{\bar{R}}, \tag{4.98}$$

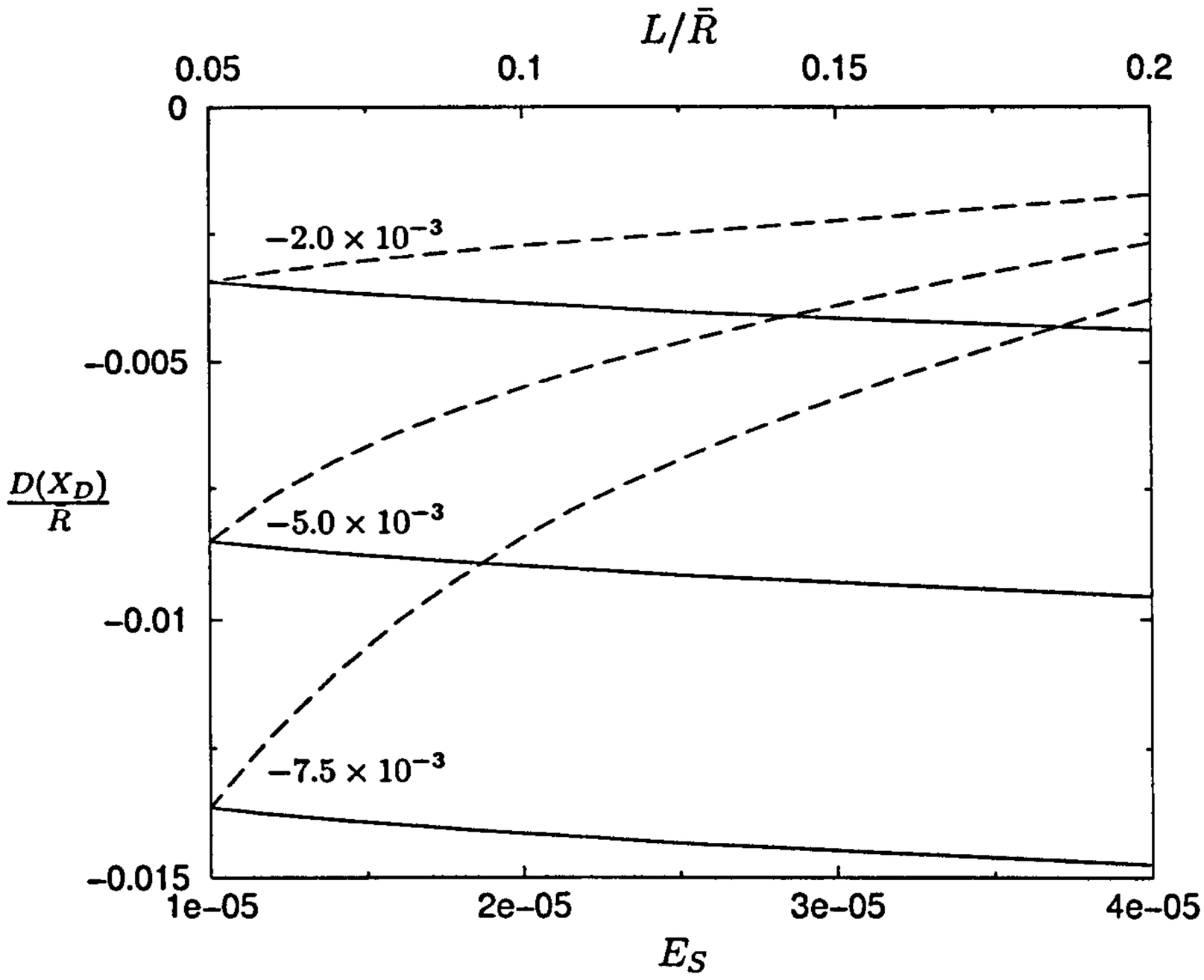

Figure 4.14: Variation of layer deformation at the meniscus with both E_S ($L/\bar{R} = 0.1$)(—) and with $L/\bar{R}$ ($E_S = 10^{-5}$)(- - -) for three values of $B_0/\bar{R}$. $B_0/\bar{R} = -2.0\times10^{-3}$, -5.0×10^{-3} and -7.5×10^{-3}, $Ca = 1$.

and

$$B(X_D) = \Theta H^{\infty}, \qquad \Theta = \frac{1.34 Ca^{2/3}}{1 + 3.88 Ca^{2/3}}. \tag{4.99}$$

Note (4.99) represents the leading order relationship with terms due to the non-constant gap width neglected. For negative gaps with Θ =constant and B_0 =constant, if E_S or $L/\bar{R}$ are increased then flow rate, H^{∞}, increases (figures 4.12 and 4.10) as does $B(X_D)$ via (4.99). In particular:

(i) If E_S increases, $D(X_D)$ remains effectively constant — see figure 4.14 and so via (4.98) it follows that X_D must increase — see figure 4.13.

(ii) If $L/\bar{R}$ increases, $D(X_D)/\bar{R}$ increases (becomes less negative) and it is precisely this behaviour of $D(X_D)/\bar{R}$ that determines the behaviour of X_D:

  (a) when $B_0/\bar{R} = -2 \times 10^{-3}$ the increase in $D(X_D)/\bar{R}$ is relatively small and so X_D must increase to ensure that $B(X_D)$ increases in accordance with (4.99);

  (b) when $B_0/\bar{R} = -7.5 \times 10^{-3}$ the increase in $D(X_D)/\bar{R}$ is relatively large; in fact "too large" so that X_D must decrease for $B(X_D)$ to increase in accordance with (4.99);

  (c) when $B_0/\bar{R} = -5 \times 10^{-3}$ the increase in $D(X_D)/\bar{R}$ appears to be just sufficient for $B(X_D)$ to increase in accordance with (4.99) and as a consequence X_D remains almost constant.

Therefore layer swelling plays an integral role in determining the meniscus location and as spring models do not preserve volume they cannot predict layer swelling and hence will fail to accurately predict X_D.

4.4.2.4 The effect of *Ca*

For rigid roll coaters with flooded inlets operating in the range $Ca > 1$, x_d and λ are virtually independent of Ca - see figures (4.3) and (4.4). The same is true in deformable roll coating for large positive gaps yet as $B_0/\bar{R}$ is decreased and eventually becomes negative the behaviour depends upon the manner in which Ca is varied, that is whether the viscosity, speed or surface tension is varied. In this range of negative gaps the layer plays a significant role and the scaling for the flux is given by (4.96). Indeed the flux is determined by the gap width in the contact region which in turn is governed by the

balance of viscous and dry contact pressures. Hence both μ and U_R affect the coating thickness and (4.99) forces X_D to alter accordingly. On the other hand changing Ca by varying surface tension T only affects the pressure condition at the meniscus, (4.14), which has a minor effect on both λ and x_d.

4.4.3 Fixed load operation

Flow rate and meniscus location

Graphs of λ and x_d against f are shown in figures 4.15 and 4.16 for fixed $L/\bar{R}$ and E_S respectively. The graphs extend from the rigid load limit (small loads) to the dry contact limit (high loads).

Close observation of figures 4.15 and 4.16 reveals that E^{-1} and L have the same effect when λ and x_d are plotted against f. This is in sharp contrast to the case of fixed gap when subtle differences due to the effect of E_S and L on layer swelling become apparent. At first these results appear to counteract the fixed gap results and support the spring model argument. However, this is not so as B_0 is a function of the applied load and E_S and L_R do not necessarily have the same effect on it.

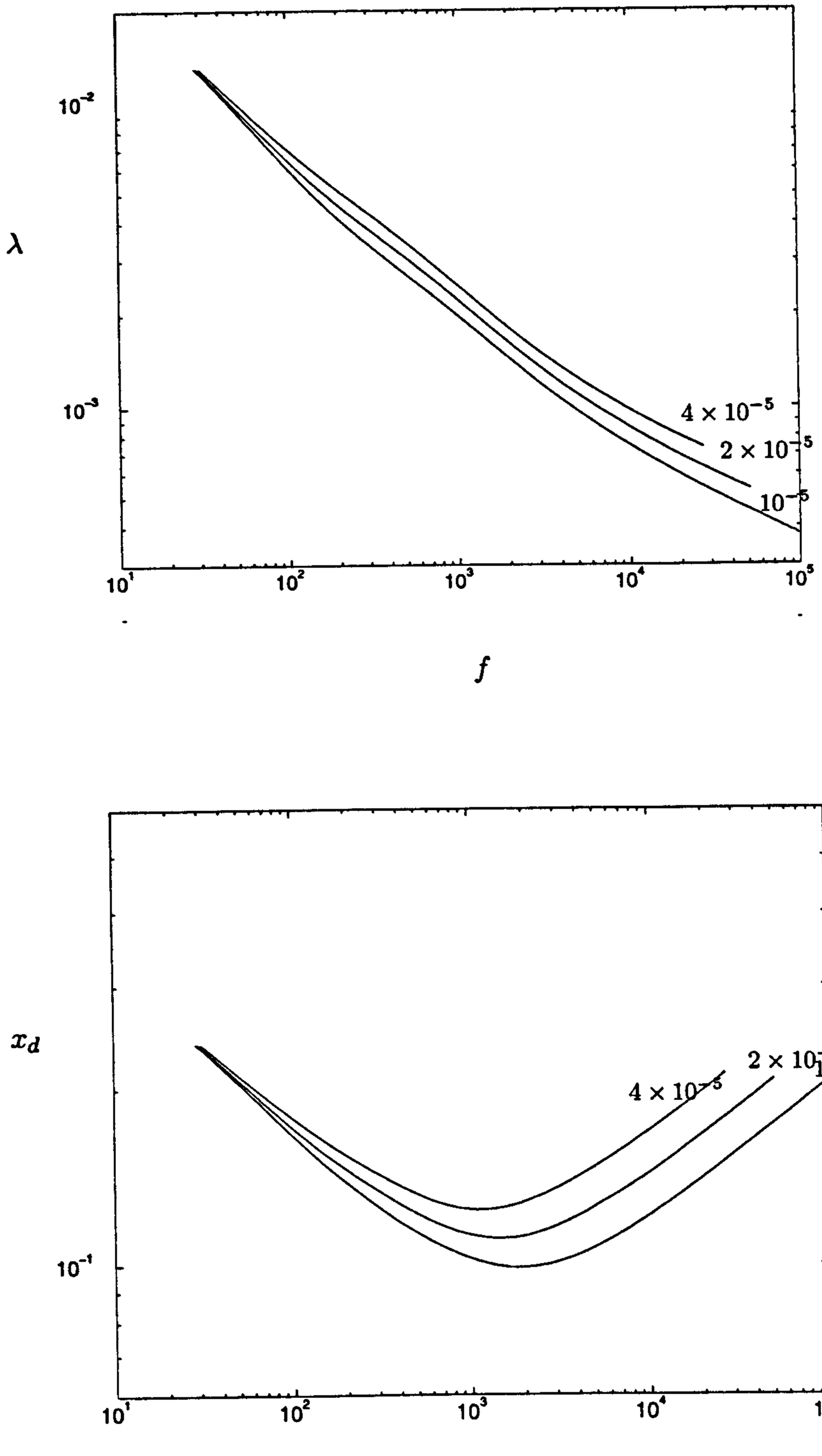

Figure 4.15: The variation of λ and x_d with f for the FSM deformation model. $L/\bar{R} = 0.1$, $E_S = 4 \times 10^{-5}, 2 \times 10^{-5}$, and 10^{-5}, $Ca = 1$.

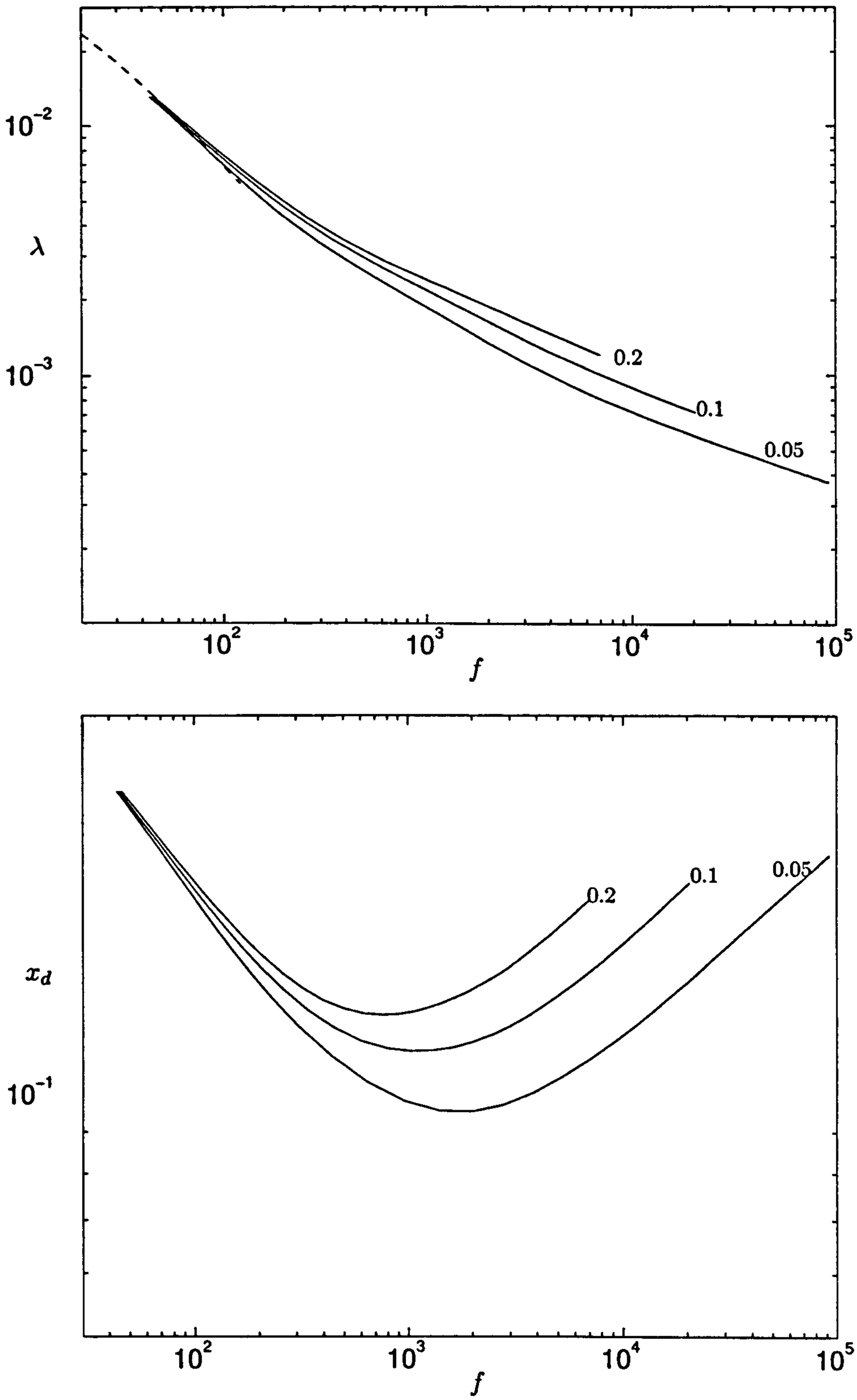

Figure 4.16: The variation of λ and x_d with f for the FSM deformation model. $L/\bar{R} = 0.05, 0.1$ and 0.2, $E_S = 10^{-5}$, $Ca = 1$.

4.5 Viscoelastic effects

Figures 4.17a, 4.17b and 4.17c show the deformation, pressure and gap thickness profiles for several values of T_ϵ with $T_\sigma = 0$. As $T_\epsilon \to 0$ the elastic profiles are recovered as expected. As T_ϵ is increased the magnitude of the deformation maximum decreases but the location of the maximum is unaffected. The deformation maximum is reduced due to the strain retardation but the location of the maximum is unaffected due to the fixed shape of the indenting roll that dominates the form of the deformation profile. Figure 4.17b shows that the pressure maximum moves upstream as T_ϵ is increased. The reason for this that the strain in the compliant layer takes a finite amount of time to react to an applied load, thus the large pressure must occur upstream of the deformation maximum that it gives rise to. As the deformation maxiumum is reduced when T_ϵ is increased, the gap thickness, shown in figure 4.17c, is reduced. (4.96) implies that this reduction in gap width would decrease the flux and this is confirmed by figure 4.19a. The figure also shows for $De < 10^{-2}$, the strain retardation has little effect. Figure 4.19b shows that increasing De beyond 10^{-2} causes the meniscus position to move upstream.

Unfortunately, insufficient information concerning the thickness and compressibility of the deformable layer generally precludes any comprehensive comparison between theoretical predictions and available experimental data. An exception is the work of Cohu and Magnin (1995), in which coated film thickness was measured for a range of applied loads with all relevant information recorded to enable a comparison with predictions from the purely elastic FSM. As applied load is varied both the predicted and measured values of coated film thickness, H^∞, are compared in figure 4.18, along with values for L/X_D. Predicted and measured values of L/X_D are seen to be in good agreement especially for high load whereas predictions for H^∞ exceed the experimental results by a factor of two. Possible reasons for this discrepancy are as follows:

- experimental error due to the accuracy of scraping when measuring a coated film thickness of approximately $10\mu m$,
- viscoelastic effects in the deformable layer.

Cohu & Magnin state that experimental error could be as much as 30% for thin films but this alone cannot explain the difference between theory and experiment. Here,

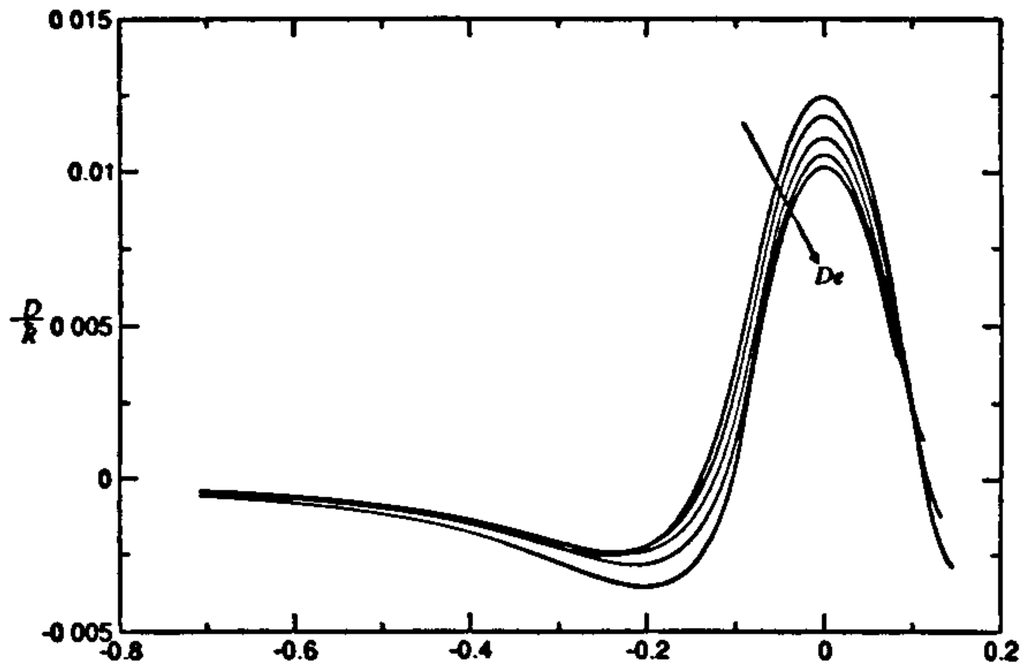

$\frac{X}{\bar{R}}$

(a) The deformation profile for several values of $0 < De < 0.1$

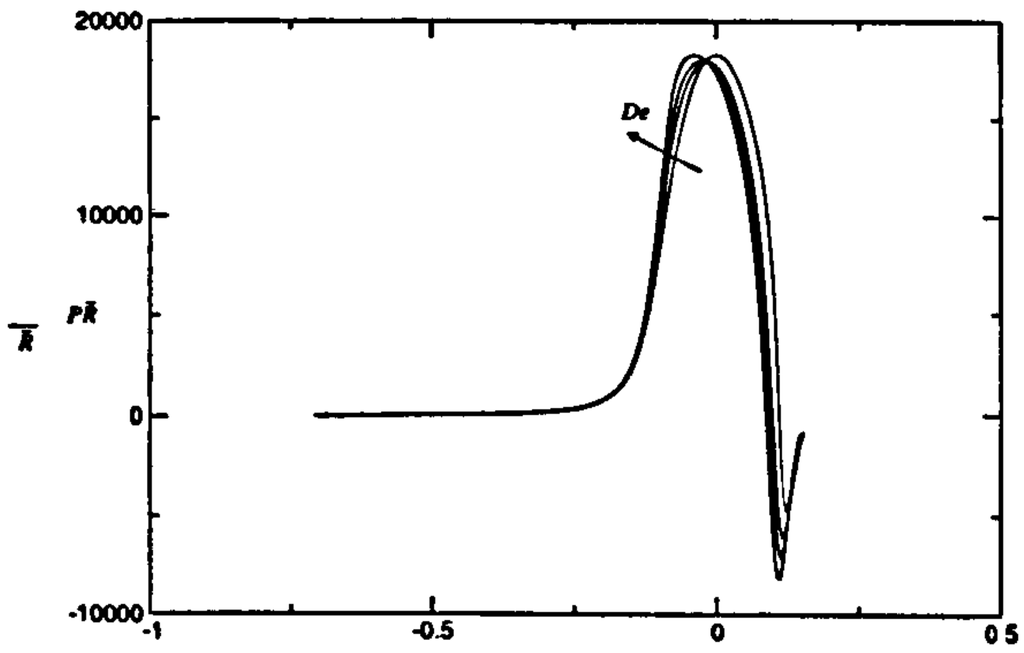

$\frac{X}{\bar{R}}$

(b) The pressure profile for several values of $0 < De < 0.1$

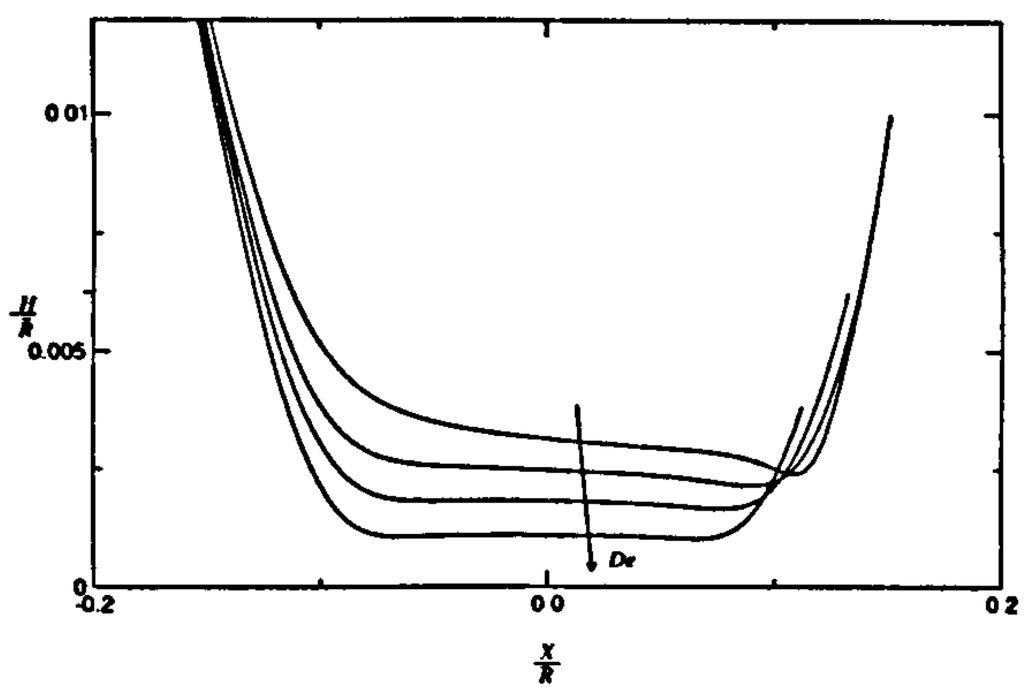

$\frac{X}{\bar{R}}$

(c) The gap thickness profile for several values of $0 \leq De \leq 0.1$

Figure 4.17: Variation in the flux and meniscus position with De. $B_0/\bar{R} = -5 \times 10^{-3}$, $L/\bar{R} = 0.2$, $Ca = 1$, $E_s = 10^{-5}$, $T_\sigma = 0$.

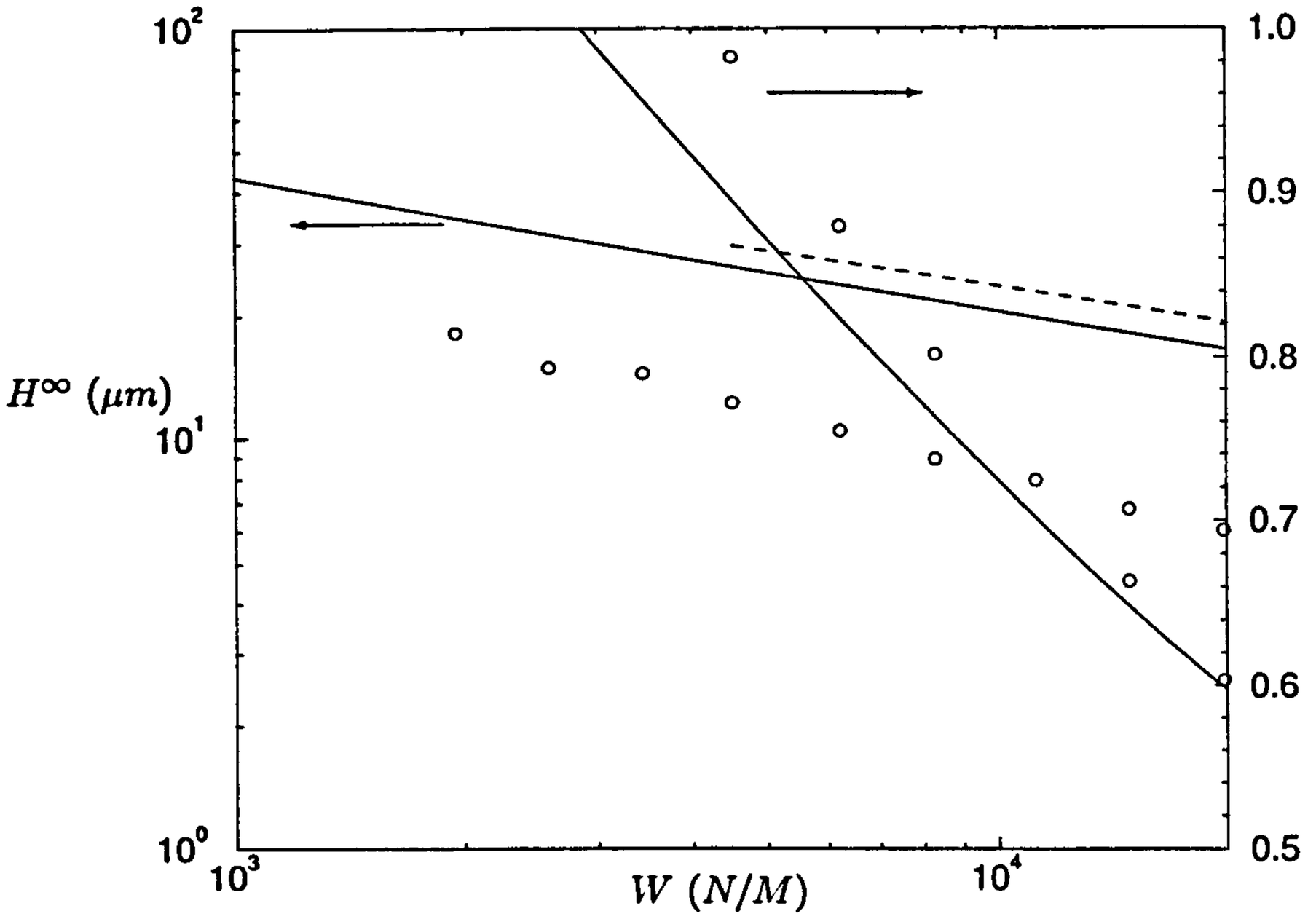

Figure 4.18: A comparison of mathematically predicted (—) and experimentally measured (o) H^∞ and L/X_D for a range of loads — $B_0/\bar{R} \in [-10^{-3}, -10^{-2}]$, $E_S = 0.576 \times 10^{-6}$, $Ca = 0.1$, $\nu = 0.5$, and $L/\bar{R} = 0.102$.

viscoelastic effects are examined by setting T_σ and T_ϵ in (4.18 a-c) to non-zero values. To accurately model an elastomer a spectrum of retardation and relaxation times should be used but as no data exists for the viscoelastic properties (i.e. shear modulus G' and loss modulus G'') of the elastomers used in the experiments, single values of T_σ and T_ϵ were selected (giving a modified Deborah number $De(B_0/\bar{R})^{1/2} = 3 \times 10^{-2}$ and $T_\epsilon/T_\sigma = 10^2$). Hence the model is being used to provide an indication of the effect of the viscoelastic properties rather than describe a particular compliant layer.

The effect of stress relaxation was examined by setting T_ϵ to zero and varying T_σ and the result was that the pressure maximum moved downstream relative to the elastic case and there was an increase in both x_d and λ.

Figure 4.20 shows for typical operating conditions the variation of the flux and meniscus position with load as predicted by the FSM, both with and without the viscoelastic terms included. It is clear that the introduction of these terms has a dramatic effect on the magnitude of the flux, with the reduction being of the order of 60% for

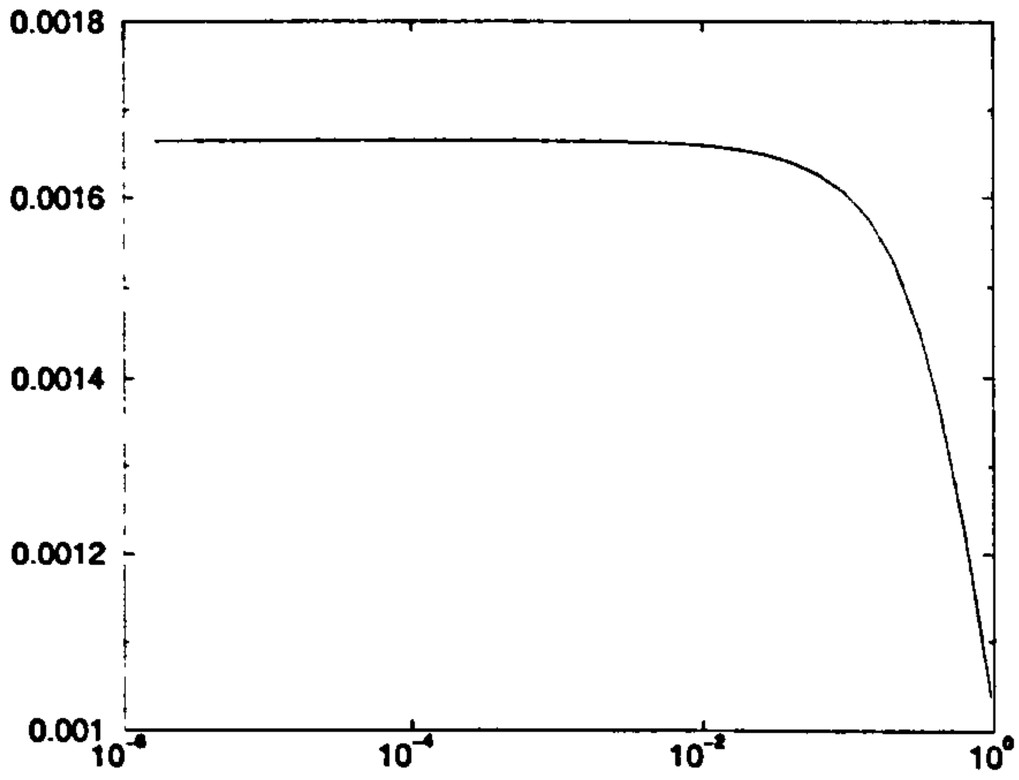

(a) The variation in flux with D_e.

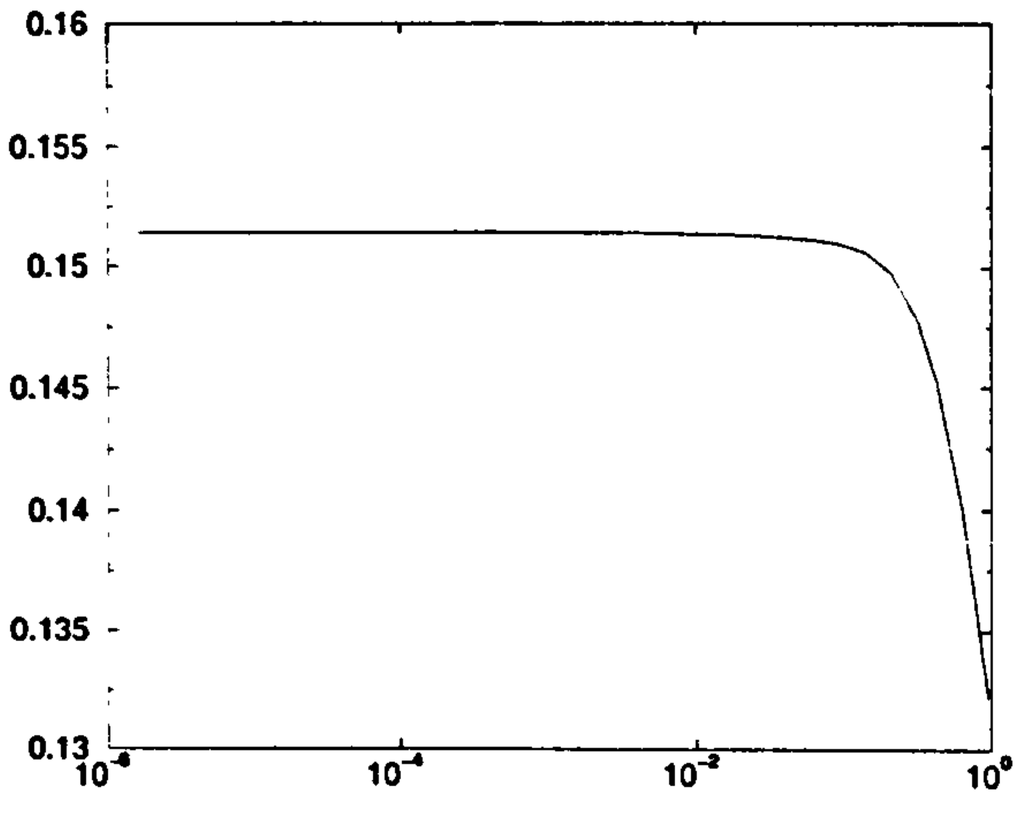

(b) The variation in meniscus position with D_e.

Figure 4.19: Variation in flux and meniscus location with De. $B_0/\bar{R} = -5 \times 10^{-3}$, $L/\bar{R} = 0.2$, $Ca = 1$, $E_s = 10^{-5}$, $T_\sigma = 0$.

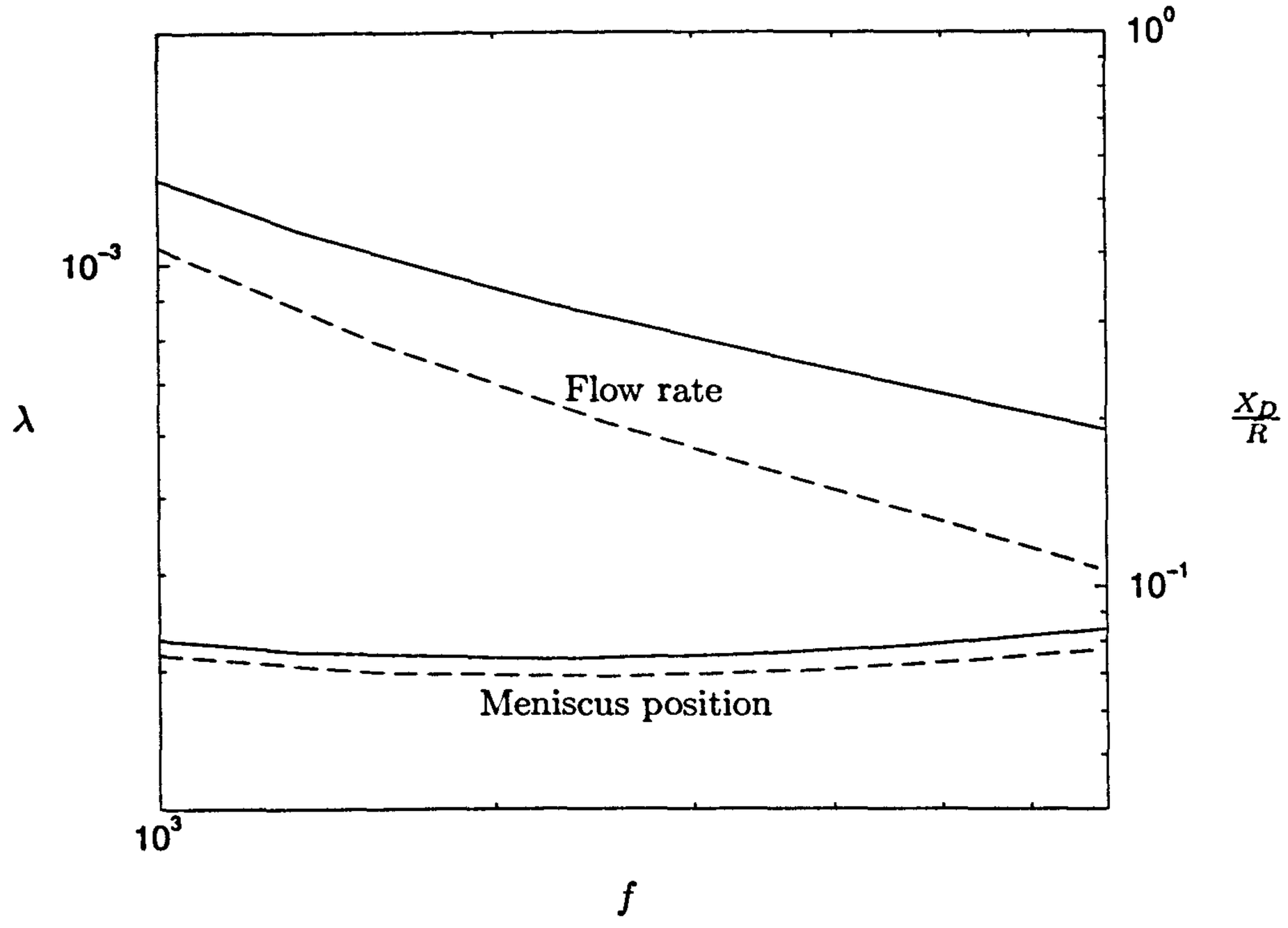

Figure 4.20: Variation of flux and flow rate against load with (- -) and without (—) viscoelastic terms. $L/\bar{R} = 0.2$, $E_S = 10^{-6}$ and $Ca = 1$. $De(B_0/\bar{R})^{1/2} = 3 \times 10^{-2}$, $T_r = 10^2$.

high loads, yet the effect on X_D is much less pronounced, the maximum difference being 6%. It is therefore apparent that viscoelastic effects could be responsible for the discrepancy between theoretical predictions and experimental measurements of the flux. Furthermore, as the FSM with the inclusion of viscelastic effects, gives results of the same order as experiment its use is justified and it will form the basis of the stability analysis in the following chapter.

4.6 Summary

In this chapter a model was developed to study the steady state operation of a forward deformable roll coater.

The lubrication equations were again used to model the fluid. As industrial roll coaters often operate at $Ca \sim O(1)$, the boundary conditions developed in chapter 2 were not applicable. However, a method was found of extending the boundary conditions of chapter 2 to the large capillary limit. This was a major step forward as a single 'analytic' boundary condition covering the entire Ca range has not been used before.

In a deformable roll coater the fluid pressure affects can deform the compliant layer and so a model is needed to describe the response of the layer to a load applied to its surface. The plane strain equations of linear elasticity can be solved to give an integral equation linking the surface deformation to the surface load. This model for the compliant layer had previously been used by Young but difficulties were encountered due to the singular nature of the integrand. Here an alternative formulation of the same integral equation, involving the Fourier transform of the pressure, was used and all singularities dissappeared in the case of interest, namely $\nu = 0.5$.

The model was used to investigate the effects of E and L^{-1}. A scaling analysis suggested that E and L^{-1} should have the same effect and this is the assumption of the spring models used by previous authors. The results of this chapter show that E and L^{-1} do indeed have the same effect in the positive gap and small negative gap regimes. However, as the gap becomes increasingly negative the role of the layer depth on the meniscus position is reversed and E not L^{-1} no longer have the same effect. The reason for the effect of L upon X_D depending on the gap setting was explained in terms of layer swelling - a phenomenon that spring models cannot predict as they do

not conserve the volume of the layer. As the accurate prediction of X_D is essential if the results are to be used as a base state for a stability analysis it was concluded that spring models were inadequate for a stability analysis.

The results were compared with the experimental resuts of Cohu and Magnin (1997) and it was found that although the prediction of meniscus position was reasonable, the flow rate prediction was much too large. In an attempt to explain these results the integral equation was extended to include linear viscoelastic effects and it was found that these could reduce the flux by the desired amount whilst having little effect on X_D. Thus it would appear that the inclusion of viscoelastic terms can explain the difference between theory and experiment. This point is important as it demonstrates that the compliant layer model used here could be used to accurately predict the performance of deformable roll coaters in the laboratory.

Therefore a model has been developed that is valid over a wide range of Ca and is capable of capturing the essential physics (layer swelling and viscoelasticity effects) of the compliant layer.

Chapter 5

Deformable roll coating - linear stability analysis

5.1 Introduction

This chapter considers the linear stability of the flow within a deformable roll coater. Whilst this problem has been looked at before (Carvalho and Scriven (1997a), Carvalho and Scriven (1999)) each analysis has relied on a spring model to describe the compliant layer and as was shown comprehensively in the previous chapter, such models are inadequate. It is therefore the aim of this chapter to carry out a thorough linear stability analysis of a deformable roll coating system building on the steady state results of the previous chapter.

To model the stability problem accurately, the integral equation of chapter 4 is extended to include sinusoidal variations in the lateral direction. The 3-D extension complicates the solution procedure developed in the previous chapter, necessitating a new scheme that uses complex analysis to evaluate the resulting integral.

5.2 Governing equations

In this section the equations that determine the linear time dependent behaviour of a small disturbance to the system are formulated. The method is similar to that used for the stability analysis of the DFF bead but the governing equations differ due to the added variable of the compliant layer. In order to analyse the linear stability of

the system the equations that govern the behaviour of the fluid and the solid in the presence of a lateral sinusoidal perturbation need to be developed. As in chapter 3, the meniscus position is perturbed:

$$X_D = X_D^0 + \xi X_D' \sin KZ e^{\Sigma T}, \tag{5.1}$$

where X_D^0 is the steady state meniscus position of chapter 4 and $|\xi X_D'/X_D^0| \ll 1$. To make the formulation consistent with chapter 3, X_D' is chosen such that $X_D' = B_D/2$. The reader will note that K is used for the kernel in (1.16) and elsewhere thereafter and also here for the wavenumber, the intended meaning will be clear from the context.

The governing fluid equations are similar to those developed in chapter 3 but differ due to the deformation of the compliant layer that forms the fluid boundary and so are reformulated below.

5.2.1 Fluid Equations

The velocity, deformation and pressure are written as the sum of the steady solution and a small, time dependent and laterally varying perturbation:

$$\mathbf{U} = \mathbf{U}^0(X,Y) + \xi \begin{pmatrix} U'(X,Y)\sin KZ \\ V'(X,Y)\sin KZ \\ W'(X,Y)\cos KZ \end{pmatrix} e^{\Sigma T}, \tag{5.2}$$

$$D(X) = D^0(X) + \xi D'(X)\sin KZ e^{\Sigma T}, \tag{5.3}$$

$$P(X) = P^0(X) + \xi P'(X)\sin KZ e^{\Sigma T}, \tag{5.4}$$

where $|\xi| \ll 1$. $\mathbf{U}^0 = (U^0, V^0)$, D^0 and P^0 are the steady state solutions found in the previous chapter and $\mathbf{U}' = (U', V', W')$, D' and P' are the unknown responses to the perturbation. As before, it is assumed that the gap between the rolls is small in comparison to the effective roll radius so that the lubrication approximation is valid.

The Navier-Stokes equations then reduce to:

$$\frac{\partial}{\partial X}(P^0 + \xi P') = \mu \frac{\partial^2}{\partial Y^2}(U^0 + \xi U'), \tag{5.5}$$

$$\frac{\partial}{\partial Y}(P^0 + \xi P') = 0, \tag{5.6}$$

$$K\xi P' = \mu \frac{\partial^2}{\partial Y^2}\xi W'. \tag{5.7}$$

Note that $\partial P^0/\partial Z \equiv 0$ and $W^0 \equiv 0$. The leading order terms give the steady state equations of chapter 4 whereas the $O(\xi)$ terms give the equations that determine the pressure and velocity perturbations. The no-slip boundary conditions are

$$\begin{aligned} U_R &= U|_{Y=-D} \\ &= U^0|_{Y=-D^0} - \xi D' U^0_Y|_{-D^0} + \xi U'|_{-D^0} + O(\xi^2), \qquad (5.8) \\ U_R &= U|_{Y=S} \\ &= U^0|_{Y=S} + \xi U'|_{Y=S} + O(\xi^2), \qquad (5.9) \\ 0 &= W|_{Y=-D,S} = \epsilon W'|_{Y=-D,S} + O(\xi^2), \qquad (5.10) \end{aligned}$$

where $S = 2B_0 + X^2/\bar{R}$ is the undeformed gap width. Having balanced terms of equal order, (5.5) - (5.7) can be integrated and (5.8) - (5.10) applied to give the velocity fields as

$$\begin{aligned} U^0 &= \frac{1}{2\mu}\frac{\partial P^0}{\partial X}(Y-S)(Y+D^0) + U_R, \qquad (5.11) \\ U' &= \frac{1}{2\mu}\frac{\partial P'}{\partial X}(Y+D^0)(Y-S) + \frac{1}{2\mu}\frac{\partial P^0}{\partial X}D'(Y-S), \qquad (5.12) \\ W' &= \frac{1}{2\mu}KP'(Y-S)(Y+D^0). \qquad (5.13) \end{aligned}$$

A 2-D mass balance leads to the 2-D Reynolds equation

$$\frac{\mathrm{d}}{\mathrm{d}X}\left(B^{03}\frac{\mathrm{d}P'}{\mathrm{d}X} + 3\frac{\mathrm{d}P^0}{\mathrm{d}X}D'B^{02}\right) - K^2B^{03}P' = 12\mu\left(U_R\frac{\mathrm{d}D'}{\mathrm{d}X} + \Sigma D'\right), \qquad (5.14)$$

where $B^0 = S + D^0$, the total gap width at leading order. This equation is similar to (3.16) except that the right hand side is non zero due to the change in gap width at $O(\xi)$.

At this point the problem could be simplified considerably by assuming that D' has a negligible effect on the perturbed flow and so removing all terms in the above 2-D Reynolds equation that contain it. However, two arguments, set out below, appear to support the point of view that D' could play an important role and hence it was decided to retain it in the 2-D Reynolds equation and formulate a corresponding mathematical model in the following section.

The first of the 'pro - D'' arguments is based on the fact that it appears to be logical to assume that

$$D' \sim D^0, \qquad P' \sim P^0, \qquad (5.15)$$

hence the two terms within the first pair of brackets on the left hand side of the 2-D Reynolds equation would be of the same order and it follows that the perturbation to the layer profile (D') plays an important role in the stability or otherwise, of the system.

A second argument that supports the importance of D' is as follows; the term on the right hand side is a squeeze film effect that acts to damp the pressure perturbation and so increase the stability of the system. This is simple to understand since a local rise/fall in the pressure will lead to the solid deforming so that the local gap width grows/reduces which, in turn, gives rise to a decrease/increase in the local pressure field due to the squeeze film effect. Therefore the squeeze film effect acts to counteract any disturbance in the fluid pressure field. The model for D' derived below is used to examine whether these arguments hold true and to determine the significance or otherwise of the role played by D'.

In order to solve (5.14) and find the perturbed film thickness, three boundary conditions are required. The first of these is simply that the pressure is required to decay to ambient far upstream of the nip:

$$P(-\infty) = P^0(-\infty) + \xi P'(-\infty) = 0 \quad \Rightarrow \quad P'(-\infty) = 0. \tag{5.16}$$

The remaining two conditions are found from perturbing the conditions developed in chapter 4 for the pressure at the film split location and the expression for the outgoing film thickness. Equations (4.14) and (4.17) for the pressure drop across the meniscus and the outgoing film thickness are:

$$P^0(X_D^0) = -\frac{\gamma}{\alpha B_D^0}, \tag{5.17}$$

and

$$H^\infty = \beta B_D^0,$$

where α and β are given by

$$\alpha = \frac{1}{2}\left(1 + \frac{1}{2}\frac{\mathrm{d}B^0}{\mathrm{d}X} - 3.88Ca^{2/3}\right), \tag{5.18}$$

$$\beta = \frac{1}{2}\frac{1.34\left(1 + B_X^0|_{X_D^0}\right)Ca^{2/3}}{1 + 3.88Ca^{2/3}}. \tag{5.19}$$

The pressure jump condition can be found by perturbing (5.17) as was done in chapter 3 to give

$$P'(X_D^0) = \frac{B_D^0}{2}\left(\frac{\gamma}{\alpha(B_D^0)^2}\left.\frac{\mathrm{d}B^0}{\mathrm{d}X}\right|_{X_D^0} + \frac{\pi}{4}\gamma K^2\right). \tag{5.20}$$

The factor of $B_D^0/2$ is due to the choice of X_D'. The long wave limit has again been assumed and as such the factor of $\pi/4$ in the lateral curvature term has been used in this analysis. The perturbed coated film thickness can be found in a similar fashion:

$$H^{\infty\prime} = \beta\frac{B_D^0}{2}\left.\frac{\mathrm{d}B^0}{\mathrm{d}X}\right|_{X_D^0}. \tag{5.21}$$

In the formulation of these perturbed conditions α and β have been treated as constants. In chapter 3 it was shown how the kinematic boundary condition balanced the fluxes entering and leaving the meniscus region with the rate of change of the meniscus position. This can be applied here to give

$$\int_{-D^0-\xi D'}^{-D^0} U^0|_{X_D^0}\mathrm{d}Y + \int_{-D^0}^{S}\xi U'|_{X_D^0}\mathrm{d}Y - 2U_R\xi H^{\infty\prime} = \xi\frac{\mathrm{d}X_D'}{\mathrm{d}T}(B_D^0 - 2H^{\infty\prime}). \tag{5.22}$$

This leads to

$$-\frac{1}{12\mu}P_X'|_{X_D^0}B^{0^3} - \frac{1}{4\mu}P_X^0|_{X_D^0}B^{0^2}D' - U_R\beta B_D^0\left.\frac{\mathrm{d}B^0}{\mathrm{d}X}\right|_{X_D^0} = \Sigma\frac{B_D^0}{2}(B_D^0 - 2\beta B_D^0). \tag{5.23}$$

Therefore in the instability problem the kinematic condition becomes an equation for the growth rate, Σ. The boundary conditions have been derived and the governing equations for the solid are now developed.

5.2.2 The solid equations

In chapter 4 an integral equation was presented that determined the profile of the compliant layer from the traction acting on its surface, the equation being derived from the plane strain equations of linear elasticity. This formulation was appropriate since it was assumed that there was no variation in the physical variables along the rollers. In the unsteady case this assumption is relaxed as a perturbation with lateral variation is considered, therefore the integral equation is no longer valid and an equivalent integral equation, not relying on plane strain assumptions, has to be developed. The author was unaware of the existence of such an analysis in the literature and so returned to the full 3-D linear elasticity equations in order to develop an equivalent integral equation. In this section all viscoelastic terms are neglected.

In a 3-D linear elasticity problem there are six independent components of stress and in general these can be written in terms of the Maxwell stress functions Φ_1, Φ_2 and Φ_3, as follows:

$$\sigma_X = -\frac{\partial^2\Phi_3}{\partial Y^2} - \frac{\partial^2\Phi_2}{\partial Z^2}, \quad \sigma_Y = -\frac{\partial^2\Phi_1}{\partial Z^2} - \frac{\partial^2\Phi_3}{\partial X^2}, \quad \sigma_Z = -\frac{\partial^2\Phi_1}{\partial Y^2} - \frac{\partial^2\Phi_2}{\partial X^2}, \tag{5.24}$$

$$\tau_{XY} = \frac{\partial^2\Phi_3}{\partial Y\partial X}, \quad \tau_{XZ} = \frac{\partial^2\Phi_2}{\partial X\partial Z}, \quad \tau_{YZ} = \frac{\partial^2\Phi_1}{\partial Y\partial Z}, \tag{5.25}$$

where σ_i and τ_{ij} represent the normal and tangential components of stress, respectively. The uniqueness of the solution is guaranteed if the following compatibility equations are satisfied:

$$(1+\nu)\nabla^2\sigma_X + \frac{\partial^2\Theta}{\partial X^2} = 0, \tag{5.26}$$

$$(1+\nu)\nabla^2\sigma_Y + \frac{\partial^2\Theta}{\partial Y^2} = 0, \tag{5.27}$$

$$(1+\nu)\nabla^2\sigma_Z + \frac{\partial^2\Theta}{\partial Z^2} = 0, \tag{5.28}$$

$$(1+\nu)\nabla^2\tau_{YZ} + \frac{\partial^2\Theta}{\partial Y\partial Z} = 0, \tag{5.29}$$

$$(1+\nu)\nabla^2\tau_{ZX} + \frac{\partial^2\Theta}{\partial Z\partial X} = 0, \tag{5.30}$$

$$(1+\nu)\nabla^2\tau_{XY} + \frac{\partial^2\Theta}{\partial X\partial Y} = 0. \tag{5.31}$$

In line with the perturbation applied to the fluid domain, it is assumed that the stress functions have the form $\Phi_i(X,Y,Z,T) = \phi_i(X,Y)e^{\Sigma T}\sin KZ$, where K is the wavenumber. As stated before, a general disturbance can be thought of as a sum of these Fourier modes and as this is a linear analysis, it is adequate to consider the behaviour of each mode independently. The compatibility equations can be rewritten in terms of the Maxwell stress functions and then it follows from (5.26) and (5.27) that

$$\nabla_K^2\frac{\partial^2}{\partial Z^2}\left(\frac{\partial^2\phi_3}{\partial Y^2} - K^2\phi_2\right) = \nabla_k^2\frac{\partial^2}{\partial X^2}\left(\frac{\partial\phi_1}{\partial Y^2} + \frac{\partial\phi_2}{\partial X^2}\right), \tag{5.32}$$

where

$$\nabla_K^2 = \frac{\partial^2}{\partial X^2} + \frac{\partial^2}{\partial Y^2} - K^2. \tag{5.33}$$

(5.29) – (5.31) combine to give

$$\nabla_K^2 K\frac{\partial^2\phi_2}{\partial X\partial Y} = \nabla_K^2 K\frac{\partial^2\phi_1}{\partial X\partial Y}, \tag{5.34}$$

$$\nabla_K^2 K\frac{\partial^2\phi_2}{\partial X\partial Y} = \nabla_K^2 K\frac{\partial^2\phi_3}{\partial X\partial Y}. \tag{5.35}$$

Eliminating ϕ_1 and ϕ_3 from (5.32) leads to

$$\frac{\partial}{\partial X}\nabla_K^2\left(K^2\frac{\partial^2\phi_2}{\partial Y^2} - K^4\phi_2 + \frac{\partial^4\phi_2}{\partial X^2\partial Y^2} + \frac{\partial^4\phi_2}{\partial X^4}\right) = 0. \tag{5.36}$$

The Fourier transform of ϕ_i, $\tilde{\phi}_i$, is defined as

$$\tilde{\phi}_i(\omega) = \int_{-\infty}^{\infty}\phi_i(X,Y)e^{-i\omega X}\mathrm{d}X \tag{5.37}$$

and taking the transform of (5.36) gives:

$$(K^2 - w^2)\nabla_\omega^4\tilde{\phi}_2 = 0, \tag{5.38}$$

where

$$\nabla_w^2 = \frac{\partial^2}{\partial X^2} - \omega^2 - K^2. \tag{5.39}$$

The reader will note that ω and k play a similar role in this differential operator. Solving for $\tilde{\phi}_2$ gives

$$\tilde{\phi}_2 = (A_2 + B_2Y)\cosh(\omega^2 + K^2)^{1/2}Y + (C_2 + D_2Y)\sinh(\omega^2 + K^2)^{1/2}Y. \tag{5.40}$$

$\tilde{\phi}_1$ and $\tilde{\phi}_3$ are determined from (5.34) and (5.36) and can be shown to have similar forms to that of $\tilde{\phi}_2$. It is found that $B_1 = B_2 = B_3$ and $D_1 = D_2 = D_3$ and as such their subscripts are dropped.

Boundary conditions are imposed on the two surfaces of the solid and are given below. The deformable strip is bonded to a rigid base giving the zero displacement boundary conditions on $Y = 0$:

$$U_S = V_S = W_S = 0, \tag{5.41}$$

where U_S, V_S and W_S represent the displacements in the X, Y and Z directions. The S subscripts have been introduced to highlight the fact that the variables relate to *solid displacements* and not *fluid velocities* that are labelled by U, V and W elsewhere. The stress conditions on the upper surface ($Y = -L$) of the strip are

$$\sigma_Y = -P(X)\sin KZe^{\Sigma T}, \tag{5.42}$$

$$\tau_{XY} = Q(X)\sin KZe^{\Sigma T}, \tag{5.43}$$

$$\tau_{YZ} = R(X)\sin KZe^{\Sigma T}. \tag{5.44}$$

Thus there are six boundary conditions to be satisfied yet there are eight unknown constants (B, D, A_i and C_i $1 \leq i \leq 3$). This problem is overcome by substituting

the expressions for the $\tilde{\phi}_i$'s into the transformed compatibility equations which, as stated earlier, guarantee the uniqueness of the solution. This leads to the following two expressions:

$$B = \frac{\omega^2 C_1 - (\omega^2 + k^2)C_2 + k^2 C_3}{2(\omega^2 + k^2)^{1/2}(\nu - 1)}, \quad D = \frac{\omega^2 A_1 - (\omega^2 + k^2)A_2 + k^2 A_3}{2(\omega^2 + k^2)^{1/2}(\nu - 1)}, \tag{5.45}$$

giving, in total, eight equations for the eight unknowns.

In order to apply the zero displacement and stress boundary conditions they have to be cast in a suitable form. The traction conditions (5.42 - 5.44) can be Fourier transformed to give

$$-\tilde{P}(\omega) = K^2\tilde{\phi}_1 + \omega^2\tilde{\phi}_3, \tag{5.46}$$

$$\tilde{Q}(\omega) = i\omega\frac{\partial\tilde{\phi}_3}{\partial Y}, \tag{5.47}$$

$$\tilde{R} = K\frac{\partial\tilde{\phi}_1}{\partial Y}. \tag{5.48}$$

The zero displacement conditions are applied by writing the strain in terms of the stress (and hence the stress functions) via Hookes law.

$$\frac{\partial U_S}{\partial X} = \frac{1}{E}(\sigma_X - \nu(\sigma_Y + \sigma_Z), \tag{5.49}$$

$$\frac{\partial V_S}{\partial Y} = \frac{1}{E}(\sigma_Y - \nu(\sigma_X + \sigma_Z), \tag{5.50}$$

$$\frac{\partial W_S}{\partial Z} = \frac{1}{E}(\sigma_Z - \nu(\sigma_X + \sigma_Y). \tag{5.51}$$

Substituting for the stress components in terms of the Maxwell stress functions and then transforming gives:

$$i\omega\tilde{U}_S = \frac{1}{E}\left[-\frac{\partial^2\tilde{\phi}_3}{\partial Y^2} + K^2\tilde{\phi}_2 - \nu\left(K^2\tilde{\phi}_1 + \omega^2\tilde{\phi}_3 - \frac{\partial^2\tilde{\phi}_1}{\partial Y^2} + \omega^2\tilde{\phi}^2\right)\right], \tag{5.52}$$

$$\frac{\partial\tilde{V}_S}{\partial Y} = \frac{1}{E}\left[K^2\tilde{\phi}_1 + \omega^2\tilde{\phi}_3 - \nu\left(-\frac{\partial^2\tilde{\phi}_3}{\partial Y^2} + K^2\tilde{\phi}_2 - \frac{\partial^2\tilde{\phi}_1}{\partial Y^2} + \omega^2\tilde{\phi}_2\right)\right], \tag{5.53}$$

$$K\tilde{W}_S = \frac{1}{E}\left[-\frac{\partial^2\tilde{\phi}_1}{\partial Y^2} + \omega^2\tilde{\phi}_2 - \nu\left(-\frac{\partial^2\tilde{\phi}_3}{\partial Y^2} + K^2\tilde{\phi}_2 + K^2\tilde{\phi}_1 + \omega^2\tilde{\phi}_3\right)\right]. \tag{5.54}$$

The condition of zero displacement in the X direction can now be imposed using (5.52) to give:

$$A_1 = A_2 + A_3, \tag{5.55}$$

whereas (5.41) and (5.54) give

$$A_3 = A_1 + A_2. \tag{5.56}$$

These two relations yield

$$A_2 = 0, \quad A_1 = A_3 = A, \quad \text{say.} \tag{5.57}$$

The second component of Hookes law (5.53) integrates to give

$$\begin{aligned} E\tilde{V}_S = &\left[\frac{C_1K^2 + C_3\omega^2}{(\omega^2+K^2)^{1/2}} - \nu(\omega^2+K^2)^{1/2}(C_2 - C_3 - C_1)\right. \\ &\left. + (3\nu-1)B + (1+\nu)(\omega^2+K^2)^{1/2}DY\right]\cosh(\omega^2+K^2)^{1/2}Y \\ &+ \left[\frac{A_1K^2 + A_3\omega^2}{(\omega^2+K^2)^{1/2}} - \nu(\omega^2+K^2)^{1/2}(A_2 - A_3 - A_1)\right. \\ &\left. + (3\nu-1)D + (1+\nu)(\omega^2+K^2)^{1/2}BY\right]\sinh(\omega^2+K^2)^{1/2}Y, \end{aligned} \tag{5.58}$$

and the zero displacement in the Y direction can now be applied which results in

$$0 = \nu(\omega^2+K^2)(C_1 - C_2 + C_3) + K^2C_1 + \omega^2C_3 + (\omega^2+K^2)^{1/2}(3\nu-1)B. \tag{5.59}$$

Thus there exist two equations, (5.45) and (5.59), linking B and the C_i's which can be combined to give

$$(1-2\nu)B = \frac{K^2C_1 + \omega^2C_3}{(\omega^2+K^2)^{1/2}} \tag{5.60}$$

and

$$B = (\omega^2+K^2)^{1/2}(C_2 - C_1 - C_3). \tag{5.61}$$

(5.60), along with (5.45), is used to write the stress conditions in the following form:

$$\left[2(\omega^2+K^2)^{1/2}(\nu-1)\cosh\omega L + (\omega^2+K^2)L\sinh\omega L\right]D$$
$$+ \left[(2\nu-1)(\omega^2+K^2)^{1/2}\sinh\omega L - (\omega^2+K^2)L\cosh\omega L\right]B = -\tilde{P}, \tag{5.62}$$

$$\left[(\omega^2+K^2)(1-2\nu)\sinh\omega L - (\omega^2+K^2)^{3/2}L\cosh\omega L\right]D$$
$$+ \left[(\omega^2+K^2)^{3/2}\sinh\omega L + 2(1-\nu)(\omega^2+K^2)\cosh\omega L\right]B = K\tilde{R} - i\omega\tilde{Q} \tag{5.63}$$

The equations are solved for B and D and the results, along with (5.60) and (5.61) are substituted into the expression for $\tilde{v}$. Inverting the Fourier transform then gives

$$V_S(-L) = D(X) = \frac{1-\nu^2}{E}\int_{-\infty}^{\infty} K'(X-X')P(X')\mathrm{d}X', \tag{5.64}$$

where

$$K'(X) = \mathrm{Re}\frac{1}{2\pi}\int_{-\infty}^{\infty} \frac{(3-4\nu)\sinh 2(\omega^2+\kappa^2)^{1/2} - 2(\omega^2+\kappa^2)^{1/2}}{((\omega^2+\kappa^2) + (1-2\nu)^2 - (4\nu-3)\cosh^2(\omega^2+\kappa^2)^{1/2}} \times \frac{e^{i\omega X/L}}{(\omega^2+\kappa^2)^{1/2}}\mathrm{d}\omega \tag{5.65}$$

and $\kappa = KL$. The 2-D result is recovered by setting $\kappa = 0$. The form of the kernel function K' is not unexpected as it was noted earlier that ω and K play similar roles in the transformed differential operators. Note that as in the steady case investigated in the previous chapter, contributions from the tangential surface tractions have been discarded. Thus the governing fluid and solid equations have been developed along with appropriate boundary conditions and the numerical solution method is now discussed.

5.3 Numerical solution

The governing equations are solved using the F.E. method described in chapter 4. As before the unknown field variables, D' and P', are represented by quadratic interpolation functions. Thus in a given element, denoted by e, the pressure and deformation are written as

$$D'(x) = \Sigma_e D'^e_i \psi^e_i(x), \qquad P'(x) = \Sigma_e P'^e_i \psi^e_i(x) \tag{5.66}$$

where $1 \leq e \leq N$, $i = 1, 2, 3$ and the ψ^e_i are the interpolation functions given in chapter 4. These expressions are substituted into both the integral and differential equations. In the case of the 2-D Reynolds equation the residual equations are formed by taking a weighted average of the error and then integrating by parts giving:

$$\begin{aligned} R^{lub^e}_i = & \left[\psi^e_i \left((\psi^e_j B^{0^e}_j)^3 P'^e_k \frac{\partial \psi^e_k}{\partial X} + 3P^{0^e}_k \frac{\partial \psi^e_k}{\partial X} D'^e_j \psi^e_j (\psi^e_l B^{0^e}_l)^2\right)\right]^{x^e_3}_{x^e_1} \\ & + \int_{x^e_1}^{x^e_3} \frac{\partial \psi^e_i}{\partial x} \left((\psi^e_j B^{0^e}_j)^3 P'^e_k \frac{\partial \psi^e_k}{\partial X} + 3P^{0^e}_k \frac{\partial \psi^e_k}{\partial X} D'^e_j \psi^e_j (\psi^e_l B^{0^e}_l)^2\right) \\ & + \psi^e_i \left(K^2 (\psi^e_j B^{0^e}_j)^3 P'^e_i \psi^e_i - 12\mu \left(U_R D'^e_k \frac{\partial \psi^e_k}{\partial X} + \Sigma D'^e_i \psi^e_i\right)\right) \mathrm{d}x. \end{aligned} \tag{5.67}$$

When the global equations are formed all contributions from the terms in square brackets cancel, apart from at the endpoints of the solution domain. At X^1_1 the extra contribution is neglected as it is assumed that the pressure gradient decays to zero far upstream of the nip. At X^N_m there is an extra contribution of

$$B^{0^3} P'_X + 3P^0_X D' B^{0^2}.$$

A term proportional to this appears in the kinematic condition (5.23) and so this condition can be naturally incorporated. Therefore the extra contribution to R^N_m can be written as

$$-12\mu \left(\beta B^0_D U_R B^0_i \left.\frac{\mathrm{d}\psi^N_i}{\mathrm{d}X}\right|_{X^0_D} + \Sigma \frac{B^{0^2}_D}{2}(1 - 2\beta)\right). \tag{5.68}$$

The condition that $P'(-\infty) = 0$ is incorporated by setting $P'^1_1 = 0$ and by not assembling the residual R^1_1 into the global equations.

The final boundary condition to be incorporated is the perturbed pressure drop equation:

$$R^{pd} = P'^N_m - \frac{B^0_{\texttt{NUMNODES}}}{2}\left(\frac{\gamma}{\alpha(B^0_{\texttt{NUMNODES}})^2}\, B_i^{0^N}\frac{\mathrm{d}\psi_i^n}{\mathrm{d}X}\bigg|_{X^0_D} + \gamma K^2\right). \tag{5.69}$$

The residuals from the deformation equation now have to be evaluated. The deformation of the solid surface is calculated from the pressure distribution within the fluid via the integral equation (5.64). When the wavenumber is zero the integrand reduces to the one encountered in the solution of the steady state problem in the previous chapter, the solution of which involved the numerical approximation of several functions (C, S and N), given by (4.71) - (4.73). This approach was favourable in the steady case as the functions were defined in such a way that they did not depend on any of the parameters of the model and therefore were unchanged in all simulations. Thus before any simulations were carried out, the functions were numerically evaluated at a set of points and the information stored as a list in a file that could be called upon to construct approximate values of the functions using an interpolating routine during the simulations. The numerical evaluation of the functions was a relatively expensive computation in comparison to constructing the approximation from the stored values and so only having to create the list once, at the outset, was advantageous. However, in the unsteady case considered in this chapter, the equivalent functions would be dependent on the value of the wavenumber and so the list would have to be regenerated each time the wavenumber changed which would lead to an extremely expensive scheme.

For the steady case Young (1997) evaluated the kernel function at a set of points and stored the information. This information was then used to approximate the kernel during the direct integration of (1.16). As mentioned in chapter 4 Young encountered problems due to the singular nature of the kernel. An additional problem with applying such a scheme here would be that the file containing the values of the kernel would be used in an analogous way to the one described above for C, S and N and would suffer from the same problem, i.e. it would have to be regenerated for each wavenumber, K. A possibility would be to generate a file containing the values of the relevant function at a wide range of values of X *and* K but this was dismissed as the number of points

needed to adequately cover the required portion of (X, K) space would be prohibitive. An alternative procedure for evaluating the integral was thus sought and led to the examination of calculating $K'(X)$ via the use of contour integration.

5.3.1 Evaluation of integral via contour integration

The analysis is restricted to the use of incompressible materials ($\nu = 0.5$) and so (5.65) reduces to

$$K'(X) = \mathrm{Re}\frac{1}{2\pi}\int_{-\infty}^{\infty} \frac{\sinh 2(\omega^2+\kappa^2)^{1/2} - 2(\omega^2+\kappa^2)^{1/2}}{(\omega^2+\kappa^2)^{1/2}((\omega^2+\kappa^2)+\cosh^2(\omega^2+\kappa^2)^{1/2})} e^{i\omega X/L}\mathrm{d}\omega \quad (5.70)$$

$$= \mathrm{Re}\frac{1}{2\pi}\int_{-\infty}^{\infty} I(\omega; X, \kappa)\mathrm{d}\omega, \qquad \text{say.} \quad (5.71)$$

Due to the terms containing square roots, the integrand is multivalued and has branch points at $\omega = \pm i\kappa$. In order to carry out the integration, a branch cut is taken to run along the imaginary axes between the two branch points as indicated in figure 5.1. The branch used here is now defined. Let:

$$\omega - i\kappa = r_- e^{i\theta_-}, \qquad \omega + i\kappa = r_+ e^{i\theta_+}, \quad (5.72)$$

then

$$(\omega^2+\kappa^2)^{1/2} = (r_- r_+)^{1/2} e^{i(\theta_- + \theta_+)/2}, \quad (5.73)$$

and the branch is defined by restricting the range of θ_- and θ_+ to

$$-\frac{\pi}{2} < \theta_- \leq \frac{3\pi}{2} \quad \text{and} \quad -\frac{3\pi}{2} < \theta_+ \leq \frac{\pi}{2}. \quad (5.74)$$

If $\Im(\omega) \gtrless 0$ and $X \gtrless 0$ then the integrand decays exponentially as $|\omega| \to \pm\infty$. Here it is assumed $X > 0$, the case of $X < 0$ is dealt with later. The contour of integration is shown in figure 5.1 and consists of six sections C_1, C_2,... C_6. C_1 and C_5 are two straight lines lying on the real axis, C_2 and C_4 are a pair of straight lines lying respectively just to the left and right of the cut, C_3 is a small circle of radius $R_B \ll 1$ centred about $i\kappa$ and C_6 is a semicircle of radius $R_A \gg 1$ centred about the origin. The integral is computed in the limit $R_A \to \infty$, $R_B \to 0$. It is clear that the integrals around C_3 and C_6 both tend to zero in this limit. Also the integrals along C_2 and C_4 cancel which leaves only the integrals along C_1 and C_5 and therefore

$$\lim_{\substack{R_A\to\infty \\ R_B\to 0}} \int_{C_1+C_2+\ldots+C_6} I\mathrm{d}\omega = \lim_{\substack{R_A\to\infty \\ R_B\to 0}} \int_{C_1+C_5} I\mathrm{d}\omega = \int_{-\infty}^{\infty} I\mathrm{d}\omega. \quad (5.75)$$

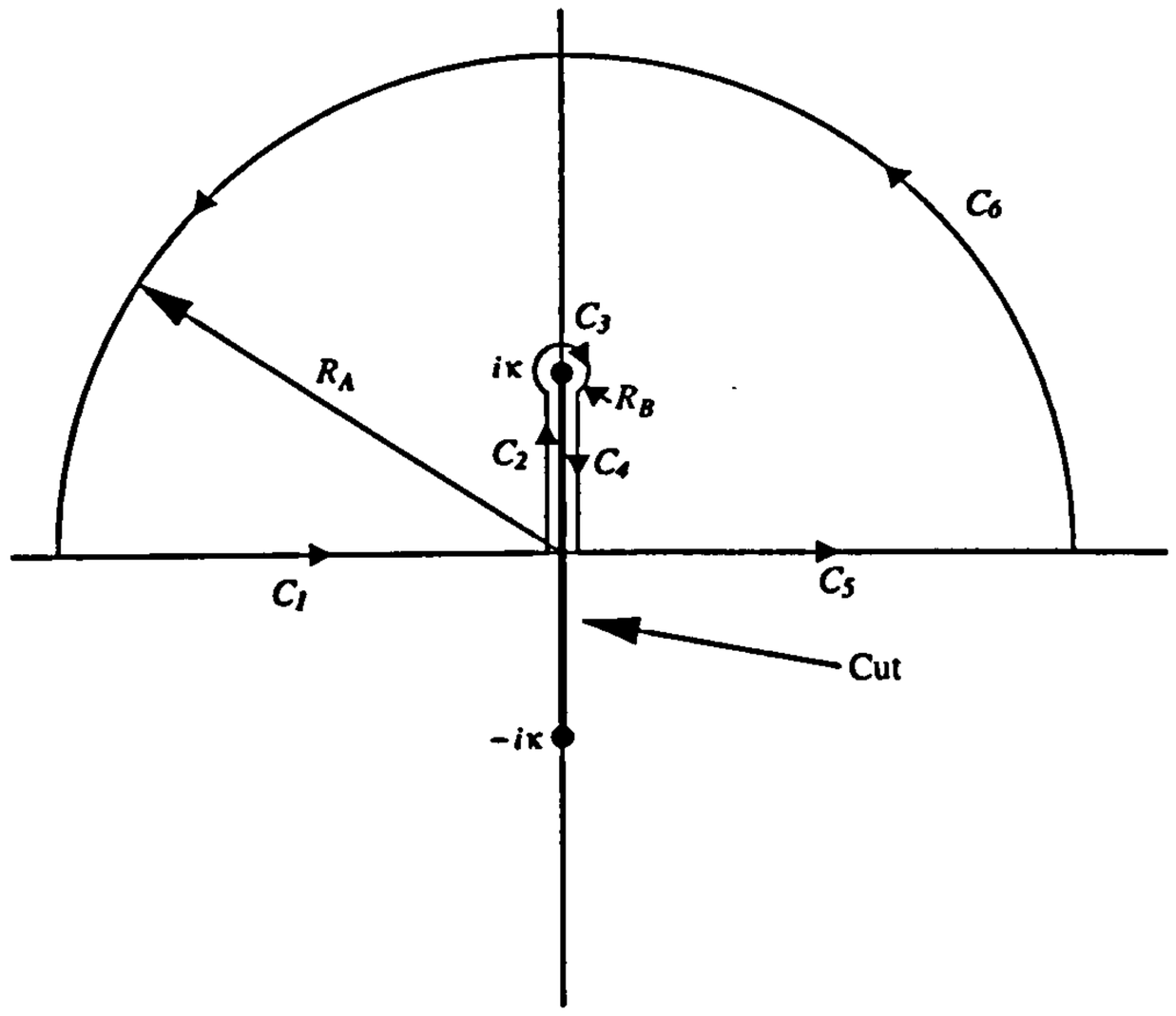

Figure 5.1: The contour and cut used in the evaluation of K'.

Therefore $C_1 + C_2 + ... + C_6$ is a valid choice of contour when $X > 0$ and this implies that all the poles lying in the upper half plane need to be found and the corresponding residues evaluated.

The poles of the integrand, I, are located at the zeroes of the denominator, i.e. where

$$(\omega^2 + \kappa^2)^{1/2} = \pm i \cosh(\omega^2 + \kappa^2)^{1/2}. \tag{5.76}$$

Note that $\omega = \pm i\kappa$ do not represent poles of I as both the numerator and denominator have zeroes of order one here. Putting

$$(\omega^2 + \kappa^2)^{1/2} = a + ib, \tag{5.77}$$

leads to the following two pairs of simultaneous equations:

$$a = \mp \sin b \sinh a, \tag{5.78}$$

$$b = \pm \cos b \cosh a. \tag{5.79}$$

Each pair of simultaneous equations will be considered in turn, starting with that given by the upper sign in (5.78) and (5.79), i.e. the roots of $(\omega^2+\kappa^2)^{1/2} - i\cosh(\omega^2+\kappa^2)^{1/2}$. Rearranging (5.79) gives

$$a = \cosh^{-1}\left(\frac{b}{\cos b}\right) = \pm \ln\left(\frac{b}{\cos b} + \sqrt{\frac{b^2}{\cos^2 b}}\right), \tag{5.80}$$

which, when substituted into (5.78), leads to the following equation for b:

$$\ln\left(\frac{b}{\cos b}+\sqrt{\frac{b^2}{\cos^2 b}-1}\right)=-\sin b\sqrt{\frac{b^2}{\cos^2 b}-1}, \tag{5.81}$$

where the fact that $\mathrm{sgn}\,(a)=\mathrm{sgn}\,(\sinh a)$ has been used. The reader will note that for every value of b that satisfies (5.81), (5.80) implies that there are two corresponding values of a of equal magnitude and opposite sign (the special case of a=0 is dealt with later). These pairs will be represented by a_+ and a_-,with $a_\pm \gtrless 0$. Once a and b have been found from the above it is possible to find the poles of the integrand from (5.77). Putting $\omega=c+id$ and substituting into (5.77) leads to

$$c^2-d^2+k^2 = a^2-b^2, \tag{5.82}$$

$$cd = ab. \tag{5.83}$$

Eliminating c leads to an equation that is quadratic in d^2 which can be solved to give:

$$d^2=\frac{\kappa^2+b^2-a^2\pm\sqrt{(a^2-b^2-\kappa^2)^2+4a^2b^2}}{2}. \tag{5.84}$$

In order for d to be real then the positive square root has to be taken in (5.84). As $\kappa\to 0$ then it is required that $d\to b$ which indicates that when d is found by square rooting the right hand side of (5.84), the sign should be chosen such that

$$\mathrm{sgn}\,(\Im(\omega))=\mathrm{sgn}(d)=\mathrm{sgn}(b). \tag{5.85}$$

Therefore, in the case of $X>0$, the requirement for $\Im(\omega)>0$ is equivalent to looking for solutions of (5.81) with $b>0$. Finally, (5.83) and (5.85) imply that c is given by

$$\mathrm{Re}(\omega)=c_\pm=a_\pm\left|\frac{b}{d}\right|, \tag{5.86}$$

where $c_\pm \gtrless 0$. (5.86) implies that for every solution of (5.81), there exist a pair of poles with 'equal and opposite' real part. As the location of poles residing in the upper half plane need to be determined then (5.85) implies that all solutions of (5.81) with $b>0$ need to be found. There are an infinite number of solutions to (5.81), these are denoted by $\{b_n : n\in\mathbb{N}, b_{n+1}>b_n\}$ and the corresponding a, c and d's are given by $a_{n_\pm}$, $c_{n_\pm}$ and d_n. It can be shown that the residue at $c_{n_\pm}+id_n$, $\mathrm{Res}(c_{n_\pm}+id_n;X/L)$, is:

$$\begin{aligned}\mathrm{Res}(c_{n_\pm}+id_n;X/L)=&\frac{(b_n^2\tan^2 b_n-1+b_n^2\tanh^2 a_{n_\pm}-2ib_n\tanh a_{n_\pm})}{(1+b_n\tan b_n)^2+b_n^2\tanh^2 a_{n_\pm}}\\ &\times\frac{c_{n_\pm}-id_n}{c_{n_\pm}^2+d_n^2}e^{(-d+ic_{n_\pm})X/L}.\end{aligned} \tag{5.87}$$

A solution to (5.78) not mentioned so far is $a = 0$ which implies that $b = \cos b$. This solution differs from the others as there is only one value of a corresponding to b. The values of a, b, c and d relating to this solution are denoted by a_0, b_0, c_0 and d_0, respectively. Therefore the residues corresponding to the first pair of simultaneous equations given by (5.78) and (5.79) have been found and it remains to find the residues that arise from the second pair, i.e. the roots of $(\omega^2 + k^2)^{1/2} + i\cosh(\omega^2 + k^2)^{1/2} = 0$. The analysis is similar to the previous case, setting $(\omega^2 + k^2)^{1/2} = a' + ib'$ leads to:

$$\ln\left(\frac{-b'}{\cos b'} + \sqrt{\frac{b'^2}{\cos^2 b'} - 1}\right) = \sin b' \sqrt{\frac{b'^2}{\cos^2 b'} - 1}, \tag{5.88}$$

and a' is given by

$$a' = \cosh^{-1}\left(\frac{-b'}{\cos b'}\right) = \pm \ln\left(\frac{-b'}{\cos b'} + \sqrt{\frac{b'^2}{\cos^2 b'} - 1}\right). \tag{5.89}$$

c' and d' are given by equations of the same form as (5.82) and (5.83). The residues at $c'_{n\pm} + id'_n$ are given by an expression indentical to (5.87). Therefore K', via the Cauchy residue theorem, is given by

$$\begin{aligned} K'(X/L;k) = \quad & \Re\{i\mathrm{Res}(c_0 + id_0; X/L) + i\sum_{n=1}^{\infty}[\mathrm{Res}(c_{n+} + id_n; X/L) \\ & + \mathrm{Res}(c'_{n+} + id'_n; X/L) \\ & + \mathrm{Res}(c_{n-} + id_n; X/L) + \mathrm{Res}(c'_{n-} + id'_n; X/L)]\} \quad X > 0 \end{aligned} \tag{5.90}$$

The above expression has been calculated for the case $X > 0$. However, (5.70) implies that K' is an even function and so the above definition can be extended for all X as follows:

$$\begin{aligned} K'(X/L;k) = \Re\{ & i\mathrm{Res}(c_0 + id_0; |X/L|) + i\sum_{n=1}^{\infty}[\mathrm{Res}(c_{n+} + id_n; |X/L|) + \\ & \mathrm{Res}(c'_{n+} + id'_n; |X/L|) + \mathrm{Res}(c_{n-} + id_n; |X/L|) \\ & + \mathrm{Res}(c'_{n-} + id'_n; |X/L|)]\} \quad \forall X. \end{aligned} \tag{5.91}$$

The location of the poles in the upper righthand quadrant of the complex plane are shown in figure 5.2.

Figure 5.2 reveals that the relationship between a and b is well approximated by $b = \cosh a$ and similarly for a' and b'. (5.80) and (5.89) then indicate that the roots

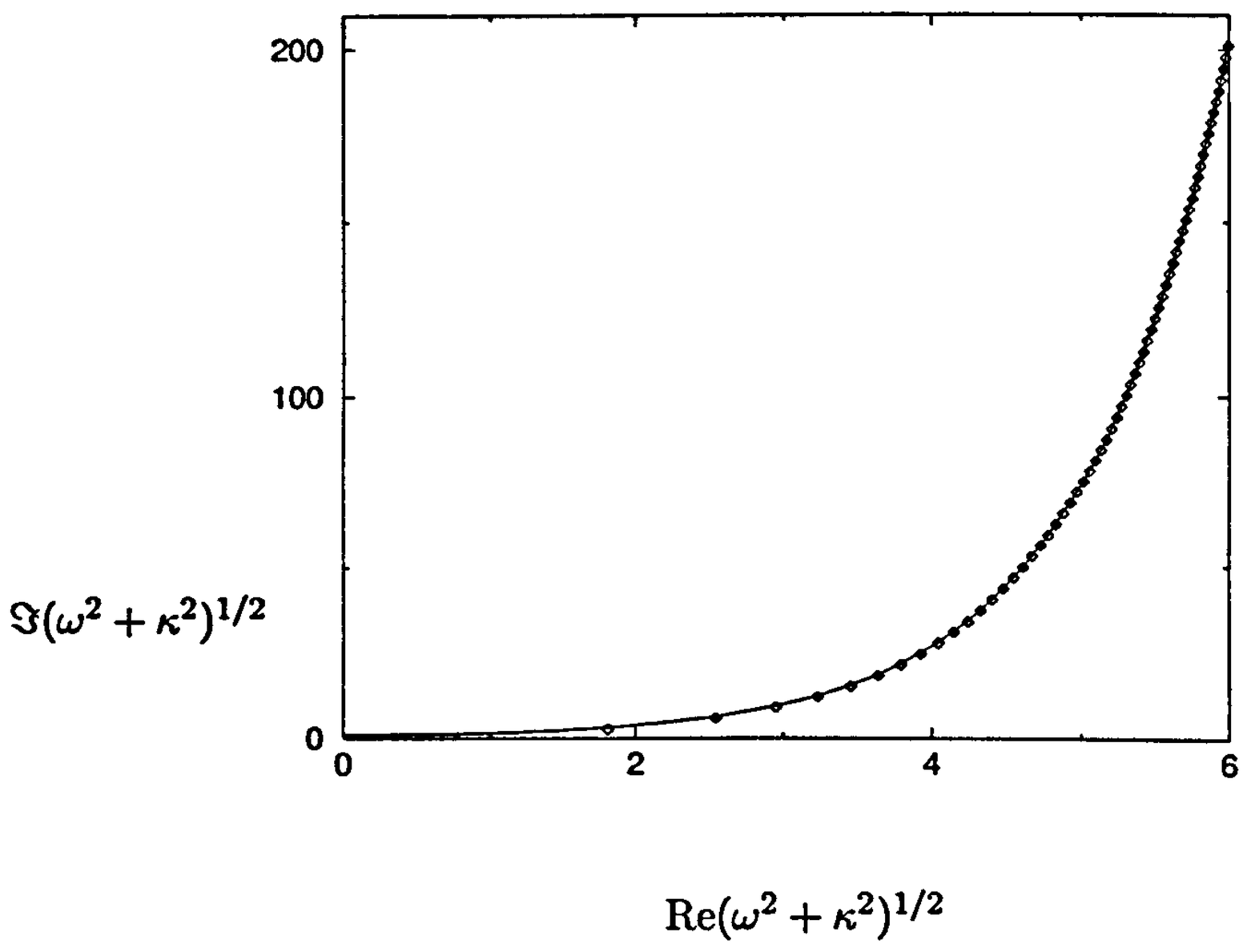

Figure 5.2: The location of the poles of the integrand found in the definition of K'. ♦ represent $a_{n+} + ib_n$ and ◊ represent $a'_{n+} + ib'_n$

must occur near to $\cos b = 1$ and $\cos b' = 1$, i.e. $b_n \approx 2n\pi$, $b'_n \approx (2n+1)\pi$. These relationships can be investigated by defining two small parameters, Δb_n and $\Delta b'_n$:

$$b_n = 2n\pi + \Delta b_n \quad \text{and} \quad b'_n = (2n+1)\pi + \Delta b'_n, \tag{5.92}$$

where $|\Delta b_n|$, $|\Delta b'_n| \ll 1$. Substituting these expressions into (5.81) and (5.88) respectively leads to

$$\Delta b_n = -\frac{\ln 4n\pi}{2n\pi} + O(n^{-1}) \quad \text{and} \quad \Delta b'_n = -\frac{\ln(4n+2)\pi}{(2n+1)\pi} + O(n^{-1}). \tag{5.93}$$

As $a_{n\pm}$, $b_{n\pm}$, $a'_{n\pm}$ and $b'_{n\pm}$ are independent of the system variables, they were calculated before any simulations were carried out and stored in a file. Now the kernel has been evaluated attention is turned to the deformation integral equation in which it appears. As quadratic basis functions are being used for the field variables (5.64) can be rewritten as

$$D(X) = \frac{1-\nu^2}{E} \sum_{e=1}^{N} \int_{X_{e_1}}^{X_{e_3}} K'(X-X')(a_{e_0} + a_{e_1}X' + a_{e_2}X'^2)\mathrm{d}X'. \tag{5.94}$$

The expression for K' (5.91) was substituted into (5.94) and this allowed the integral to be computed analytically in terms of the a's, b's, K and L. As K' was written as an infinite sum, so the resulting linear relationship between P_i' and D_i' contains infinite sums. However, the sums are well behaved leading to an efficient method. A big advantage of this semi-analytic approach is that the resulting equations are extremely robust and all problems relating to singular nature of K' have been avoided.

The relationship between the P_i' and D_i' is described above and as it linear it can be expressed in the form

$$R_i^{def} = D_i' - K_{ij}' P_j' \qquad 1 \leq i, j \leq \texttt{NUMNODES} \tag{5.95}$$

The complete set of equations to be solved for is

$$\mathbf{R} = \begin{pmatrix} \mathbf{R}^{lub}(\mathbf{u}) \\ \mathbf{R}^{def}(\mathbf{u}) \\ R^{pd}(\mathbf{u}) \end{pmatrix}, \tag{5.96}$$

and the unknowns to be solved for are

$$\mathbf{u} = (P_2', P_3', ..., P_{\texttt{NUMNODES}}', D_1', D_2', ..., D_{\texttt{NUMNODES}}', \Sigma). \tag{5.97}$$

The aim is to find the value of the roll speed for which the system is neutrally stable, i.e. $\Sigma = \partial\Sigma/\partial K = 0$. This was achieved as follows. For a given set of operating parameters the base flow of chapter 4 was solved for. Following this the perturbed equations, described in this chapter, were solved and hence Σ was found. $\partial\Sigma/\partial K$ was found numerically by repeating the whole process for a slightly different value of K. The idea is to perform a Newton iteration on the pair of equations

$$\Sigma = 0, \tag{5.98}$$

$$\frac{\partial\Sigma}{\partial K} = 0. \tag{5.99}$$

The parameters being varied were U_R and K. This was a computationally intensive method but was found to be extremely robust requiring minimum operator intervention.

The method was tested by computing the critical capillary number Ca_{crit}, for a positive gap regime with $E = 10^{40}$ and comparing with the F.E. results of Coyle et al. (1990d) that relate to a rigid roll coater with a fully flooded upstream inlet. Results are shown in figure 5.3 and it is clear that they are in good agreement with the worst error

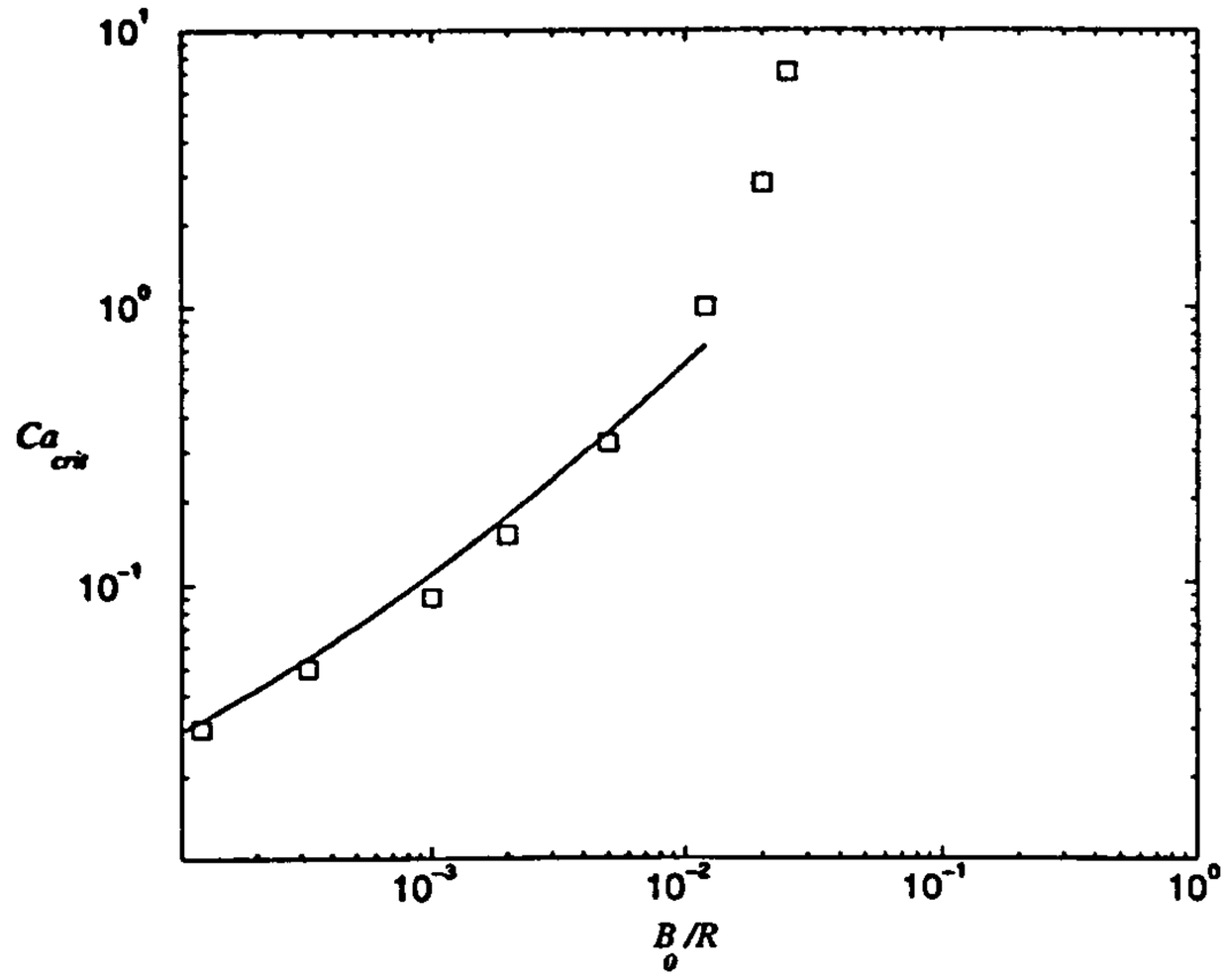

Figure 5.3: Critical capillary number against $B_0/\bar{R}$. Solid line generated by present model with $E = 10^{40}$. □ corresponds to F.E. results of Coyle et al (1990d).

being 10%. However, as the gap is reduced the agreement improves and as deformable roll coaters operate with narrow gaps the model was thought to be more than adequate for predicting the stability of flows found in deformable roll coating.

5.4 Results

Under certain operating conditions, $\sigma < 0 \; \forall \; k$ and hence the flow is stable to small perturbations. However, under different conditions $\sigma > 0$ over a range of k and the flow will be unstable to all perturbations that have a Fourier component whose wavelength falls within this range. In between these two cases exists the critical case for which $\sigma < 0$ for all k except at k_{crit} where $\sigma(k_{crit}) = 0$ and it follows that $\partial\sigma(k_{crit})/\partial k = 0$. The conditions under which this occurs are said to be critical. Results will be presented in terms of the critical capillary number, though as will now be discussed below, care has to be taken in interpreting the results correctly.

5.4.1 Interpretation of results

Although the results below are presented in a nondimensional form, the numerical code is written in a dimensional form to aid the transition from positive to negative gaps, as

discussed in chapter 4. During the numerical search for the critical capillary number, the values of all the physical parameters were held constant, except for the roll speed U_R which was allowed to vary until the conditions became critical. This is the situation most often encountered in the laboratory and in industry, i.e. for a given pair of rollers and a given fluid, what is the maximum speed that the system can operate at before an instability occurs? Obviously this means that $E_S = \mu U / E\bar{R}$ is not constant along the critical curves and so to aid the presentation of results, a new nondimensional number, E_T, is introduced and is defined as:

$$E_T = \frac{T}{E\bar{R}}. \tag{5.100}$$

It follows from the above discussion that E_T is indeed constant on the critical curves, even though Ca varies and results from now on will be presented in terms of this number where appropriate. Note that Carvalho and Scriven (1999) present results in terms of constant E_S yet state that larger critical capillary numbers imply a faster maximum speed of operation for a given set of rolls. This cannot be inferred directly from their results as constant E_S for a *fixed pair of rollers and fluid* implies fixed U_R which in turn implies that surface tension is the only parameter that can be varied when searching for the critical capillary number. Thus a critical curve with E_S held constant can be thought of as a curve of critical surface tension, whereas a curve with E_T held constant can be thought of as a curve of critical roll speed.

5.4.2 Flow restabilisation

Figure 5.4 shows a typical solution curve as the gap setting passes from positive to negative. A curve for an equivalent pair of rigid rolls is shown for comparison. It is clear from the figure that as the gap decreases from large and positive, the critical capillary number falls, in line with the rigid roll results. However, as the point of transition from positive to negative gap is approached, the critical capillary number relating to the deformable roll pair becomes less sensitive to the gap setting whilst the critical capillary number relating to the rigid pair falls dramatically. Therefore, a deformable roll pair are substantially more stable than an equivalent rigid roll pair at the same small positive gap setting. When the gap width becomes increasingly negative the critical capillary number actually rises, a result not predicted by the work

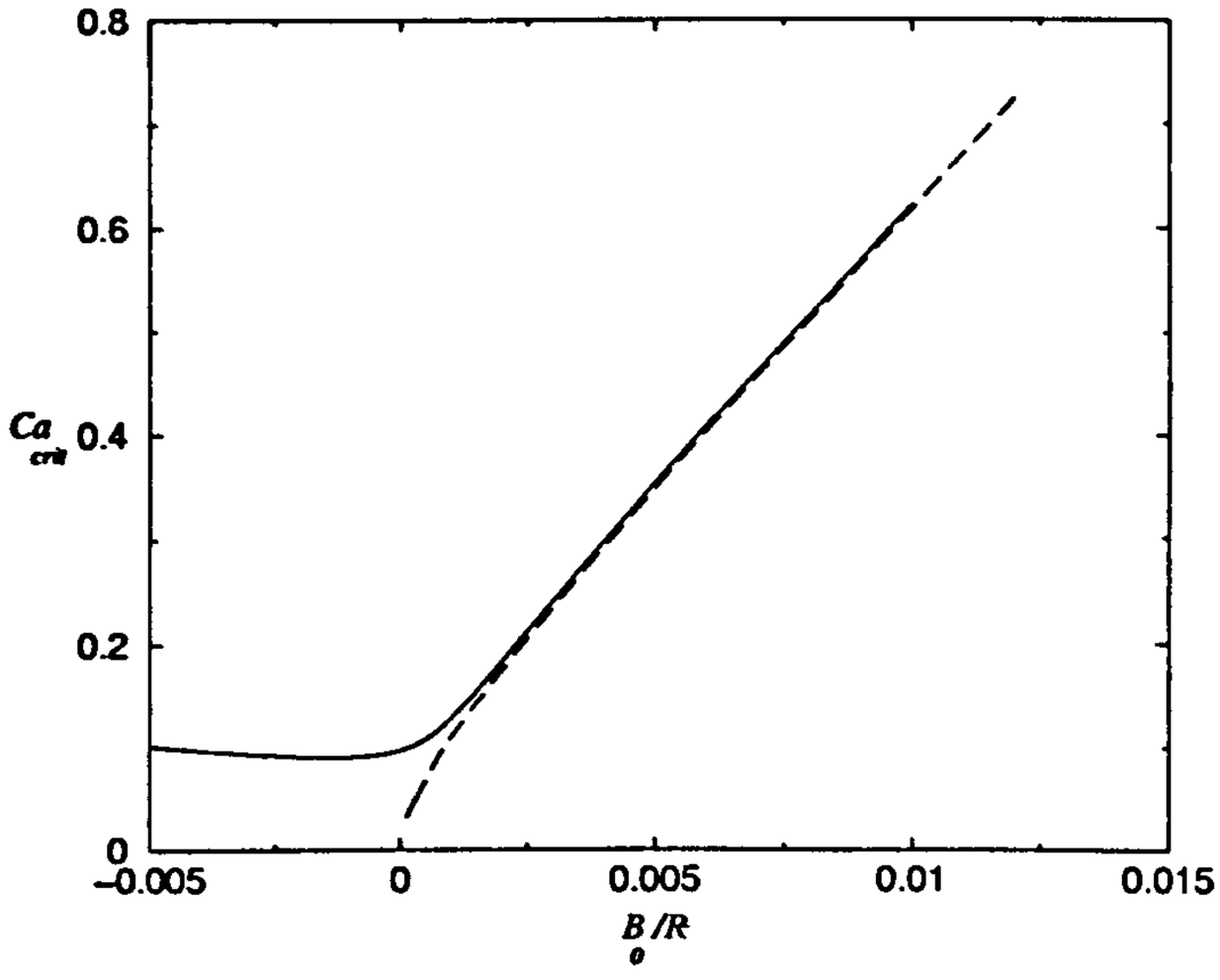

Figure 5.4: Critical capillary number against $B_0/\bar{R}$ both a deformable (—) and rigid roll (– –) coater.

of Carvalho and Scriven. Thus at certain speeds of operation, the flow will be stable for a large positive gap, destabilise as the gap is narrowed and becomes negative and then restabilises for sufficiently negative gaps.

5.4.3 Comparison of effects of E and L

Figure 5.5 shows critical capillary number curves for several different values of E_T. In the regions where the deformable layer plays a roll in the physics of the problem, i.e. at negative gap settings and for small positive gaps, there is an appreciable difference in the critical curves for different values of E_T. This is not unexpected since as $E_T \rightarrow 0$, the behaviour of the compliant roller approaches that of the equivalent rigid roller and as has already been seen previously, the critical curves of rigid and deformable rollers are quite different. Thus decreasing the Youngs modulus of the compliant layer will increase the stability of the corresponding coating flow.

In the previous chapter, the similarities and differences between the roles of E^{-1} and L were examined in detail. A major motivation for this was to see whether the similarities predicted by simple scaling arguments and implicitly assumed by the spring models of other workers were valid. The conclusion drawn from steady state results was that such spring models could never reproduce the physics of the problem in sufficient

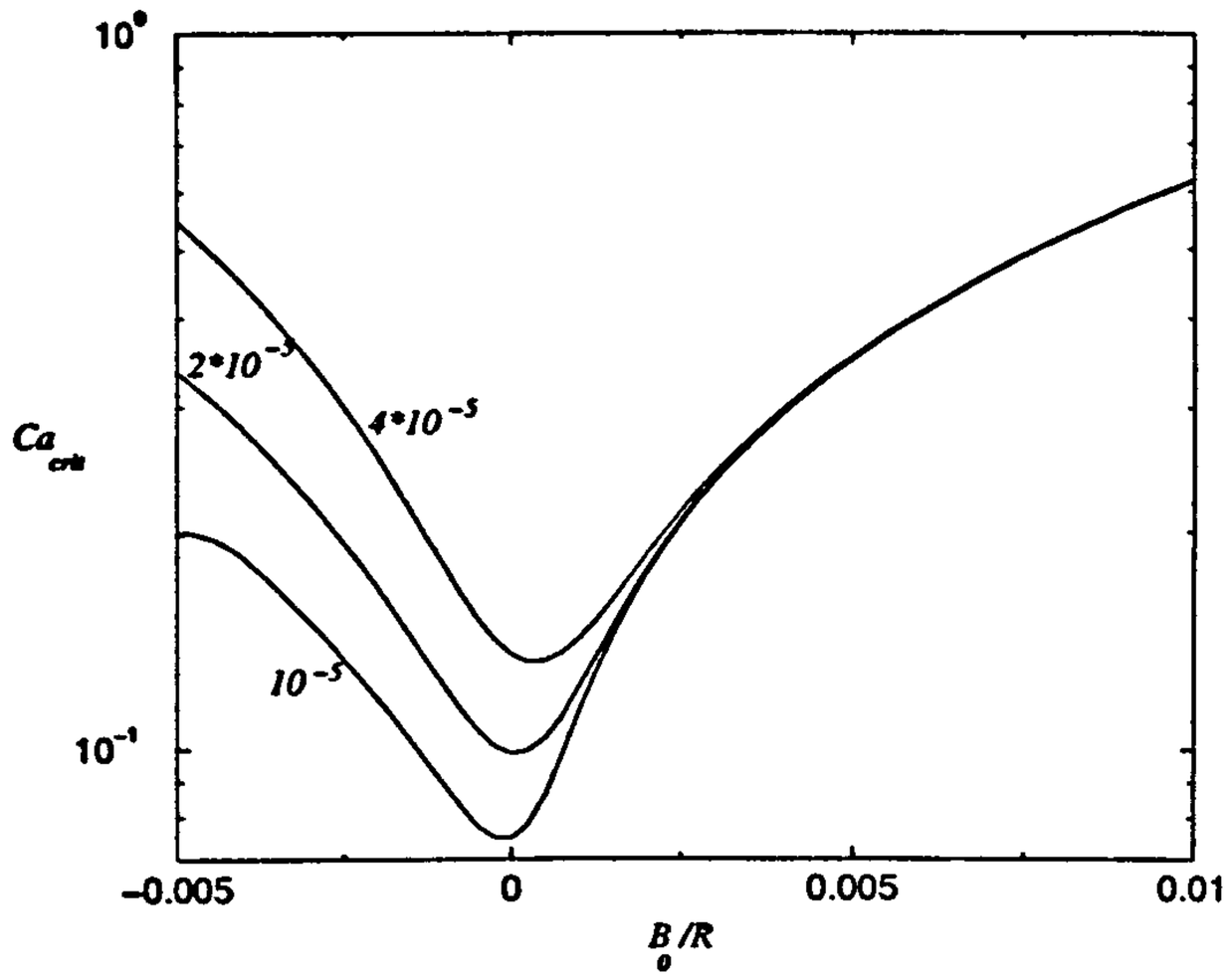

Figure 5.5: Critical capillary number against $B_0/\bar{R}$ for different values of E_T. $L/\bar{R} = 0.05$.

detail to give results that were qualitatively correct, nevermind quantitativily correct. The reader is reminded that such spring models found favour due to their simplicity and hence ease of use in formulating models to predict the stability of deformable roll coating systems. In the following section the effect of $L/\bar{R}$ on the critical capillary number is examined and compared with the results of the previous section in order to determine whether the conclusions of the previous chapter carry through to the stability results.

Critical capillary curves for a range of values of $L/\bar{R}$ are shown in figure 5.6. Again, for large positive gaps, all curves follow that of the rigid roll equivalent. For small positive and negative gaps it can be seen that deeper layers afford more stability than their shallower counterparts and therefore, in this region L and E^{-1} have the same qualitive effect on the stability of the system. However, as the gap becomes more negative, the differences between the critical curves corresponding to differing values of $L/\bar{R}$ reduce and if the gap is increased in magnitude still further, the critical curves actually intersect and the systems with shallow layers become the most stable. Hence it is not possible to make a general comment such as 'deep layer systems are more stable than shallow systems' since the results are dependent on B_0. This is clearly not the case when the effect of E_T is considered and so, as in the previous chapter, the conclusion

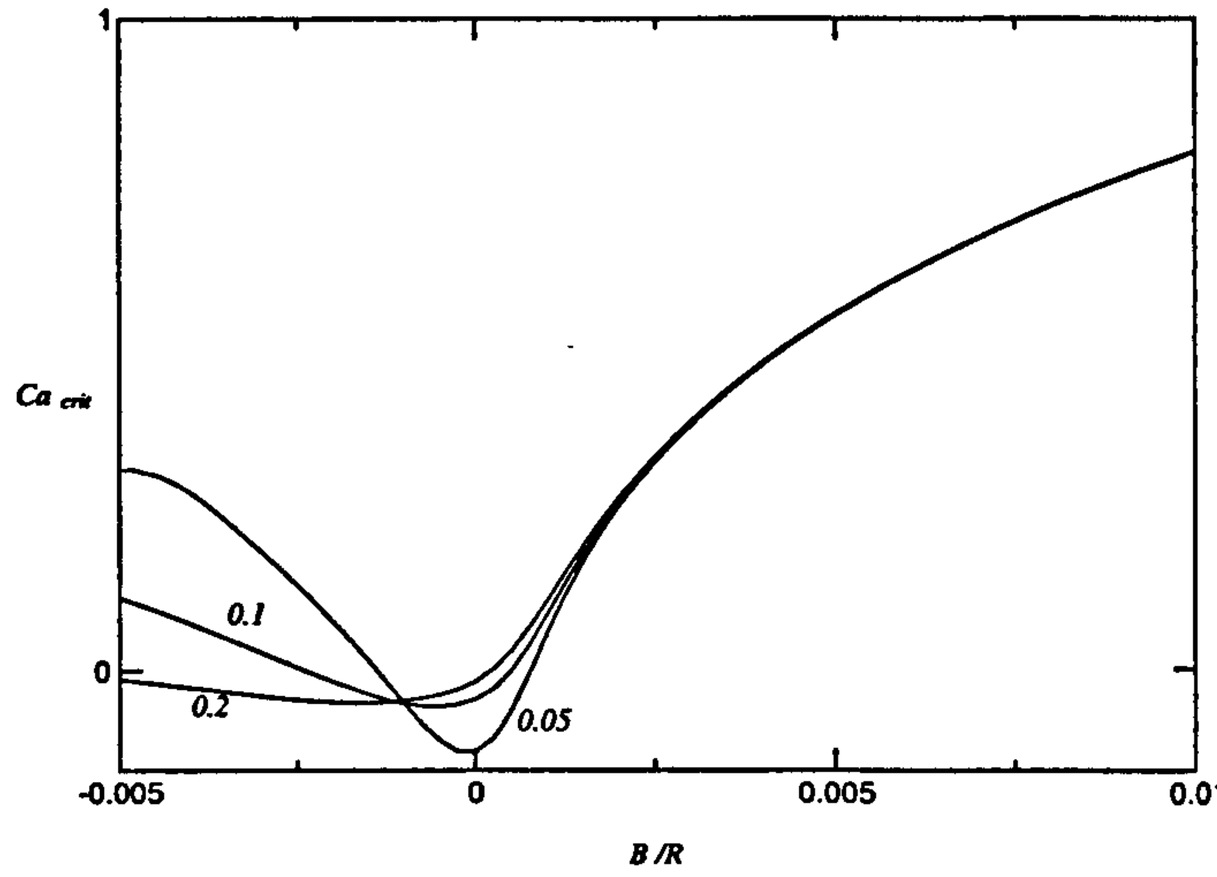

Figure 5.6: Critical capillary number against $B_0/\bar{R}$ for different values of $L/\bar{R}$. $E_T = 10^{-5}$

is drawn that L and E^{-1} do not have the same effect throughout parameter space and hence the use of spring models to predict the stability of the system is invalid.

The question of why L and E^{-1} have different effects remains open. The answer can be found in chapter 4 where the steady state results were presented. It was shown that L and E^{-1} have a similar effect on the flow rate yet differ in their effects on X_D and this is the key to why they differ in their respective effects on the stability of the system. The role of X_D and layer swelling in the determination of the stability of the system can be understood via the stability hypothesis (1.19). The S.H. states that the flow is stable iff

$$\left.\frac{\mathrm{d}P^0}{\mathrm{d}X}\right|_{X_D^0} < \left.\frac{1}{B_D^{02}}\frac{\mathrm{d}B^0}{\mathrm{d}X}\right|_{X_D^0}. \tag{5.101}$$

This can be rewritten using (4.9) and (4.17) to give

$$B_D^{02}\left.\frac{\mathrm{d}P^0}{\mathrm{d}X}\right|_{X_D^0} = 12Ca\left(1-\frac{1.34Ca^{2/3}}{1+3.88Ca^{2/3}}\left(1+\frac{1}{2}B_X^0|_{X_D^0}\right)\right) < \left.\frac{\mathrm{d}B^0}{\mathrm{d}X}\right|_{X_D^0}, \tag{5.102}$$

which in turn gives

$$12Ca\left(1-\frac{1.34Ca^{2/3}}{1+3.88Ca^{2/3}}\right) < \left(1+\frac{1}{2}\frac{1.34Ca^{2/3}}{1+3.88Ca^{2/3}}\right)\left.\frac{\mathrm{d}B}{\mathrm{d}X}\right|_{X_D}. \tag{5.103}$$

This relationship reveals how the gap gradient affects the stability of the meniscus - increase the gradient and the flow will become more stable. In the cases studied here an increase in X_D led to an increase in the gap gradient due to the rigid roll contribution.

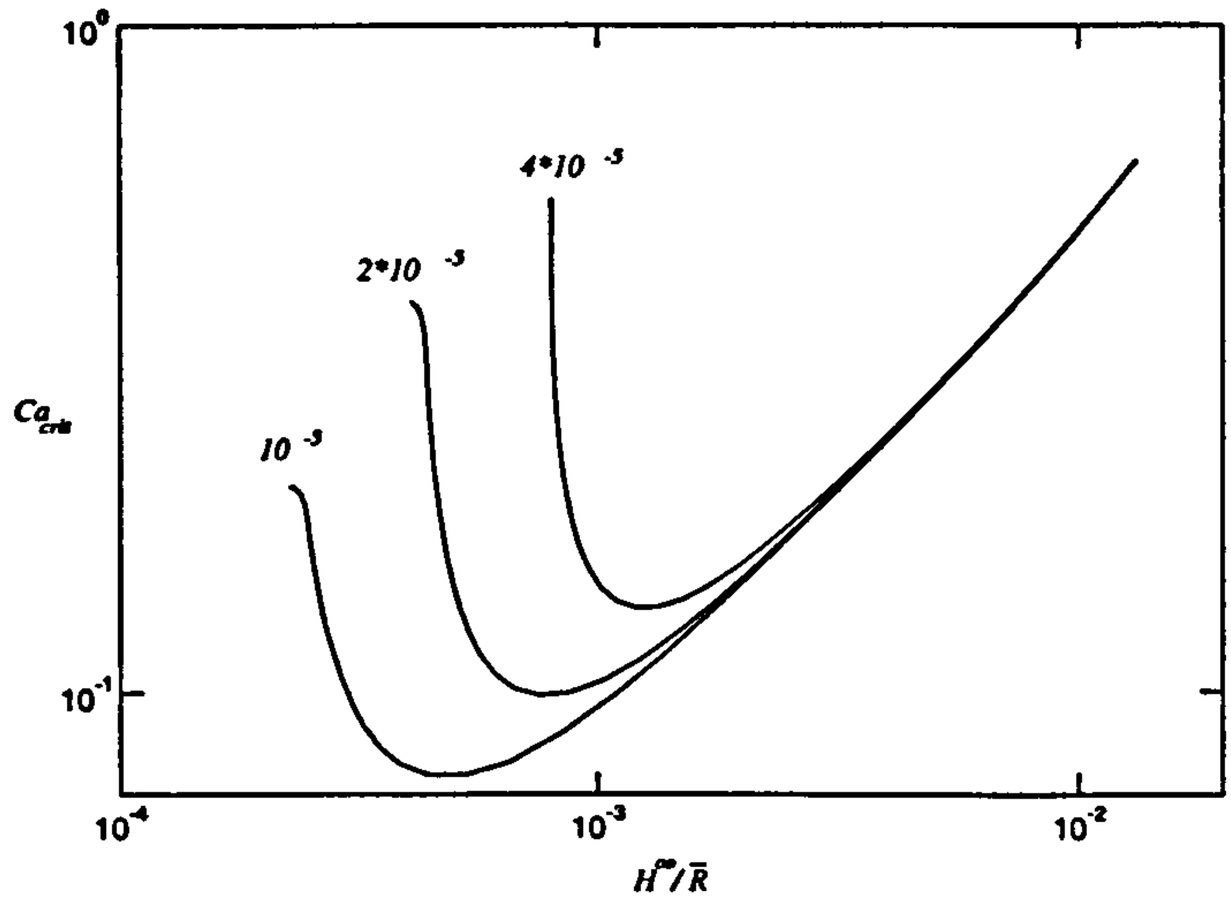

Figure 5.7: Critical capillary number against $H^\infty/\bar{R}$ for different values of E_T. $L/\bar{R} = 0.05$.

Therefore an increase in X_D will lead to a more stable system. The true significance of figures (4.10) and (4.12) is now evident as they show that increasing E decreases X_D for all values of B_0 whereas the situation for variable L is dependent upon B_0. For small negative gaps increasing L leads to an increase in X_D but for large negative gaps the reverse is true. This ties in exactly with the stability results that show increasing E decreases stability for all B_0 whereas the results for varying L depend upon B_0 with deeper layers being more stable at small negative gaps and less stable at large negative gaps.

5.4.4 The relationship between Ca_{crit} and H^∞

As was stated in the outset of this thesis, the industrialist is concerned with both the thickness and the uniformity of the outgoing film. Hence a convenient way to present the stability results is to plot the critical capillary number against H^∞. This is shown in figure 5.7 for various values of E_T. It is clear that for a given value of H^∞, the critical capillary number increases as E_T increases and therefore the speed of the process could be increased by softening the compliant layer.

Figure 5.8 shows the results when E_T is fixed and $L/\bar{R}$ varies. As the layer is deepened the critical capillary number rises but the results indicate that this relationship has a pratical limit as the difference in the stability curves for $L/\bar{R} = 0.1$ and 0.2 are

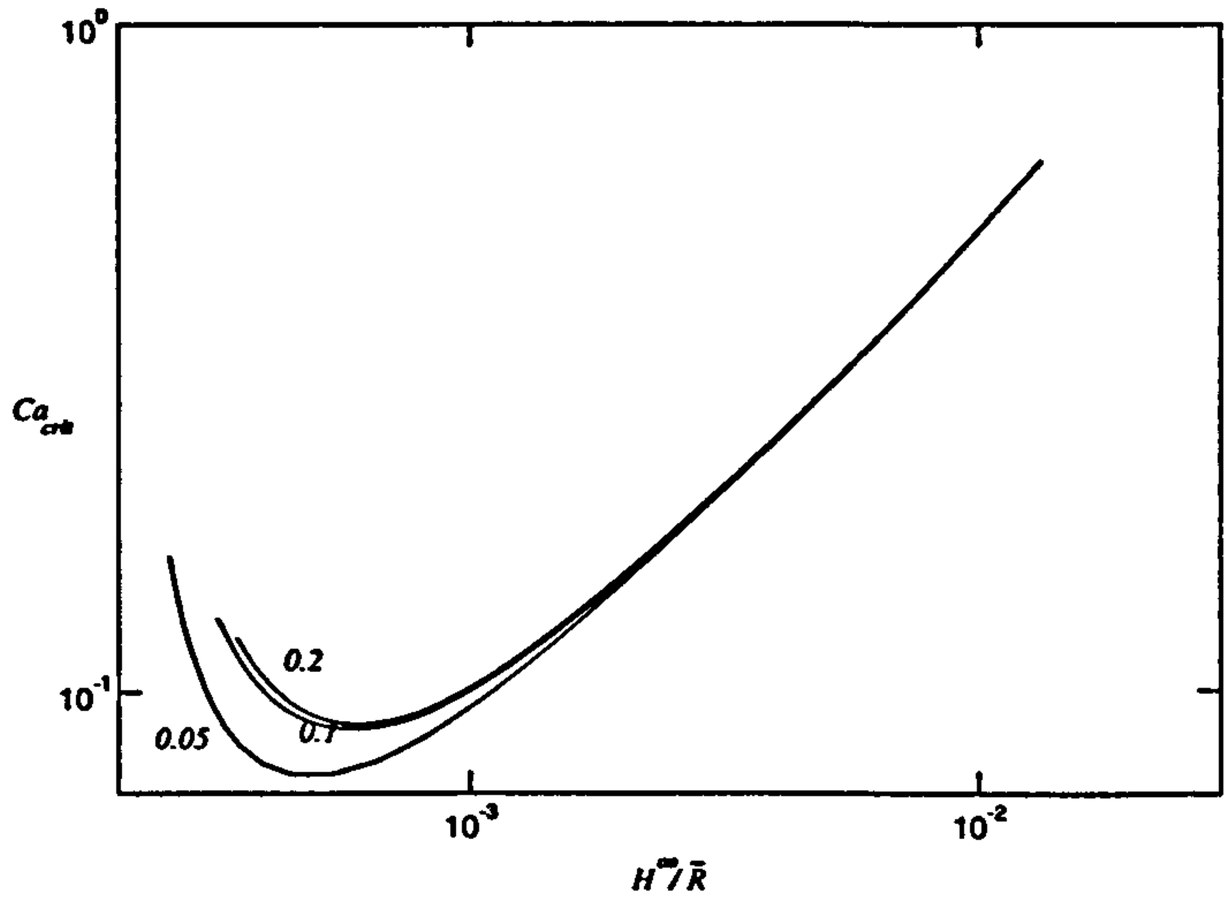

Figure 5.8: Critical capillary number against $H^\infty/\bar{R}$ for different values of $L/\bar{R}$. $E_T = 10^{-5}$.

similar. This effect is studied in more detail by fixing $B_0/\bar{R}$ and plotting Ca_{crit} against $L/\bar{R}$. The results are shown in figure 5.9 and it can be seen that the deeper the layer the less sensitive Ca_{crit} is to it.

5.4.5 The relative importance of D'

In section 5.2.1 arguments were presented to justify the inclusion of the perturbations to the deformable layer, D' and it was suggested that these could play a significant role in determining the stability of the system. The inclusion of the deformable layer perturbations added considerably to the complexity of the model as the integral equation representing the deformation had to be solved simultaneously with the 2-D Reynolds equation and so if it could be shown that these perturbations could be neglected legitimately, the resulting set of equations would be considerably simplified. The effect of D' on the results was examined by retaining the correct value of E_T in the steady state calculations but letting $E \rightarrow \infty$ in (5.65) Figure 5.10 shows critical capillary number against $B_0/\bar{R}$ curves both with the correct value of E (i.e. the value used to obtain the steady base flow results) and with a much larger value. In the figure little difference can be seen between the two sets of results and the maximum difference found over the range of $B_0/\bar{R}$ covered is 2% and from this it is inferred that it is legitimate to neglect the D' terms. This result indicates that the reasons presented earlier for the inclusion

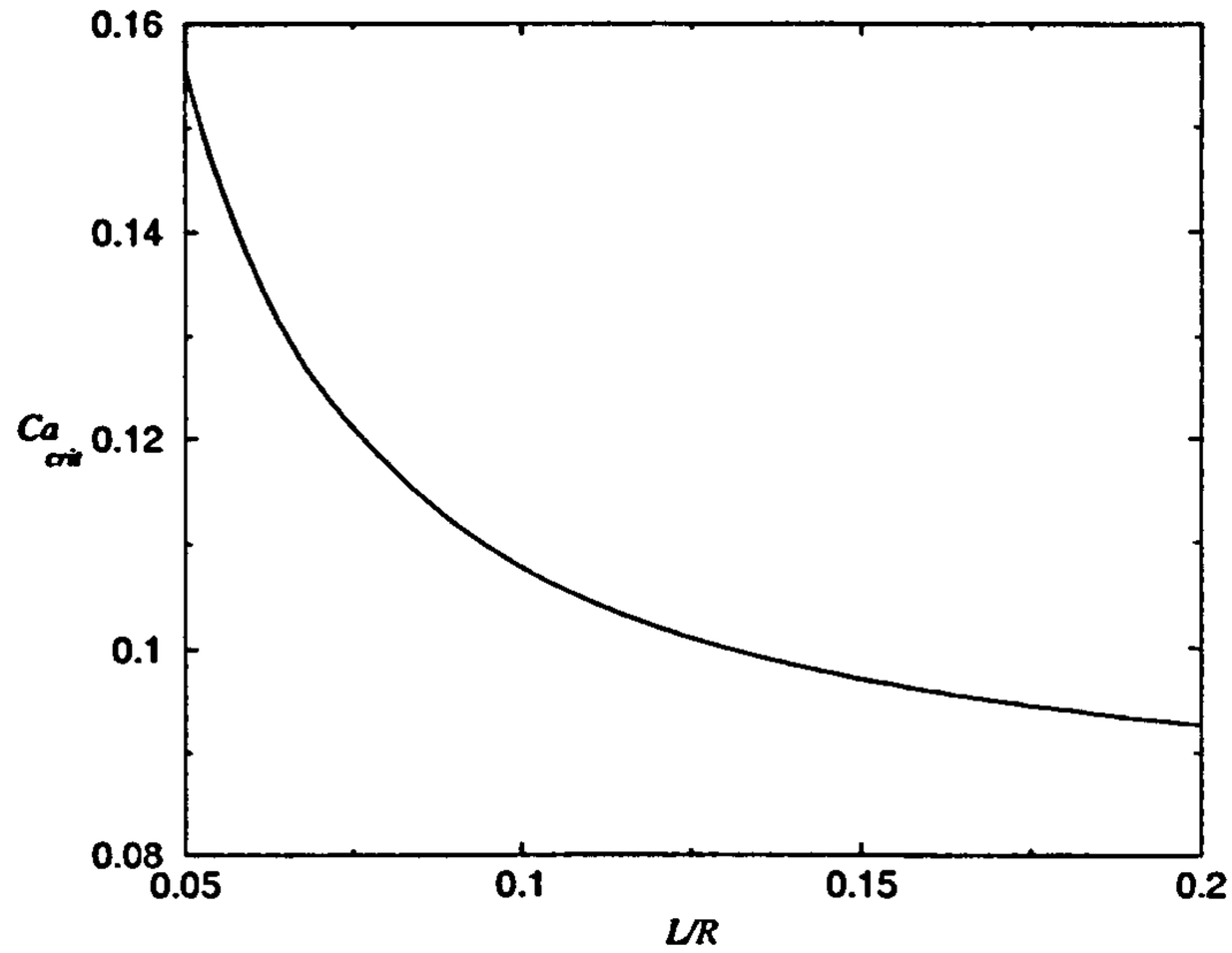

Figure 5.9: Critical capillary number against L/R. $B_0/\bar{R} = 0.00325$, $E_T = 10^{-5}$.

of D' are false and the reason why is now explained.

P' is caused by the disturbance to the meniscus and so is balanced by the capillary pressure caused by the perturbed meniscus. As was seen in the steady state results for positive gaps, a pressure of this magnitude was not sufficient to produce a significant roll deformation and the same occurs here - the pressure generated by the perturbation to the meniscus location is insufficient to deform the compliant layer and hence D' can be neglected.

The fact that D' can be neglected has significant consequences for any stability analysis as it implies that a model for the deformation of the compliant layer need only be included in the base state calculations and only the fluid equations need be retained for the solution of the perturbed quantities and the growth rate. Therefore the work of Carvalho and Scriven in using a plain strain model to calibrate a spring model that was then used to model both the base and perturbed states in a stability analysis was unneccesary - better results could have been obtained by using the plain strain model to calculate the base state and then solving the perturbed fluid equations with the solution domain being provided by the base state results.

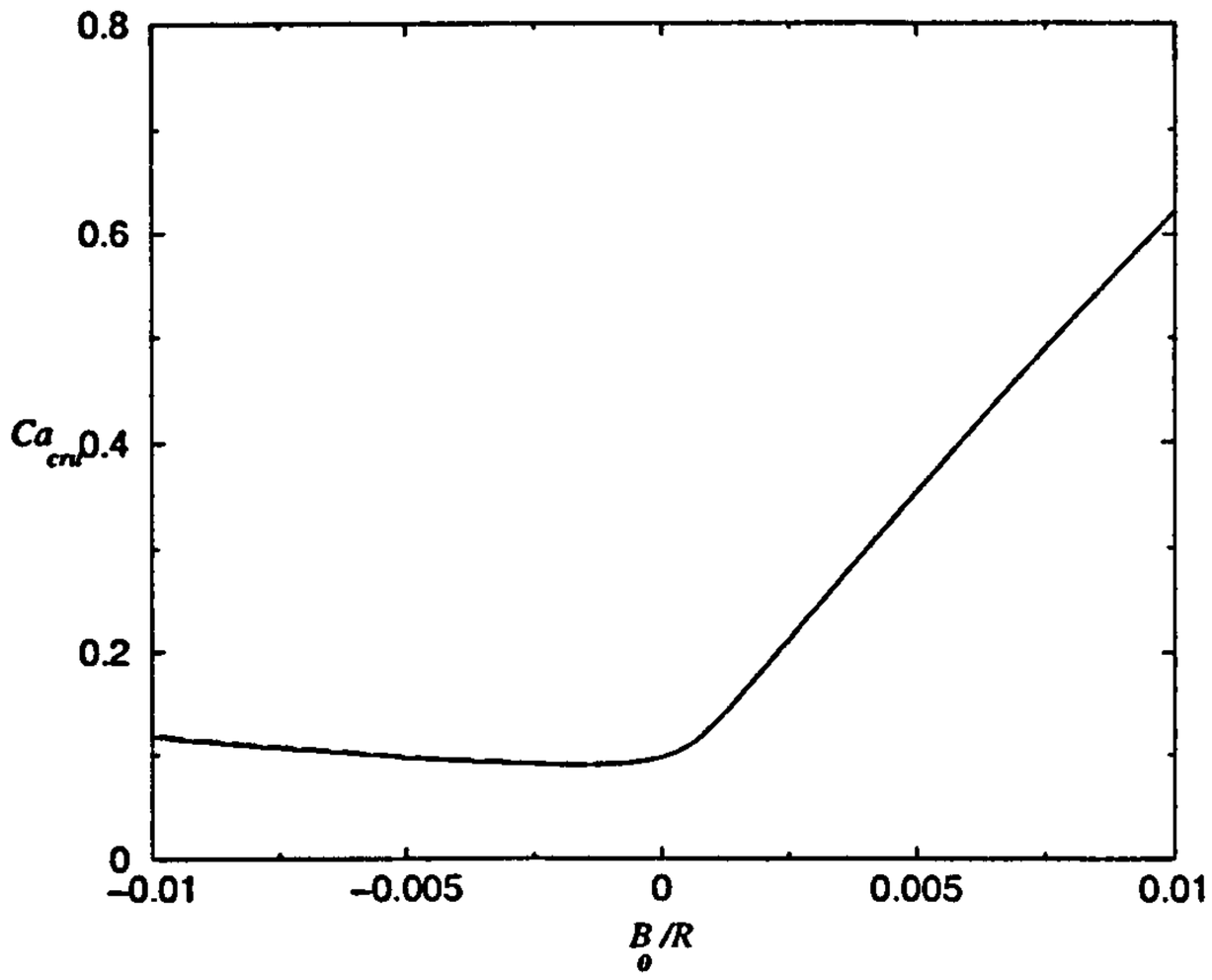

Figure 5.10: Critical capillary number against $B_0/\bar{R}$ with (—) and without (– –) D' included. $L/\bar{R} = 0.2$, $E_T = 10^{-5}$.

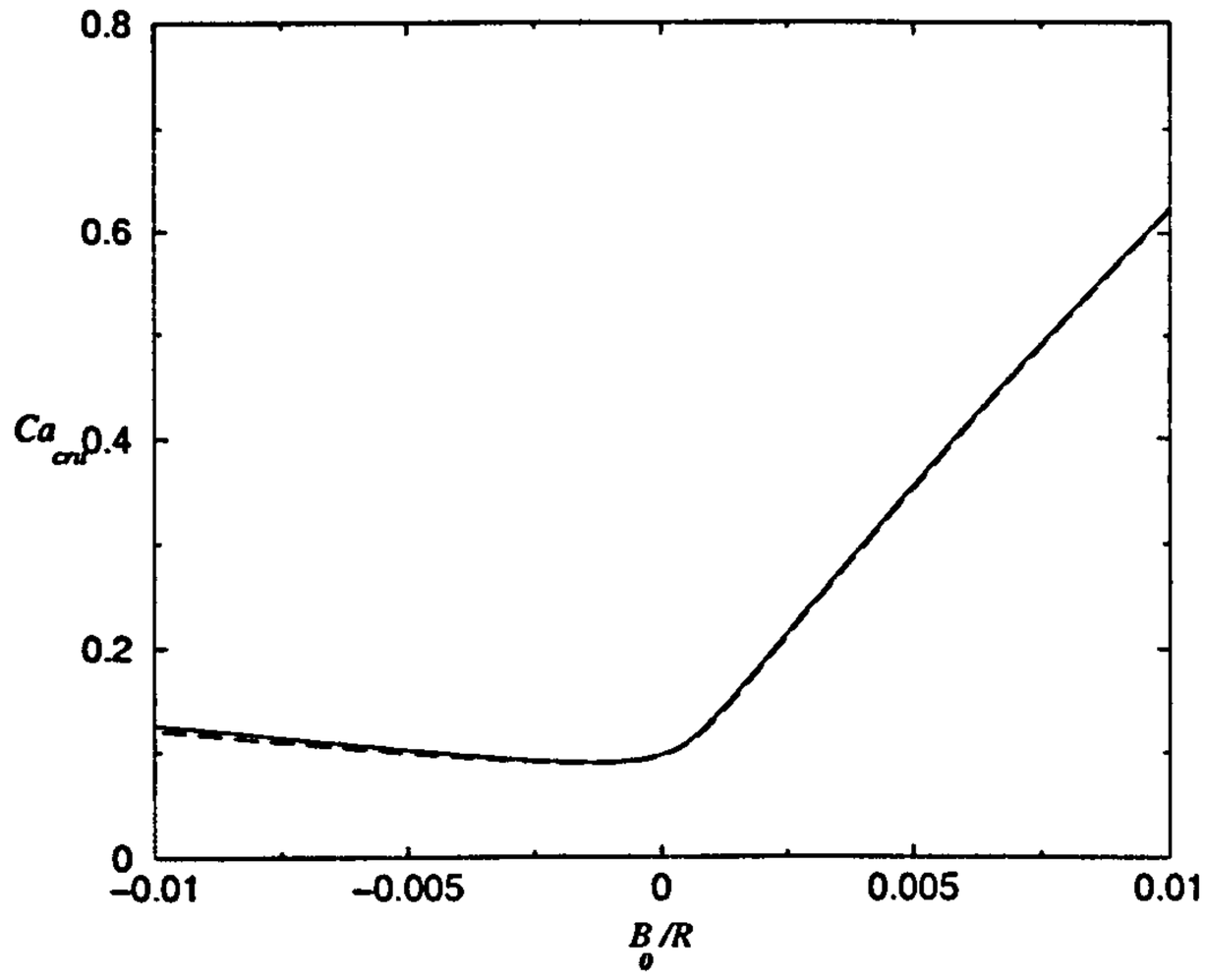

Figure 5.11: Critical capillary number against $B_0/\bar{R}$ with (– –) and without (—) viscoelastic terms included. $L/\bar{R} = 0.2$, $E_T = 10^{-5}$.

5.4.6 Viscoelastic effects

As it has been shown that D' can safely be neglected, the effect of viscoelastic phenomena on the stability of the system can be determined by making use of the viscoelastic model introduced in chapter 4.

In chapter 4 it was shown that the difference between theory and experiment could be explained by introducing viscoelastic effects. The same values were used in a stability analysis and the results are shown in figure 5.11 along with the equivalent elastic results and the figure reveals that the viscoelastic terms have little effect. At first this seems to contradict the findings of the previous chapter that showed how the viscoelastic terms could play a significant role but those results were presented for $Ca = 1$. However, the critical capillary number in the negative gap regime is $O(0.1)$ implying a roll speed one tenth of that used to generate the results of the previous chapter. The viscoelastic terms are proportional to $T_\sigma U_R$ and $T_\epsilon U_R$ and therefore a ten fold decrease in U_R results in viscoelastic terms one tenth the size as those encountered in chapter 4.

It is expected that an increase in De would result in the viscoelastic terms playing a role in the system's stability but further investigation into this was beyond the scope of this thesis. However, the important point is that the FSM has been successfully extended to include viscoelastic terms and this model, due to the valid neglect of D', can be used to study the stability of such systems.

5.5 Summary

In this chapter the stability of the flow in a forward deformable roll coater was analysed.

The model of chapter 4 was used to provide base states for a linear stability analysis. The perturbed fluid equations gave rise to a 2-D Reynolds equation but the form of this equation differed from the 2-D Reynolds equation of chapter 3 as it included terms due to the perturbation of the compliant layer. The elastic version of the integral deformation equation of chapter 4 was extended to include sinusoidal lateral variations. The boundary conditions imposed at the meniscus were the long wave limit of the conditions developed in chapter 3.

As in chapter 4, a finite element method was employed to solve the governing equations though the fact that the integrand of the integral deformation equation depended

upon the wavenumber would have meant that any numerical scheme that handled the integral equation in the same manner as chapter 4 would have been computationally expensive. This led to the form of the integral containing P, rather than $\tilde{P}$ being used and the kernel, also defined through an integral, being evaluated via complex analysis techniques.

Results were presented in the form of critical capillary number verus gap width. For large positive gaps the system behaved like a rigid roll system. As the gap width was decreased the critical capillary number fell. As the transition to negative gaps was approached it was found that Ca_{crit} became less sensitive to the gap width and in fact as the gap became increasingly negative Ca_{crit} increased. This flow restabilisation has not been reported before.

It was found that for positive gaps E and L^{-1} played a similar role but for large negative gaps the role of L^{-1} was reversed. This was linked to the effect of L^{-1} on the steady state meniscus position via a stability hypothesis.

Results of Ca_{crit} against H^{∞} reveal that a given film thickness can be coated faster with softer deeper layers. The effect of the deformation perturbations was examined and it was found that they play a minor role. Thus an accurate picture of the system's stability can be obtained from solving the layer deformation equations in the steady state only and this approach enabled the viscoelastic model of chapter 4 to be briefly looked at.

Chapter 6

Conclusions and suggestions for further work

6.1 Conclusions

The aim of this chapter is review the main results of this thesis and make suggestions for further work.

Chapter 1 presented a review of the relevant literature. It was demonstrated how lubrication theory has been applied to the modelling of roll coating flows and special attention was given to reviewing the various boundary conditions that have been used to terminate the flow domain.

In chapter 2 the two dimensional steady base state solutions of the DFF bead found in multiple roll coaters were studied. It was found that the leading order Landau Levich conditions that have been employed successfully in related problems were inadequate in this case. A matched asymptotic analysis confirmed the leading order corrections suggested by Reinelt and it was found that these small terms could play a significant role. The small terms were able to play a large role because in the DFF, it is possible that the difference in the radii of curvature of the two menisci (and hence the difference in the pressure drop across each interface) is of the same order as the small correction terms. The asymptotic analysis also gave a solution for the menicus profile in the case of unequal roll speeds.

The influence of the small correction terms is greatest at the critical value of S, S_c, beyond which no steady two dimensional solutions exist. The critical phenomena of

bead break was associated with S_c and this was supported by a stability hypothesis that predicted the upstream meniscus to be neutrally stable and therefore the inclusion of the small terms is vital for an accurate prediction of the limits of operation of a multiroll coater. It was shown that as the returning film fraction approached one, the system is finely balanced between a system that is susceptible to bead break as S is increased and one that is susceptible to flooding as S is increased. The value of the flux at the predicted point of flooding was in good agreement with experiment and numerical work. Regions of parameter space were also found where the stability hypothesis predicted two stable 2-D steady states.

As the returning film fraction was reduced to zero, the correction terms at the upstream meniscus allowed the HOM DFF model to give results in qualitative agreement with experiment for the SFF bead.

Chapter 3 presented a linear stability analysis of the DFF bead problem. The asymptotic framework of chapter 2 was used to study the relationship between the pressure drop across the meniscus and the wavenumber of the disturbance. This analysis revealed the link between two distinct and often used forms of the boundary condition. The turning points of the x_u solution curves had been predicted by the stability hypothesis to correspond to states with upstream menisci that were neutrally stable with respect to 2-D disturbances and this was confirmed by the linear stability analysis. The linear stability analysis confirmed that there are regions of paremeter space where two stable steady states exist. The linear stability analysis also predicted the occurence of ribbing on the downstream meniscus under certain conditions.

In chapter 4 the steady base state solutions of a forward deformable roll coater were examined. The boundary conditions of chapter 2 were extended to cover a wide range of Ca and results were in excellent agreement with F.E. predictions in the literature. The compliant layer was model was based on a linear plain strain model previously used by Young (1997) and was extended to include viscoelastic efffects. The effects of E and L^{-1} on the field variables were studied and revealed that they do not have the same effect on the meniscus location in the negative gap regime. This was an important result as the widely used spring models make the assumption that E and L^{-1} have identical effects on the system. The reason for this difference was shown to be caused by layer swelling at the edge of the contact region - a phenomena that cannot

be reproduced by spring models as they do not preserve the volume of the layer.

The effects of the viscoelastic terms were briefly looked at and it was seen that they could be used to explain the difference between theoretical predictions and experimental measurements. However, an exact comparison between theory and experiment was ruled out as the compliant layer used in the experiments had not been fully characterised.

The stability of the deformable roll coater was analysed in chapter 5. Lubrication theory was again used to model the flow and the boundary conditions of chapter 4 were perturbed. The integral equation that was used to describe the compliant layer in chapter 4 was extended to include sinusoidal lateral variations and the kernal of the resulting integral equation was evaluated using a complex analysis and this led to an efficient and robust numerical scheme.

The validity of the model was confirmed by testing it against rigid roll results available in the literature and good agreement was found.

The model was used to investigate the effect of E and L^{-1} on the stability of the system. For positive gaps the results it was found that E and L^{-1} had the same effect. However, for negative gaps the role of L^{-1} was reversed and this was explained in terms of the effect of L^{-1} on the steady state meniscus location. The model also showed that a given film thickness can be coated at a faster rate with softer deeper layers.

The role of the deformation perturbations was shown to be negligible and this had the important implication that the solid equations only needed to be solved for the steady state base flow. The effect of the viscoelastic terms was briefly investigated but the results were inconclusive.

6.2 Suggestions for further work

The analysis of the DFF bead provided some interesting and unexpected results and it would be interesting to try and confirm the results via computations. Of particular interest would be a detailed computational analysis of the turning points to investigate how accurately these are described with the leading order corrections. An experimental program would be of interest as well. The transition from bead break to flooding could be investigated as could the meniscus profile - all with aim of proving or disproving the

theory.

A nonlinear stability analysis could reveal if the system can can realign itself from state to another in the regions of parameter space where multiple states were predicted. The analysis may also reveal the form of the disturbance on the downstream meniscus - whether it is ribbing or some more complicated time dependent disturbance.

For the deformable roll problem the most useful avenue of work would be to carry out an experimental program with the accurate characterisation of the compliant layer paramount. This would be of great use to anyone trying to develop usful models as currently there is a lack of information on the properties of the layer.

In both coating flows considered in this chapter the effects of inertia and gravity could be explored. In addition both systems can be run in the reverse mode and currently little work has been done on either system in this mode, inparticular the deformable roll coater.

Bibliography

ADACHI, T. J. 1988 *AIChE Spring National Meeting.* Orlando, Paper 3c.

ALEKSANDROV, V. M. 1962 Contact problem of a stamp on an elastic layer: English translation. *Prikl. Mat. Mekh.* **27**, 1490.

ARMSTRONG, C. G. 1986 An analysis of the stress in a thin layer of articular cartilage in a synovial joint. *Eng. Med.* **15**, 55.

BAPAT, C. N, & BATRA, R. C. 1984 Finite plain strain deformations of nonlinear viscoelastic rubber covered rolls. *Int. J. Num. Methods in Engg.*, **20**, 1911–1927.

BATCHELOR, G. K. 1967 An introduction to fluid dynamics. Cam. Univ. Press

BATRA, R. C. 1980 Rubber covered rolls - the non-linear elastic problem. *Trans. ASME* **47**, 82–86.

BENJAMIN, D. F, & SCRIVEN, L. E. 1992 Coating flows analysed by form and function. *Coating press* **2**, 1–31.

BENJAMIN, D. F. 1994 Roll coating flows and multiple roll systems. PhD thesis. University of Minnesota.

BENJAMIN, D. F, ANDERSON, T. J. & SCRIVEN, L. E. 1995a Multiple roll systems: steady state operation. *AIChE* **41** 5, 1045–1060.

BENJAMIN, D. F, ANDERSON, T. J. & SCRIVEN, L. E. 1995b Multiple roll systems: residence times and dynamic response. *AIChE* **41** 10, 2198–2211.

BENKREIRA, H., EDWARDS, M. F. & WILKINSON, W. L. 1981a A semi-empirical model of the forward roll coating flow of Newtonian fluids. *Chem. Eng. Sci.* **36**, 423–427.

BENKREIRA, M. F., EDWARDS, M. F. & WILKINSON W. L. 1981b Roll coating of purely viscous liquids. *Chemical Engineering Science* **36**, 429–34.

BENTALL, R. H, & JOHNSON, K. L. 1968 An elastic strip in plane rolling contact. *Int. J. Mech. Sci.*, **10**, 637–663.

BIRKHOFF, G, & HAYS, D. F. 1963 Free boundaries in partial lubrication. *J. Mathematics and Physics (M.I.T.* **42**(2), 126–138.

BIXLER, N. E. 1982 Stability of a coating flow. PhD thesis, University of Minnesota.

BOHAN, M. F. J., LIM, C. H., KOROCHKINA, T. V., CLAYPOLE, T. C., GETHIN, D. T. & ROYLANCE, B. J. 1997 An investigation of the hydrodynamic and mechanical behaviour of a soft nip rolling contact. *J. Engng. Trib.*, **211**, No. J1, 37–49.

BRETHERTON, F. P. 1961 The motion of long bubbles in tubes. *J. Fluid Mech.* **10**, 166-88.

CARTER, G. C., & SAVAGE, M. D. 1987 Ribbing in a variable speed two roll coater *Math. Engng. Ind.* **1**, 83–95.

CARVALHO, M. S 1999 Non-Linear Elastoviscous Model of Deformable Roll Cover. *Advances in Coating and Drying of Thin Films: Proceedings of The third European Symposium.*, 265.

CARVALHO, M. S, & SCRIVEN, L. E. 1994 Effect of deformable roll covering on roll coating. *TAPPI journal*, **77**(5), 201.

CARVALHO, M. S, & SCRIVEN, L. E. 1995a Deformable roll coating: Analysis of ribbing instability and it's delay. *The mechanics of thin film coating: Proceedings of The first European Symposium.*, 75–84.

CARVALHO, M. S, & SCRIVEN, L. E. 1995b Deformable roll coating: Modeling of steady flow in gaps and nips. *The mechanics of thin film coating: Proceedings of The first European Symposium.*, 221–230.

CARVALHO, M. S, & SCRIVEN, L. E. 1996 Capillary and Viscoelastic Effects on Elastohydrodynamic Lubrication in Roller Nips. *Trans. ASME*, **118** 872–879.

CARVALHO, M. S, & SCRIVEN, L. E. 1997a Deformable roll coating: Steady state and linear perturbation analysis. *J. Fluid Mechanics*, **339**, 143–172.

CARVALHO, M. S, & SCRIVEN, L. E. 1997b Flows in Forward Deformable Roll Coating Gaps: Comparison between Spring and Plane-Strain Models of Roll Cover. *J. Computational Physics*, **138**, 449–479.

CARVALHO, M. S, & SCRIVEN, L. E. 1999 Three-Dimensional Stability Analysis of Free Surface Flows: Applications to Forward Deformable Roll Coating. *J. Computational Physics*, **151**, 534–562.

COHU, O, & MAGNIN, A. 1995 Experimental investigations on roll coating with deformable rolls. *The mechanics of thin film coating: Proceedings of The first European Symposium.*, 179–188.

COHU, O, & MAGNIN, A. 1997 Forward roll coating of Newtonian fluids with deformable rolls: an experimental investigation. *Chem. Eng. Sci*, **52** 1339–1347.

COYLE, D. J, MACOSKO, C. W, & SCRIVEN, L. E. 1986 Film-splitting flows in forward roll coating. *J. Fluid Mech.*, **171**, 183–207.

COYLE, D. J. 1988a Forward roll coating with deformable rolls: A simple one dimensional elasto-hydrodynamic model. *Chemical Eng. Science*, **43**, 2673–2684.

COYLE, D. J. 1988b Experimental studies of flow between deformable rolls. *AIChE Spring National Meeting*, Orlando. Paper 3d.

COYLE, D. J, MACOSKO, C. W, & SCRIVEN, L. E. 1990a The fluid dynamics of reverse roll coating. *AICHe Journal* **36**, No. 2, 161–174.

COYLE, D. J, MACOSKO, C. W, & SCRIVEN, L. E. 1990b A simple model of reverse roll coating. *Ind. Eng. Chem. Res.* **29**, 1416–1419.

COYLE, D. J. 1990c (March) Nonlinear squeeze theory of deformable roll coating. In *AIChE Spring National Meeting*, Orlando. Paper 35h.

COYLE, D. J, MACOSKO, C. W, & SCRIVEN, L. E. 1990d Stability of symmetric film splitting between counter-rotating cylinders *J. Fluid Mech.* **216**, 437–458.

COYLE, D. J. 1997 Knife and Roll Coating. In *Liquid Film Coating* (eds. S. F. Kistler and P. M. Schweizer), pp. 539–571. Chapman and Hall Publishers.

DANIELS, N. 1998 Instabilities in roll and slot coating flows. PhD thesis. University of Leeds.

DECRE, M., GAILLY, E., & BUCHLIN, J. M. 1995 Meniscus shape experiments in forward roll coating. *Phys. Fluids* **7**, No.3, 458–467.

DENNERY, P. & KRZYWICKI, A. 1967 Mathematics for physicists. Harper International.

DOWSON, D, & WHITAKER, A. V. 1965 The iso-thermal lubrication of cylinders. *ASLE Transactions*, **8**, 224–234.

DOWSON, D, & HIGGINSON, G. R. 1966 *Elasto-hydrodynamic lubrication.* Pergamon Press.

ELSHARKAWY, A. A, & HAMROCK, B. J. 1995 Elasto-hydrodynamic lubrication of elastomeric covered surfaces in line contact. *Proceeding of the Institite of Mech. Engineers*, **209**.

FALL, C. 1978 Surface ribbing of a thin viscous fluid film emerging from a spreader or roller. *Trans. ASME J. Lub. Tech.*, **100** 462–466

FALL, C. 1982 A theoretical model of striated film-rupture. *Trans. ASME J. Lub. Tech.*, **104** 164–167

GASKELL, P. H., INNES, G. E., & SAVAGE, M. D. 1998 An experimental investigation of meniscus roll coating. *J. Fluid Mech.* **355**, 17–44.

GASKELL, P. H., SAVAGE, M. D., SUMMERS, J. L., & THOMPSON, H. M. 1995 Modelling and analysis of meniscus roll coating. *J. Fluid Mech.* **298**, 113–137.

GASKELL, P. H., SAVAGE, M. D., THOMPSON, H. M. 1998 Stagnation-saddle points and flow patterns in Stokes flow between contra-rotating cylinders. *J. Fluid Mech.* **370**, 221–247.

GORYACHEVA, I. G. 1998 *Contact mechanics in tribology.* Boston : Kluwer Academic Publishers.

GREENER, J. & MIDDLEMAN, S. 1975 A theory of roll coating of viscous and viscoelastic fluids. *Polymer Eng. and Sci.* **15** 1

GREENER, J. & MIDDLEMAN, S. 1979 Theoretical and experimental studies of the fluid dynamics of a two-roll coater *Ind. Engg. Chem. Fund.* **18** 35-41

HALL R. W., & SAVAGE, M. D. 1988a Two-dimensional elastohydrodynamic lubrication .1. The associated dry contact problem *Proc. Instn. Mech. Engrs. Part C - J. Mech. Eng. Sci.* **202**, No. 5, 347–353

HALL R. W., & SAVAGE, M. D. 1988b Two-dimensional elastohydrodynamic lubrication .2. Solution of the line contact problem. *Proc. Instn. Mech. Engrs. Part C - J. Mech. Eng. Sci.* **202**, No. 5, 354–360.

HAMROCK, B. J. 1966 *Elasto-hydrodynamic lubrication.* Pergamon Press.

HASEGAWA T., & SORIMACHI, K. 1993 Wavelength and depth of ribbing in roll coating and its elimination *AIChE* **39**, 6, 935–945.

HERREBRUGH, K. 1968 Solving the incompressible and isothermal problem in elasto-hydrodynamics through an integral equation. *ASME J. Lubric. Tech.* **90**, 262–270.

HERTZ, H. 1882 On the contact of solids *J. reine und angewandte Mathematik.* **92** 156–171.

HINCH, J. 1995 Perturbation Methods. Cam. Univ. Press

HO, W. S., & HOLLAND, F. A. 1978 Between rolls metering coating technique: A theoretical and experimental study. *Tappi* **61**, No. 2, 53–56.

HOOKE, C. J. 1986 Elasto-hydrodynamic lubrication of a cylinder on a elastomeric layer. *WEAR*, **111**, 83–99.

HOOKE, C. J., & O'DONOGHUE, J. P. 1972 Elasto-hydrodynamic lubrication of soft, highly deformed contacts. *J. Mech. Engg. Sci.*, **14**, 34–48.

HOPKINS, M. R. 1957 Viscous flow between rotating cylinders and a sheet moving between them. *Brit. J. Appl. Phys.*, **8**, 442.

HOUPERT, L. D., & HAMROCK, B. J. 1986 Fast approach for calculating film thickness and pressure in elasto-hydrodynamically lubricated contacts at high loads. *Trans. ASME J. Tibology*, 411–420.

HUEBNER, K. H. 1975 The finite element method for engineers. Wiley.

JAFFAR, M. J. & SAVAGE, M. D. 1988 On the numerical solution of line contact problems involving bonded and unbonded strips. *J. Strain Analy.*, **23**, 67–77.

JAFFAR, M. J. 1990 Two-dimensional elasto-hydrodynamic lubrication of elastic strips. *Wear*, **139**, 335–350.

JIN, Z., & DOWSON, D. 1989 The influence of elastic deformation upon film thickness in lubricated bearings with low elastic modulus. In *Proceedings of the Leeds-Lyon Symposium.* pp263–269

JOHNSON, K. L. 1970 Regimes of elasto-hydrodynamic lubrication. *J. Mech. Engng. Sci.*, **12**, 9–16.

JOHNSON, K. L. 1985 *Contact mechanics* Cam. Univ. Press

KAPUR, N. 1999 Flow phenomena in fixed-gap and gravure roll coating systems. PhD thesis. University of Leeds.

KAPUR, N., GASKELL, P. H. & SAVAGE, M. D. 2000 Bead break instability. *Accepted for publication, Phys. Fluids*

LANDAU, L, & LEVICH, B. 1942 Dragging of a liquid be a moving plate. *Acta Physicochemia U.R.S.S.*, **XVII(1–2)**, 42–54.

MALONE, B. 1992 An experimental investigation of roll coating phenomena, PhD thesis, University of Leeds.

MEIJERS, P. 1968 The contact problem of a rigid cylinder on an elastic layer. *Appl. Sci. Res.*, **18**, 353–382.

MICHALLAND S. 1992 Etude des differents regimes dynamiques de l'instabilite de l'impremeur. Thesis L'Ecole Normale Superieure, Paris.

MICHALLAND S., RABAUD, M. & COUDER, Y. 1996 Instabilities of the upstream interface in directional viscous fingering. *J. Fluid Mech.* **312** 125–148.

MYERS, T. G., SAVAGE, M. D. & GASKELL, P. H. 1994 The indentation of an elastic layer by a sharp punch. *J. Mech. App. Maths.*, **47**, 129–140.

PARK, C. W. & HOMSY, P. H. 1984 Two-phase displacement in Hele Shaw cells: theory. *J. Fluid Mech.* **139**, 291–308.

PEARSON, J. R. A. 1960 The instability of uniform viscous flow under rollers and spreaders. *J. Fluid Mech.* **7**, 481–500.

PITTS, E. & GREILLER, J. 1961 The flow of thin liquid films between rollers. *J. Fluid Mech.* **11**, 33–50.

PRANDTL, L. 1904 Motion of fluids with very little viscosity. *Tech. Memor. Nat. Adv. Comm.*, **452**.

QUERE, D. 1999 Fluid coating Proceedings of 3^{rd} European coating symposium 1999 Ed. Durst, F. & Raszillier, H.

RABAUD, M., MICHALLAND S. & COUDER, Y. 1990 Dynamical regimes of directional viscous fingering - spatiotemporal chaos and wave propogation. *Physical Review Letters* **64**, 184–87.

RABAUD, M. & HAKIM, V. 1991 Shape of stationary and travelling cells in the printer's instability. *Instabilities and nonequilibrium structures III* ed. Tirapegui and Zeller.

REINELT, D. A. 1995 The primary and inverse instabilities of directional viscous fingering. *J. Fluid Mech.* **285**, 303–327.

RUSCHAK, K. J. 1982 Boundary conditions at a liquid–air interface in lubrication flow. *J. Fluid Mech.*, **119**, 107–120.

RUSCHAK, K. J. 1985 Coating flows. *Ann. Rev. Fluid Mech.*, **17**, 65–89.

SAVAGE, M. D. 1977a Cavitation in lubrication. Part 1. On boundary conditions and cavity-fluid interfaces. *J. Fluid Mech.* **80** 743–755

SAVAGE, M. D. 1977b Cavitation in lubrication. Part 2. Analysis of wavy interfaces. *J. Fluid Mech.* 80 757–767

SAVAGE, M. D. 1984 Mathematical model for the onset of ribbing. *AIChE* 30 6 999–1001

SCHNEIDER, G. 1962 Analysis of forces causing flows in roll coaters. *Trans. Soc. Rheology* 6 209-221

STIEBER, W. 1933 Das scwimmlager, hydro-dynamische thorie des gleitlagers. *Berlin, VDI.*

SWIFT, H. W. 1931 The stability analysis of lubricating films in journal bearings. *Proc. Inst. Civil Engrs.*, **233**, pp267.

TAYLOR, G. I. 1963 Cavitation of a viscous fluid in a narrow passage. *J. Fluid Mech.*, **16**, 565-619.

WILSON, M. 1997 Free surface flows between co-rotating and contra-rotating cylinders. PhD thesis. University of Leeds.

WINKLER, E. 1867 Die lehre von der elasticiteat und festigkeit. *Prog. Dominicus*

XUE, Y. K, GETHIN, D. T, & LIM, C. H. 1994 Numerical modelling of the contact between lithographic printing press rollers by soft EHL thory. *J. of Eng. Tribology*, **208**.

XUE, Y. K, GETHIN, D. T, & LIM, C. H. 1996 Elastohydrodynamic lubrication analysis of layered line contact by the boundary element method. *Int. J. Num. Meth. Eng.*, **39**, No. 15, 2531-2554.

YOUNG, A. E. 1997 A theoretical and experimental investigation of deformable roll coating. Ph.D. thesis, University of Leeds.